La structure nucléaire dans le voisinage de noyaux doublement magiques : mesure des temps de vie au voisinage du^{68}Ni et recherche d'isotopes autour du ^{100}Sn

I. Celikovic

To cite this version:

I. Celikovic. La structure nucléaire dans le voisinage de noyaux doublement magiques : mesure des temps de vie au voisinage du^{68}Ni et recherche d'isotopes autour du ^{100}Sn. Physique Nucléaire Expérimentale [nucl-ex]. Université de Caen, 2013. Français. <tel-00981493>

HAL Id: tel-00981493
https://tel.archives-ouvertes.fr/tel-00981493

Submitted on 22 Apr 2014

HAL is a multi-disciplinary open access archive for the deposit and dissemination of scientific research documents, whether they are published or not. The documents may come from teaching and research institutions in France or abroad, or from public or private research centers.

L'archive ouverte pluridisciplinaire **HAL**, est destinée au dépôt et à la diffusion de documents scientifiques de niveau recherche, publiés ou non, émanant des établissements d'enseignement et de recherche français ou étrangers, des laboratoires publics ou privés.

Université de Caen Basse-Normandie
U.F.R. de Sciences
ÉCOLE DOCTORALE SIMEM

Thèse de doctorat

présentée et soutenue le : 9 Décembre 2013
par
M. Igor ČELIKOVIĆ
pour obtenir le
DOCTORAT de l'UNIVERSITÉ de CAEN
Spécialité : Constituants élémentaires et physique théorique
Arrêté du 07 aout 2006

préparée dans le cadre d'une cotutelle internationale de thèse

entre l'Université de Caen Basse-Normandie et l'Université de Belgrade

Nuclear structure around doubly-magic nuclei: lifetime measurements in the vicinity of ^{68}Ni and search for isomers around ^{100}Sn

Jury :

M. Bertram BLANK	Directeur de recherches	CENBG (***Rapporteur***)
M. Frédéric NOWACKI	Directeur de recherches	Université de Strasbourg (***Rapporteur***)
M. Jovan PUZOVIĆ	Associate Professor	Faculty of Physics, University of Belgrade
M. Miodrag KRMAR	Associate Professor	Faculty of Sciences, University of Novi Sad
M. Krunoslav SUBOTIĆ	Principal research fellow	Institute of Nuclear Sciences "Vinča"
M. Dragan TOPREK	Senior research associate	Institute of Nuclear Sciences "Vinča
M. Gilles DE FRANCE	Directeur de recherches	GANIL (***Directeur de Thèse***)
M. Marek LEWITOWICZ	Directeur de recherches	GANIL (***Codirecteur de Thèse***)

laboratoire commun CEA/DSM CNRS/IN2P3

GANIL T 2013 03

Université de Caen Basse-Normandie
U.F.R. de Sciences
ÉCOLE DOCTORALE SIMEM

Thèse de doctorat

présentée et soutenue le : 9 Décembre 2013
par

M. Igor ČELIKOVIĆ

pour obtenir le

DOCTORAT de l'UNIVERSITÉ de CAEN

Spécialité : Constituants élémentaires et physique théorique
Arrêté du 07 aout 2006

préparée dans le cadre d'une cotutelle internationale de thèse

entre l'Université de Caen Basse-Normandie et l'Université de Belgrade

Nuclear structure around doubly-magic nuclei: lifetime measurements in the vicinity of ^{68}Ni and search for isomers around ^{100}Sn

Jury :

M. Bertram Blank	Directeur de recherches	CENBG (***Rapporteur***)
M. Frédéric Nowacki	Directeur de recherches	Université de Strasbourg (***Rapporteur***)
M. Jovan Puzović	Associate Professor	Faculty of Physics, University of Belgrade
M. Miodrag Krmar	Associate Professor	Faculty of Sciences, University of Novi Sad
M. Krunoslav Subotić	Principal research fellow	Institute of Nuclear Sciences "Vinča"
M. Dragan Toprek	Senior research associate	Institute of Nuclear Sciences "Vinča
M. Gilles de France	Directeur de recherches	GANIL (***Directeur de Thèse***)
M. Marek Lewitowicz	Directeur de recherches	GANIL (***Codirecteur de Thèse***)

Acknowledgement

First of all, I would like to express my sincere gratitude to my mentor Gilles de France for his patience, guidance and continuous support through all the phases of my Ph.D. studies. Even when I was worrying about something, it would turn out that he had already had those things in mind and under control. I am also thankful to my co-supervisor Marek Lewitowicz for his guidance and for always finding time for me in his full agenda. My joint meetings with Gilles and Marek were enlightening to me, giving me good directions. Their passion and devotion to research were always like a burst of elan to me.

Also, I would like to thank my supervisor from Serbia, Prof. Jovan Puzović for his help and support while I was in Serbia. In addition, I would like to thank Bertram Blank and Frédéric Nowacki for accepting to be referees of my thesis and for thoroughly going through my manuscript. I would like to thank committee members from Serbia of my thesis defence: Miodrag Krmar, Krunoslav Subotić and Dragan Toprek. I am thankful to Dragan Toprek who was the leader of the bilateral project between my home institute "Vinča" and GANIL. He was my unofficial co-mentor from Institute "Vinča".

I would like to thank to the French Institute in Serbia, particularly Mr. Frederic Remay and Vesna Adamović for giving me scholarship to study both in GANIL and "Vinča".

I would like to sincerely acknowledge Piet for having the nerves to guide me through theoretical nuclear physics. He was always pedagogical and patiently answered all my, sometimes very basic questions. My deep gratitude goes to Manu for always being there for me, for his sharp and enlightening comments and suggestions regarding the analysis.

I would not be writing these lines now if there wasn't for Aurore, my office-mate who has been helping and supporting me in almost all stages of my work. We have also shared great moments of fun and joy that made my stay in GANIL pleasant. I am also thankful to Jean, Laurent, George, Bruno and Bertrand for taking care of EXOGAM, VAMOS and for beam tuning.

My gratitude also goes to the permanent stuff in GANIL: Francois, Beyhan, Fanny, Olivier, Lucia, Christelle and Maurycy for helping or supporting me in different ways.

During the three years of my PhD studies, a lot of students and post-docs have been in GANIL and I would like to thank them for the nice moments we shared together: Emil, Yannen, Kasia, Olivier, Mark, Julien, Kevin, Diego, Florent, Maria, Hongliang. Special thanks goes to Paola, Danilo and Carme for their friendship and for sharing a lot of beautiful moments.

Last but not least comes my acknowledgement for my colleagues from Institute "Vinča". First of all, I want to thank Zora S. Žunić, who brought me to Vinča a day after my graduation. I am thankful to Kruno for taking me into the world of nuclear physics and who started our collaboration with GANIL.

My colleagues and friends from the lab: Ivana, Mira, Sale, Zoran, Bojan, Aleksandar were always supportive and encouraging, for which I am grateful. I want to thank Peđa, "my brother in arms" for struggling with me in science starting from our first day at faculty, through Vinča and GANIL...

Finally, I want to thank my mum and dad for always believing in me, for encouraging and supporting me. Your kid has become a doctor, but not the medical one. What to do, nobody is perfect.

My last words and thoughts go to my beloved wife. Thank you Vesna for your patience, understanding, strength, support and love. You and our baby Jovan are the main driving force to me. You and Jovan gave me a new meaning of the word "nucleus".

Contents

Acknowledgement ii

1 General introduction 1

I The lifetime measurements around N=40 Zn isotopes 3

2 Introduction 5

2.1 The benchmark observables of nuclear structure 8

2.1.1 The seniority scheme 8

2.2 Collectivity in nucleus 10

2.2.1 Vibrational motion 10

2.2.2 Rotational motion 11

2.2.3 The Nilsson model 12

2.3 Evolution of collectivity around ^{68}Ni 12

2.3.1 Systematics of Ni isotopes 12

2.3.2 Systematics of even Z nuclei around Ni 16

2.3.3 Systematics of odd Z nuclei around Ni 21

2.4 Conclusions 23

3 Experimental set-up 25

3.1 Lifetime Measurements 25

3.1.1 Techniques for direct lifetime measurements 25

3.1.2 RDDS method and a plunger device 26

3.2 Deep-inelastic collisions 29

3.3 Detection system 31

3.3.1 VAMOS spectrometer 31

3.3.1.1 General description 32

3.3.1.2 Detection system for VAMOS 33

3.3.1.3 Trajectory reconstruction 34

3.3.1.4 Particle identification 35

3.3.2 EXOGAM 36

4 Data Analysis **39**
4.1 Calibration 39
4.1.1 Calibration of SED detectors 39
4.1.2 Energy calibration of Si detectors and ionisation chamber . . 41
4.1.3 Calibration of TAC and TOF 42
4.2 Particle identification 43
4.2.1 M/Q identification 43
4.2.2 M identification 46
4.2.3 Z identification 48
4.3 Recover of incomplete events 50
4.4 EXOGAM calibration 51
4.4.1 The addback and correction on Compton scattering 51
4.4.2 Calibration of Ge detectors 52
4.4.3 Doppler correction 53
4.5 The lifetime analysis: The differential decay curve method 55

5 Experimental results **59**
5.1 Zn isotopes 59
5.1.1 ^{70}Zn 59
5.1.2 ^{72}Zn 63
5.1.3 ^{68}Zn 64
5.1.4 ^{69}Zn 67
5.1.5 ^{71}Zn 68
5.1.6 ^{73}Zn 72
5.2 Cu isotopes 72
5.2.1 ^{69}Cu 73
5.3 Summary of the experimental results 74

6 Discussion **77**
6.1 Systematics of the even Zn isotopes 77
6.1.1 Excitation energy of low-lying excited states 77
6.1.2 B(E2; $2^+ \rightarrow 0^+$) in even Zn isotopes 80
6.1.3 B(E2; $4^+ \rightarrow 2^+$) in even Zn isotopes 82
6.1.4 Comparison of E* and B(E2) with calculations 83
6.1.5 B_{42} ratios and seniority 84
6.2 Systematics of the odd Zn isotopes 88
6.3 Systematics of the Cu isotopes 91

II The partial conservation of seniority in the $g_{9/2}$ shell **93**

7 The partial conservation of seniority in the $g_{9/2}$ shell **95**
7.1 Pairing and seniority 95
7.2 Total and partial conservation of seniority 96

7.3 Seniority and one-particle transfer 98
7.4 Conclusion 105

III Search for new isotopes and isomers in the vicinity of ^{100}Sn 107

8 Motivation 109
8.1 Search for new isotopes 114
8.2 Experimental overview 115

9 The ^{100}Sn test experiment 119
9.1 Choosing optimal settings 119
9.2 Particle identification 122
9.3 Production cross section 126
9.4 Conclusion 131

10 The main ^{100}Sn experiment 133
10.1 Experimental setup 133
10.2 Particle identification and identification of new isotopes 135
10.3 Conclusion 139

11 Conclusion 141

12 Annex A: Electromagnetic transitions 145

13 Annex B: Seniority and particle transfer: detailes and proofs 149
13.1 Proof that $\left|\left\langle (g_{9/2})^4 0_2^+ \left\| a_{9/2}^+ \right\| (g_{9/2})^3 9/2_1^+ \right\rangle\right| = 0$ 150
13.2 Proof that $\left|\left\langle (g_{9/2})^4 4_2^+ \left\| a_{9/2}^+ \right\| (g_{9/2})^3 9/2_1^+ \right\rangle\right| = 0$ 152

Bibliography 155

List of Figures 171

List of Tables 179

1 General introduction

Contrary to the structure of atoms for which the electromagnetic force between the electrons and the nucleus is well known, the interaction between nucleons, the strong force, is not so well known. Studying the properties that emerge from the complex structure of the nucleus helps us understanding the nature of nuclear forces. Nuclei with certain number of protons or neutrons (called "magic numbers") are more strongly bound than others. When both the neutron and proton numbers are magic, the nucleus is even more tightly bound and possess an increased stability as compared to its neighbours. The relative simplicity of the intrinsic structure of magic and adjacent nuclei make them ideal for testing models and understanding nuclear structure. In recent years, it was found that by going away from the valley of β-stability some magic numbers vanish, while others show up.

Considerable theoretical and experimental efforts have been deployed in order to reach and describe doubly magic nuclei far away from the valley of β-stability on both the neutron- and proton-rich sides. Several fundamental questions directly related to the nature of these doubly magic-nuclei are still to be answered. For instance: do the shell gaps persist far from stability? Can these exotic doubly-magic isotopes be considered as inert cores (which would allow shell-model calculations to be performed for even more exotic nuclei)? How fast are the residual interactions between valence nucleons attenuating the magic character of the core and how rapidly is collectivity developing with the number of valence nucleons? For these reasons the regions around ^{100}Sn and ^{78}Ni (the two most exotic doubly-magic nuclei) concentrate the interest of many research groups studying various aspects of nuclear structure including the residual interaction, the spin-isospin correlations, shape evolution as well as the isovector part of the nuclear mean field. In the scope of this thesis we have investigated nuclei in the vicinity of doubly-magic nuclei on both the neutron rich side (^{68}Ni) and the proton rich side (^{100}Sn).

In the first part of the thesis, we address the question of the evolution of collectivity and the interplay between collective and single-particle degrees of freedom in neutron-rich nuclei around ^{68}Ni. An experiment was performed at GANIL to measure lifetimes in neutron-rich Zn isotopes around N = 40 in order to extract the reduced transition probabilities B(E2) which give us insights into the evolution of collectivity in this region. The first chapter is an introduction to nuclear structure presenting the aspects that will be relevant in the context of this thesis. The physics motivations to study the evolution of collectivity around ^{68}Ni with an emphasis on

Zn isotopes are also given. The details of the experimental setup and techniques used to address our physics case are given in the second chapter. The data analysis is described in the third chapter, while the results are given in the following chapter. Finally in the fifth chapter the results we obtained are compared with existing experimental data and discussed in the framework of shell model calculations.

In both the ^{68}Ni and ^{100}Sn regions, the valence nucleons occupy the $g_{9/2}$ shell. Some of the common properties in these two regions can be investigated through the influence of the valence $g_{9/2}$ shell such as seniority isomers and particle transfer. Hence, in the second part of the thesis, we have discussed investigation of the partial conservation of seniority in $g_{9/2}$ shell and its influence on one-particle transfer.

Contrary to neutron-rich regions in which protons and neutrons occupies different orbitals, neutron deficient N=Z nuclei provide information on the interactions between protons and neutrons occupying identical orbits. A particularly interesting case is ^{100}Sn, presumably the heaviest doubly magic and particle-stable nucleus with N=Z, to which is dedicated the third part of this work. ^{100}Sn is predicted to have the purest Gamow-Teller decay and its large Q_{EC} window for decay allows to experimentally observe the almost full Gamow-Teller strength (B_{GT}). The comparison between the measured B_{GT} with theoretical predictions can shed light on the long standing issue of the missing strength in GT decay. In the third part of the thesis we present and discuss the analysis of a one-day in-beam test experiment where two different configuration settings of the BigRIPS separator of RIKEN (Japan) were evaluated in order to optimize the production and selection of ^{100}Sn. Besides studying nuclei far from the valley of stability, production cross-section measurements are used to design and plan experiments in this region. This study of production cross-sections has been used subsequently to setup our experiment, which was dedicated to the measurement of the Gamow-Teller strength in the decay of ^{100}Sn to ^{100}In, to the mapping of the proton drip-line in the region of Te-Ru and to the search of short-lived isomeric states in this region of the nuclear chart. The analysis of this experiment is ongoing and the identification of new isotopes is presented.

Finally, some general conclusions of this thesis work are discussed in the last chapter.

Part I

The lifetime measurements around N=40 Zn isotopes

2 Introduction

In the early days of nuclear physics, the liquid-drop model was developed as a basis for the description of some nuclear properties, in particular binding energies. The atomic shell model was developed by N. Bohr [1] in order to describe magic numbers in atoms and it did not appear that this model would be successful for the description of the nucleus. In time, the experimental evidences for a shell structure of the nucleus was growing. For example, sharp discontinuities in nucleon separation energies were found for certain values of proton and neutron numbers. Those numbers for Z and N known today as ¨magic¨ numbers are: 2, 8, 20, 28, 50, 82 and 126.

In the first approximation of the nuclear shell model, it is assumed that nucleons are moving independently in a central potential that corresponds to the average interaction with the other nucleons. A nucleus consisting of A nucleons can be described by a Hamiltonian:

$$H = \sum_{i=0}^{A} T_i + \frac{1}{2} \sum_{i,j=1}^{A} V(i,j) \tag{2.1}$$

where T_i represents the kinetic energy of nucleon i and $V(i,j)$ is the two body nucleon-nucleon interaction. Therefore, the Hamiltonian consists of the kinetic energy of all nucleons and the sum over the two body nucleon-nucleon interaction for all pairs of nucleons. Adding the central potential for each particle $U(r_i)$, the Hamiltonian becomes:

$$H = \sum_{i=0}^{A} [T_i + U(r_i)] + \left[\frac{1}{2} \sum_{i,j=1}^{A} V(i,j) - \sum_{i=0}^{A} U(r_i) \right] = H_0 + H_1 \tag{2.2}$$

where H_0 is the unperturbed Hamiltonian and corresponds to the independent particle motion, while H_1 represents a residual interaction reflecting the fact that nucleons are not moving completely independently.

When the harmonic oscillator was used as a central potential in an independent particle model, it was possible to reproduce only the first three magic numbers. To explain the properties associated to the next one, Mayer and Haxel, Jensen and Suess [2, 3] independently proposed a correction of the single-particle potential by adding a spin-orbit term. A realistic shell model potential that managed to reproduce the observed magic numbers can be expressed as:

$$U(r) = \frac{1}{2}m\omega^2 r^2 + D\vec{l^2} - C\vec{l}\cdot\vec{s} \tag{2.3}$$

where $\frac{1}{2}m\omega^2 r^2$ is the kinetic energy of a harmonic oscillator, $\vec{l}$ is the orbital angular momentum operator and $\vec{s}$ is the spin operator, while C and D are constants.

The single particle energies (SPE) of the nuclear mean field from a potential given by the formula 2.3 are shown in Fig. 2.1. On the left-hand side of Fig. 2.1 the shell structure of the simple harmonic oscillator is presented. In order to correct for steep rise of the harmonic oscillator potential at the nuclear surface, an $\vec{l^2}$ term is phenomenologically introduced which lowers SPE. A similar effect is achieved if a Wood-Saxon potential [4] is used instead. This leads to the splitting of energy levels with the same n - radial quantum number but different l as shown in the middle of Fig. 2.1. Finally, the third term is a spin-orbit term, which takes into account the fact that a different force is felt by a given nucleon with a parallel alignment of the intrinsic and an orbital angular momenta (higher total angular momentum - j) or anti-parallel (lower j). Hence, each nl level is split into two orbitals: one is lowered in energy for parallel alignment (higher j value) and another is raised in energy for anti-parallel (lower j value). The splitting is more pronounced for higher l values. This leads to a reproduction of the known magic numbers (right hand side of Fig. 2.1).

In the shell model, protons and neutrons are grouped in the shells which are separated with a large energy gap. Shells that are completely filled by nucleons form an inert core in the shell model calculations, while orbitals available for valence nucleons form valence space. Shells that are assumed not to be occupied by nucleons form an outer space. Therefore, the shell model focuses on the interactions between valence nucleons, taking into account the effects of the inert core. This yields the effective residual interaction, which should reproduce the eigenvalues of the realistic interaction in the full space, but in the restricted valence space. Any Hamiltonian describing the effective interactions can be split in two parts: monopole and multipole [6]. The monopole part of the Hamiltonian is related to the evolution of the spherical mean field while the multipole part tends to describe correlations that are not included in the spherical mean field.

The monopole part describes a shift of the single particle energies of the neutron(proton) orbitals, due to the mean field generated by protons(neutrons) added to the inert core. The monopole corrected part of the single particle energies is called the effective single particle energy (ESPE), and the expression for proton ESPE is given by following formula:

$$\tilde{\varepsilon}_{j_\pi} = \varepsilon_{j_\pi} + \sum_{j_\nu} \overline{E}(j_\pi, j_\nu)\hat{n}_{j_\nu} \tag{2.4}$$

where ε_{j_π} is the proton single particle energy in j_π orbital and $\hat{n}_{j_\nu}$ is the number of neutrons occupying the j_ν neutron orbital and $\overline{E}(j_\pi, j_\nu)$ is the monopole term of

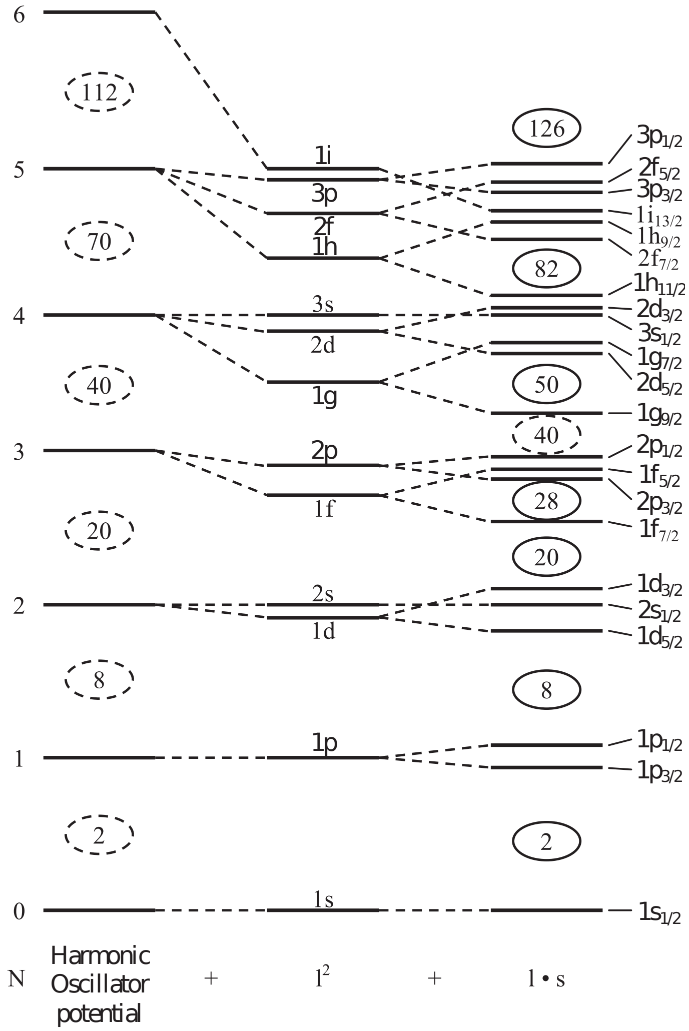
6
5
4
3
2
1
0
N
Harmonic Oscillator potential
+
l^2
+
$l \cdot s$
112
70
40
20
8
2
1i
3p
2f
1h
3s
2d
1g
2p
1f
2s
1d
1p
1s
126
82
50
40
28
20
8
2
$3p_{1/2}$
$2f_{5/2}$
$3p_{3/2}$
$1i_{13/2}$
$1h_{9/2}$
$2f_{7/2}$
$1h_{11/2}$
$2d_{3/2}$
$3s_{1/2}$
$1g_{7/2}$
$2d_{5/2}$
$1g_{9/2}$
$2p_{1/2}$
$1f_{5/2}$
$2p_{3/2}$
$1f_{7/2}$
$1d_{3/2}$
$2s_{1/2}$
$1d_{5/2}$
$1p_{1/2}$
$1p_{3/2}$
$1s_{1/2}$

Figure 2.1: *The structure of the spherical mean field (Modified from Casten [5]). Starting from the left-hand side single particle energies (SPE) are presented for a simple harmonic oscillator, followed by the modification of SPE due to a surface-correction* $\vec{l}^2$ *term and a spin-orbit* $\vec{l} \cdot \vec{s}$ *term.*

two body interaction defined as:

$$\overline{E}(j_\pi, j_\nu) = \frac{\sum_J (2J+1)\langle j_\nu j_\pi; J|V|j_\nu j_\pi; J\rangle \hat{n}_{j_\nu}}{\sum_J (2J+1)} \tag{2.5}$$

The analogous expression goes for the neutron ESPE. Since the monopole term corresponds to the proton-neutron interaction in orbitals j_π, j_ν averaged over the angular momentum J, it is independent of the relative orientation of their orbitals. The nucleon - nucleon interaction is strongest for the states in which two nucleons are orbiting in the coplanar plane and is weakest for J corresponding to the nucleons orbiting perpendicularly to each other. This J - dependent part of the interaction is included in the multipole part of the interaction containing dipole, quadrupole... By increasing the number of valence protons and neutrons, the residual interaction becomes dominant and cannot be treated as a perturbation of the spherical mean field. Since many nucleons are becoming active, it is said that nuclei exhibit collective behaviour.

2.1 The benchmark observables of nuclear structure

The ground state of the even-even nuclei is always 0^+ and the first excited state is usually 2^+, making the only possible decay from $2^+ \rightarrow 0^+$ state to be electric quadrupole (E2) radiation. Since low-lying states in collective nuclei are quadrupole in character, it is not surprising that one of the benchmarks of nuclear structure is the energy of the 2^+ state as well as the E2 strength, i.e. B(E2) values, defined as[1]:

$$B\left(E2; J_i \rightarrow J_f\right) = \frac{1}{2J_i+1}\langle \psi_f \| E2 \| \psi_i \rangle^2 \tag{2.6}$$

where $\langle \psi_f \| E2 \| \psi_i \rangle$ is the reduced E2 matrix element between initial and final states.

In magic nuclei, it is necessary to bring a large energy to the system in order to create excitation across the closed shell, leading to the high energy of 2_1^+ excited state. Including more nucleons in the valence space will lead to configuration mixing which lowers the 2_1^+ state energy and increases B(E2) strength, a signature of a collective behaviour.

By increasing the number of both protons and neutrons in the valence space, the collective behaviour rapidly evolves due the p-n interaction. The situation is somewhat different for the identical nucleons filling the same orbitals j, which is described in the following section.

2.1.1 The seniority scheme

The two nucleons in the same orbitals tend to pair to J=0^+ through the strongly attractive pairing interaction. This property is explored in the so-called seniority scheme. The seniority - υ is defined as the number of particles that are not in pairs coupled to angular momentum $J = 0$ [7]. In general, states with low seniority occur at low energy. For example ground state of an even-even magic nucleus has $\upsilon \approx 0$ while its yrast levels with angular momenta J = 2,4,6... have $\upsilon \approx 2$, corresponding to one broken pair with J $\neq$ 0 [8].

---

[1] For details about electro-magnetic transitions check Annex A

Some of the important results deduced from a seniority coupling scheme are given here without proof, while a detailed analysis can be found elsewhere [5, 8]. Considering an odd-tensor two body interaction $V_{i,j}$ in the j^n configuration, the matrix elements can be written as:

$$\left\langle j^n \upsilon \alpha J \left| \sum_{i<k}^{n} V_{i,j} \right| j^n \upsilon \alpha' J \right\rangle = \left\langle j^\upsilon \upsilon \alpha J \left| \sum_{i<k}^{n} u V_{i,j} \right| j^\upsilon \upsilon \alpha' J \right\rangle + \frac{n-\upsilon}{2} V_0 \delta_{\alpha\alpha'} \quad (2.7)$$

where α and α' denote any additional quantum numbers needed, V_0 is the interaction energy for each pair coupled to 0.

From equation 2.7 the energy difference between states with seniority $\upsilon = 2$ and $\upsilon = 0$ can be derived:

$$E\left(j^n, \upsilon = 2, J\right) - E\left(j^n, \upsilon = 0, J = 0\right) = \left\langle j^2 J | V | j^2 \right\rangle - V_0 \quad (2.8)$$

$$E\left(j^n, \upsilon = 2, J\right) - E\left(j^n, \upsilon = 2, J'\right) = E\left(j^2, \upsilon = 2, J\right) - E\left(j^2, \upsilon = 2, J'\right) \quad (2.9)$$

leading to the important conclusion that all energy differences of seniority $\upsilon = 0$ and $\upsilon = 2$ states in n-particle configuration are identical to those in the two-particle system and are independent of n [5].

The even-tensor one body operator does not necessarily need to conserve seniority ($\Delta\upsilon = 0,\ 2$). The operator concerning E2 transition rates is an even-tensor one body operator and it can be shown [5, 8] that B(E2) values follow different behaviour depending on whether seniority is conserved or not:

$$B\left(E2; 2_1^+ \rightarrow 0_1^+\right) \propto f(1-f) \quad \Delta\upsilon = 2 \quad (2.10)$$

$$B\left(E2; \upsilon J \rightarrow \upsilon, J-2\right) \propto (1-2f)^2 \quad \Delta\upsilon = 0 \quad (2.11)$$

where f corresponds to the fractional filling of shell defined as $f = n/(2j+1)$.

The B(E2;$2^+ \rightarrow 0^+$) values show a parabolic behaviour when filling a single j shell, rising toward mid-shell and falling thereafter. The B(E2) values for the seniority conserving transition (eq. 2.11), such as isomeric transition, show an opposite behaviour as compared to the seniority changing transition with a parabola reaching zero at mid-shell. This behaviour comes from the property of the particle-hole operator that changes sign at the mid-shell, therefore must be zero at the mid-shell. [8]. The schematic behaviour of B(E2) values in terms of fractional filling is shown in Fig. 2.2.

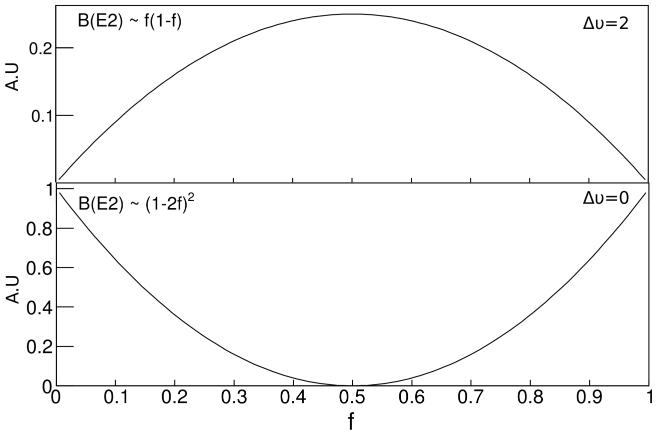

Figure 2.2: *Systematics of B(E2) values as a function of fractional filling* $f = \frac{n}{2j+1}$ *of j orbital for seniority conserving transition (lower part) and in case when seniority is changed (upper part). n is the number of identical nucleons in the j orbital.*

2.2 Collectivity in nucleus

With more and more nucleons in the valence space, the nucleus tends to deviate from its spherical shape toward a deformed shape. A model that describes non-spherical nucleus in the frame of the single-particle motion in a field of that shape (deformed shell model) is the Nilsson model [9]. In the macroscopic approach a nucleus is modeled as a classical charged liquid drop therefore neglecting the nucleonic structure of nucleus. A geometric collective model describing vibrational and rotational types of motion was first proposed by Bohr and Mottelson [10]

2.2.1 Vibrational motion

A motion of nuclear surface can be described by an expansion in spherical harmonics $Y_{\lambda\mu}(\theta,\phi)$ with time-dependent shape parameters $\alpha_{\lambda\mu}(t)$ with following formula :

$$R(\theta,\phi,t) = R_0\left(1 + \sum_{\lambda=0}^{\infty}\sum_{\mu=-\lambda}^{\lambda}\alpha_{\lambda\mu}(t)Y_{\lambda\mu}(\theta,\phi)\right) \tag{2.12}$$

where $R(\theta,\phi,t)$ is the nuclear radius in (θ,ϕ) direction.

In the multipole expansion $\lambda = 0$ so called monopole mode corresponds to a change of radius of sphere and describes compressibility of nuclear matter. A dipole mode ($\lambda = 1$) describes a shift of the center of mass and therefore corresponds to a translation of the nucleus and not nuclear excitations. The second order in the expansion ($\lambda = 2$) corresponds to the quadrupole deformations and they are the most important collective excitations of nucleus. An octupole mode ($\lambda = 3$)

describes symmetric modes associated with a negative parity band. Finally, a hexadecapole mode ($\lambda = 4$) is the highest mode known to have any importance in nuclear theory. This mode seems to play an important role as an admixture to quadrupole excitations. In the analysis of vibrational motion, we restrict ourselves to quadrupole mode as the most dominant, neglecting higher expansions ($\lambda \geq 3$). It describes oscillations of the nucleus due to the quadrupole residual interaction. The first quadrupole phonon excitation carries a spin and a parity 2^+. Involving more phonon excitations will correspond to higher and higher lying excited states. From the two phonon excitations, a triplet of states with spin $J^\pi = 0^+, 2^+, 4^+$ is allowed, having the energy that is twice the energy of the first 2^+ state. At three times the energy of the first 2^+ state lies the three-phonon multiplet states: 0^+, 2^+, 4^+ and 6^+. The energy ratio $E(4^+)/E(2^+)$ equals to 2 corresponds to nuclei with pure harmonic vibrations. This ratio is in a range between 2 and 2.5 for nuclei that exhibit vibrational character.

In vibrational nuclei, the destruction of collective excitation is governed by selection rule: $\Delta N_{ph} = \pm 1$, where N_{ph} is the number of phonons. Any phonon from N_{ph} excitation state can undergo destruction leading to $N_{ph} - 1$ phonon state. This makes B(E2) values proportional[2] to N_{ph}. Since the first 4^+ state is the two-phonon excitation state and the first 2^+ state is the one-phonon state, the B(E2) ratio becomes:

$$B_{42} = \frac{B(E2; 4^+ \rightarrow 2^+)}{B(E2; 2^+ \rightarrow 0^+)} = 2 \tag{2.13}$$

which is a typical value for nuclei being a good vibrator.

2.2.2 Rotational motion

In the rotational model, the nucleus is approximated as an axially symmetric rigid system that rotates along an axis perpendicular to symmetry axis. The rotational Hamiltonian is:

$$H_{rot} = \frac{\hbar}{2\mathcal{I}} \vec{I}^2 \tag{2.14}$$

where $\mathcal{I}$ is the moment of inertia, and $\vec{I}$ is the total angular momentum consisting of the intrinsic angular momentum $\vec{J}$ and the rotational angular momentum $\vec{R}$. The expression for the rotational energy goes as:

$$E_{rot} = \frac{\hbar^2}{2\mathcal{I}} [J(J+1) - K^2] \tag{2.15}$$

where K denotes the projection of $\vec{I}$ on the symmetry axes.

---

[2] The sum of the N_{ph} decays to the possible $N_{ph} - 1$ final states in N_{ph} times higher than B(E2) value coming from the decay of one-phonon state to the ground state.

Assuming the ground state with $J^\pi = 0^+$ and $K = 0$ (ground-state band) the energy ratio for an ideal rotating nucleus is $E_{4_1^+}/E_{2_1^+} = 3.33$. This result is one of the best signatures for rotational motion.

The expression for the B(E2) transition for rotational nuclei is given by the following formula:

$$B(E2; J_i \rightarrow J_f) = \frac{5}{16\pi} e^2 Q_0^2 \langle J_i 020 | J_f 0 \rangle^2 \tag{2.16}$$

where Q_0 is the intrinsic quadrupole moment and $\langle J_i 020 | J_f 0 \rangle$ is the Clebsch-Gordan coefficient connecting J_i and J_j. The important signature of rotational behaviour given as the ratio between B(E2; $4^+ \rightarrow 2^+$) and B(E2; $2^+ \rightarrow 0^+$) values can be extracted:

$$B_{42} = \frac{B(E2; 4^+ \rightarrow 2^+)}{B(E2; 2^+ \rightarrow 0^+)} = 1.43 \tag{2.17}$$

2.2.3 The Nilsson model

The Nilsson model is a shell model developed to describe deformed nuclei [9]. It takes into account the fact that the interaction of a valence nucleon with the core depends on the relative orientation of nucleon's orbital with respect to the nuclear symmetry axis. Single particle energies are lowered in energies for orbitals that lies closer to the symmetry axis, while those lying at larger distances are raised in energy. The Nilsson diagram showing the splitting of single-particle energies as a function of the projection of angular momentum j on the symmetry axis is shown in Fig. 2.3.

2.3 Evolution of collectivity around ^{68}Ni

2.3.1 Systematics of Ni isotopes

The region in the vicinity of ^{68}Ni has attracted much attention in recent years. The nickel isotopes (Z=28) cover three doubly-closed shells: on the proton rich side ^{48}Ni [11] most neutron deficient nucleus with T_z=-4 known to date; ^{56}Ni self-conjugated N = Z nucleus and very neutron rich ^{78}Ni [12] nucleus with T_z=11. This makes of nickel isotopes an ideal case for testing the evolution of the shell structure as a function of isospin.

A schematic representation of the occupation of proton and neutron orbitals for ^{68}Ni is shown in Fig. 2.4. The neutron orbitals $\nu p_{3/2} f_{5/2} p_{1/2}$ are completely filled. The first empty orbital is the intruder $\nu g_{9/2}$ separated from the previous levels with the N=40 harmonic oscillator sub-shell gap. At first, the N=40 sub-shell closure was not considered as magic but this was questioned when precise spectroscopic data became available.

The first spectroscopic results obtained by Bernas et al.[13] show that the first excited state of ^{68}Ni is 0_2^+ and not 2_1^+ state. A similar behaviour is observed in

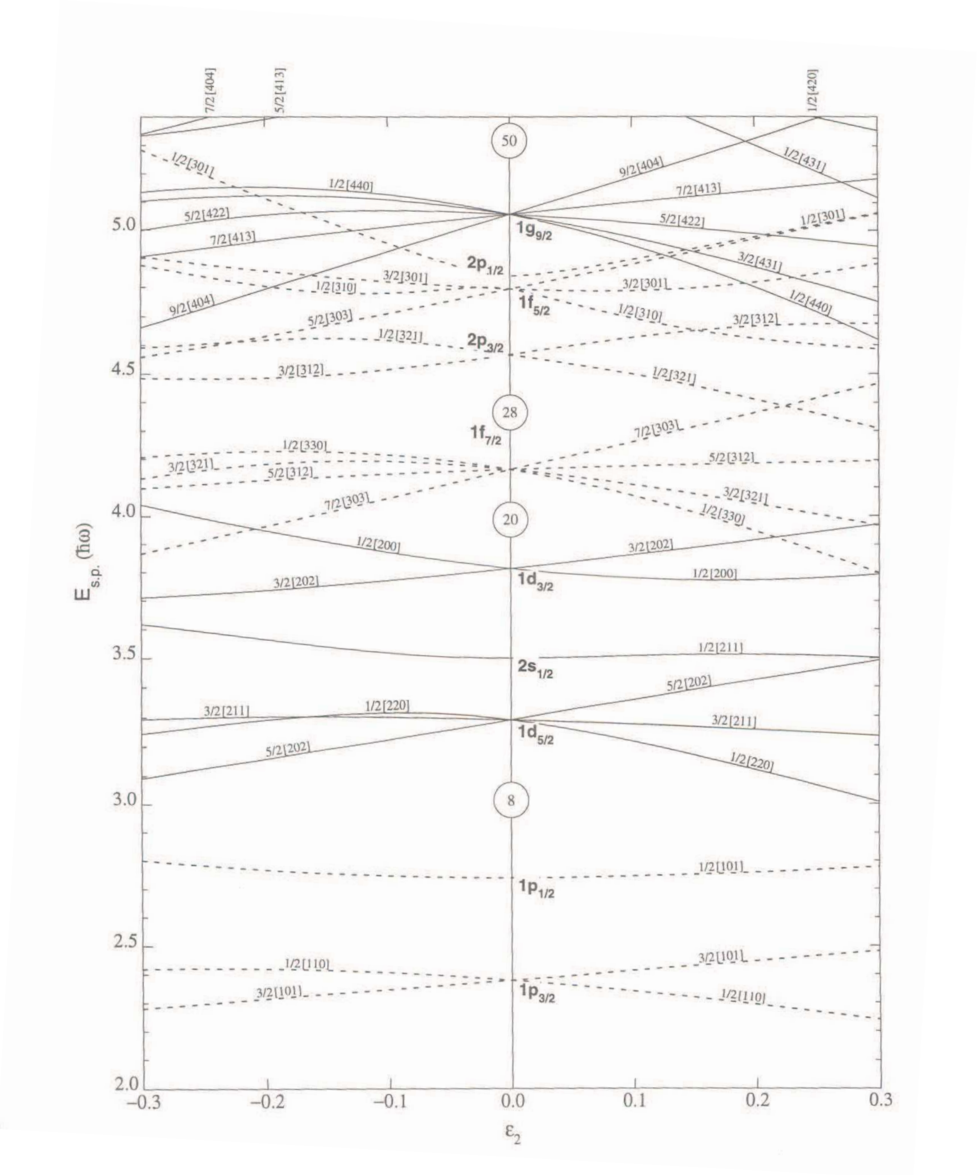

Figure 2.3: *Nilsson diagram for $Z \leq 50$. The abscissa is deformation parameter ε close to β.*

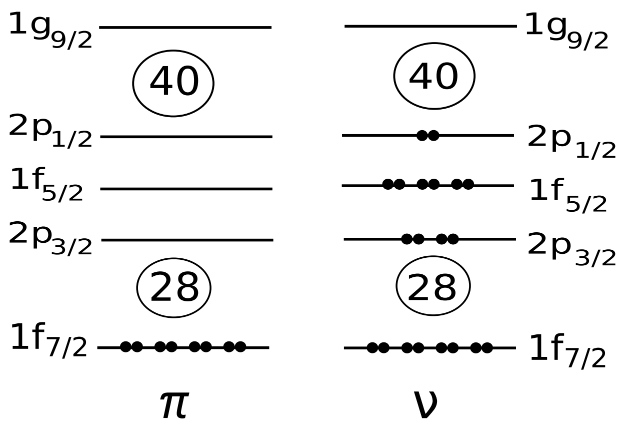

Figure 2.4: *The occupation of proton and neutron orbitals for* ^{68}Ni

doubly-magic nuclei like ^{16}O, ^{40}Ca as well as in the semi-magic ^{90}Zr. Therefore, this observation was the first hint of a possible magicity of ^{68}Ni [13]. Measured 0_2^+ state was followed by the measurement of the high 2^+ state [14] and the low transition probability B(E2; $2^+ \rightarrow 0^+$) [15] comparable to values in other doubly-magic nuclei. The systematics of the first 2^+ energies and transition probabilities B(E2; $2^+ \rightarrow 0^+$) are shown in the upper and middle part of Fig. 2.5, respectively. The B(E2) systematics follow a parabola with a maximal value at mid-shell and reaching a minimum at closed-shells (see Fig. 2.2), a behaviour characteristic for semi-magic nuclei well described in the seniority coupling scheme.

Conversely, mass measurement shows that the N = 40 sub-shell gap is not well pronounced [16]. Direct signature for shell closure is the two-neutron separation energy S_{2n} calculated from binding energies, or more conveniently expressed as the δ_{2n} two-neutron separation energy difference defined as [17]:

$$\delta_{2n}(Z,N) = S_{2n}(Z,N+2) - S_{2n}(Z,N) \tag{2.18}$$

The systematics of δ_{2n} for Ni isotopes, presented at the bottom part of Fig. 2.5, shows a distinct peak indicating N=28 shell gap is well pronounced for ^{56}Ni while there is no visible peak at N=40 for ^{68}Ni.

These contradictory signals from experimental data can be explained by the role of the high-spin intruder $\nu g_{9/2}$ orbital above the odd-parity $pf_{5/2}$ orbitals [15, 22, 23]. At N = 40, due to parity change, it is necessary to break a pair and to excite two neutrons into the $\nu g_{9/2}$ to build the first 2_1^+ state, hence raising its excitation energy. The small B(E2) value arises from the fact that the first 2^+ state is mainly from (2p-2h) neutron excitation, while only a small fraction comes from proton excitations across the Z = 28 shell gap. Most of the B(E2) strength resides at higher excitation energy states and they are proton excitations in nature [23]. Neutrons do not contribute directly to the B(E2) values but they induce core polarisation which occurs through quadrupole excitations via $(\pi \mathrm{f}_{7/2})^{-1}(\pi \mathrm{p}_{3/2})^{+1}$ configurations

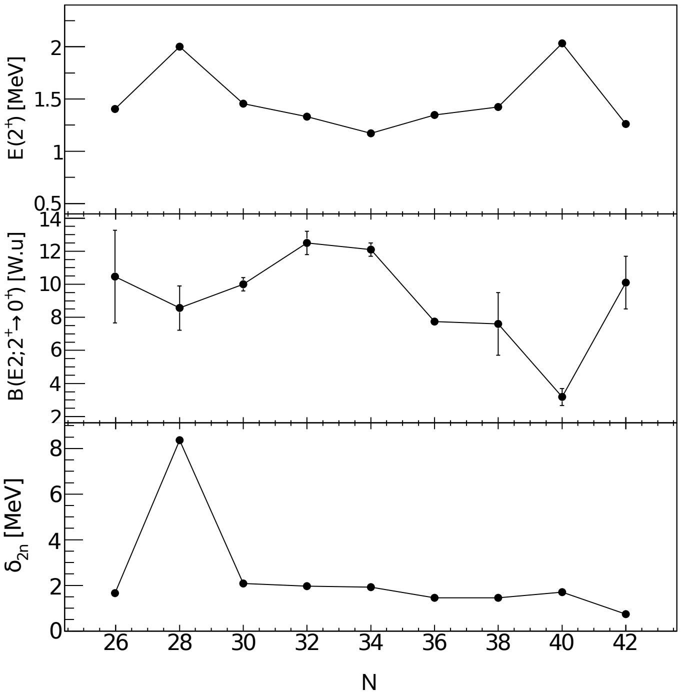

Figure 2.5: *Systematics of the first 2$^+$ energies (upper figure), B(E2;2$^+$ →0$^+$) values (middle figure) and δ_{2n} in Ni isotopes. Data are taken from [18, 19, 20, 21]*

[24, 15, 25]

Beyond N = 40, the neutrons start to fill the $\nu g_{9/2}$ orbital. A rapid increase of the B(E2; $2^+ \rightarrow 0^+$) value in ^{70}Ni compared to ^{68}Ni has been observed. The B(E2; $2^+ \rightarrow 0^+$) value measured in ^{70}Ni by Coulomb excitation at $v/c \sim 0.28$ induced on a ^{208}Pb target [19] was found to be 3 times higher than the one obtained for ^{68}Ni [26]. Another way to determine the amount of ^{68}Ni proton core polarization in ^{70}Ni is through the systematics of the B(E2; $J^+ \rightarrow (J\text{-}2)^+$) of $(\nu g_{9/2})^2$ multiplet. The experimental B(E2) values are found to be: B(E2; $8^+ \rightarrow 6^+$)=19 ± 4 [26], B(E2; $6^+ \rightarrow 4^+$)=43 ± 1 [27] and B(E2; $2^+ \rightarrow 0^+$)=172 ± 28 e^{2}fm^4 [19]. The results were compared with the theoretical B(E2) values calculated by a large scale shell model calculations based on the empirical T=1 effective interaction derived in the pure neutron $pf_{5/2}g_{9/2}$ model space [28]. The calculated B(E2) values from higher lying transitions B(E2; $8^+ \rightarrow 6^+$)=17.3 and B(E2; $6^+ \rightarrow 4^+$)=44.6 e^{2}fm^4 are in a good agreement with the experimental results. A disagreement for the $2^+ \rightarrow 0^+$ transition B(E2; $2^+ \rightarrow 0^+$)=92.2 e^{2}fm^4 was observed which points to an enhanced proton core polarization for low-lying states [19]. The increased proton core polarisation is likely to originate from the attractive $\pi f_{5/2} - \nu g_{9/2}$ monopole interaction [29, 30, 31] ascribed to the tensor force of nucleon-nucleon interaction [32]. The tensor force also acts repulsively between $\pi f_{7/2}$ and $\nu g_{9/2}$ which in combination with an attractive interaction between $\pi f_{5/2}$ and $\nu g_{9/2}$ tends to reduce $\pi f_{7/2} - \pi f_{5/2}$ spin-orbit splitting and therefore favouring the development of collectivity.

As it was pointed out in section 2.1.1 from equations 2.8 and 2.9 one can deduce that the excitation energy of the 2_1^+ state should be constant along the isotopic chain between N=40 and N=50. Experimental results show the monotonic decrease of E(2_1^+) with neutron filling $\nu g_{9/2}$, toward ^{78}Ni which might be an indication of weakening of the magical character of Z = 28 or N = 50 [33].

2.3.2 Systematics of even Z nuclei around Ni

The local magicity of the N = 40 sub-shell closure is further confirmed by adding or removing protons from ^{68}Ni core. Removing only two protons from the ^{68}Ni core leads to a sharp decrease of the 2_1^+ energy from 2033 keV in ^{68}Ni to 573 keV in ^{66}Fe [34] and further to 517 keV in ^{68}Fe [35]. More recent results of the B(E2) values of the first 2^+ state in ^{62,64,66}Fe isotopes gave us a deeper insight into the evolution of collectivity. Results were obtained from the lifetime measurements using the recoil-distance Doppler shift method after multinucleon transfer reactions [36] and projectile Coulomb excitation reactions [37]. The measured B(E2; $2^+ \rightarrow 0^+$) values indicate an enhanced collectivity of the Fe isotopes at N = 40. Large scale shell model calculations were performed in different model spaces and compared with the experimental data: the shell model in the pf shell space for protons and $pf_{5/2}g_{9/2}$ space for neutrons reproduce ^{62,64}Fe data well, but overestimates the energy of 2_1^+ state indicating an increase of collectivity at N = 40 and the necessity to include the $d_{5/2}$ level into the model space [38]. Shell model calculations with a recent effective interaction (LNPS) [39] that includes the neutron $d_{5/2}$ orbital manage to reproduce E(2^+) and B(E2) values for Fe isotopes. The calculated structure of ground-state wave functions for Fe isotopes indicates an increase in occupancy of $g_{9/2}d_{5/2}$ orbitals going from ^{62}Fe toward ^{66}Fe implying an important role of the $\nu g_{9/2}$ and $\nu d_{5/2}$ intruders for the development of collectivity.

The Fe isotopes reveal a behaviour similar to the one observed in Mg isotopes, where a decrease of the 2_1^+ energies and an increase of B(E2) values cannot be explained within the *sd* shell. Due to the reduction of the N = 20 shell gap (gap between *sd* shell and $f_{7/2}$), the neutrons tend to occupy the $\nu f_{7/2}$ and $\nu p_{3/2}$ orbitals making it necessary to introduce those orbitals into the model space. This behaviour around ^{32}Mg is the so-called island of inversion [40]. Hence, since the situation in Fe isotopes is analogous to the region around ^{32}Mg, one can also speak about new "island of inversion" around N=40 in this mass region [36, 37].

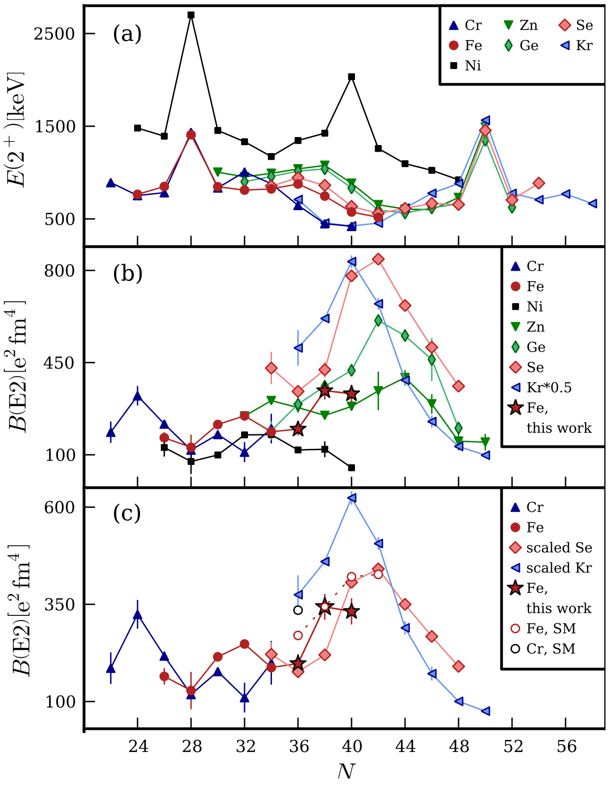

Figure 2.6: *Systematics of a) E(2_1^+) energies, b) B(E2; $2^+ \rightarrow 0^+$) values for even-even nuclei along several isotopic chain. In c) are presented scaled B(E2) values for Se and Kr isotopes and results of SM calculations with LNPS interaction. The figure is taken from [37]).*

By looking at the systematics of the E(2_1^+) energy along isotopic chains in even-even nuclei around Ni, one can notice similar behaviour for the pairs of nuclei: Cr

(Z=24) and Kr (Z=36), Fe (Z=26) and Se (Z=34), Zn (Z=30) and Ge (Z=32) Fig. 2.6a. [41, 37]. Therefore one could apply the valence proton symmetry (VPS) scheme in which the pairs of isotones with the same number of particles and holes from the closed shell are considered [42]. For the center of symmetry, Z=30 was used, which is justified by the fact that Zn is in the middle of $2p_{3/2}$ shell and in the VPS scheme by adding two protons/holes it will reach fully occupied/empty $2p_{3/2}$ shell having the identical effect. In the VPS scheme proton holes in $1f_{7/2}$ orbital and particles in $1f_{5/2}$ orbital were considered as pairs. As detailed in [37], the B(E2) values of valence partners can be compared provided a scaling factor is applied to one of the partner (here the heavier). The scaled B(E2) values of the Se and Kr isotopes are compared to those obtained for the Fe and Cr chains. A good agreement for B(E2) values for the Fe/Se pairs at N=34 and N=36 has been observed, while comparison deviates for N=38 and N=40, nonetheless indicating an increase of collectivity for Fe isotopes toward N=40 or 42. For Cr/Kr isotopes, due to the lack of experimental data for the same N, results of shell model calculations in Cr isotopes were compared with experimental B(E2) value of Kr isotopes and a good agreement was found [37].

Therefore, from the valence proton symmetry, the effect of depopulating $\pi 1f_{7/2}$ is similar to the role of protons populating $\pi 1f_{5/2}$ orbital for developing collectivity.

The systematics of the low-lying states in even-even Zn isotopes indicates that they follow a vibrational behaviour. The first 2_1^+ state level can be interpreted as one-phonon state followed by a triplet of two-phonon states (2_2^+, 4_1^+, 0_2^+) at approximately twice the energy of 2_1^+ state (Fig. 2.7).

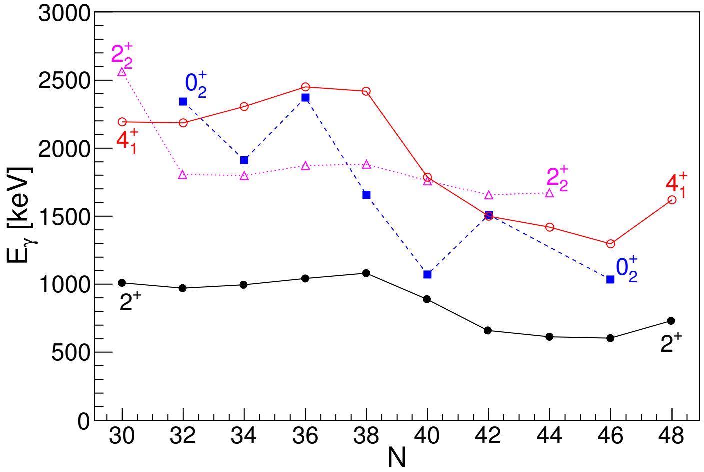

Figure 2.7: *Systematics of the low-lying states in Zn isotopes.*

The energy ratios E(4^+)/E(2^+) along the isotopic chain range between 2 and 2.5, a typical range for nuclei that exhibit a vibrational character. Moreover, the g-factor measurements of 2_1^+ and 4_1^+ states in $^{62-70}$Zn isotopes gave results that are in agreement with the predicted collective g-factor value g=Z/A for vibrational nuclei [43, 44, 45, 46, 47]. A recent g -factor measurement of the 2_1^+ state in ^{72}Zn suggests a slight deviation from the Z/A limit, which can be explained by the filling of the $\nu g_{9/2}$ and a neutron dominated configuration [48].

However, a drop of the 0_2^+ level has been observed at ^{70}Zn, similar to the one in ^{68}Ni. Bernier et al. [13] argued that the low energy of 0_2^+ state in ^{68}Ni comes from a neutron pair excitation from pf shell to the $g_{9/2}$ orbital, which is lowered in energy because of the strong coupling of the pair in this orbital. Hence, similar effect might be expected for Z=30, although less pronounced due to the presence of two valence particles outside the Z=28 shell closure.

The B(E2) values of the light Zn isotopes were determined from several independent Coulomb and lifetime measurements. The systematics of B(E2; $2^+ \rightarrow 0^+$) values, follows a similar trend as the light Ni isotopes up to ^{66}Ni, corresponding to ^{68}Zn. The higher B(E2) values indicate more collectivity due to the additional two protons outside the Ni core, which increases $\pi - \nu$ interaction. The B(E2) values reach a maximum at N=34, corresponding to mid-shell between N=28 and N=40 (Fig. 2.6). A sudden increase of the B(E2; $2^+ \rightarrow 0^+$) values observed in ^{70}Zn and ^{72}Zn with respect to ^{68}Ni has been interpreted as an increased collectivity due to combination of three effects [49]: the influence of the two additional protons outside the Ni core, the maximum in neutron pairing correlations at N=40 and the influence of intruder positive parity orbital into the region of negative parity states. Namely, the absence of clear separation between positive and negative parity states in ^{70,72}Ni compared to ^{68}Ni allows a lot of states to be built from both protons and neutrons leading therefore to large B(E2) values [49].

The B(E2) values of the heavy, neutron rich $^{72-80}$Zn isotopes have been extracted using low-energy Coulomb excitation of radioactive ion beams [50] with a maximum of collectivity obtained for N=44. In recent lifetime measurements obtained with recoil distance Doppler shift method, the 2_1^+ state in ^{74}Zn was populated with projectile-fragmentation reaction and with deep inelastic reactions as well. A lower B(E2) value of 2_1^+ state in ^{74}Zn was found indicating a maximum of collectivity for N=42 [51, 52] as shown in Fig. 2.8, which is also the case for Se and Ge isotopes as shown in the systematics in Fig. 2.6.

A severe discrepancy in experimental B(E2; $4^+ \rightarrow 2^+$) values for $^{70-74}$Zn obtained between recent RDDS [52] and DSAM [47] experiments as well as Coulomb excitations [50] has been observed, as shown in Fig. 2.8. Experimental results were compared with different theoretical calculations: shell model calculations with JUN45 interaction (valence space $pf_{5/2}g_{9/2}$ with effective charges: $e_p = 1.5e$ and $e_n = 1.1e$ [53]), and with LNPS interaction (valence space: $pf_{5/2}g_{9/2}d_{5/2}$; effective charges: $e_p = 1.4e$ and $e_n = 0.4e$ [39]). The results of beyond-mean-field calculations using Gogny D1S interaction in a 5-dimensional collective Hamiltonian are also presented [54]. Theoretical results fail to reproduce B(E2; $4^+ \rightarrow 2^+$) values.

Contrary to the vibrational character of Zn isotopes, as suggested by the E(4^+)/E(2^+), the B(E2) ratios show a surprising non-collectivity of the low-lying states. There-

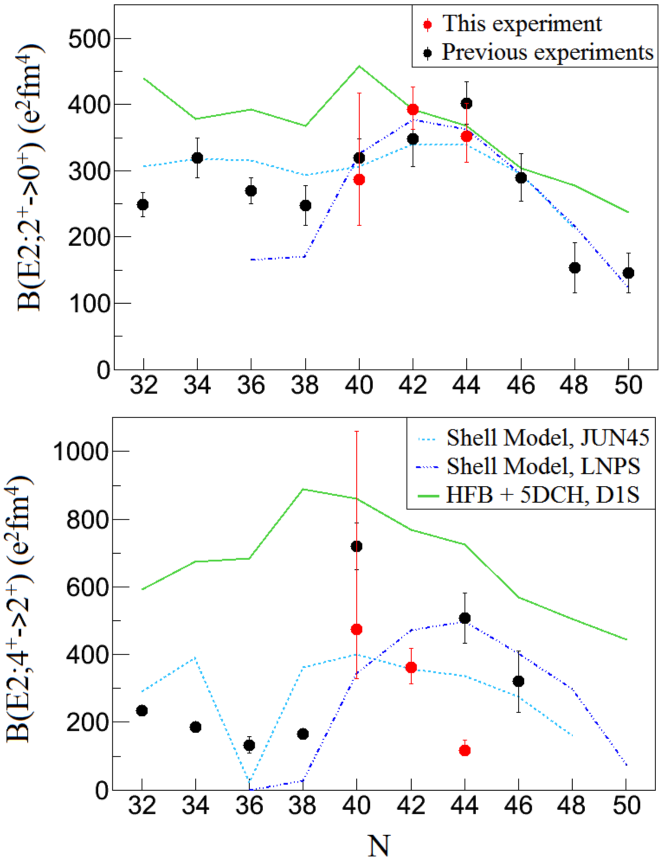

Figure 2.8: *Systematics of the experimental B(E2; $2^+ \rightarrow 0^+$) and B(E2; $4^+ \rightarrow 2^+$) values compared with several theoretical calculations. The figure is taken from [52]).*

fore, we have performed an experiment with the goal to confirm the evolution of the collectivity in even neutron-rich Zn isotopes beyond N=40. This has been done by measuring the lifetimes of the low-lying states above the 2^+ state using the plunger technique and a different reaction channel than the one reported in [52]. In addition, since the spectroscopy of the odd nuclei around the N=40 sub-shell allows us to probe the role of a hole or a particle in the single-particle orbitals of interest, another aim was to investigate the collectivity of excited states in ^{69,71}Zn.

2.3.3 Systematics of odd Z nuclei around Ni

Up to now, the local magicity of the N=40 sub-shell closure has been shown for the even Z nuclei close to Ni. It is also interesting to investigate odd Z nuclei around Ni, since they allow us to test the influence of proton particle/hole on the evolution of the single-particle orbitals and hence collectivity. Looking at the systematics of odd-mass Cu isotopes beyond N=40, a rich variety of the nature of the low-lying states has been observed [29, 55]. Low lying states of neutron-rich $^{69-73}$Cu isotopes were studied from the β - decay experiment following proton induced ^{238}U fission [29]. The ground state in all isotopes was found to be $3/2^-$ corresponding to one proton in $\pi p_{3/2}$. The energy of the first excited state $5/2^-$ which exhibits a rather constant value around 1 MeV for stable and proton-rich Cu isotopes, decreases rapidly from 1214 keV in N=40 ^{69}Cu to 534 keV in ^{71}Cu and 166 keV in ^{73}Cu (see Fig. 2.9). Having in mind the single-particle nature of the $5/2^-_1$ state obtained from the shell model calculations, the energy decrease of the $5/2^-_1$ state can be explained with the tensor force of nucleon-nucleon interaction (as introduced in section 1.3.1). Namely, with neutrons filling the $\nu g_{9/2}$ orbital, the $\pi f_{5/2}$ orbital is being pushed down in energy due to the attractive interaction between the $\nu g_{9/2}$ and $\pi f_{5/2}$. This effect could lead to the inversion of $\pi f_{5/2}$ and $\pi p_{3/2}$ causing the change of ground state from $3/2^-$ to $5/2^-$. The inversion of the ground state and the first excited state was predicted to occur in ^{75}Cu [31], which was experimentally confirmed by the spin and magnetic moment measurement of the ground state [56].

In order to check the nature of other low-lying states around N=40 Cu isotopes, one can look at excitation energy of, and the transition strength from, the low-lying excited states, see Fig. 2.9 given by [55]. The left side of the figure shows the evolution of the $1/2^-$ and $5/2^-$ excitation energy as well as the B(E2) values of the transitions associated to their decay to the ground state as a function of the neutron number in Cu isotopes. The $1/2^-$ state shows identical energy evolution as the $5/2^-$ state, but with much larger B(E2) values for $N \geq 40$. This excludes $\pi p_{3/2}$ single-particle character and indicates a rather collective nature of this low-lying state.

The energy systematics of the $7/2^-$ state in Cu isotopes and associated B(E2) values follow the systematics of the energy of the 2^+ state and B(E2; $2^+ \rightarrow 0^+$) value in Ni isotopes as shown in the left part of Fig. 2.9. Based on the particle-core coupling model [57], the $7/2^-$ state in ^{71,73}Cu isotopes were interpreted as $\pi 2p_{3/2}$ coupled to 2^+ in ^{70,72}Ni, respectively. Therefore, one can summarize that low-lying

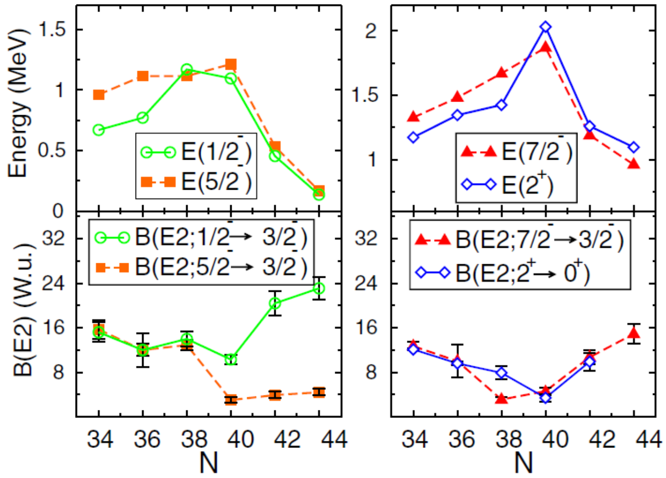

Figure 2.9: *Systematics of: the energies of the* $5/2^-$ *and* $1/2^-$ *in* $^{63-73}$*Cu isotopes (top left figure), the energies of the* $7/2^-$ *in Cu isotopes and* 2^+ *state in Ni isotopes (top right figure). Systematics of the experimental B(E2) values for transitions from* $5/2^-$ *and* $1/2^-$ *to the* $3/2^-$ *ground state (bottom left figure) in* $^{63-73}$*Cu isotopes and the experimental B(E2) value for transition from* $7/2^-$ *to ground state in Cu isotopes with B(E2;* $2^+ \rightarrow 0^+$*) values in corresponding Ni isotopes. Figure is taken from [55].*

states in odd-mass Cu isotopes around N=40 and beyond are triple in their nature: single-particle nature, collective nature at low energies and particle-core coupled.

A coexistence of single-particle and collective states is expected also in Co isotopes similarly to Cu isotopes, since they are mirror chains around the semi-magic Ni isotopes. The low-lying levels of lighter odd-mass Co isotopes [58] and more neutron rich Co isotopes [59] were already described as a single $\pi f_{7/2}$ hole coupled to the adjacent even-even Ni isotopes. The energy systematics of the $9/2_1^-$ level in Co isotopes follows the systematics of 2_1^+ energy level in Ni isotopes with the same number of neutrons, indicating that $9/2_1^-$ level can be considered as $(\pi f_{7/2})^{-1} \otimes 2_1^+(Ni)$, while $3/2_1^-$ state follows the systematics of 2_1^+ energy level in Fe isotopes suggesting that $3/2_1^-$ state can be described as $\pi f_{7/2}$ coupled to the 2_1^+ state in Fe. The $B\left(E2; 9/2_1^- \rightarrow 7/2_1^-\right)$ of Co isotopes follows to some extent the $B\left(E2; 2_1^+ \rightarrow 0_1^+\right)$ of Ni isotopes. Conversely, the $B\left(E2; 7/2_1^- \rightarrow 7/2_1^-\right)$ values in Co isotopes do not follow the systematics of $B\left(E2; 2_1^+ \rightarrow 0_1^+\right)$ values in Fe isotopes. The fact that the former has a constantly lower values than the latter indicates that the N=40 has not collapsed in Co isotopes [60].

2.4 Conclusions

In this chapter, we have discussed nuclear structure in the vicinity of ^{68}Ni. An existing experimental results established a local magicity around N = 40 sub-shell closure. A rapid onset of collectivity when adding a few particles/holes to the ^{68}Ni core and the coexistence of different character of low-lying states makes this region attractive to both experimental and theoretical research.

Particularly, some ambiguous results in the systematics of Zn isotopes above N = 40 have been observed. Namely, the systematics of energy of the low-lying states in even-even Zn isotopes indicates their vibrational behaviour.

A sudden increase of collectivity has been noticed through measurements of B(E2; $2^+ \rightarrow 0^+$) values at ^{70}Zn and ^{72}Zn with respect to ^{68}Ni. Although the systematics of E(4^+)/E(2^+) ratio suggest the vibrational character of Zn isotopes, non-collective nature of low-lying states above 2^+ state has been observed. The experimental B(E2; $4^+ \rightarrow 2^+$) values for $^{70-74}$Zn isotopes are sparse. In addition, the theoretical results obtained with a shell model calculations using JUN45 [53] and LNPS interaction [39] and with a beyond-mean-field calculation using Gogny D1S interaction in a 5-dimensional collective Hamiltonian [54] failed to reproduce the B(E2; $4^+ \rightarrow 2^+$) values.

Therefore, we have performed an experiment with the goal to measure the evolution of the collectivity in even neutron-rich Zn isotopes beyond N=40. In addition, we were aiming to explore the spectroscopy of the odd ^{69,71}Zn in order to probe the role of a hole or a particle outside the N = 40 sub-shell closure.

This has been done by measuring the lifetimes of low-lying excited states using the plunger technique. The nuclei of interest were produced in deep-inelastic collisions. The detection system used to identify produced nuclei and the experimental technique used to extract the lifetimes of interest are described in the following chapter.

3 Experimental set-up

In this chapter, the details of the experimental setup are discussed. The technique used for the lifetime measurements is given in the first section followed by a general description of deep-inelastic collisions in order to illustrate why this specific reaction was used. A general information on the VAMOS spectrometer together with a brief explanation of the complete detection system is given. The principles of the trajectory reconstruction and particle identification are given as well as a brief description of the EXOGAM array.

3.1 Lifetime Measurements

As it was mentioned earlier, one of the benchmarks of the shell evolution are the B(E2) values of the low-lying states. In the first place those are B(E2; $2^+ \rightarrow 0^+$), B(E2; $4^+ \rightarrow 2^+$) as well as the B(E2) values from the yrast states. Coulomb excitation is a direct method to measure B(E2) values. In this method, the energy of the projectile is sufficiently below the Coulomb barrier ensuring that the projectile does not perturbate the target nucleus. Thus, nuclear excitations are solely arising from the electro-magnetic interaction between the projectile and a target nucleus. The measured excitation probability is directly proportional to the B(E2) value [61]. In addition, Coulomb excitation allows populating low-lying non-yrast states which are also important to obtain a more coherent picture of the low-lying level structure of a nucleus.

Since there is a direct relation between lifetime and B(E2) values it is also possible to extract some information on the collectivity from lifetime measurements of the excited states[1]:

$$\tau(E2) = 8.1766 \cdot 10^{-10} E_\gamma^{-5} B(E2)^{-1} \tag{3.1}$$

where E_γ is the de-excitation energy given in MeV, the reduced transition probability is given in e^2fm^4 and the lifetime τ is given in ps.

3.1.1 Techniques for direct lifetime measurements

Several experimental techniques are available for direct lifetime measurements:

---

[1] For details about electro-magnetic transitions and lifetimes check Annex A

- The delayed coincidence method is a direct method for measuring the lifetimes of excited states through the measurement of time difference between the radiation populating the excited state of interest and the one de-exciting that state. A special method of delayed coincidence is fast timing which requires the usage of detectors with fast response, like BaF_2 scintillators or Ce doped $LaBr_3$ scintillators and a very precise calibration of electronics and detectors [62]. The method is sensible typically in the range from ∼ps to ∼ns.
- Recoil Distance Method (RDM) / Recoil Distance Doppler Shift Method (RDDS): In these methods, the lifetime is extracted from the measurement of the intensities of γ-rays emitted before and after a degrader, which can be placed at a variable distances after the target. The excited nuclei produced in the target, fly out with a velocity v_1, toward the degrader. The method in which the degrader is thick enough to stop the recoiling nuclei is called the recoil distance method. In the RDDS method, a thin degrader foil is used in order to slow down the recoiling nuclei. Hence, the recoils lose their energy in the degrader and exit with a velocity v_2. Therefore, γ-rays emitted before and in the degrader (or after, depending whether we consider RDM or RDDS method), observed in the detectors at the same angle θ, will undergo a different Doppler shift which will give rise to two components for a given photopeak. From the relative intensities of those two components, one can extract the lifetime of excited state [63]. The method is sensitive in the picosecond region.
- Doppler Shift Attenuation Method is applied for the states whose lifetime is of the sub-picosecond order, where the RDDS method cannot be applied anymore, since the target-degrader distance would be too small. The method is applied to states which lifetime is of the same order as the recoil nuclei slowing down time. Knowing the slowing down velocity as a function of time (obtained for instance from LSS theory [64]) and extracting the average velocity from the centroid of the γ-ray spectrum one can extract information of the lifetime from the following formula:

$$v_{av} = \frac{1}{\tau}\int_0^\infty v(t) e^{-\frac{t}{\tau}}\,\mathrm{d}t \tag{3.2}$$

3.1.2 RDDS method and a plunger device

Since the predicted lifetimes of the populated low-lying states of interest are in the picosecond range and since it is necessary to identify the recoil nuclei in A and Z, the best method to measure those lifetimes is the recoil distance Doppler shift method. A schematic illustration of the RDDS method is shown in Fig. 3.1.

The reaction products in an excited state exit from the target with a velocity v_1 which is reduced to v_2 after the degrader foil. Due to the Doppler effet, γ-rays emitted at the same angle θ with respect to the recoil direction, have a different observed energy E_i depending on whether they are emitted before or after the degrader as described by the formula 3.3.

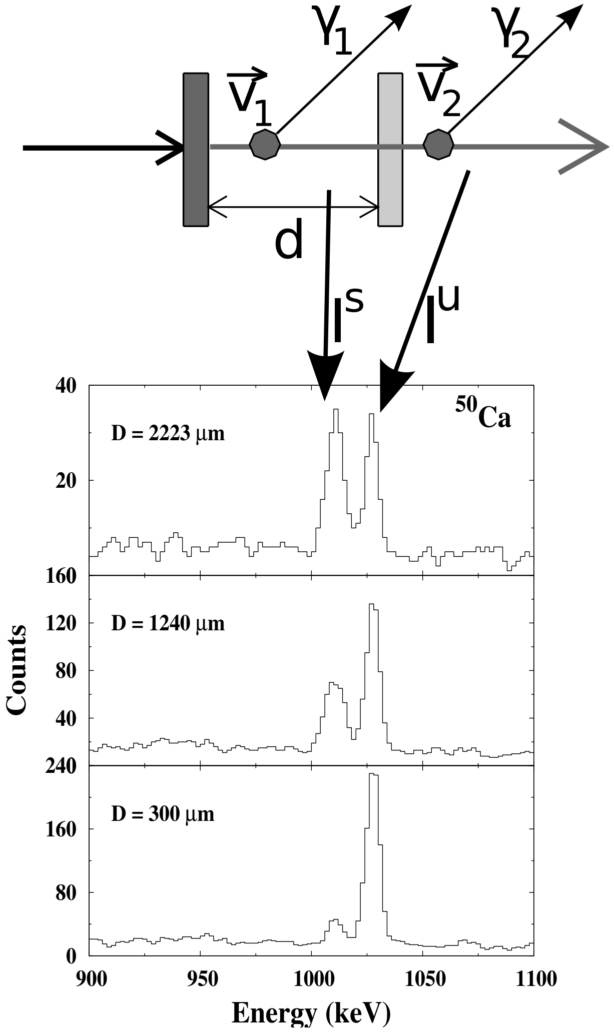

Figure 3.1: *Schematic illustration of lifetime measurements using the RDDS method.* v_1 *and* v_2 *correspond to recoils velocities before and after the degrader placed at a distance* d *after the target. The corresponding peaks intensities are denoted* I^s *and* I^u*. The evolution of the peak intensity of the shifted (*I^s*) and unshifted (*I^u*) components as a function of the target-degrader distance is given in the case of* ^{50}Ca *[65].*

$$E_i = E_0\gamma_i(1 - \beta_i cos\theta) \tag{3.3}$$

where v_i is the recoil velocity, E_0 is the energy of γ-ray emitted at rest, β_i is the ratio v_i/c, γ_i is related to β_i as: $\gamma_i = 1/\sqrt{1-\beta_i^2}$. It is clear that for a better separation between the two components of the peak it is necessary to detect more backward or forward emitted γ-rays.

By changing the target-degrader distance one will change the intensities of the γ components corresponding to the emission before and after the degrader. The intensity of the peak originating from the de-excitation of recoil nuclei after the degrader I^u is:

$$I^u = I_0 e^{\frac{-d}{v_1\tau}} \tag{3.4}$$

where I_0 is the total number of emitted γ-rays of interest. An index u in I^u stands from "unshifted" while s stands for "shifted". Namely, in the RDDS method, the recoils velocity is measured after the degrader. A Doppler corrected γ-ray emitted after the degrader has an energy that corresponds to the energy of nuclei de-excited at rest. But a γ-ray emitted before the degrader and corrected by the measured velocity has an energy which is shifted with respect to the energy measured for a nucleus at rest.

The intensity of the "shifted" peak originating from the de-excitation of recoil nuclei before the degrader (I^u) is:

$$I^s = I_0(1 - e^{\frac{-d}{v_1\tau}}) \tag{3.5}$$

The mean lifetime τ can be extracted from the measurement of I^u and I^s at a given distance d. Different designs of plunger are developed to optimise the measurement of lifetimes in nuclei produced via different nuclear reactions mechanisms. In deep-inelastic reactions, the mechanism we have used in this experiment, the direction of the recoiling nuclei differs from the beam axis. As a consequence, the plunger symmetry axis has to be aligned along the axis of the magnetic spectrometer. The target and degrader foils were placed on aluminum rings parallel to each-other and mounted on rails so that they could maintain their parallel relative position while moving. The ring with a degrader was moved to a desired position with a small motor with μm resolution. An automatic distance regulation was obtained by measuring the capacitance between the target and the degrader. In this experiment we have used the Köln plunger device mounted in the target chamber as shown in picture Fig. 3.2. In our experiment, we have placed target-degrader at two distances: 33.6 ± 1.0 μm and 99 ± 3.0 μm.

The choice of the degrader should be done carefully since it has to meet certain constraints. The degrader should be thin enough so that the recoiling nuclei will have sufficient energy to be identified in the spectrometer. In addition, the degrader thickness should be large enough so that the two components arising from the emission before and after it are well separated. The degrader material should be chosen in such a way to minimise reaction production cross-section in it. If possible, the nuclei originating from reaction with the degrader material should have different kinematics (magnetic rigidity) from those produced in the target since this will reduce the amount of degrader-like contaminants at the focal plane. The degrader should also have certain mechanical characteristics, melting temperature, etc.

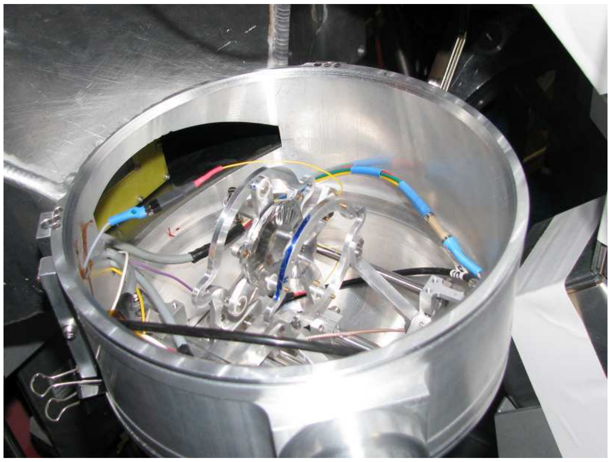

Figure 3.2: *Photography of the Köln plunger device placed in the target chamber*

3.2 Deep-inelastic collisions

Different nuclear interactions can occur between heavy ions depending on the energy of the system and the impact parameter. Deep-inelastic reactions are known to be one of the best mechanisms to produce neutron rich nuclei in the region where they are not accessible by fusion evaporation reactions [66]. Considerable experimental data, produced using the deep-inelastic collisions (DIC), has been collected starting from the late fifties [67, 68].

Some of the main features of deep-inelastic collisions can be summarised as follows [66]:

- In DIC the projectile and the target remain practically unchanged except for a net exchange of a few nucleons.
- An exchange of nucleons and the energy of colliding nuclei goes toward the equilibration of N/Z ratios of the final products [69].
- A large amount of the kinetic energy of the collision partners is transformed into internal excitations.
- Angular momentum is transferred from a relative orbital motion to the intrinsic spin of the system.

- Primary fragments produced at DIC de-excite mainly through the emission of the γ-rays and/or evaporation of light particles: protons, neutrons, α-particles. For the heavier systems, de-excitation can occasionally go via fission.

Since the exchange of nucleons of colliding nuclei goes toward the N/Z equilibration, with a choice of both neutron-rich target and projectile, one can reach neutron rich products that are far away from the line of stability. The largest production cross-section goes for nuclei around the target and the projectile, but nuclei along the N/Z line of the system can also be produced. The maximal cross-section is produced at the grazing angle of the reaction defined as a deflection angle of the incident particle in the Coulomb field of the target at the distance of the closest approach [70, 71].

$$d = \frac{Z_t Z_p e^2}{4\pi\varepsilon_0 E_k}(1 + csc\frac{\theta}{2}) \tag{3.6}$$

where d is the distance of touching spheres given by d=1.25($A_t^{1/3}$+$A_p^{1/3}$), A and Z with indices t and p are the atomic mass and atomic number of the target and projectile respectively, E_k [MeV] is the kinetic energy of projectile and θ is the grazing angle. Deep-inelastic reactions take place with beam energies typically 10 - 15 % above the Coulomb barrier allowing the exchange between the nucleons and energy of colliding nuclei which goes toward the equilibration of N/Z ratios of the final products.

Although the fusion-evaporation reactions are the best type of reaction to produce high-spin states, since most of the input angular momentum is converted into intrinsic angular momentum, in deep-inelastic collisions it is also possible to populate high-spin states since one part of the initial angular momentum is transferred to the intrinsic spin of the system. For a few decades already, large arrays of germanium detectors have been used to conduct spectroscopic studies of exotic nuclei [72, 73].

In order to maximize the detection of the recoiling nuclei it is necessary to set the spectrometer close to the grazing angle of the reaction since at this angle the production cross section is largest. Dozens of nuclei produced in deep-inelastic reactions are emitted in a wide range of angles. In order to efficiently collect and identify the nuclei of interest the use of a very wide solid angle spectrometer with a proper focal plane detector system is desired. Moreover, the usage of inverse kinematics is preferred because the reaction products are focused in forward directions therefore increasing the effective detection efficiency of the magnetic spectrometer.

In order to catch up the physics goals defined in the previous chapter, an experiment was performed by choosing the appropriate method for the lifetime measurements and the type of nuclear reaction for production of nuclei of interest. The details of the setup are given in the following sections.

3.3 Detection system

The experiment was performed at the Grand Accélérateur National d´Ions Lourds (GANIL) by applying the recoil distance Doppler Shift method (Fig. 3.3).

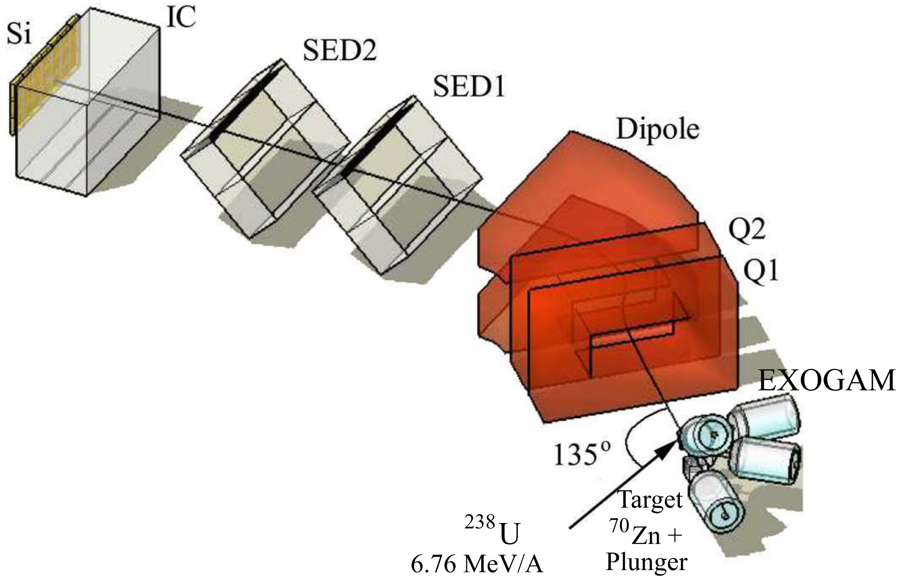

Figure 3.3: *Schematic representation of the experimental setup used. VAMOS spectrometer was set-up in dispersive mode and its focal plane detectors were used to identify recoiling nuclei. The segmented Ge clover detectors of the EXOGAM array were placed around the reaction chamber to detect prompt γ-rays.*

The nuclei of interest were produced using deep-inelastic reactions in inverse kinematics with a ^{238}U beam at 6.76 MeV/A impinging on a 800 μg/cm^2 ^{70}Zn target deposit on a 550 μg/cm^2 of Mg backing. Target-like reaction products were detected and identified on an event-by-event basis using the focal-plane detectors in the large acceptance VAriable MOde Spectrometer (VAMOS) [74, 75]. to the segmented germanium clover detectors of the EXOGAM array [76] for studying prompt γ-rays spectroscopy of recoil nuclei identified in VAMOS. The plunger device used for the lifetime measurements was installed in the reaction chamber. An Mo degrader foil with a thickness of 6.13 mg/cm^2 was used to slow down the recoiling nuclei.

3.3.1 VAMOS spectrometer

The VAMOS spectrometer has been designed to allow the identification of nuclei produced in different reaction mechanisms such as elastic and inelastic scattering, deep-inelastic and transfer reactions as well as fusion-fission reactions. Since reaction products are coming from a wide range of nuclear reactions in both direct and inverse kinematics, it is necessary to cover nuclei emitted at large angles with a wide range of energies. In order to meet these requirements, VAMOS was constructed to work in different modes.

3.3.1.1 General description

A picture of the VAMOS spectrometer and focal plane detectors is shown in Fig. 3.4. In its complete configuration VAMOS consists of two magnetic quadrupoles with a large aperture, a Wien filter and a magnetic dipole. The first quadrupole focuses in the vertical plane and defocuses in the horizontal plane, while the second quadrupole is focusing in the dispersive (horizontal) plane. The distance between the target and the first quadrupole can vary from 40 to 150 cm therefore allowing different ancillary detector arrays to be installed. The dipole magnet in VAMOS at a nominal bending radius of 1.5 m, corresponding to the bending angle of $\theta_{nom} = 60°$ has the maximum rigidity of Bρ=1.6 Tm. The VAMOS spectrometer can be rotated from 0° to 60° causing a variation of momentum dispersion at the focal plane. The Wien filter, placed between the quadrupole doublet and the dipole, is practically used only with fusion reaction where the low energy evaporation residues are emitted at 0°.

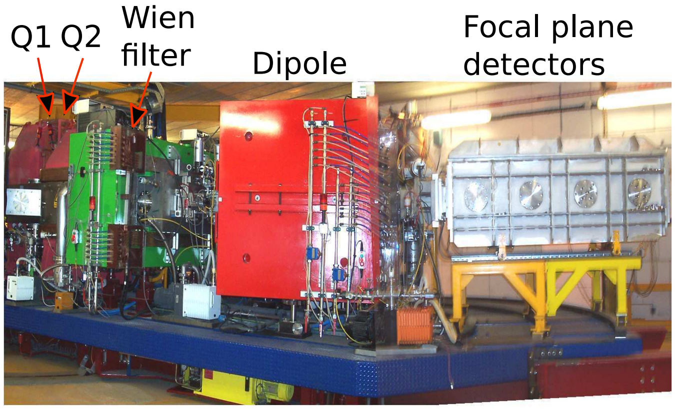

Figure 3.4: *Complete configuration of VAMOS spectrometer.*

Depending on the type of reactions to be studied and the experimental setup, the VAMOS spectrometer can be used in different modes:

- focusing mode: The configuration consists only of two quadrupoles providing non-dispersive mode with a large acceptance coming from the quadrupoles. The focusing mode was initially designed to maximise acceptance when the dispersion was not required. Recently, an upgrade of VAMOS which allows to use the full acceptance was accomplished [77] and therefore there is no more gain in statistics in the focusing mode with respect to the dispersive mode.

Nevertheless, without the dispersive elements, the recoil nuclei are well focused at the focal plane allowing therefore isomer tagging [78].

- dispersive mode: In the dispersive mode, VAMOS operates with the two quadrupoles and the dipole as a traditional magnetic spectrometer. The recoil nuclei are dispersed in the horizontal plane with a dispersion of 1.8 cm/% when a dipole deflection angle is set to 45°. Since the magnetic rigidity is proportional to the momentum of the recoiling nuclei, the identification in mass is done with the $B\rho$ selection. For this experiment we have used VAMOS in the dispersive mode.

- recoil separator: In this mode, VAMOS operates with the two quadrupoles, the Wien filter and the dipole. The setup is used for detecting fusion evaporation residues at 0°. Recently, VAMOS was successfully tested in a gas filled mode [79].

3.3.1.2 Detection system for VAMOS

In nuclear reactions, a large number of reaction products are produced. They exit from a target with different angles, having different masses, charge, charge states, energy, momentum... In order to successfully reconstruct a particle trajectory and obtain a unique particle identification, VAMOS uses focal plane detectors for measuring the x and y space positions, the energy loss ΔE, the total energy E and the time of flight TOF. The focal plane detectors in our experiment, schematically showed in Fig. 3.3, consisted of two secondary electron detectors (SeD) [80] for 2D position and TOF measurements; an ionisation chamber divided into 3 segments for energy-loss measurements and a Silicon wall consisting of 21 Si detectors for the measurement of the residual energy.

3.3.1.2.1 Multi-Wires Proportional Chamber(MWPC) The MWPC was installed at 13.8 cm from the target, at the entrance of the spectrometer. Due to the good time resolution, 500 ps for FWHM, it was supposed to be used for TOF measurements. For the time measurements it provides a signal which is independent of the beam pulse. A long TOF measured between the MWPC and the focal plane detectors should provide a better mass resolution, compared to the shorter TOF signal measured between the focal plane detectors. Unfortunately, the Mylar foil after the MWPC was broken during the rotation of VAMOS and the detector could not be used anymore since used isobutan gas C_4H_{10} escaped. The MWPC was not removed since we did not want to open the chamber. Therefore it was necessary to include the thickness of two Mylar foils (0.9 μm) to estimate the non-measured energy loss of the recoil nuclei.

3.3.1.2.2 Secondary electron detector (SED) For VAMOS used in a dispersive mode it is necessary to reconstruct the trajectory of the recoils in order to calculate the momentum and the scattering angle. Two different types of position sensitive detectors were developed for VAMOS, depending on the charge and energy of the nuclei of interest. For the high energy (2-20 MeV/A) lighter ($Z<15$) ions a low-pressure drift chamber has been used. In the case of heavier ions at lower energy ($E<2$ MeV/A) a drift chamber would introduce a large energy and angular stragglings which would deteriorate the detector resolution. Instead, a secondary electron detector (SED) is used [80]. The emissive foil, which is a 0.9 μm thick Mylar film, aluminised on both sides, is mounted 45° with respect to the beam direction. The secondary electrons (Se^-) emitted from the foil are accelerated in a 10kV longitudinal electric field between the foil and the electrostatic grid in order to minimise their dispersion. A magnetic field is used to focus the Se^- and to maintain good resolution. After their acceleration the Se^- penetrate through a thin Mylar foil (0.9 μm) into a low-pressure proportional counter where the Se^- will be multiplied enough to be detected. The first cathode which consists of 150 wires connected in groups of 3, is used to extract the position along the y-axis. The second cathode, consisting of 128 strips, is used to measure the position along the x-axis. The charge from each strip (48 and 128) is collected separately, allowing 2D position measurement with a resolution of 1.4 mm (FWHM).

The anode wires are placed perpendicularly and separated 1.6 mm from the wires of the first cathode. The wires, grouped in 3 independent parts are processed with a fast amplifier and used to provide 3 timing signals. A time resolution of 300 ps (FWHM) is achieved for heavy ions.

3.3.1.2.3 Ionisation chamber (IC) The ionization chamber (IC) is used for energy loss measurements. For this experiment, an IC based on a standard design was used, consisting of a segmented anode, a Frish grid and a cathode. The anode is divided into 3 segments along the flight path and the signal from each segment is processed individually. The segments are 106, 126 and 126 mm long. The entrance window is made of aluminised Mylar foil while the exit port is directly coupled to the Silicon wall. The detector is operating under an isobutan gas pressure of 40 mbar.

3.3.1.2.4 Silicon detectors An array of Silicon detectors is placed at the end of the focal plane detectors. It consists of 21 silicon detectors, with 7 detectors in each row, schematically presented in Fig. 3.5. The dimensions of each silicon detector are 7x5 cm^2 and the Si wall covers the full active area of the focal plane. The detected particles are fully stopped in 0.5 mm thick layer of Si thus allowing a measurement of the residual energy.

3.3.1.3 Trajectory reconstruction

Although corrections of optical aberrations were taken into account in the design of VAMOS spectrometer, it was nevertheless necessary to apply additional software

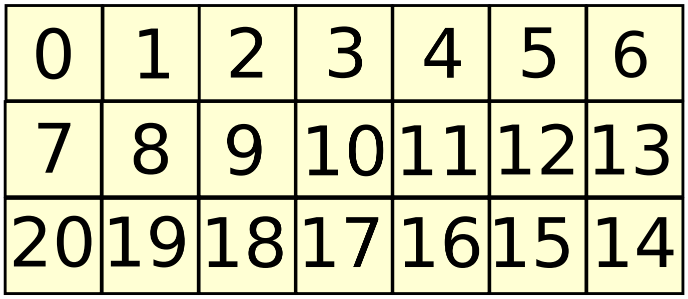

0	1	2	3	4	5	6
7	8	9	10	11	12	13
20	19	18	17	16	15	14

Figure 3.5: *Mapping of silicon detectors.*

procedures in order to obtain a proper reconstruction of the particle trajectories. The main parameter for the trajectory reconstruction is the position measurement. Starting from the position measurements in both SED detectors and knowing that the emissive foil is mounted 45° with respect to the beam axis it is possible to extract x_f, y_f a 2D particle position at the image focal plane located between two SED detectors. In addition, it is possible to reconstruct the θ_f and ϕ_f angles defined as the angles between a reference trajectory and a projection of particle trajectory (velocity vector) to the xz and yz plane, respectively. The reference trajectory corresponds to the trajectory of particle having momentum (in other words $B\rho$) that is used to set the magnetic field of the dipole. From the obtained x_f, y_f, θ_f, ϕ_f parameters, knowing the electric and magnetic fields of the spectrometer, it is possible to fully reconstruct the particle trajectory. A detailed description of the reconstruction procedure is given in [75, 74]. The reconstructed parameters are: $B\rho$ of the particle, the initial angles θ_i, ϕ_i and *Path* the total path of the particle from the target to the image focal plane.

3.3.1.4 Particle identification

The reaction products produced in the target have different mass A, charge Z and charge state Q. In order to make a proper particle identification, the determination of the mass A and charge Z is not sufficient. Namely, a dipole disperses the ions according to their momentum and charge state making it difficult to resolve M/Q for different combinations of M and Q. Therefore it is also necessary to measure the charge state Q as well. The identification of the reaction product is done event-by-event, based on $B\rho - dE - TOF$ method.

A complete procedure for particle identification can be summarised as follows:

- determination of x_f, y_f, θ_f, ϕ_f from the measured positions in the two SED detectors
- reconstruction of $B\rho$, θ_i, ϕ_i and *Path* from x_f, y_f, θ_f, ϕ_f values
- calculation of the velocity from the measured TOF and reconstructed *Path* using $v = Path/TOF$

- determination of M/Q from the reconstructed $B\rho$ and calculated velocity using the simple formula:
$$\frac{M}{Q} = \frac{B\rho}{v} \tag{3.7}$$
- determination of the total energy E from the measurement of the energy loss ΔE and the residual energy deposited in the Si detectors E_{res}.
- In general, the mass number M is determined from the calculated velocity and the total energy of the reaction product E using
$$M = \frac{2E}{931.5\beta^2} \tag{3.8}$$
  where E is the total energy given in [MeV] and $\beta = v/c$

  In our case the mass number M was determined from the M/Q values. Namely, we have a strong production of ^{70}Zn (elastic channel) and with the proper alignment in M/Q we can extract the charge state and subsequently mass M.
- in general procedure: determination of charge state is done from M/Q and M
- determination of atomic number Z from the energy loss measurements using Bethe-Block formula:
$$\frac{dE}{dx} \sim k\frac{AZ^2}{2E} \tag{3.9}$$
  where k is a factor that takes into account intrinsic parameters as density, ionisation potential...

A flow chart illustrating the identification algorithm is shown in Fig. 3.6.

3.3.2 EXOGAM

For the detection of prompt γ-rays emitted from the recoil nuclei, EXOGAM detector was used [76]. EXOGAM is an array of maximum 16 high resolution germanium detectors, while in our experiment 8 detectors were used: 4 placed at 90° and 4 placed at 135° with respect to the beam direction. Each detector consists of 4 n-type high purity Ge crystals grouped in the same cryostat in the configuration of a clover. Combining signals that correspond to scattered γ-ray in the adjacent crystals increases the efficiency and this gain with respect to the individual crystals is called the addback factor.

Each crystal is further electronically segmented into 4 segments (Fig. 3.7). Detectors can be arranged in two different configurations: configuration A with detectors placed 11.4 cm from the target and configuration B with detectors placed 14.7 cm from the target. The compact configuration A allows covering a large solid angle with Ge. The drawback is a larger uncertainty in the angle at which a γ-ray is detected. The main advantage of the electrical segmentation of the crystals is in reducing this uncertainty which leads to a reduced Doppler broadening of a peak.

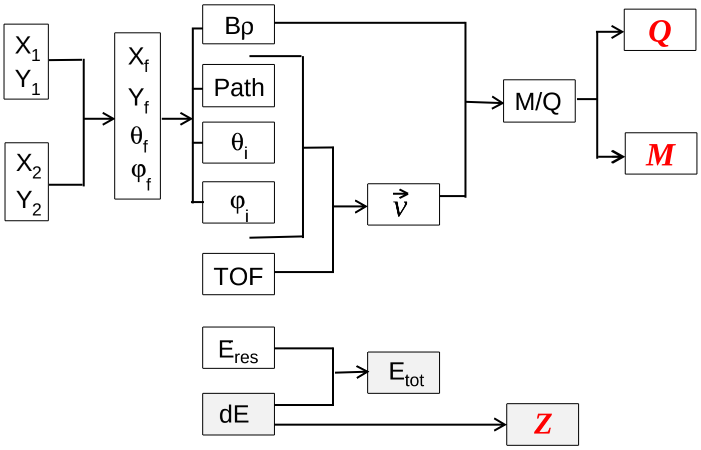
X1
Y1
X2
Y2
Xf
Yf
θf
φf
Bρ
Path
θi
φi
TOF
v
M/Q
Q
M
Eres
dE
Etot
Z

Figure 3.6: *Flow chart for particle identification.*

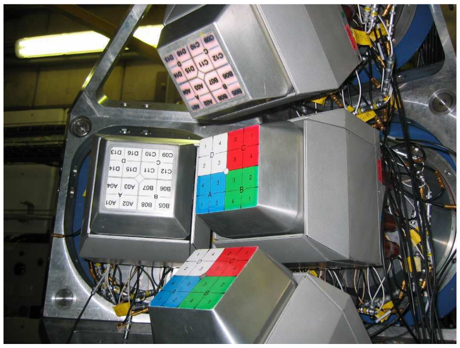

Figure 3.7: *Photo of a few clower detectors also showing the segmentation of the 4 crystals.*

Each clover detector is surrounded by an escape suppression shield shown in Fig. 3.8. The BGO and CsI crystals surrounding the Ge detectors are used as an anti-Compton detector suppressing the γ-rays that escape from the Ge detectors, increasing therefore the peak to total ratio.

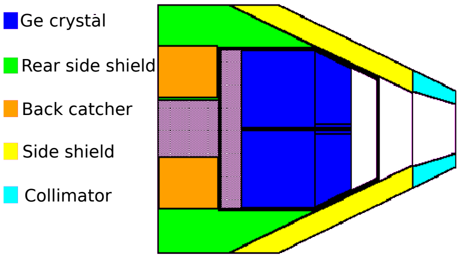

Figure 3.8: *A scheme of the escape suppression shield.*

Coupling the EXOGAM array with the VAMOS spectrometer offers a unique possibility to associate the detected γ-rays with the corresponding recoil nuclei identified by the VAMOS spectrometer. In addition, the reconstruction of the velocity and angle for each recoiling nuclei allows one to perform an event-by-event Doppler correction of the detected γ-rays, thus increasing the resolving power.

4 Data Analysis

4.1 Calibration

For an appropriate interpretation of the measured signals it is important to calibrate the detector i.e. to find the conversion factor that links the measured signals (in C, V) to the associated measured quantity (in ns, mm, MeV...). The calibration can be described as a two step process where the first step corresponds to the conversion from a measured signal to channels (digitization) and the second one to the conversion from channels to the measured quantity.

4.1.1 Calibration of SED detectors

In order to reconstruct the particle trajectories one should calibrate the secondary electron detectors. It is necessary to calibrate the signals coming from each of the 128 strips to determine the X position, and from each of the 48 strips for the Y position. To obtain an accurate measurement of the X(or Y) position it is crucial that all the strips deliver the same response for the same amount of collected charges. Different pulse amplitudes coming from the pulse generator were used to align and check the linearity of the response over a full range of detector. Pedestal value, (detector response without any pulse applied) was taken into account. The response of the SED detector in X position for different pulse amplitudes before and after alignment is shown in the left and right hand side of Fig. 4.1.

A mean position of the induced signal is extracted if in its passage the heavy-ion induces a signal in three adjacent strips. Knowing that each strip is 3 mm wide with a 0.125 mm interstrip distance [80], it is easy to reconstruct the X position of the intersection. The procedure is the same to reconstruct the Y position. Note that obtained the X and Y positions are relative positions. In order to find the absolute position we need to know which strips in X and Y correspond to the reference position (0,0).

The reference point was determined from 3 different runs of U beam with the magnetic field of the dipole sets to correspond to 3 different magnetic rigidities of U ions with certain charge state. The trajectory of those charge states will be central one, while other charge states will be dispersed. Therefore, by overlapping three different charge state distributions, the position where 3 peaks from different distributions overlap corresponds to reference position. The principle of determining

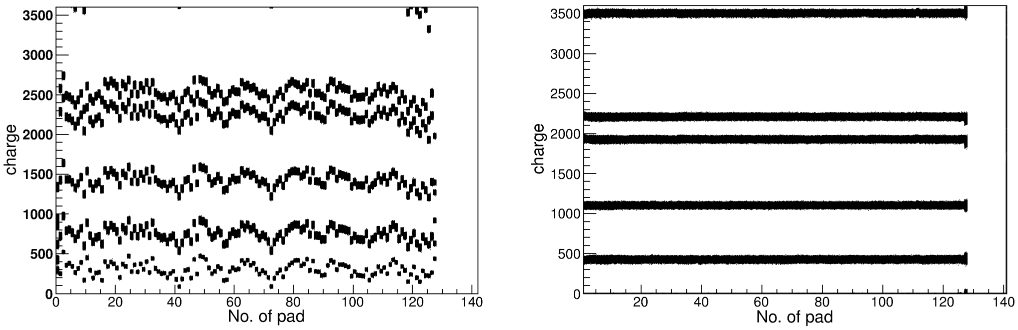

(a) *before alignment*

(b) *after alignment*

Figure 4.1: *Response of SED detector in X position to different pulse intensities before and after calibration.*

X$_{ref}$ for one SED is shown in Fig. 4.2.

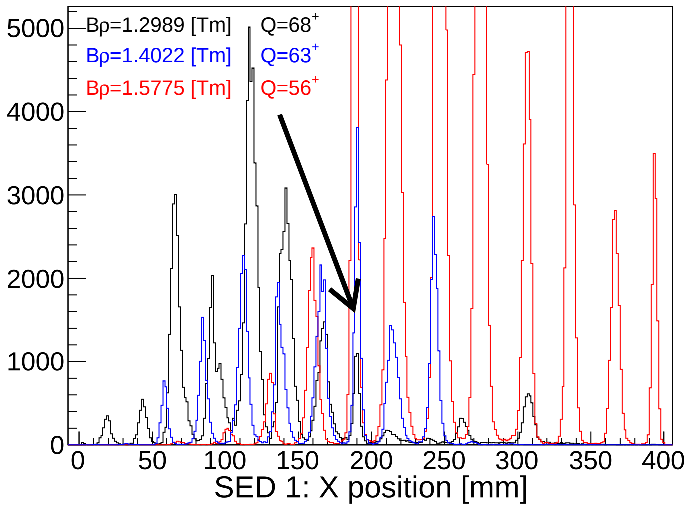

Figure 4.2: *Determination of X_{ref} with 3 runs with U beam set on different charge states. The position where the distributions overlap corresponds to the reference position.*

In the same way is obtained Y$_{ref}$, (although it is not very important to determine Y$_{ref}$ since the system is not dispersive in the Y direction). The calibration of the timing signal from the 3 anodes is described in the section Calibration of TAC and TOF.

4.1.2 Energy calibration of Si detectors and ionisation chamber

The calibration of the ionization chambers and the Si detectors is done in the same manner. The first step is to check the linearity of the detector response, i.e. to check the linear correlation between the measured signal (mV) and the output from the Analogue to Digital Converter (ADC) in channel. To do so, different pulse amplitude generated from a pulse generator and covering the full dynamical range of the preamplifier are brought to each Si detector and each pad of the IC. The linearity of the IC pads is presented in the left hand side of Fig. 4.3, while the response of the central Si detectors is shown in the right hand side of Fig. 4.3.

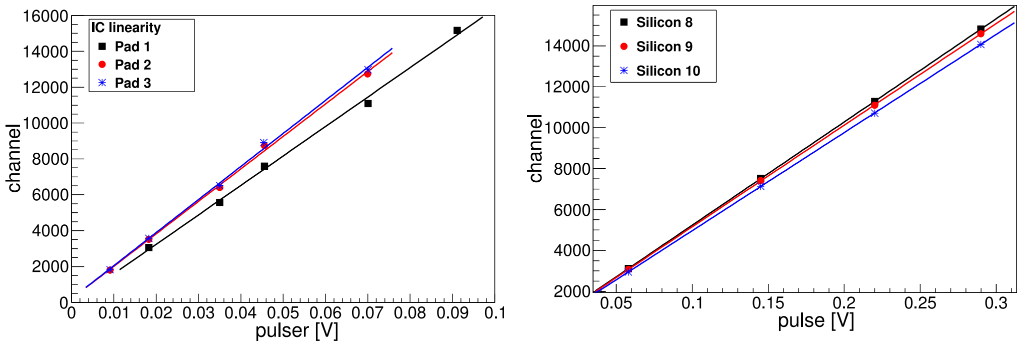

(a) *linearity of IC pads*

(b) *linearity of central Si detectors*

Figure 4.3: *Linearity of response of a) IC pads and b) central Si detectors tested with pulse generator.*

The second step is to make the absolute calibration of the Si detectors and the ICs i.e. to obtain conversion from channel to MeV. The best way would be to perform a calibration with an ^{238}U beam without target. Unfortunately, in all the runs with the ^{238}U beam and without target, the IC was not filled with gas and therefore the calibration could not be performed. The calibration of the Si detectors was neither done, since a lot of detectors did not receive any signal or, had a low statistics to make a proper fit. Instead, the calibration was performed with elastically scattered ^{70}Zn nuclei in full configuration with target and degrader installed. Knowing the kinematics of the setup, the LISE++ program [81] was used to calculate the energy of elastically scattered $^{70}\text{Zn}^{Q+}$ ions and to estimate the energy loss in the IC and Si detectors. The calibration factor links the response signal of the IC and Si detectors and the estimated energy losses in those detectors.

In order to do so, it is important to identify ^{70}Zn nuclei and its charge state. Therefore, a detailed explanation on how the calibration was done will be given in the next section.

4.1.3 Calibration of TAC and TOF

The time that particle spends flying between two detectors is called the time of flight (TOF). The TOF between detectors was measured with a Time to Amplitude Converter (TAC) coupled to an ADC. In total 5 TOFs were measured: between SED1 and Si, between SED2 and Si as well as time between SED1, SED2, Si detectors and high frequency (HF) of the beam that was used as a timing reference. It was also planned to measure TOFs using the MWPC placed in front of the VAMOS, but since it was broken during the rotation of VAMOS, it could not be used anymore.

The first step is to calibrate the TAC modules. For this purpose a time calibrator was used to produce a START and a STOP signals. The interval between the two was set according to the range of time given by each module. This should produce a spectrum of equidistant peaks where each peak arrives after a time given by the time calibrator as shown in Fig. 4.4a. This allows one to obtain a conversion from channel to ns. By drawing the calibrated response of the TAC as a function of the measured response it is possible to check the linearity of the response (shown in Fig. 4.4b) and to correct for eventual non linearities.

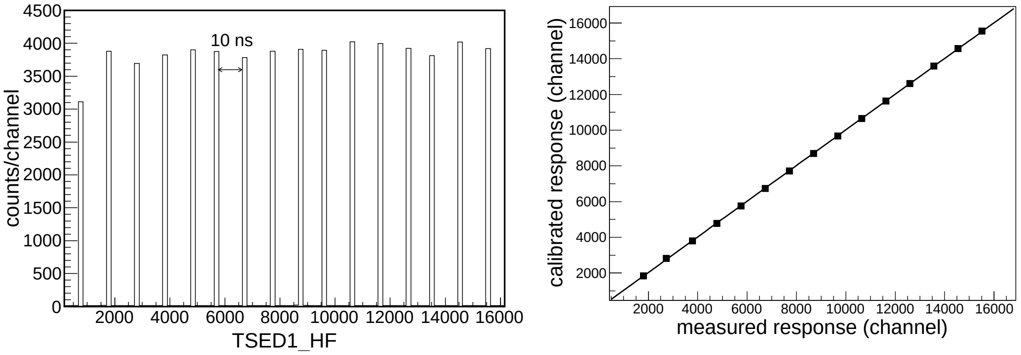

(a) *calibration of TOF in ns* (b) *linearity of response*

Figure 4.4: *Calibration of TSED1_HF time of flight with a time calibrator: a) calibration of the TAC with a time interval of 10 ns b) check of the linearity of the TAC module.*

In order to obtain an absolute value for the TOF, it was necessary to correct the measured values with a certain offset that will shift them to the real time of flight of the recoil nuclei. The first step was to identify the Zn isotopes from the dE spectra. In the M/Q spectrum of Zn isotopes, the peaks with the strongest intensity correspond to different charge states of the isotope with A=70. Since in that stage of analysis it was not possible to uniquely identify each charge state, an arbitrary M/Q peak was selected and a charge state distribution was attributed to the peaks. A central trajectory for that charge state was selected, so that the energy of the recoils along this central trajectory was well defined. Using LISE++ [81] the velocity of the fragment have been estimated taking into account the energy losses in the different layers of the detectors from which the TOF values have been deduced. An additional adjustment of the T_{offset} is necessary since calculations were done assuming a certain charge state. More subtle tuning of T_{offset} is further obtained after the alignment in M/Q which will be described in the following section.

The mass of the recoil nuclei depends on the time of flight and therefore, the mass resolution depends on the time of flight resolution. In order to check the best timing properties needed for the best mass resolution, the widths of all the TOFs distributions used in experiment were compared. The resolution was checked using the direct U beam with the selection of the charge state having the central trajectory and hitting the central Si detector. The results are summarised in Table 4.1.

Table 4.1: *Time resolution of different TOFs*

different TOFs	σ (ps)
TSi _HF	414(7)
TSED1 _Si	517(8)
TSED2 _Si	763(9)
TSED1 _HF	343(6)
TSED2 _HF	620(6)

The results show that TSED1_HF has the best resolution. The M/Q distribution of Zn isotopes, detected on the central Si detector, obtained with TSED1_HF and TSi_HF timings are shown in Fig. 4.5. One can notice a much better separation between adjacent M/Q values when the TSED1_HF timing was used.

From the above mentioned arguments, the timing from TSED1_HF was used for the mass determination of the recoil nuclei.

4.2 Particle identification

4.2.1 M/Q identification

As it was mentioned in the previous section, the M/Q ratio of recoil nuclei is obtained from the reconstructed $B\rho$ and velocity values:

$$M/Q = \frac{B\rho}{3.105\beta\gamma} \tag{4.1}$$

The β and γ are calculated from:

$$\beta = \frac{D}{c \cdot TOF} \quad \text{and} \quad \gamma = (1-\beta^2)^{-1/2}$$

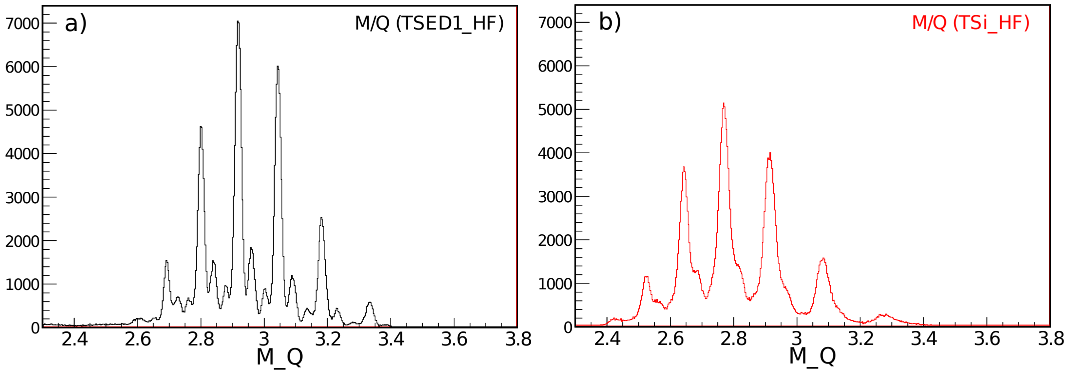

Figure 4.5: *The M/Q spectra of Zn isotopes, detected on the central Si detector, obtained with 2 different timings: a) TSED1_HF and b) TSi_HF. A clear separation of M/Q values was obtained with TSED1_HF signal contrary to TSi_HF signal. (The M/Q values were not aligned.)*

where D is the distance between the target and SED1, while TOF is the flight time of recoils based on the TSED1_HF signal corrected to match the TOF between the target and SED1.

In the reconstruction algorithm, the *Path* of the recoil nuclei has been reconstructed from the target till the image focal plane. Therefore it is necessary to subtract the distance between the image focal plane and the position of the SED1 detector from the *Path* to obtain real value for the distance D.

By looking at the M/Q spectrum obtained for Zn nuclei detected in a single silicon detector, one can see that the measured peaks do not correspond to the real M/Q values and that the spacing between two adjacent peaks of the same isotope is not accurate. The $B\rho$ values and distances D obtained from the reconstruction algorithm are considered to be correct. Therefore, the only remaining parameter from equation 4.1 that can be adjusted to restore good M/Q values is the TOF.

Since the distance between two adjacent peaks of the ^{70}Zn with a different charge state was not accurate, it was not possible to assign absolute value to each measured M/Q peaks. It was noticed that the disagreement between the absolute and measured M/Q values is increasing by going away from the charge states that correspond to the central trajectory as well as by going from central to more peripheral detectors. The first step was to adjust the difference between two adjacent M/Q$_i$ and M/Q$_{i+1}$ peaks to its real difference. The influence of changing the time offset on the difference between two successive M/Q peaks was investigated and the effect was a linear shift of M/Q values without any modifications of the difference between the two peaks. The other option to adjust the TOF for reproducing correctly the M/Q distribution is to modify the distance between the two SED detectors along the beam line (z - direction). The effects of changing the z position of the SEDs has been evaluated using the central silicon detectors.The following procedure was used: The optimal position of SED1 and SED2 detectors in z axis is obtained by minimising the sum of the standard deviations of the differences between measured M/Q values from two adjacent charge states with respect to the real one, for all identified M/Q peaks:

$$\chi^2 = \sum_i \frac{\left[\left(\left(\frac{M}{Q_i}\right)_{meas} - \left(\frac{M}{Q_{i+1}}\right)_{meas}\right) - \left(\left(\frac{M}{Q_i}\right)_{exact} - \left(\frac{M}{Q_{i+1}}\right)_{exact}\right)\right]^2}{\left[\left(\frac{M}{Q_i}\right)_{exact} - \left(\frac{M}{Q_{i+1}}\right)_{exact}\right]^2} \tag{4.2}$$

Once the optimal z position of SED detectors is obtained, it is possible to assign a charge state to each peak. The correction in T_{offset} was applied, for the central detector with the highest statistics, so that the measured M/Q values match the real M/Q values. In order to make the alignment of M/Q distributions for the various nuclei detected in each Si detector, a fine tuning of T_{offset} is done for each Si detector separately. Namely, by selecting different Si detectors we select different path. Nuclei detected on Si detectors located further from the central detector will have a longer path and therefore a longer TOF. Consequently a fine tuning of T_{offset} for each Si detector was necessary.

The M/Q and Q values for ^{70}Zn nuclei detected by Si8 detector (see Fig. 3.5), obtained by fine tuning of T_{offset} and z position of SED detectors are presented in Table 4.2. To illustrate the quality of the final M/Q alignment, the deduced charge states for ^{70}Zn are also given for Si12 (detector furthest away with enough statistics to be used).

Table 4.2: *Charge state distributions obtained after fine tuning of T_{offset} (see text) for ^{70}Zn detected in Si8 and Si12.*

M/Q_{exact}	Q_{exact}	Si8; T_{offset}	Si8; T_{offset} and SED position	Si12; T_{offset} and SED position
		Q_{meas}	Q_{meas}	Q_{meas}
2.693	26	26.075	25.997	
2.800	25	25.039	24.996	25.000
2.917	24	24.005	23.992	23.995
3.044	23	22.988	23.000	22.999
3.182	22	21.969	21.999	22.019

Fig. 4.6 shows the M/Q distributions of Zn isotopes after the alignment. With different colours are indicated the M/Q distributions originating from the selection on central Si detectors. In particular, with the dark blue line is presented the M/Q distributions of Zn isotopes detected on the central Si detector. The strongest peaks of the distribution correspond to M/Q values of elastically scattered ^{70}Zn nuclei.

The charge states for ^{70}Zn are indicated. The peaks positioned on the right-hand side (left-hand side) of these ^{70}Zn peaks correspond to M/Q values of ^{71}Zn, (^{69}Zn).

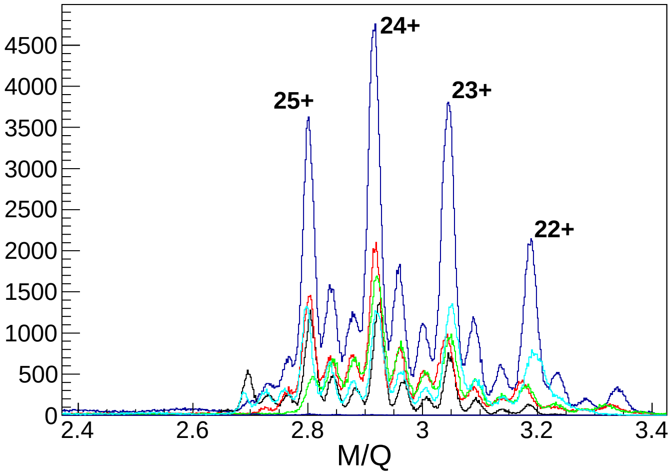

Figure 4.6: *M/Q distribution of Zn isotopes obtained for the central group of Si detectors. The M/Q distribution of Zn isotopes coming from the central Si detector is in a dark blue. The charge states that correspond to the M/Q peaks of ^{70}Zn are indicated. The peaks positioned on the right-hand side of those coming from ^{70}Zn correspond to ^{71}Zn nuclei with the same charge as for ^{70}Zn , while those peaks positioned on the left-hand side of ^{70}Zn correspond to M/Q value of ^{69}Zn.*

4.2.2 M identification

Usually, the mass identification of a recoil nucleus is obtained from the measurements of the total energy of the fragment E_{tot} and the velocity using the following formula:

$$M = \frac{E_{tot}}{931.5(\gamma - 1)} \tag{4.3}$$

On its way to the Si detector where it is stopped, the nucleus passes through various materials losing a fraction of its energy. The energy loss is measured with the in 3 pads of the IC and the residual energy in the Si detectors, while in the other layers such as SED detectors, Mylar foils and dead layers of the IC, this information is lost. Therefore, the total energy of the fragment can be expressed as:

$$E_{tot} = \Delta E_{IC} + \Delta E_{nm} + E_{Si} \tag{4.4}$$

where ΔE_{IC} is the energy loss measured in the IC, ΔE_{nm} is the nonmeasured energy loss and E_{Si} is the residual energy deposited in Si detectors.

The total energy of the recoil nuclei can be also expressed as:

$$E_{tot} = a\Delta E_{IC} + \sum_{i=1}^{21} e[i]E_{Si[i]} \tag{4.5}$$

The first term describes the total energy loss, which includes the measured and nonmeasured energy losses. By selecting the elastically scattered ^{70}Zn ions with known energy, having the central trajectory, it is possible to calculate the energy losses with the LISE++ code. The a factor is defined as the ratio between the total energy loss and the energy loss in the IC, both calculated by LISE++. Thus, the energy loss measured in the IC scaled by the factor a should give the total energy loss. The second term describes the residual energy deposited in the Si detectors where $E_{Si[i]}$ denotes the signal generated in Si detector i and $e[i]$ is the calibration factor of each Si detector used to convert the signal to a residual energy. The factors a and $e[i]$ for each Si detector were determined from calculation of the mass of ^{70}Zn for different charge states. The criterium for determining the a and $e[i]$ parameters is to obtain the best mass reconstruction for each charge state.

The final mass vs mass-over-charge state distribution including all Si detectors is shown in Fig. 4.7.

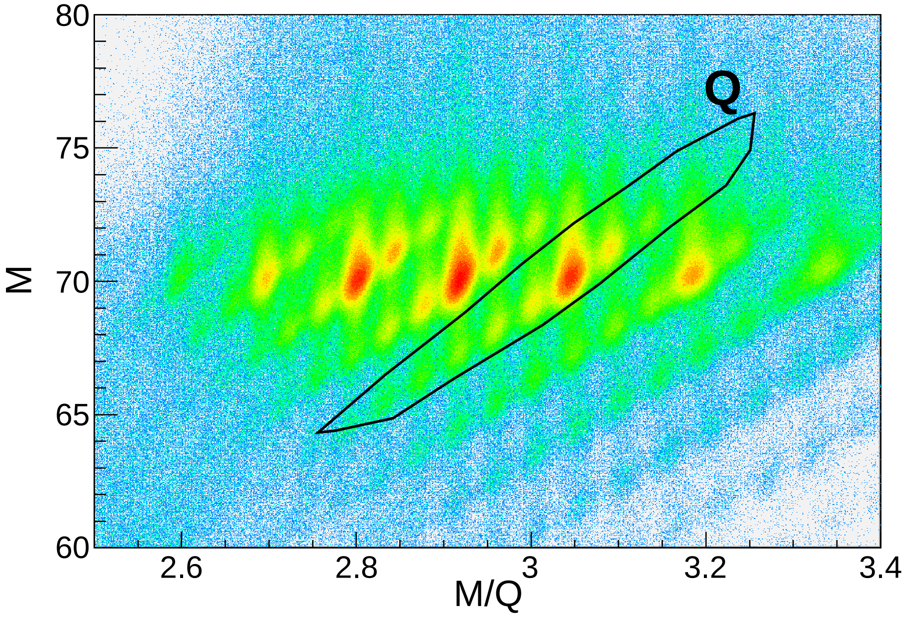

Figure 4.7: *M vs M/Q spectra*

From the M vs M/Q matrix, one can select all nuclei having the same charge state but a different mass as indicated in Fig. 4.7. Since the strongest contribution comes from the elastic scattering of ^{70}Zn one can assign a unique charge state to the elastic peaks as shown in Fig. 4.6. Finally, from the M/Q distribution and the identified charge state Q, one can extract the mass.

4.2.3 Z identification

The energy loss of a particle passing through some matter is to the first approximation proportional to Z^2. Therefore, the identification of the atomic number Z is obtained through the analysis of ΔE. The procedure used for Z identification is the same as the one used in the thesis of A. Dijon [78] and can be summarised as follows:

- from the ΔE-E_{tot} matrix draw the line going through the center of each "banana" that corresponds to different Z;
- the drawn line is approximated with a second order polynom thus approximating Bethe-Block formula for energy loss. The lines obtained in this way are presented in Fig. 4.8;
- Each line is associated with a proper Z number. The identification of Z line is trivial, since the strongest ΔE-E_{tot} banana corresponds to the Zn isotopes;
- for each data pair in the ΔE-E_{tot} matrix, the distance to the closest line was calculated and the corresponding Z value assigned to the pair.

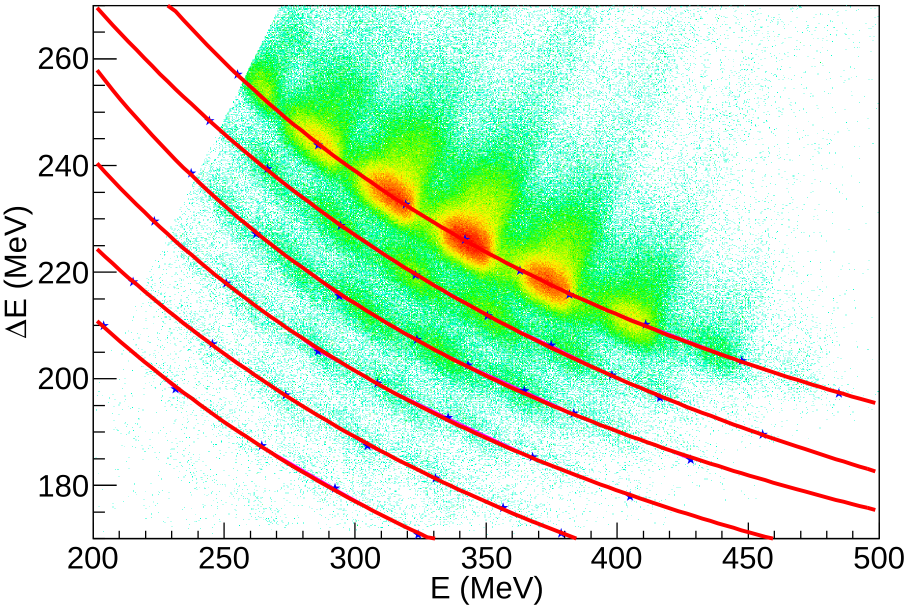

Figure 4.8: *Z identification*

The complete identification matrix in Z vs A obtained from all charge states and all Si detectors is presented in Fig. 4.9.

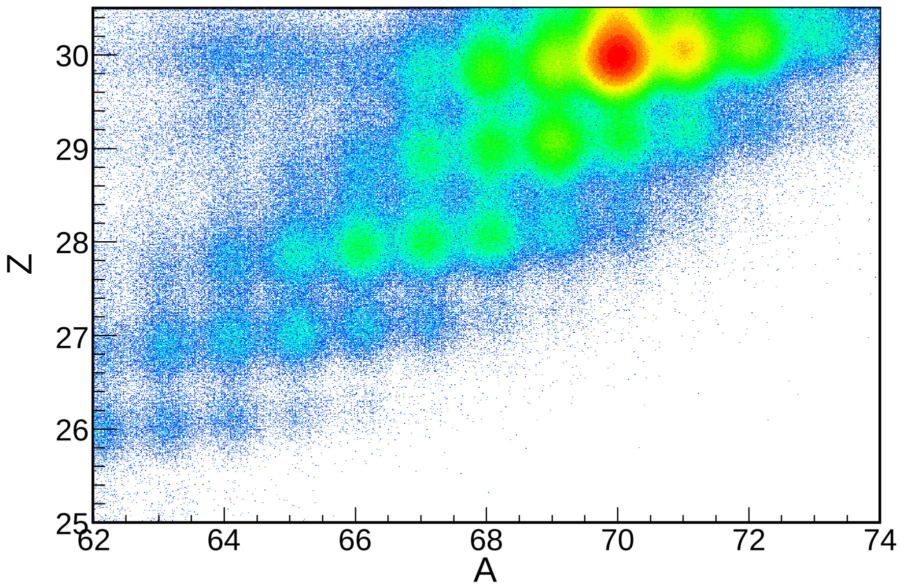

Figure 4.9: *Z vs A identification matrix obtained from all charge states and all Si detectors for one target-degrader distance.*

The Z and A distribution of all detected recoil nuclei are presented in Fig. 4.10. The measured resolutions are:

$$\frac{\Delta Z}{Z} = 0.8\% \quad \text{and} \quad \frac{\Delta A}{A} = 0.5\% \tag{4.6}$$

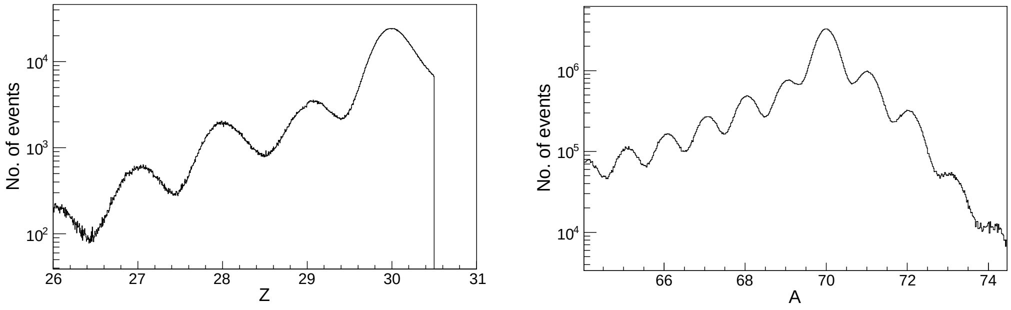

(a) *Z distribution* (b) *A distribution*

Figure 4.10: *a) Z and b) A distribution obtained from the Z vs A matrix.*

4.3 Recover of incomplete events

In the process of reconstruction, some events might be lost. The trajectory of the recoils is obtained from the X and Y measurement in both SED detectors. This lead to the determination of x_f, y_f, θ_f, ϕ_f and further on reconstruction of the *Path*, $B\rho$, θ_i, ϕ_i parameters (see 2.3.1.4). In this section is described the procedure applied to check the missing events and to recover some of those events.

The first step was to exclude Mg-like contaminants that comes from the reaction of U beam with the Mg backing of the target. This was done from selection in $\Delta E - E$ matrix. The number of events containing the X coordinates, the Y coordinates and both X and Y coordinates were compared with the total number of events for both SED detectors. For SED1: X is present in 94.5 % of the total number of events, while this proportion is, 89.8 % for Y and 89.1 % for events with both X and Y. For SED2 these numbers are 95.9 %, 94.5 % and 94.0 %, respectively.

In Fig. 4.11 are presented the number of events in which all pairs of coordinates (X_1, Y_1) and (X_2, Y_2) in SED1 and SED2 are measured, and events in which only one (or more) coordinate(s) is(are) missing. If only one coordinate is missing it is possible to reconstruct it. Depending on whether the missing coordinate is X or Y, two different approaches are used.

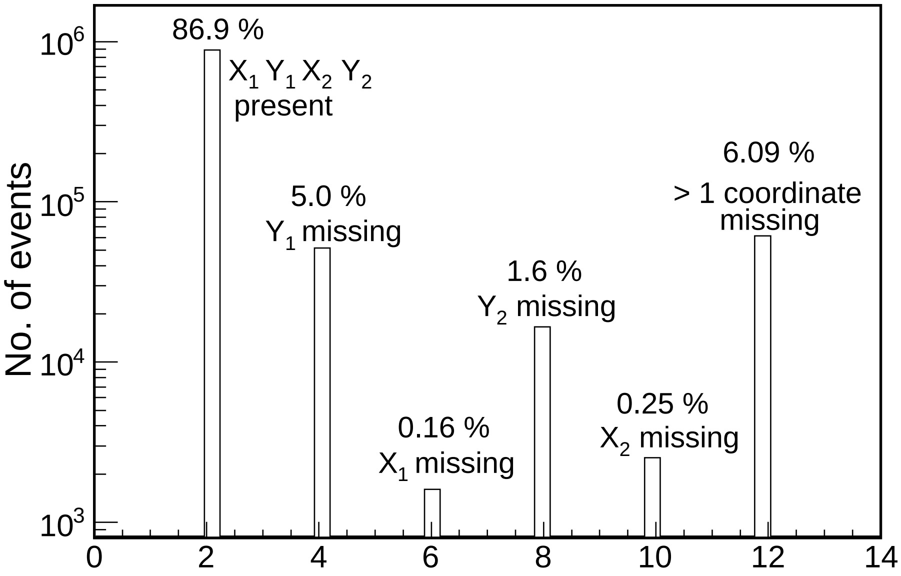

Figure 4.11: *Summary of events in which are detected all 4 coordinates in SED1 and SED2, events in which one of coordinates was not measured and events where 2 or more coordinates were missing.*

As the SED detectors are placed after the dispersive element of the spectrometer, the particles are transported in straight line between the two SED detectors. In the configuration of VAMOS we have used, there were no dispersive elements in vertical direction with respect to the beam axis and therefore, when the missing coordinate was Y, the recovering was obtained by assuming that $Y_1=Y_2$. Recovering of the missing X coordinate is less straight forward. From the events in which all coordinates are presented, a distribution of X_1 is drawn for a given X_2 value, $X_1=f(X_2)$. The distribution is approximated with a Gaussian function. The $X_1=f(X_2)$ and the corresponding Gaussian is determined by step of 5mm in X_2. Now, if X_1 is missing, the value, the appropriate Gaussian distribution is selected according to the measured X_2value and X_1 is sampled from this distribution. An analogous procedure is applied if X_2 is missing.

With this coordinates recovery coordinates, the reconstruction is improved from 86.9 % to 94 %. In the final step, from the reconstructed x_f, y_f, θ_f, ϕ_f parameters, *Path* was reconstructed in 99.87 % of events that have all coordinates measured or recovered (i.e. 93.9 % of all events). Recovery of the missing *Path* was not performed.

4.4 EXOGAM calibration

In this section, different calibration procedures for EXOGAM are described in order to increase peak-to-total ratio.

4.4.1 The addback and correction on Compton scattering

The γ-rays are detected indirectly through the conversion of photons to energy of electrons. At the γ-ray energies of interest, three basic interaction processes are dominant in converting the incident photon energy into electrons in a detector: the photoelectric effect, the Compton scattering and the pair production. The photoelectric effect is dominant below 100 keV in which the total energy of a γ-ray E_γ is absorbed in the detector crystal emitting an electron. At higher energies, the photon is preferentially scattered on an electron of the crystal (Compton scattering) transferring some amount of phonon energy, producing at the same time a new photon with a lower energy. The process can repeat several times, reducing subsequently the γ ray energy, resulting finally in a production of photoelectrons. Ideally, in an infinite size detector the sum of electron energies produced by Compton scattering and photoelectron energies gives the initial energy of γ-ray.

Due to the limited size of the detector crystal it is possible that secondary γ-rays, produced in a Compton scattering, escape the detector. This leads to incomplete charge collection rising therefore the Compton background and deteriorate the peak-to-total ratio. The construction of EXOGAM allows us to improve the peak to total ratio in two different ways. Due to the scattering, the γ-ray energy can be fully absorbed within several crystals of a clover detector. By adding the energy deposited in each crystal of one clover detector it is possible to recover a full energy of γ-ray and this treatment is called the add-back.

In addition, as described in section 3.3.2 an active shield consisting of BGO/CsI detectors is placed around the germanium crystals. The γ-rays that are not fully stopped in Ge detector can be detected in BGO/CsI. In that case the reconstructed energy from Ge crystal is therefore lower than initial γ-ray energy and the BGO/CsI is used as a veto detector suppressing this kind of events. In Fig. 4.12 three different γ spectra obtained from a ^{60}Co source are presented. From the spectrum created without any corrections peak-to-total ratio was found to be 11.7 %. By applying the treatment with add-back (blue spectrum) peak/total is improved up to 20.5%. With the inclusion of both anti-Compton system and add-back (red spectrum), the peak-to-total ratio is further increased to 24.0 %.

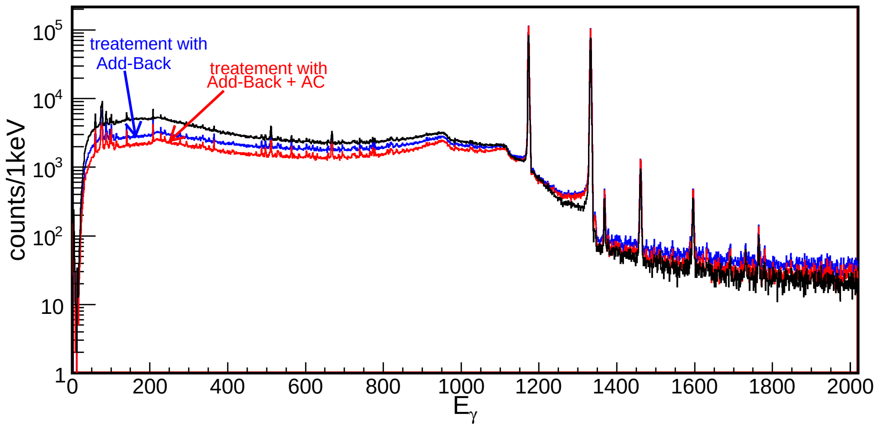

Figure 4.12: *Different γ spectra obtained from a ^{60}Co source for different corrections applied.*

4.4.2 Calibration of Ge detectors

The energy response of each germanium crystal was calibrated with a ^{152}Eu source. Eu source is suitable for energy calibration since it covers a large range of energies. The add-back and Compton suppression system are included in the calibration of the crystals. Fig. 4.13 shows the relative efficiency of an EXOGAM detector coming from 8 clovers together. The relative efficiency for the whole Ge array has been determined using the RADWARE programme and was fitted with the following function [82]:

$$\varepsilon_{rel} = e^{A+By+Cy^2+Dy^3+Ey^4} \qquad \text{where} \qquad y = ln(E_\gamma) \tag{4.7}$$

The sharp cut-off in relative efficiency of γ-rays at low energies originates from the introduction of a thick layer of absorber in front of the detectors in order to stop

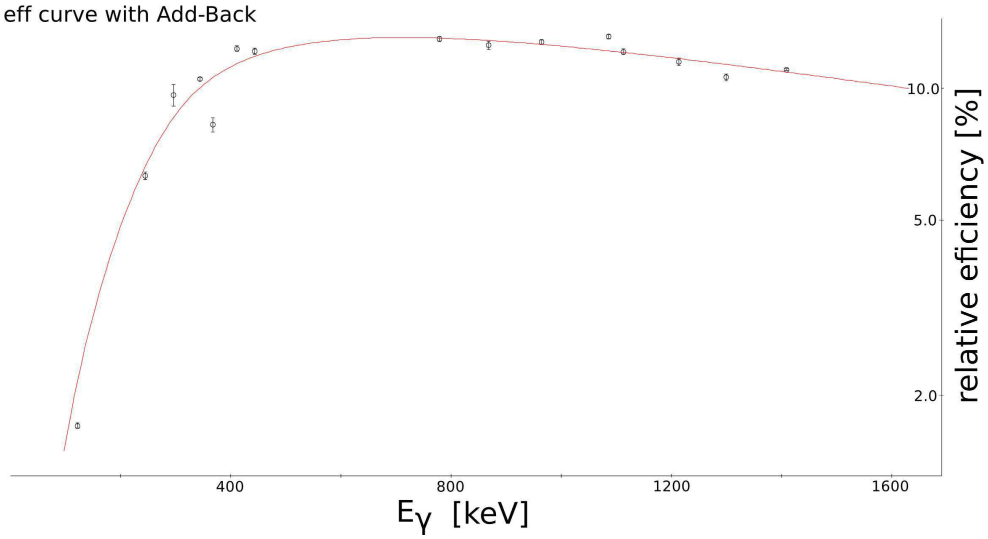

Figure 4.13: *Relative efficiency of EXOGAM array obtained with a ^{152}Eu source.*

X-rays and low energy γ-rays, and to avoid too large counting rates and pile-up in the Ge crystals.

4.4.3 Doppler correction

Typically, the reaction products from deep-inelastic collisions leave the target with 10 - 15 % of speed of light. The γ-rays emitted from those nuclei will be shifted in energy by the Doppler effect according :

$$E_{meas} = E_0\gamma(1 - \beta cos\psi) \tag{4.8}$$

where E$_{meas}$ is the measured γ-ray energy, E$_0$ is the energy of the γ-ray emitted at rest, β is the v/c of the deexciting nucleus, while ψ is the angle between trajectory of the recoil nuclei and the emitted γ-ray.

A recoil nuclei vector and a vector of emitted γ-ray are shown in Fig. 4.14. Starting from the recoil nuclei vector $\vec{R_r}$ and the vector of emitted γ-ray $\vec{R_\gamma}$:

$$\vec{R_r} = \|\vec{R_r}\| \begin{pmatrix} sin\theta_r cos\varphi_r \\ sin\theta_r sin\varphi_r \\ cos\theta_r \end{pmatrix} \tag{4.9}$$

and

$$\vec{R_\gamma} = \|\vec{R_\gamma}\| \begin{pmatrix} sin\theta_\gamma cos\varphi_\gamma \\ sin\theta_\gamma sin\varphi_\gamma \\ cos\theta_\gamma \end{pmatrix} \tag{4.10}$$

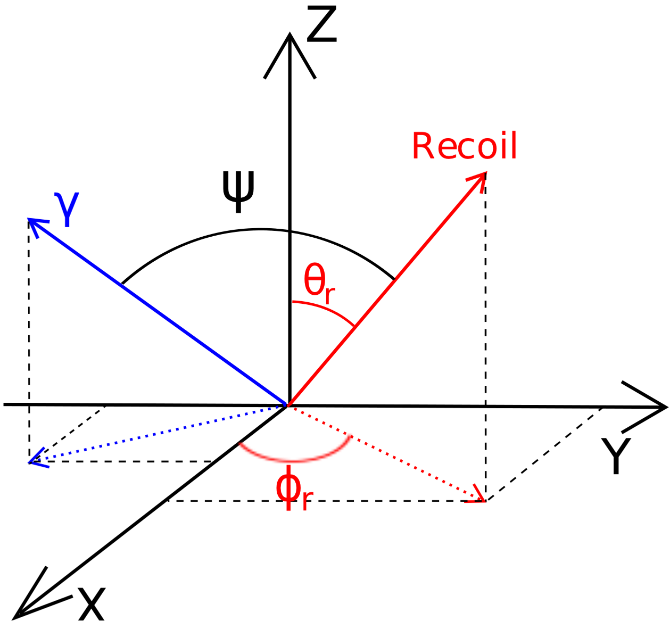

Figure 4.14: *A recoil nuclei vector and vector of emitted γ-ray are shown in spherical coordinate system. The origin is the target position and Oz is the beam axis at that origin. The indicated ψ angle is determined from the scalar products of those vectors.*

where θ_r and φ_r correspond to the angles between the recoil nuclei vector and its projection on zy- and zx-plane, respectively, while θ_γ and φ_γ correspond to the angles of the γ-ray.

The ψ angle can be determined from the scalar product of $\vec{R}_r$ and $\vec{R}_\gamma$

$$\vec{R}_r\vec{R}_\gamma = \|\vec{R}_r\|\|\vec{R}_\gamma\| cos(\vec{R}_r, \vec{R}_\gamma) \tag{4.11}$$

leading to:

$$cos\psi = cos(\vec{R}_r, \vec{R}_\gamma) = sin\theta_r cos\varphi_r sin\theta_\gamma cos\varphi_\gamma + sin\theta_r sin\varphi_r sin\theta_\gamma sin\varphi_\gamma + cos\theta_r cos\theta_\gamma \tag{4.12}$$

The θ_r and φ_r are obtained from the trajectory reconstruction in VAMOS, while the angles θ_γ and φ_γ are given by the angular position of the segment that detected a γ-ray, expressed in the coordinate system shown in Fig. 4.14. In order to check whether the angle of emitted γ-ray obtained between the trajectory of recoil nuclei and the position of segment of detector is reconstructed well or not, we have drawn the matrix of the Doppler uncorrected γ-ray energies that coincide with ^{72}Zn nuclei as a function of the angle between trajectory of the recoil nuclei and the emitted γ-ray (shown in Fig. 4.15). The calculated curve that shows γ-ray energy of the $2^+ \rightarrow 0^+$ transition of ^{72}Zn as a function of the angle between trajectory of the recoil nuclei and the emitted γ-ray, is superimposed on the matrix (the red dotted line in Fig. 4.15).

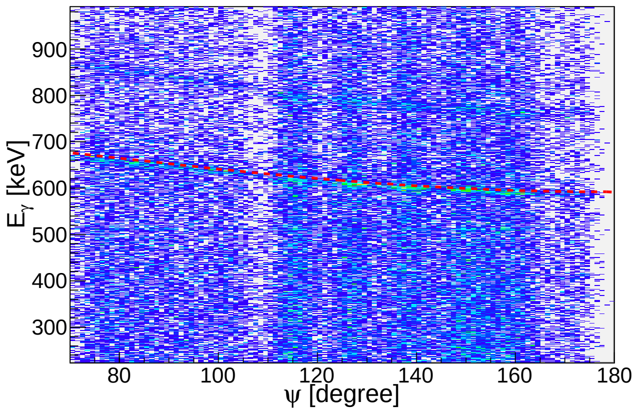

Figure 4.15: *The matrix of the Doppler uncorrected γ-ray energies that coincide with the ^{72}Zn nuclei as a function of the angle of emitted γ-ray are shown. The red dotted line shows the calculated γ-ray energy of the $2^+ \to 0^+$ transition of ^{72}Zn as a function of the angle between trajectory of the recoil nuclei and the emitted γ-ray. Good agreement between measured and calculated Doppler uncorrected γ-ray energies confirm a proper reconstruction of the angle between a recoil nuclei vector and a vector of emitted γ-ray with respect to the beam axis.*

The good agreement between the measured and theoretical γ-ray energies of the Doppler uncorrected spectrum confirms the correct reconstruction of the angle between trajectory of the recoil nuclei and the emitted γ-ray.

4.5 The lifetime analysis: The differential decay curve method

The equations 3.4 and 3.5 in the previous chapter are simplified equations that can be used to calculate the lifetime of excited state if only that state is excited. A more general decay scheme showing the h levels that populate the level of interest i which deexcites to the levels j is presented in Fig. 4.16.

As it was already mentioned, the velocity of the recoil nuclei after the degrader was measured in the VAMOS detection system and this velocity is used for the Doppler correction of the emitted γ-rays. Consequently, the γ-rays emitted after the degrader will be corrected with the appropriate velocity and therefore their energy will be "unshifted" with respect to the γ-ray energy of nuclei at rest. The energy of the γ-rays emitted before the degrader will be corrected by a "wrong" velocity and will appear shifted toward lower energies. As a result, a single transition can have two components, "shifted" and "unshifted". The differential decay curve method

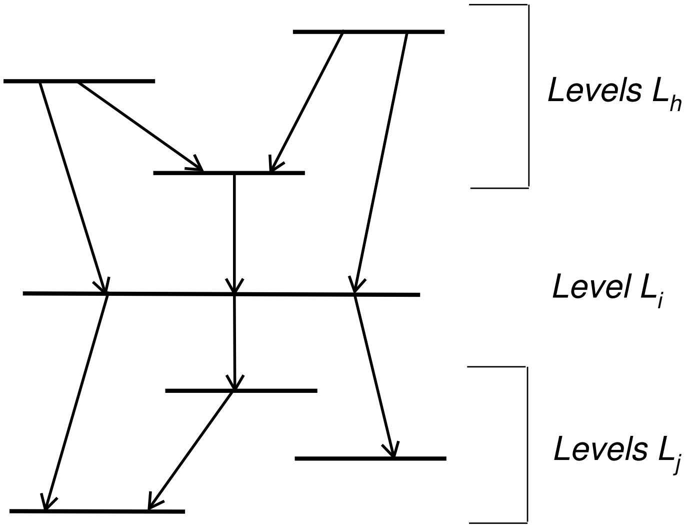

Figure 4.16: *A schematic decay scheme of the L_i - level of interest, populated by levels L_h and dexciting to L_j levels*

is based on several independent lifetime measurements determined for each target-degrader distance. Only the relative flight times, i.e. target-to-degrader distances are required which can be measured with the high precision. For each distance, the intensity ratio of unshifted component over the total peak intensity is determined, thus forming the decay curve [63]:

$$Q_{ij}(x) = \frac{I^u_{ij}(x)}{I^u_{ij}(x) + I^s_{ij}(x)} \tag{4.13}$$

where indices i and j refer to transition from i state to j state.

The Q_{ij} values obtained for each distance are fitted with a continuous differentiable function, usually exponential or polynomial. In this experiment, we have measured lifetimes at two different target-degrader distances and we have fitted data using exponential curves which is a natural choice, since it follows the decay law. However, we have tried to add a third point at large target-degrader distance (where all nuclei should decay before degrader) and to fit data using a second order polynimial, but the results (and error bars) were very sensitive to the choice of the distance.

The lifetime of the state is extracted from the obtained decay curve and the recoil nucleus velocity before degrader [63]:

$$\tau_i(x) = -\left(v\frac{dQ_{ij}(x)}{dx}\right)^{-1}\left(Q_{ij}(x) - \sum_h b\frac{I^s_{hi} + I^u_{hi}}{I^s_{ij} + I^u_{ij}}Q_{hi}(x)\right) \tag{4.14}$$

where b is the branching ratio between h level and i level. The error on the calculated lifetime is determined by standard error propagation formula.

The velocity before the degrader, v used for the lifetime calculations, is extracted from the velocity after the degrader measured in VAMOS, corrected using LISE++. In order to check the reliability of this corrections we have applied Doppler correction using velocity v to γ-rays emitted before degrader. The γ-ray energy obtained in this way corresponds to the energy of the "unsifted" peak, which means that the velocity before degrader was properly estimated.

5 Experimental results

In this chapter, the experimental results obtained from the RDDS measurement are discussed. In the deep-inelastic collisions of the ^{238}U beam on the ^{70}Zn target, several isotopes of nuclei ranging from Z=30 till Z=26 were identified. Only nuclei in which γ-ray transitions were observed are discussed. The obtained γ-ray spectra for those nuclei are presented. When both the shifted and unshifted components were observed, the lifetimes were extracted using the differential decay curve method described in previous section. When only one component was measured, an upper limit for the lifetime was extracted.

The common procedure for fitting the peaks can be summarised as follows:

- fit of the unshifted component for some transitions which are well separated from any other transitions (peaks) (e.g. $4_2^+ \rightarrow 2^+$ in the case of ^{70}Zn);
- from the results of this fit, the peak widths of the other peaks is scaled;
- the fit of these other peaks is done by fixing the obtained widths and energies for the unshifted components, since their energies are corrected with appropriate Doppler shift. Conversely, centroids were not fixed for the fit of the shifted components;
- the fit of the shifted components is rejected if the energy of the fitted peaks differs by 0.3 % from the energy calculated with LISE++;
- the background parameters, originating from the fitted spectra obtained for one target-degrader distance, the widths of all the peaks and the position of the unshifted peaks are fixed and used for fitting the spectra at the second distance.

5.1 Zn isotopes

5.1.1 ^{70}Zn

The ^{70}Zn nuclei are produced in the most intense channel that corresponds to the inelastic scattering of U beam on ^{70}Zn target. The shifted and/or unshifted components of $2^+ \rightarrow 0^+$, $4^+ \rightarrow 2^+$, $2^+_2 \rightarrow 2^+$ and $4^+_2 \rightarrow 4^+$ transitions lie close in energy making them difficult to resolve. The best separation of the peaks is obtained by selecting γ-rays emitted at the most backward angles. Due to the high statistics of identified ^{70}Zn it was possible to select γ-rays emitted at the most backward angles >135° and still to have a reasonable intensity of the peaks.

The obtained γ-ray spectra of ^{70}Zn at two distances: 33.6 ± 1.0 and 99.0 ± 3.0 μm are shown in Fig. 5.1 for detectors at angle >135°. The following transitions were observed: $2^+ \rightarrow 0^+$, $2^+_2 \rightarrow 2^+$, $4^+ \rightarrow 2^+$, $4^+_2 \rightarrow 4^+$, $6^+ \rightarrow 4^+$. The corresponding energies from NNDC [20] are 884.5, 874.3, 901.7, 906.5, 1072.5 and 1108.4 keV, respectively. The observed level scheme of ^{70}Zn, constructed from the measured γ-ray spectrum is shown in Fig. 5.2.

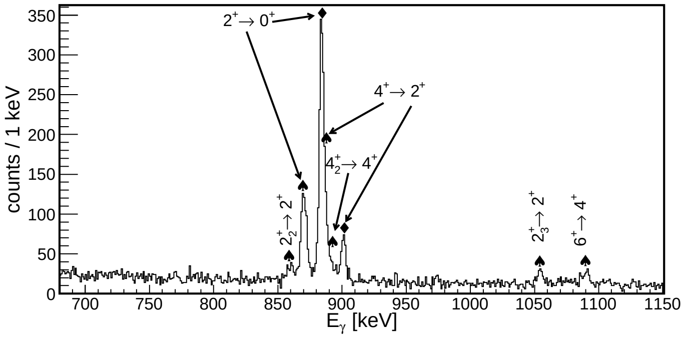

(a) ^{70}*Zn spectrum from the 33.6 μm target-degrader distance*

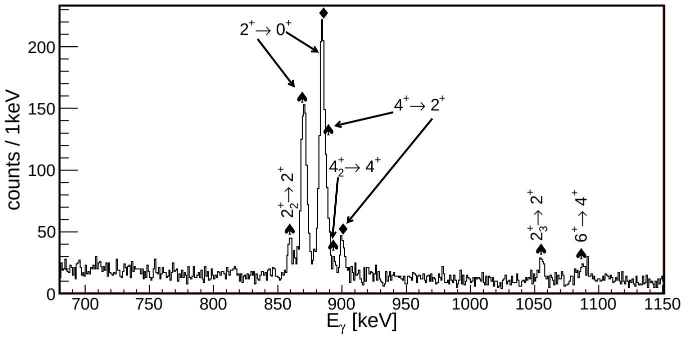

(b) ^{70}*Zn spectrum from the 99 μm target-degrader distance*

Figure 5.1: *γ-ray spectrum of ^{70}Zn obtained for two target-degrader distances. With a ♦ symbol are indicated the unshifted components while with a ♠ are indicated the shifted components of the transitions.*

According to formula 4.13, the decay curve $Q_{ij}(x)$ was calculated from the intensities of the shifted and unshifted components of $2^+ \rightarrow 0^+$ and $4^+ \rightarrow 2^+$ transitions at both distances. On the left-hand side of Fig. 5.3 the decay curves obtained for $2^+ \rightarrow 0^+$ and $4^+ \rightarrow 2^+$ transitions of ^{70}Zn are shown.

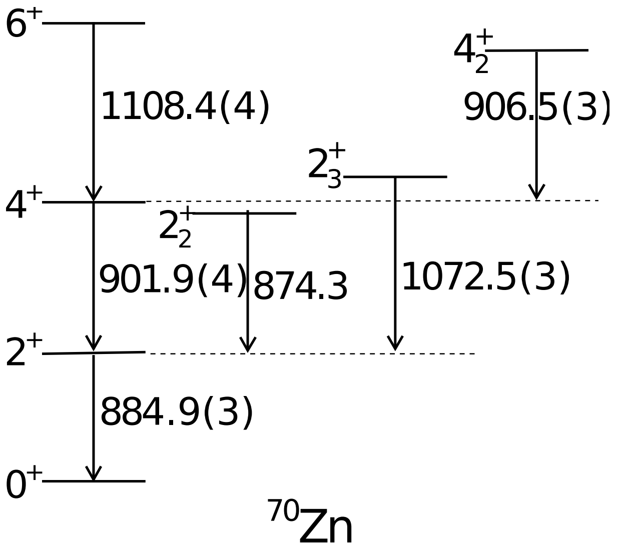

Figure 5.2: *Level scheme of ^{70}Zn obtained from the measured γ-ray spectrum*

The lifetime of the 2^+ state was calculated from the decay curve, corrected by triple feeding coming from the: $4^+ \rightarrow 2^+$, $2^+_2 \rightarrow 2^+$ and $2^+_3 \rightarrow 2^+$ transitions according to the formula 4.14, while for the lifetime of 4^+ state feedings from $6^+ \rightarrow 4^+$ and $4^+_2 \rightarrow 4^+$ were taken into account. The mean lifetime τ is calculated as a weighted average of the two values measured at both distances by taking into account the error bars for each measurement. The obtained lifetimes of the 2^+ and 4^+ states are shown on the right-hand side of Fig. 5.3 and presented in Table 5.1.

It was not possible to resolve unshifted component of $2^+_2 \rightarrow 2^+$ state, due to the proximity to the shifted component of $2^+ \rightarrow 0^+$ transition and therefore the lifetime of 2^+_2 state was not estimated. From previous experiments [83], the lifetime of the 2^+_2 state is $\tau = 0.35^{+35}_{-17}$ ps, which is too short to be measured in our experiment. Therefore only the shifted component of $2^+_2 \rightarrow 2^+$ transition was used to estimate the feeding of the 2^+ state.

The observed $4^+_2 \rightarrow 4^+$ transition at 906.5 keV energy, has only a shifted component, with no evidence of the unshifted one. This gave an upper limit of lifetime $\tau_{2^+_2}$ <0.7 ps calculated from formula 5.1:

$$\tau = -\frac{d}{v\ ln\frac{I_u}{I_u+I_s}} \tag{5.1}$$

The lifetime was estimated from the spectrum at 99 μm distance, since the corresponding peak is stronger than in the 33.6 μm distance spectrum.

Similarly to the fitting of $4^+_2 \rightarrow 4^+$ transitions, the unshifted component of the $2^+_3 \rightarrow 2^+$ and $6^+ \rightarrow 4^+$ transitions are not observed. Due to the low statistics in the shifted components, the lifetimes of the 2^+_3 and 6^+ states cannot be estimated, but it indicates an upper limit similar to the one obtained for the 4^+_2 state.

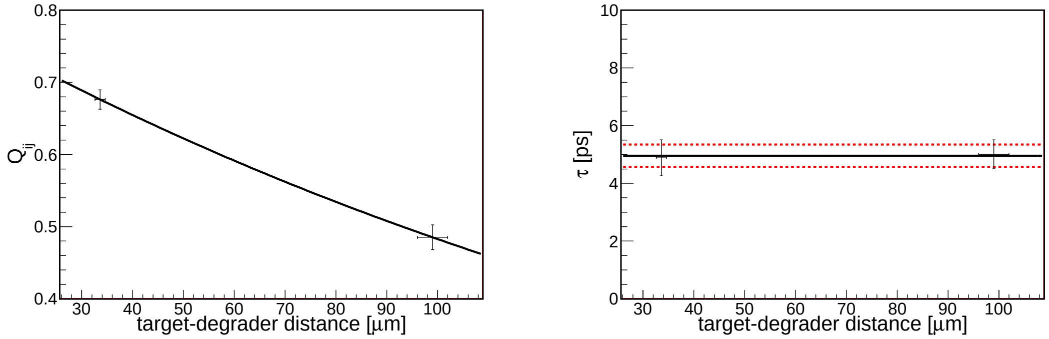

(a) *Decay curve of* 2^+ *state* (b) *Lifetime of* 2^+ *state*

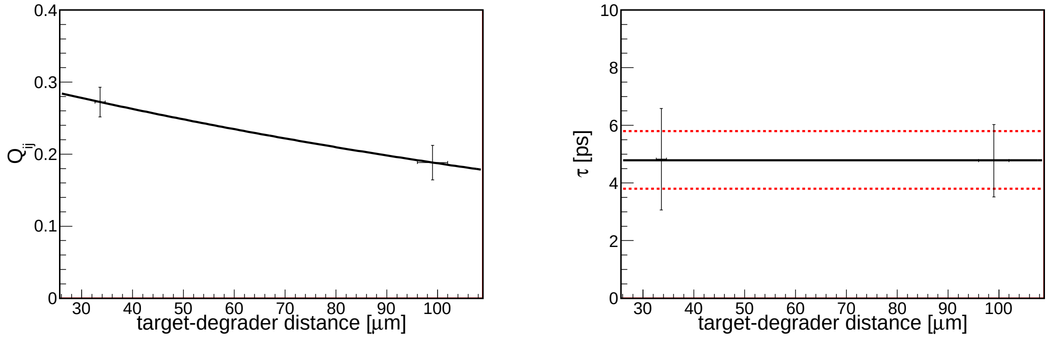

(c) *Decay curve of* 4^+ *state* (d) *Lifetime of* 4^+ *state*

Figure 5.3: *Decay curve and lifetime of* 2^+ *and* 4^+ *states of* ^{70}*Zn. The red-dotted lines represent an error bar of the mean lifetime calculated for both distances.*

The results of measured lifetimes in ^{70}Zn are given in Table 5.1.

Table 5.1: *The measured lifetimes in ^{70}Zn*

state	Excitation energy [keV]	τ [ps]
2^+	884.9	5.0 ± 0.4
4^+	1786.3	4.8 ± 1.0
4_2^+	2693.0	<0.7

5.1.2 ^{72}Zn

On the left-hand side of Fig. 5.4 the γ-ray spectrum emitted at angles >135° in coincidence with ^{72}Zn nuclei is presented. The following transitions were identified: $2^+ \rightarrow 0^+$, $4^+ \rightarrow 2^+$, $0_2^+ \rightarrow 2^+$, $6^+ \rightarrow 4^+$ and $8^+ \rightarrow 6^+$ that correspond to 652.7, 846.8, 858.3, 1153.3 and 916.3 keV energies, respectively [20]. The observed level scheme of ^{72}Zn is presented on the right-hand side of Fig. 5.4.

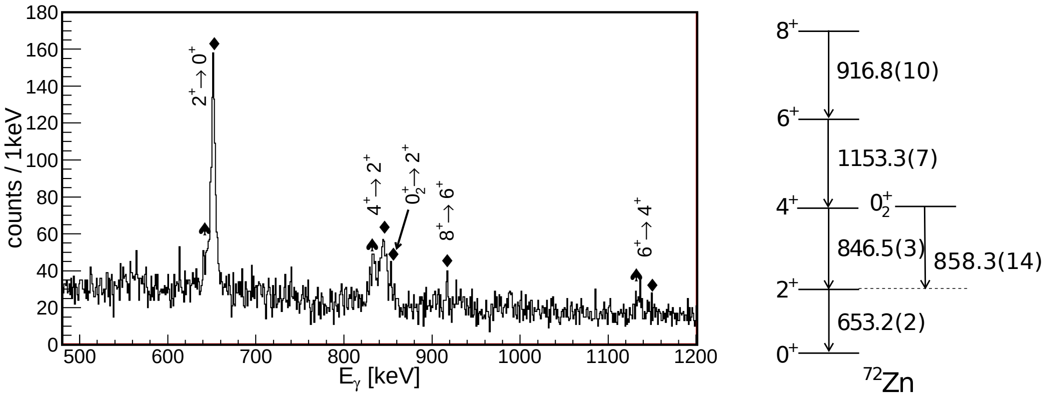

(a) *γ-ray spectrum for ^{72}Zn*

(b) *Level scheme of ^{72}Zn*

Figure 5.4: *γ-ray spectrum of ^{72}Zn for the 99 μm target-degrader distance (left-hand side) and corresponding level scheme (right side). With a ♦ symbol are indicated the unshifted components while with a ♠ are indicated the shifted components of transitions.*

The evolution of intensities measured for the shifted and unshifted components of the $2^+ \rightarrow 0^+$, $4^+ \rightarrow 2^+$ and $6^+ \rightarrow 4^+$ transitions as a function of the target-degrader distance is shown in Fig. 5.5. The unshifted component of $0_2^+ \rightarrow 2^+$ transition was observed but the existence of the $0_2^+ \rightarrow 2^+$ shifted component could not be determined due to the proximity of the $4^+ \rightarrow 2^+$ transition (see Fig. 5.5b). Therefore the lifetime of the 0_2^+ state could not be extracted. Due to the small statistics, we were not able to determine the lifetime of the 8^+ state. The results of measured lifetimes in ^{72}Zn nucleus are presented in Table 5.2.

Table 5.2: *Results of measured lifetimes in* ^{72}Zn

state	Excitation Energy [keV]	τ [ps]
2^+	652.7	19.4 ± 5.5
4^+	1499.5	6.4 ± 2.4
6^+	2653.4	3.0 ± 1.2

5.1.3 ^{68}Zn

On the left part of Fig. 5.6 the γ-ray spectrum emitted at angles >135° in coincidence with ^{68}Zn nuclei is presented. The following transitions are observed: $2^+ \rightarrow 0^+$, $4^+ \rightarrow 2^+$, $0_2^+ \rightarrow 2^+$, that correspond to 1077.3, 1340.0 and 578.6 keV energies, respectively [20]. The level scheme extracted from the γ-ray spectrum of ^{68}Zn is shown on the right-hand side of Fig. 5.6.

The lifetimes of 4^+ and 0_2^+ states could not be estimated due to the low statistics. The lifetime of 2^+ state was found to be 4.6 ± 1.1 ps, which is not in agreement with the numerous experimental data available so far, with a mean value of 2.32 ± 0.03 ps [20]. A longer lifetime can originate from the influence of an unobserved long lived state feeding the 2^+ state. The 0_2^+ state at 1655.91 keV excitation energy has a long halflife of 138 ± 23 ps which can influence the lifetime of 2^+ state. In order to exclude feeding of the 2^+ state from the 0_2^+ state and from other unobserved transitions, we have analyzed the lifetime of 2^+ state for different selection of excitation energies. The excitation energy is not measured directly, but can be extracted from the total kinetic energy of the system and from the angle of the emitting nuclei reconstructed in the VAMOS spectrometer [84, 78]. Due to the low statistics, the selection of excitation energy was made arbitrarily with an overlap of different selections. On the left-hand side of Fig. 5.7 the total kinetic energy of ^{68}Zn nuclei is shown as a function of the recoil angle of the emitting nuclei. Three different selections corresponding to low, medium and high excitation energies are indicated with red long-dashed line, black line and blue short-dashed line, respectively. The right-hand of Fig. 5.7, shows the γ-ray spectrum of ^{68}Zn obtained for nuclei selected using various excitation energy gates.

The top panel in the right-hand side of Fig. 5.7 shows the γ-ray spectrum of ^{68}Zn nuclei with a low excitation energy, while the bottom figure corresponds to the spectrum of nuclei with a high excitation energy. The evolution of intensity of the $0_2^+ \rightarrow 2^+$ transition can not be observed due to the too small statistics. The lifetime of the 2^+ state extracted from the high excitation selection, with correction for feeding, was found to be $\tau(2^+) = 2.14 \pm 0.45$ ps obtaining therefore result that

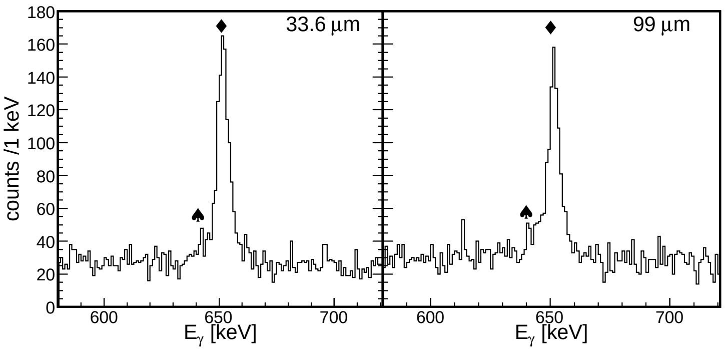

(a) *Spectrum of* $2^+ \rightarrow 0^+$ *transition in* ^{72}*Zn nucleus measured at 33.6* μ*m (left-hand side) and 99* μ*m (right-hand side) target-degrader distance.*

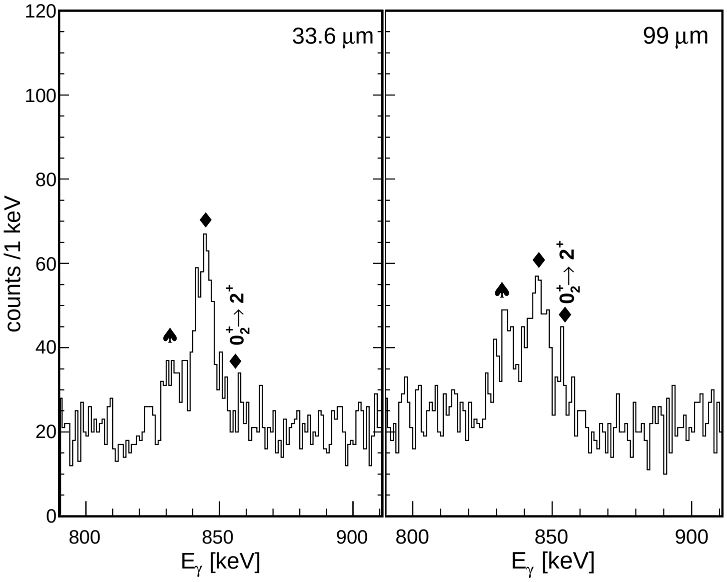

(b) *Spectrum of* $4^+ \rightarrow 2^+$ *transition in* ^{72}*Zn nucleus measured at 33.6* μ*m (left-hand side) and 99* μ*m (right-hand side) target-degrader distance. The position of the unshifted component of* $0_2^+ \rightarrow 2^+$ *transition is also indicated. The peak is observed on spectrum measured at 99* μ*m target-degrader distance while is missing at spectra from 33.6* μ*m distance.*

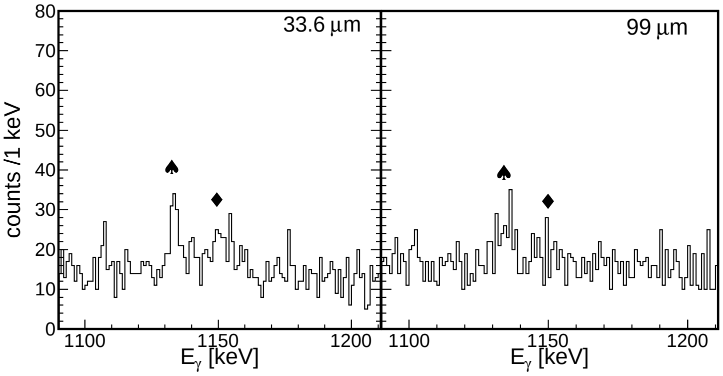

(c) *Spectrum of* $6^+ \rightarrow 4^+$ *transition in* ^{72}*Zn nucleus measured at 33.6* μ*m (left-hand side) and 99* μ*m (right-hand side) target-degrader distance.*

Figure 5.5: *Evolution of* γ*-ray spectrum of* $2^+ \rightarrow 0^+$ *(upper figure),* $4^+ \rightarrow 2^+$ *(middle figure) and* $6^+ \rightarrow 4^+$ *(lower figure) transitions in* ^{72}*Zn obtained for two target-degrader distances. With a ♦ symbol are indicated the unshifted components while with a ♠ are indicated the shifted components.*

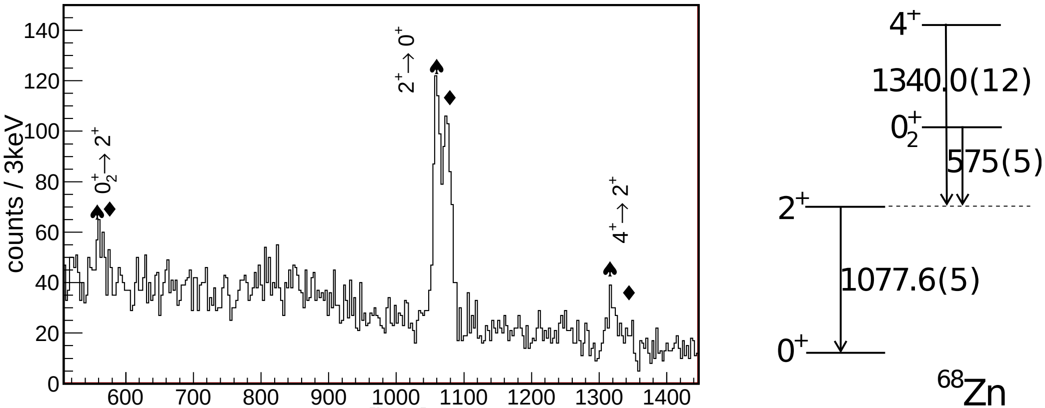

(a) *γ-ray spectrum for ^{68}Zn* (b) *Level scheme of ^{68}Zn*

Figure 5.6: *γ-ray spectrum of ^{68}Zn for 33 μm target-degrader distance (left side) and corresponding level scheme (right side)*

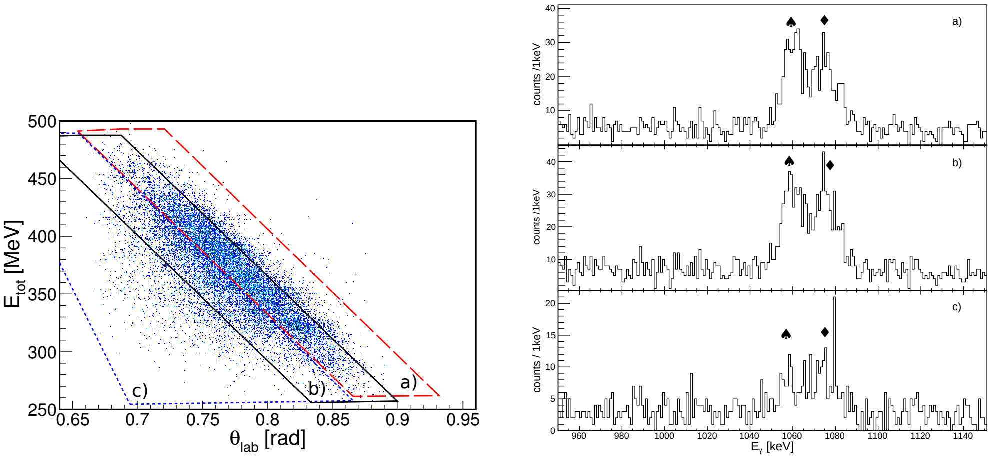

Figure 5.7: *The total energy of ^{68}Zn as a function of the angle of the emitting recoil nucleus. Different selection of excitation energies is indicated: a red long-dashed line encompasses nuclei with a low excitation energy, with black line nuclei with medium excitations are selected, while the region selected by short-dashed line corresponds to a low excitation energy. The corresponding evolution for the $2^+ \rightarrow 0^+$ transition as a function of the selected excitation region is shown on the right-hand side of the figure. Spectra from the top till the bottom of the figure corresponds to the ^{68}Zn spectrum obtained for a low (a), medium (b) and high (c) excitation energy selection.*

is in agreement with previous experimental data [20].

The result indicate that long-lived low-lying states that feed 2^+ state were excluded. In are shown the peak intensities of $2^+ \rightarrow 0^+$ and $4^+ \rightarrow 2^+$ transitions for the three different selections in excitation energy. For the peak intensities, the sum of the shifted and unshifted component were used.

Table 5.3: *Evolution of* $2^+ \rightarrow 0^+$ *and* $4^+ \rightarrow 2^+$ *transition intensities in* ^{68}Zn *as a function of selection of excitation energy E*.*

E*	Intensity of 2^+ state	Intensity of 4^+ state	ratio $4^+/2^+$
low	495	47	0.10
medium	568	68	0.12
high	132	38	0.29

From Table 5.3 one can see that ratio between intensities of the $4^+ \rightarrow 2^+$ and $2^+ \rightarrow 0^+$ transitions increases with the selection of the excitation energy. The ratio indicate that with the selection of the high excitation energy, we have removed the influence of the low-lying 0_2^+ state and mainly select states with a higher excitation energy. Thus obtained lifetime is once again given in Table 5.4.

Table 5.4: *Measured lifetime in* ^{68}Zn

state	Excitation energy [keV]	τ [ps]
2^+	1077.3	2.14 ± 0.45

5.1.4 ^{69}Zn

The γ-ray spectrum of ^{69}Zn nuclei obtained from detectors located at angles $>135°$, is presented on the left-hand side of Fig. 5.8 with a resolution of 3 keV/ch. The shifted components are indicated with a ♠ symbol, unshifted with a ⧫, while unknown transitions are indicated with a * symbol. The known transitions observed in the γ-ray spectrum of ^{69}Zn are: $5/2^- \rightarrow 1/2^-_{g.s.}$, $5/2^-_2 \rightarrow 5/2^-$, $5/2^-_2 \rightarrow 1/2^-_{g.s.}$ and $(3/2)^- \rightarrow 1/2^-_{g.s.}$. The corresponding transition energies are 531.3, 649.4, 1180.7 and 834.5 keV, respectively [20]. The constructed level scheme is presented on the right-hand side of Fig. 5.8.

In order to place the unknown transitions at 562(3), 1093(3) and 1109(3) keV energies in the level scheme, γ coincidence spectra with unknown transitions were constructed. We have built coincidence spectra with all detectors included, but we could not observe any peak. Thus the three unknown transitions could not be placed in the existing level scheme.

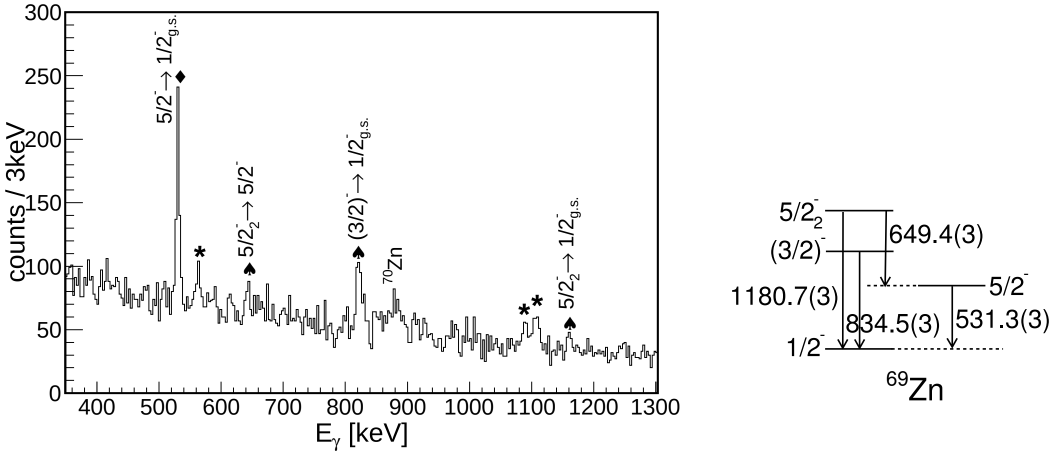

(a) *γ-ray spectrum for* ^{69}*Zn* (b) *Level scheme of* ^{69}*Zn*

Figure 5.8: *γ-ray spectrum of* ^{69}*Zn for 33 μm target-degrader distance (left-hand side) and the corresponding level scheme (right-hand side)*

A zoom on the γ spectrum obtained for ^{69}Zn, around the unassigned transitions at 1100 keV, for two different target-degrader distances is shown on the left- and right-hand sides of Fig. 5.9. The energy distance between the two unassigned peaks indicate that they could correspond to the shifted and unshifted components of a transition. Even more, by looking at the evolution of the peak intensities as a function of the target-degrader distance, one can observe the typical behaviour for lifetime measurements. The results indicate that the transition at 1093(3) keV could correspond to the shifted component of transition at 1109(3) keV.

The results of measured lifetimes in ^{69}Zn are given in Table 5.5.

Table 5.5: *The results of measured lifetimes in* ^{69}*Zn*

state	Excitation energy [keV]	τ [ps]
$(3/2)^-$	834.5	≤ 0.5
$5/2^-_2$	1180.7	≤ 0.6
Decaying with E$_\gamma$=1109(3) keV	?	3.8 ± 1.1

5.1.5 ^{71}Zn

The γ-ray spectrum of ^{71}Zn, created with a condition of γ-rays emitted at angles >135°, is presented on the left side of Fig. 5.10. The following transitions are identified: $(3/2)^- \rightarrow 1/2^-_{g.s.}$, $5/2^-, 7/2^- \rightarrow 1/2^-_{g.s.}$, $1/2^-, 3/2^- \rightarrow 1/2^-_{g.s.}$, $(5/2_3)^+ \rightarrow (3/2)^-$, $(3/2^+, 5/2^+) \rightarrow (5/2_3)^-$ at 674.8, 468, 489.7, 586.5 and 595.2

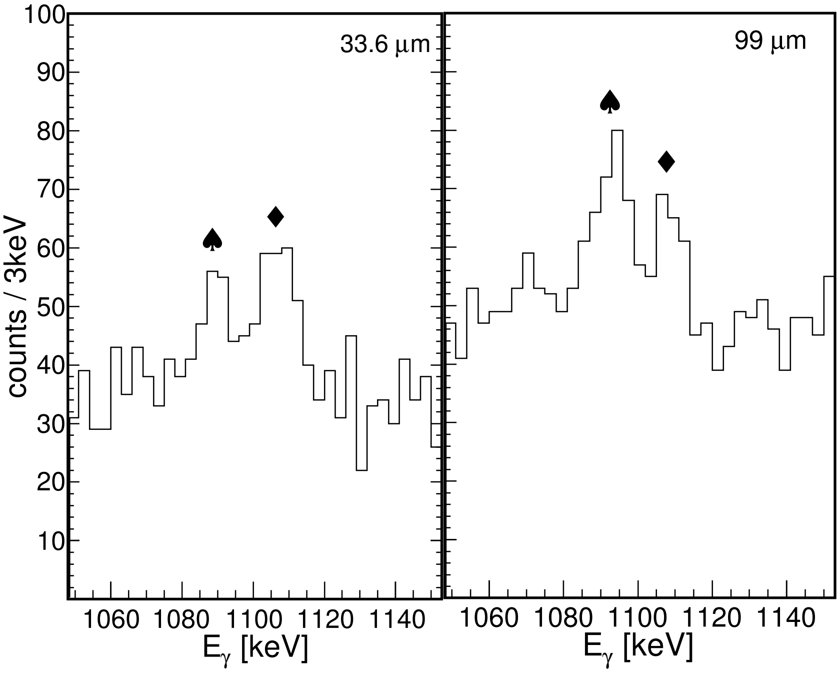

Figure 5.9: *Partial γ-ray spectrum of ^{69}Zn showing the unassigned transitions at E_γ=1109(3) keV measured at 33.6 μm (left-hand side of figure) and 99 μm (right-hand side) target-degrader distances.*

keV respectively [20]. The level scheme corresponding to these observed transitions is presented on the right-hand side of Fig. 5.10.

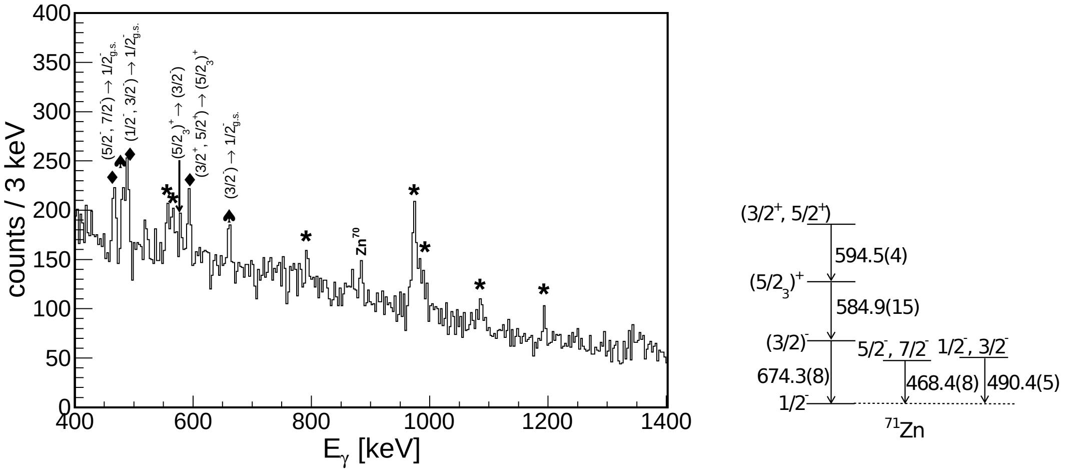

(a) γ*-ray spectrum for* ^{71}*Zn*

(b) *Level scheme of* ^{71}*Zn*

Figure 5.10: *γ-ray spectrum of ^{71}Zn for 99 μm target-degrader distance (left-hand side) and corresponding level scheme (right-hand side). The shifted components are indicated with a ♠ symbol, the unshifted ones with a ♦, while unknown transitions are indicated with a * symbol.*

The state with 465(5) keV excitation energy was assigned to $5/2^-, 7/2^-$ state from the (d, p) reaction [85]. We have measured a γ-ray at 468(3) keV and associated it to the deexcitation of the $5/2^-$ or $7/2^-$ levels to the $1/2^-_{g.s.}$. The lifetime of the state assigned to $1/2^-$ or $3/2^-$, also from the (d, p) reaction [85], is extracted from the evolution of the intensities of the shifted and unshifted components for the two distances. These spectra are presented at the top of Fig. 5.11a. The lifetime of the state decaying with a transition of 489.7 keV, and reported for the first time, is found to be $\tau = 7.3 \pm 2.0$ ps.

In Fig. 5.10 unknown transitions at 795(3), 1088(3), 1195(3) keV and around 560 and 985 keV are indicated with a * symbol. Since the two pairs of energies placed around 560 and 985 keV have the energies that correspond to the shifted and unshifted components, the γ-ray spectra around those energies are presented with more details for the two target-degrader distances in the middle and the bottom of Fig. 5.11. The peaks at 556 and 565 keV in the spectrum with a resolution of 1 keV/channel were difficult to identify and hence they were not assigned to a shifted and unshifted components. The unshifted component of $(5/2_3)^+ \rightarrow (3/2)^-$ transition is indicated with a ♣. Since the shifted component of the $(3/2^+, 5/2^+) \rightarrow (5/2_3)^-$ transition has the same energy as the unshifted component of the $(5/2_3)^+ \rightarrow (3/2)^-$ transition, it is not possible to estimate their lifetimes. For the $(3/2)^- \rightarrow 1/2^-_{g.s.}$ transition, only the shifted component was found and therefore we were only

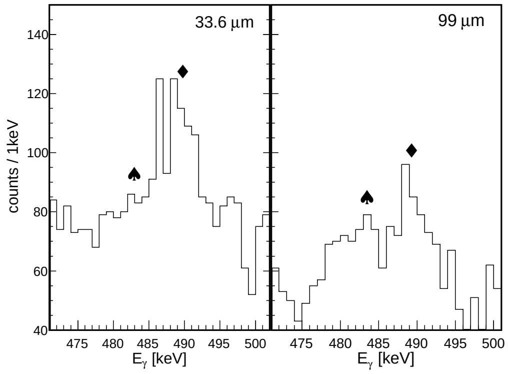

(a) *Spectrum around the transition deexciting $1/2^-$, $3/2^-$ state in ^{71}Zn nucleus measured at 33.6 μm (left-hand side) and 99 μm (right-hand side) target-degrader distance.*

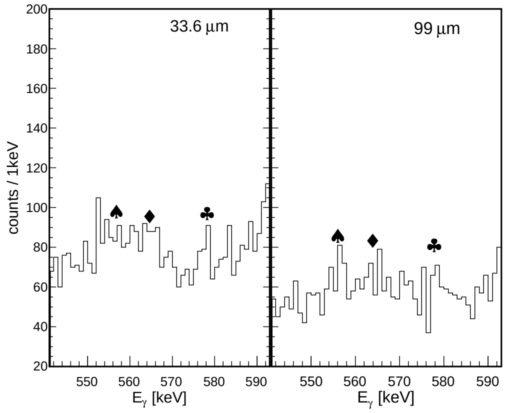

(b) *Spectrum around the unassigned transitions close to 565 keV in ^{71}Zn measured at 33.6 μm and 99 μm target-degrader distances. With a ♣ the unshifted component of* $(5/2_3)^+ \rightarrow (3/2)^-$ *is indicated.*

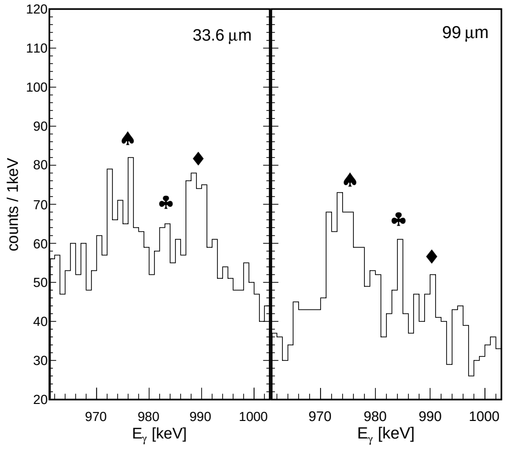

(c) *Spectrum around the unassigned transitions around 985 keV in ^{71}Zn measured at 33.6 μm and 99 μm target-degrader distances. The unknown transition at 983(3) keV is indicated with a ♣.*

Figure 5.11: *γ-ray spectra of ^{71}Zn zooming around several transitions for two target-degrader distances. Shifted components are indicated with a ♠ symbol and unshifted with a ♦ symbol. Each peak was fitted from the spectrum where it is better pronounced and its energy was then fixed for fitting in the other spectrum.*

able to extract an upper limit of lifetime of the $(3/2)^-$. The result is shown in Table 5.6.

The width obtained from the fit of the peak around 990 keV indicates that in this region 3 peaks are present, as shown in the bottom of Fig. 5.11c. The two peaks with a ♠ and a ♦ symbols correspond to the shifted and unshifted components of the transition at 991(3) keV. The lifetime of the state decaying with the transition of 991(3) keV is found to be: $\tau = 2.7 \pm 0.6$ ps. The third peak, at 983(3) keV is indicated by a ♣ symbol. The corresponding transition could be either at 983(3) keV energy, or at 997(3) keV depending on whether this peak comes from the unshifted or shifted component, respectively.

Coincidences spectra gated on the unknown transitions were built, but due to the low statistics, not any coincidence with known transitions could be observed and therefore those transitions remain unassigned. The summary of the obtained lifetimes is presented in Table 5.6.

Table 5.6: *Measured lifetimes in* ^{71}Zn

state	Excitation energy [keV]	τ [ps]
$1/2^-, 3/2^-$	489.7	7.3 ± 2.0
$(3/2)^-$	674.8	≤ 0.6
Decaying with E_γ=991(3)	?	2.7 ± 0.6

5.1.6 ^{73}Zn

The spectrum of γ-rays emitted at angles >135° in coincidence with ^{73}Zn nuclei is shown in Fig. 5.12.

The following known transitions were identified: $(3/2)^- \rightarrow 1/2^-_{g.s.}$, $(\leq 5/2-) \rightarrow (3/2^-)$ and $(\leq 5/2-) \rightarrow 1/2^-_{g.s.}$ at the following energies: 447.9, 676.4 and 501.3 keV. The tentative assignment of those states was done from the discussion of log ft values obtained in the β-decay of ^{73}Cu [86]. All identified transitions come from the unshifted components. Unknown transitions at 774(4),928(4) and 999(4) keV energies are marked in Fig. 5.12 with a * symbol. The existence of transition at 774(4) keV was also reported in the γ-ray spectrum ^{73}Zn in the thesis of A. Dijon [78]. Due to the low statistics of the $\gamma - \gamma$ coincidences, unknown transitions could not be placed in the level scheme of ^{73}Zn.

5.2 Cu isotopes

From the particle identification matrix, $^{67-71}$Cu isotopes were identified. Among them, only transitions in ^{69}Cu could be identified.

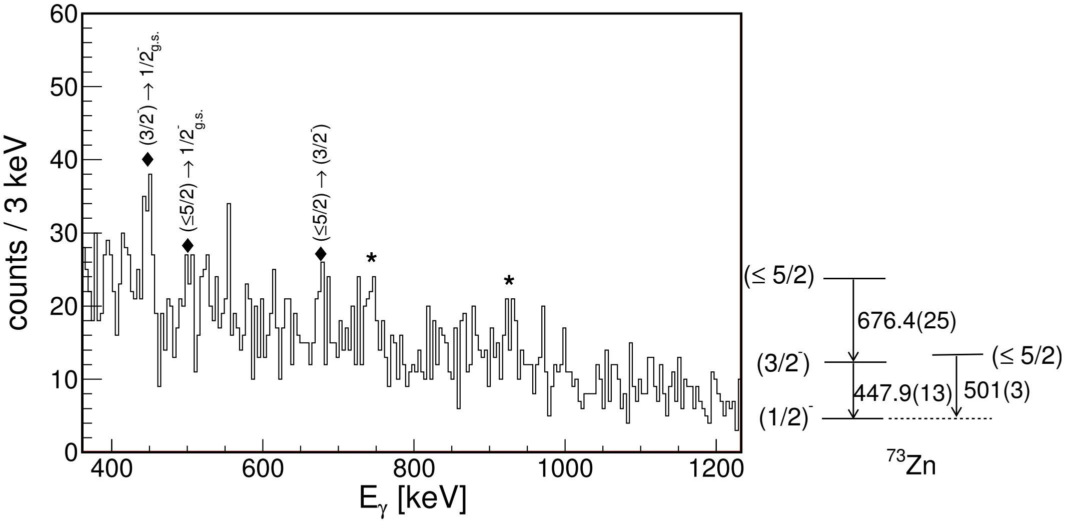

Figure 5.12: *γ-ray spectrum of ^{73}Zn (left-hand side). Unknown transitions were indicated with a * symbol. The corresponding level scheme is presented on the right-hand side.*

5.2.1 ^{69}Cu

The spectrum of γ-rays emitted at angles >135° in coincidence with ^{69}Cu nuclei is shown in Fig. 5.13.

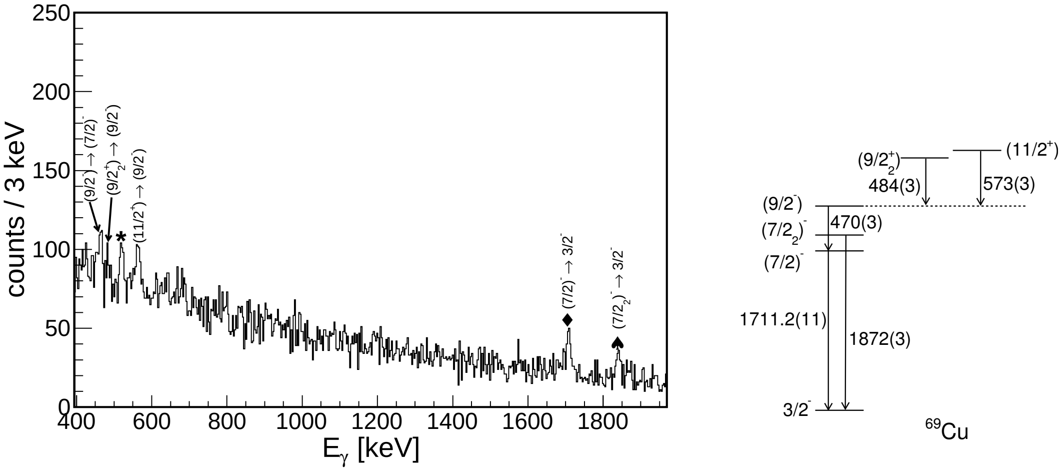

Figure 5.13: *γ-ray spectrum of ^{69}Cu (left-hand side). The shifted components are indicated with a ♠ symbol, the unshifted ones with a ♦, while unknown transitions are shown with a * symbol. The corresponding level scheme is presented on the right-hand side.*

From the spectra the following transitions were identified: $(7/2^-) \rightarrow 3/2^-_{g.s.}$, $(7/2^-_2) \rightarrow 3/2^-_{g.s.}$, $(9/2^-) \rightarrow (7/2^-)$, $(9/2^+_2) \rightarrow (9/2^-)$, $(11/2^+_2) \rightarrow (9/2^-)$ with the energies at: 1710.9, 1871.1, 470.4, 485.9 and 573 keV. From the identified transitions, the level scheme of ^{69}Cu is presented on the right side of Fig. 5.13.

In Fig. 5.14 the fit of the $(7/2^-) \rightarrow 3/2^-_{g.s.}$, $(7/2^-_2) \rightarrow 3/2^-_{g.s.}$ transitions for the two distances with the RADWARE program [82] is shown. The upper limit of the $(7/2^-_2) \rightarrow 3/2^-_{g.s.}$ transition is estimated from the shifted component fitted at 99.0 μm target-degrader distance to be: $\tau \leq$0.7 ps. An unknown transition at 521(3) keV is indicated with a * in the γ-ray spectrum of ^{69}Cu (Fig. 5.13). Due to the low statistics of γ-γ coincidences, it was not possible to set this transition into the level scheme of ^{69}Cu.

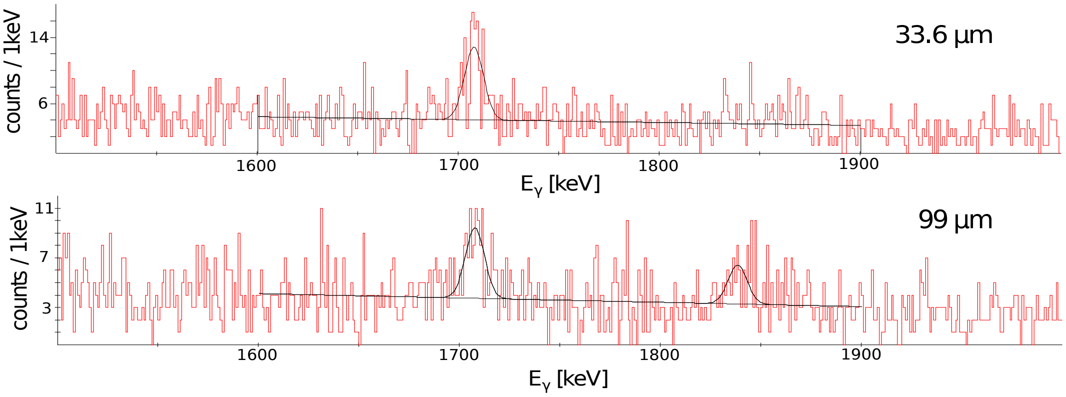

Figure 5.14: *Fit of the* $(7/2^-) \rightarrow 3/2^-_{g.s.}$, $(7/2^-_2) \rightarrow 3/2^-_{g.s.}$ *transitions from the spectrum obtained for the 33.6* μ*m target-degrader distance (upper spectrum) and 99.0* μ*m (lower spectrum).*

5.3 Summary of the experimental results

In this chapter, the γ-ray spectra of identified nuclei have been presented. All spectra were obtained from γ-rays emitted at the most backward angles >135°, since this provides the best separation of the shifted and unshifted component of the given transition. One of the main problems in this lifetime analysis of vibrational-like nuclei were close γ-ray energies of shifted and/or unshifted components of different transitions, which make difficult to resolve different peaks and estimate their intensity. Another difficulty was the influence of the low-lying long-lived states as well as possible unobserved feedings. Former difficulties were minimised using fitting procedure described in the beginning of this chapter, while latter was solved using different selection in excitation energy.

Possible improvement for the next lifetime experiments would be to have large statistics that will allow us to make γ coincidence spectra with state that directly feeds our state of interest. In this way, we will have only single feeding of state of interest and therefore get rid of other transitions and unobserved feedings.

A list of lifetimes that we measured are summarized in Table 5.7. The discussion about the reduced transition probabilities extracted from the measured lifetimes and comparison with the previous experimental results as well as results from different theoretical approaches is given in the following chapter.

Table 5.7: *Summary of measured lifetimes in this experiment. The lifetimes reported for the first time are in bold characters.*

Nucleus	State	Excitation energy [keV]	τ [ps]
^{68}Zn	2^+	1077.3	2.14 ± 0.45
^{70}Zn	2^+	884.9	5.0 ± 0.4
	4^+	1786.3	4.8 ± 1.0
	4^+_2	2693.0	<0.7
^{72}Zn	2^+	625.7	19.4 ± 5.5
	4^+	1499.5	6.4 ± 2.4
	6^+	2653.4	3.0 ± 1.2
^{69}Zn	$\mathbf{(3/2)^-}$	**834.5**	$\mathbf{\leq 0.5}$
	$\mathbf{5/2^-_2}$	**1180.7**	$\mathbf{\leq 0.6}$
	Decaying with E$_\gamma$=1109(3)	**?**	**3.8 ± 1.1**
^{71}Zn	$\mathbf{1/2^-, 3/2^-}$	**489.7**	**7.3 ± 2.0**
	$\mathbf{(3/2)^-}$	**674.8**	$\mathbf{\leq 0.6}$
	Decaying with E$_\gamma$=991(3)	**?**	$\mathbf{\leq 0.6}$
^{69}Cu	$7/2^-_2$	1871.1	≤ 0.7

In addition to the results of the lifetime measurements, several new prompt γ-rays were observed. These results are summarized in Table 5.8.

Table 5.8: *Summary of new γ-rays identified in this experiment.*

Nucleus	Energy [keV]
^{69}Zn	562(3) 1109(3)
^{71}Zn	565(3) 795(3) 991(3) 1088(3) 1195(3)
^{73}Zn	774(4) 828(4) 999(4)
^{69}Cu	521(3)

6 Discussion

In the previous chapter, the results of lifetime measurements performed in GANIL by applying the RDDS method were presented. Nuclei produced with enough statistics using deep-inelastic reactions with ^{238}U beam at 6.76 A MeV energy impinging on a 800 μm/cm^2 ^{70}Zn target were analysed. In this chapter, the B(E2) values extracted from the measured lifetimes are compared with previous results and theoretical predictions. The discussion is separately done for even and odd Zn isotopes and for Cu isotopes.

6.1 Systematics of the even Zn isotopes

6.1.1 Excitation energy of low-lying excited states

The low-lying states in Zn isotopes have already been presented in Fig. 2.7. The energy ratio between the 4_1^+ and 2_1^+ states along the isotopic chain, ranging between 2 and 2.5, indicates a vibrational character of Zn isotopes. As it was pointed out, g-factor measurements also agreed with a vibrational description for lighter isotopes [44, 45, 46, 43, 47]. In the systematics of the 0_2^+ state, a drop at ^{70}Zn has been observed similarly to ^{68}Ni. Although this effect was argued to come from a neutron pair excitation from the pf shell to the $g_{9/2}$ orbital, lowering therefore the energy of 0_2^+ state [13], or from a coupling between the quadrupole and pairing-vibrational modes [87], this effect is not fully understood.

By looking at the systematics of Zn isotopes in the middle of the $g_{9/2}$ shell (N=42-46) an almost constant energy of the 2_1^+ state can be observed. The behaviour is typical for systems having seniority as a good quantum number in which the energy difference between seniority $\nu = 0$ and $\nu = 2$ states in n-particle configuration is identical to that in the two-particle system and independent of n [5]. A similar behaviour has been observed for Ni isotopes in the $1g_{9/2}$ orbital. The systematics of 2^+ states in Zn and Ni isotopes as well as N=50 isotones is shown in Fig. 6.1. The N=50 isotones with protons confined in the $\pi g_{9/2}$ orbital, as well as Ni isotopes with neutrons filling the $\nu g_{9/2}$ orbital are identified as nuclei having seniority as a good quantum number. A detailed discussion about conservation of seniority in the $g_{9/2}$ shell and its implication to the one-particle transfer is presented is the second part of this thesis.

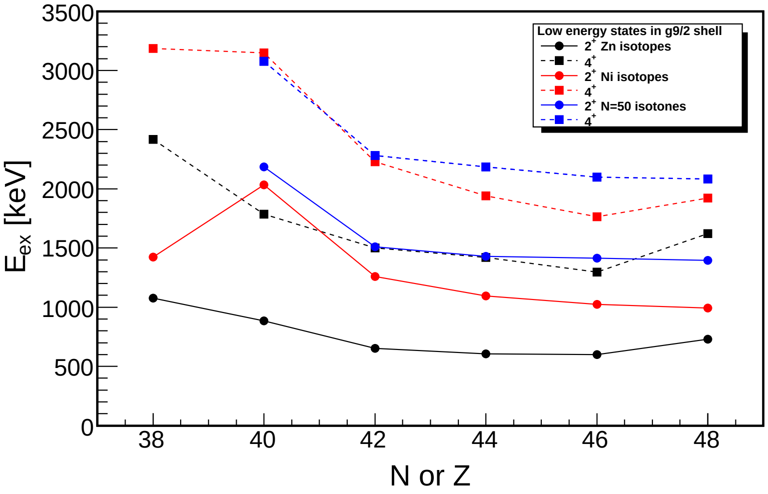

Figure 6.1: *Systematics of low-lying states in Zn and Ni isotopes with neutrons filling the* $\nu g_{9/2}$ *orbital and N=50 isotones with protons confined in* $\pi g_{9/2}$ *orbital.*

A small decrease of the energy of the 2^+ state in Ni isotopes when filling the $\nu g_{9/2}$ orbital can be attributed to the reduction of the $\pi f_{7/2}$-$\pi f_{5/2}$ spin-orbit splitting due to the tensor force [32] as already explained in the introductory chapter. The importance of introducing the proton-core excitations in the SM approach pointed out the reduction of Z=28 shell closure with neutrons filling the $g_{9/2}$ orbital [88]. Nevertheless, the influence of proton-core excitations might be less pronounced in the case of Zn isotopes. Namely, by looking at the Nilsson orbit (Fig. 6.2) one can notice that in Zn isotopes, 2 protons outside the Z=28 shell, occupy the 1/2[321] orbital making therefore proton-core excitations less energetically favoured compared to Ni. This makes the Ni isotopes more affected by increasing the single particle energy of $\pi f_{7/2}$ due to the interaction between the $\nu g_{9/2}$ and $\pi f_{7/2}$ orbitals. This effect also explains the more abrupt decrease of the 2^+ state energies in Ni compared to Zn isotopes.

The evolution of the proton occupational number for the ground state and the first excited 2_1^+ state in Zn isotopes as the function of neutron number is shown on the left hand side and right hand side of Fig. 6.3. The occupancy was calculated with the JUN45 interaction that uses ^{56}Ni as a core and $pf_{5/2}g_{9/2}$ as a valence space [53]. The schematic representation of valence space used in JUN45 is shown on the left part of Fig. 6.4.

With neutrons starting to fill the $\nu g_{9/2}$ orbital, the proton occupancy number evolves from 1.4 to 0.6 and 0.2 to 1.2 in the $\pi p_{3/2}$ and $\pi f_{5/2}$ orbitals respectively for N≥46. This increased occupancy of the $\pi f_{5/2}$ orbital with the filling of the $\nu g_{9/2}$ orbital influences the evolution of the single particle energies due to the increased attractive monopole interaction between the $\pi f_{5/2}$ and $\nu g_{9/2}$ orbitals.

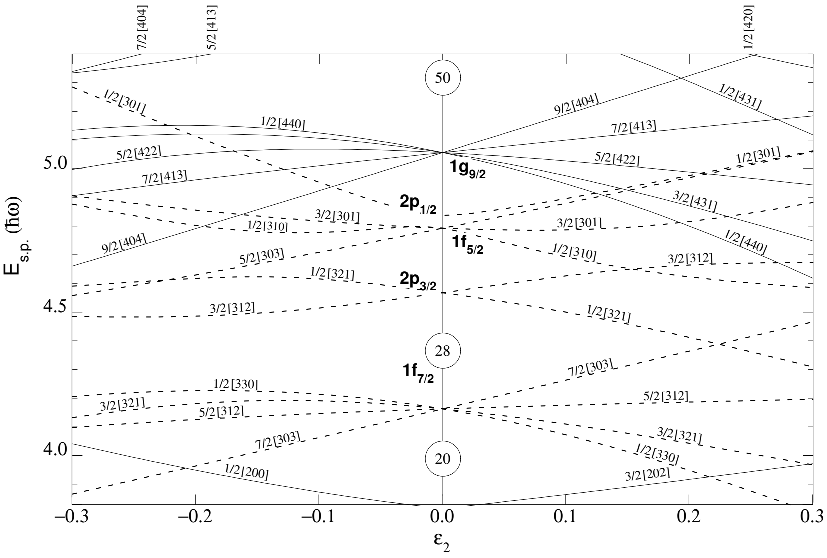

Figure 6.2: *The Nilsson orbitals around N=40 (modified from [89])*

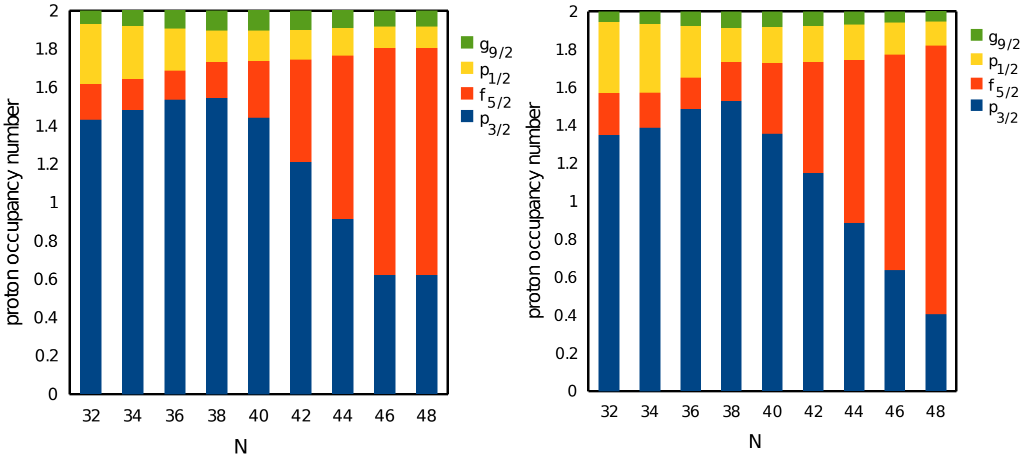

(a) 0^+

(b) 2_1^+

Figure 6.3: *The proton occupancy of the 0^+ (left-hand side) and 2_1^+ state (right-hand side) of Zn isotopes obtained with a JUN45 interaction [53]*

Table 6.1: *Measured lifetimes and B(E2; J→ J-2) values for low-lying states in ^{68}Zn, ^{70}Zn and ^{72}Zn, compared with previous experiments and shell-model calculations.*

		This experiment	PRISMA-AGATA [52]	Previous work	SM JUN45	SM LNPS
	J^π	B(E2; J → J-2) [e^2fm^4]				
^{68}Zn	2^+	263 ± 56		242± 3 [90]	289	376
^{70}Zn	2^+	303 ± 24	286^{+131}_{-68}	305 ± 15 [91]	302	327
	4^+	286 ± 61	475^{+584}_{-147}	720 ± 70 [47]	394	345
^{72}Zn	2^+	354 ± 100	392^{+34}_{-29}	348 ± 42 [49] 385 ± 39 [51]	336	376
	4^+	292 ± 110	361^{+57}_{-47}		349	471
	6^+	133 ± 51	134^{+57}_{-31}		228	437

6.1.2 B(E2; $2^+ \rightarrow 0^+$) in even Zn isotopes

The measured lifetimes and corresponding B(E2) values are presented in Table 6.1 and compared with the previous experiments and theoretical values. The results of recent experiment performed at INFN Lenaro is given in a separate column since the same method for lifetime measurement (RDDS method) was used with the same type of reaction (deep-inelastic). Using the same method, but with a different reaction will lead to different excitation of nuclei and therefore to a different feeding of the states of interest. Obtaining similar result will give additional confidence in the applied method and analysis.

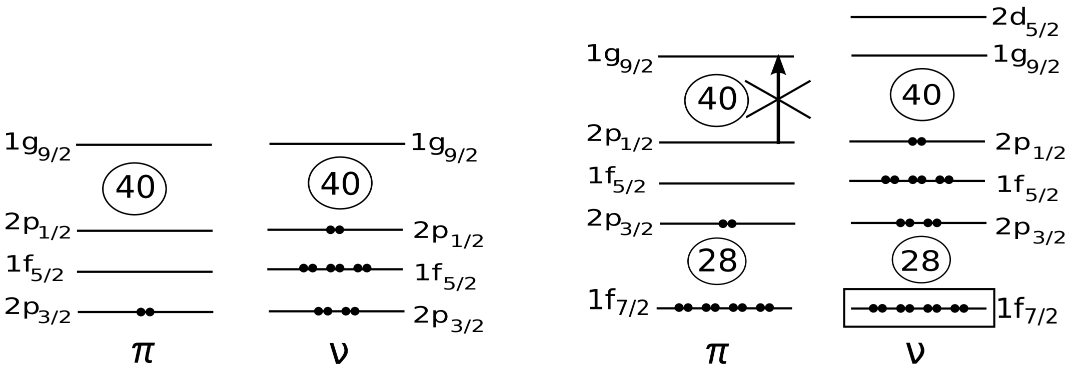

Figure 6.4: *Schematic representation of ^{70}Zn and valence space used for JUN45 interaction [53] (left hand side) and LNPS interaction [39] (right hand side)*

The experimental results obtained for B(E2; $2^+ \rightarrow 0^+$) and B(E2; $4^+ \rightarrow 2^+$) values in Zn isotopes, are compared with previous experimental data and shell model calculations in Fig. 6.5.

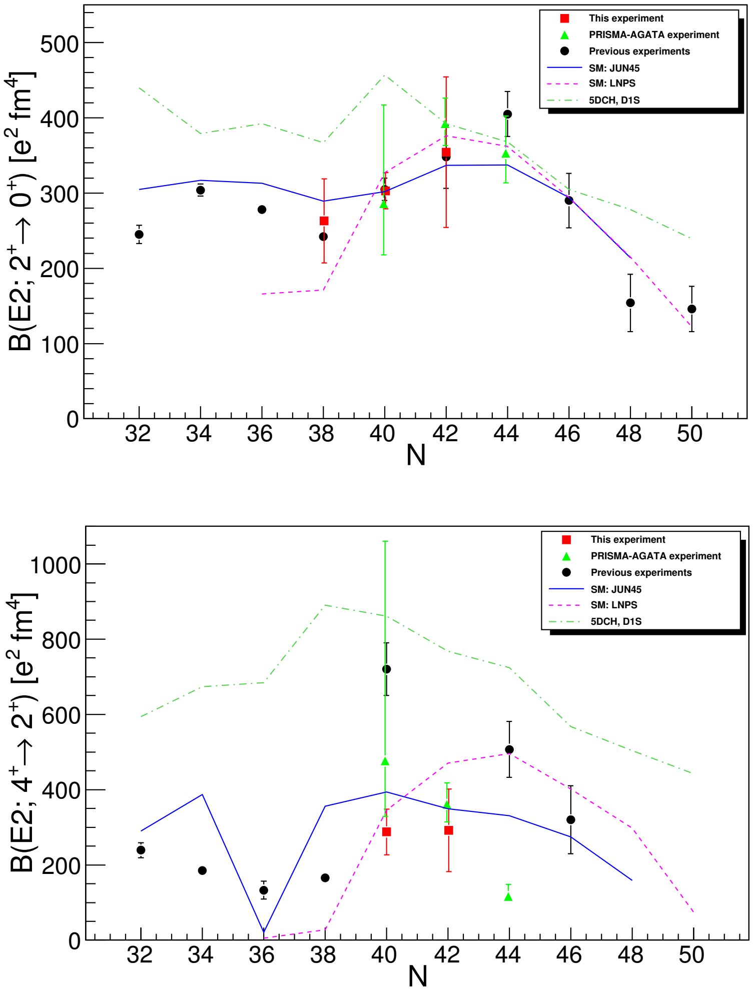

Figure 6.5: *Results of B(E2; $2^+ \rightarrow 0^+$) (top figure) and B(E2; $4^+ \rightarrow 2^+$) (bottom figure) values for Zn isotopes obtained in this experiment, compared with a recent deep-inelastic experiment and other experimental results. The results are compared with a beyond mean-field calculations with Gogny D1S interaction and shell model calculations using JUN45 [53] and LNPS [39] interactions.*

The measured B(E2; $2^+ \rightarrow 0^+$) values of Zn isotopes are in agreement with the previous experiments performed with different measurement techniques and types of reaction.

For ^{68}Zn, a lot of experimental data coming from different techniques including Coulomb excitations at low and intermediate energies, Doppler-shift attenuation method, scattering reactions (e, e′), (d, d′), (γ, γ') are summarised by McCutchan

[90] giving B(E2; $2^+ \rightarrow 0^+$)=242 ± 3 e^2fm^4 which is compatible with our result: 263 ± 56 e^2fm^4.

The B(E2; $2^+ \rightarrow 0^+$) = 303 ± 24 e^2fm^4 value for ^{70}Zn extracted from our experiment is in agreement with the value B(E2; $2^+ \rightarrow 0^+$) = 305 ± 15 e^2fm^4 [91] summarised from the Coulomb excitation measurements [15, 92, 93] and the DSA measurements [43]. It is also in agreement with the B(E2; $2^+ \rightarrow 0^+$) = 303^{131}_{-68} results obtained from the recent RDDS measurements where nuclei were populated in deep-inelastic reactions with ^{76}Ge impinging ^{238}U target [52].

The first measurement of B(E2; $2^+ \rightarrow 0^+$) for ^{72}Zn measured by Coulomb excitation at intermediate energy gave 348 ± 42 e^2fm^4. In two recent lifetime measurements with the RDDS method [51], the states of interest were populated using the fragmentation of a ^{76}Ge beam in one experiment and by the already mentioned deep-inelastic reaction in the other experiment [52]. The measured lifetimes are 385 ± 39 e^2fm^4 for the former and 392^{34}_{-29} e^2fm^4 for the latter, which is slightly higher than the results from the Coulomb experiment but still in agreement. Our lifetime measurement gives B(E2; $2^+ \rightarrow 0^+$) = 354 ± 100 e^2fm^4 which is in very good agreement with the previous results.

Although in our measurements, we did not populate ^{74}Zn nucleus, it is also interesting to discuss its B(E2) values. It was measured with a relativistic Coulomb excitation giving B(E2; $2^+ \rightarrow 0^+$)=408 ± 30 e^2fm^4 [19], Coulomb excitation at low-energy with B(E2; $2^+ \rightarrow 0^+$)=401 ± 32 e^2fm^4 [50] and, already mentioned the two RDDS experiments giving 370 ± 33 e^2fm^4 [51] and 352^{+50}_{-39} e^2fm^4 [52].

In the papers of Niikura et al. [51] and Louchart et al. [52] a slight decrease of the B(E2; $2^+ \rightarrow 0^+$) value for ^{74}Zn and increase for ^{72}Zn with respect to results from the previous Coulomb measurements were observed. With these results, it was mentioned that the maximum of collectivity is at N=42, as in the case of Ge and Se isotopes. The weighted average from all measured B(E2; $2^+ \rightarrow 0^+$) values for ^{72}Zn and ^{74}Zn are 377 ± 21 e^2fm^4 and 382 ± 20 e^2fm^4 respectively. These rather constant B(E2) values indicate that there is no significant difference in collectivity between ^{72}Zn and ^{74}Zn.

6.1.3 B(E2; $4^+ \rightarrow 2^+$) in even Zn isotopes

The experimental data for B(E2; $4^+ \rightarrow 2^+$) are sparse. The lifetime experiment of Mücher performed by Doppler shift attenuation method for ^{70}Zn gave B(E2; $4^+ \rightarrow 2^+$) = 720 ± 70 e^2fm^4 [47]. This value is almost 5 times larger than B(E2; $4^+ \rightarrow 2^+$) value for ^{68}Zn. The B(E2; $4^+ \rightarrow 2^+$) = 475 $^{584}_{-147}$ e^2fm^4 obtained in the Louchart experiment [52] has a large error bar and cannot provide any answer about this sharp discontinuity in B(E2) systematics. Our experiment gave a much lower value of 286 ± 61 e^2fm^4, indicating a slight increase of collectivity and therefore restoring a smooth evolution of the B(E2; $4^+ \rightarrow 2^+$) values with N.

Recently, the first experimental result of B(E2; $4^+ \rightarrow 2^+$) value for ^{72}Zn was found to be 361 $^{57}_{-47}$ e^2fm^4 [52]. Our experimental result 292 ± 110 e^2fm^4, although with a large error bar is in agreement with this previous result and nicely follows the B(E2) systematics. The B(E2; $6^+ \rightarrow 4^+$) = 133 ± 51 e^2fm^4 extracted from our experiment is also in agreement with a previously reported value of 134 $^{57}_{-31}$ e^2fm^4 [52]. The evolution of the B(E2) value with angular momentum for ^{72}Zn indicates a drop of B(E2) values when going from $2^+ \rightarrow 0^+$ to $6^+ \rightarrow 4^+$ transition.

For the sake of completeness the B(E2; $4^+ \rightarrow 2^+$) value in ^{74}Zn is also discussed, although it was not part of our measurements. In the Louchart experiment, a sharp decrease of the B(E2; $4^+ \rightarrow 2^+$) value was found in ^{74}Zn, compared to ^{72}Zn. The obtained value of 116 $^{32}_{-10}$ e^2fm^4 significantly differs from the Coulomb excitation experiment at low energy where the B(E2) was found to be 507 ± 74 e^2fm^4 [50]. Experimental data are therefore calling for new measurements to determine B(E2; $4^+ \rightarrow 2^+$) value in ^{74}Zn and beyond.

6.1.4 Comparison of E* and B(E2) with calculations

We have compared the experimental transition probabilities with beyond-mean-field and shell model calculations. The beyond-mean-field calculations were performed using the Gogny D1S interaction [94, 95] in the 5-dimensional Collective Hamiltonian (5DCH) formalism [54]. The existing calculations of B(E2; $2^+ \rightarrow 0^+$) along the Zn isotopic chain from N=32 to N=50, overestimate the experimental values by approximately 30 %, while for the B(E2; $4^+ \rightarrow 2^+$) the calculated results overestimate experimental data by a factor between 2 and 3 (Fig. 6.5).

The shell model calculations were performed with two different interactions. The first one is the already mentioned JUN45 [53] interaction (Fig. 6.4). In order to reproduce the low-lying states and magnetic moments in Cu isotopes, it was suggested to include proton excitations and to choose ^{48}Ca as an inert core. Moreover, with the inclusion of the $d_{5/2}$ orbital into the valence space, it was possible to reproduce the experimental data of Fe and Cr isotopes around the N = 40 sub-shell closure [36, 37, 96]. This lead to the new LNPS interaction. Our results were also compared with calculations using this new interaction that uses the ^{48}Ca as a core and $pf_{5/2}g_{9/2}d_{5/2}$ as a valence space [39]. The schematic representation of the valence space of the LNPS interaction is shown on the right hand side of Fig. 6.4. The experimental energy levels of 2^+ and 4^+ states are compared with theoretical calculations obtained with the JUN45 and LNPS interactions (Fig. 6.6).

The experimental data of 2^+ and 4^+ energy for Zn isotopes with N>40 are nicely reproduced with the LNPS reaction, while JUN45 overestimates the energies of the 2^+ and 4^+ states by about 350 keV (see Fig.6.6). This could indicate that the collectivity of Zn isotopes with N>40 is not well taken into account and that the $\nu d_{5/2}$ and/or $\pi f_{7/2}$ orbitals should be included. Alternatively this could also point to core polarisation effects. The same conclusion can be drawn from the systematics of B(E2; $2^+ \rightarrow 0^+$) in ^{70,72,74}Zn since JUN45 slightly underestimates the results, although the values are still within the error bars, while LNPS interaction nicely reproduces the experimental values.

A discrepancy again arrives with the B(E2; $4^+ \rightarrow 2^+$) systematics. Our result of B(E2; $4^+ \rightarrow 2^+$) value for ^{70}Zn, or weighted value with result from Louchart

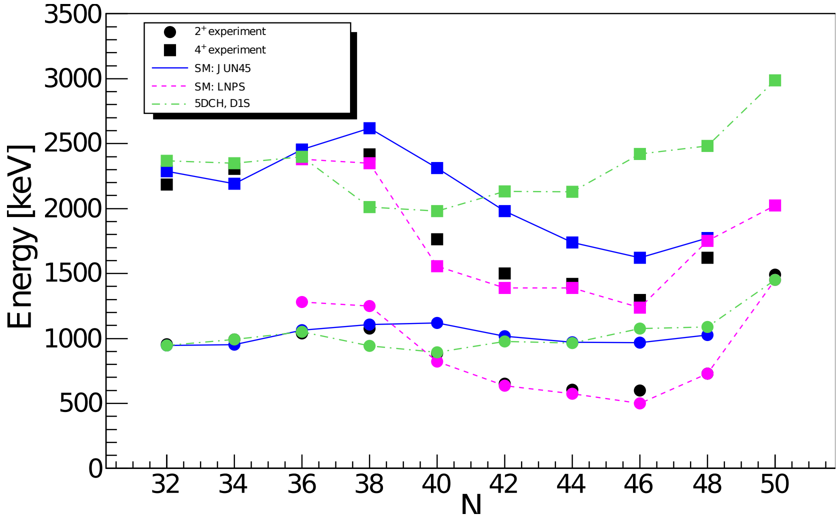

Figure 6.6: *Experimental energy for the 2^+ and 4^+ states as a function of the neutron number N for Zn isotopes compared with theoretical calculations: shell model with the JUN45 and LNPS interactions and with a beyond mean-field calculations using the Gogny D1S interaction*

experiment is reasonably well reproduced by the LNPS interaction while JUN45 gives slightly more collective value. The B(E2; $4^+ \rightarrow 2^+$) values calculated with LNPS increase to reach a maximum at N = 44. Adding more neutrons to the $\nu g_{9/2}$ causes a regular decrease of the B(E2; $4^+ \rightarrow 2^+$) values. The B(E2) values calculated by the LNPS interaction follow the experimental results for ^{74,76}Zn isotopes obtained by Coulomb excitation [50], while completely overestimates a recent B(E2; $4^+ \rightarrow 2^+$) measurements for ^{74}Zn [52]. The B(E2; $4^+ \rightarrow 2^+$) values calculated using JUN45 exhibits a maximum at N=40 and then slightly decrease. The measured B(E2; $4^+ \rightarrow 2^+$) value of ^{72}Zn is in agreement with the one calculated using the JUN45 interaction. Our experimental B(E2; $4^+ \rightarrow 2^+$) values for ^{70,72}Zn are very similar. The RRDS measurements agree well for ^{72}Zn, but the error bar for ^{70}Zn in Louchart et al. [52] is very large. It is therefore not possible to conclude on the evolution of collectivity between N=40 and N=42 neither on the location of the maximum.

6.1.5 B_{42} ratios and seniority

Additional information about the collective properties of nuclei can be extracted from the B(E2) ratio, B_{42} = B(E2; $4^+ \rightarrow 2^+$)/B(E2; $2^+ \rightarrow 0^+$) which, for collective excitations, is expected to be larger than one. Moreover, for nuclei with pure vibrational character, this ratio is equal to two, while for pure rotors it is equal to 1.43. The B_{42} values obtained for ^{70}Zn and ^{72}Zn are 0.94 ± 0.21 and 0.82 ± 0.39, respectively. The values are close to 1 and below the value expected for the pure rotational object. The B_{42} values lower than 1 are found in nuclei where seniority is

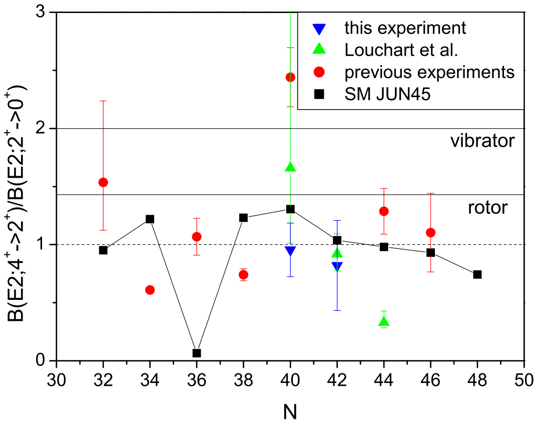

Figure 6.7: *Systematics of the B(E2; $4^+ \rightarrow 2^+$)/B(E2; $2^+ \rightarrow 0^+$) ratio for the Zn isotopes*

a good quantum number [97]. The B_{42} values measured and calculated for the Zn isotopes are plotted in Fig. 6.7 indicating that Zn isotopes are having seniority like behaviour.

There was an attempt to use more advanced collective models to reproduce and interpret these B_{42} values. Namely, Koizumi et al. [98] have calculated ^{68}Zn using the Nilsson-Strutinsky model and they predict two minima at $\gamma = 60°$ for $\beta = 0.1$ and $\beta = 0.18$. According to these calculations, the neutron single particle energy of the lowest Nilsson orbit with parentage in $1g_{9/2}$ orbital decreases as deformation increases, so that this intruder level is far from the Fermi surface at $\beta = 0.1$ (1^{st} minimum) but becomes active at $\beta = 0.18$ (2^{nd} minimum). The increasing influence of the $\nu g_{9/2}$ orbital affects the collectivity of the bands built on top of the 0^+ and 0_2^+ states associated to the two minima. However, these calculations lead to B_{42} which is not in agreement with the experimental value $B_{42} = 0.84 \pm 0.06$, hence weakening the argument.

In the first chapter we have discussed the effect of a seniority change on B(E2) values. The B(E2) value for a $2^+ \rightarrow 0^+$ transition that changes seniority $\delta\nu = 2$, is rising toward mid-shell (for nuclei in which neutrons or protons are filling a single-j shell). Conversely, the B(E2) values of seniority conserving transitions, such as isomeric transitions, show the opposite behaviour with a parabola minimising at mid-shell. A schematic behaviour of B(E2) values in the seniority scheme as a function of the fractional filling is shown in Fig. 2.2.

In the excerpt of nuclear chart, the regions where seniority might be a good quantum number are indicated in Fig. 6.8 [99]. The experimental values of B(E2; 2J-1→ 2J-3) systematics for the magic nuclei are also indicated, confirming a seniority behaviour. With black dots are indicated known existing data in nuclei that were proposed to exhibit good seniority, while in gray are marked regions where this behaviour is also expected (Zn region included).

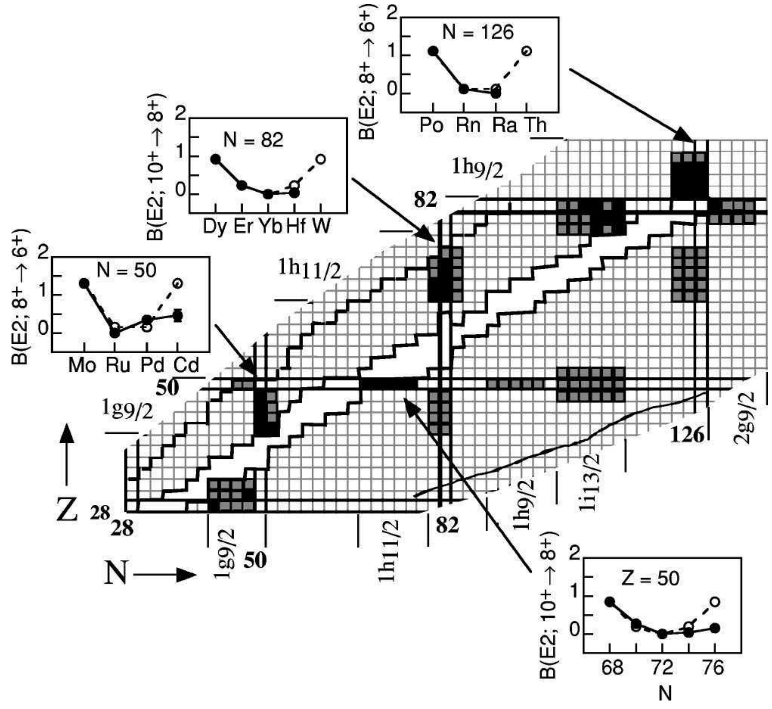

Figure 6.8: *An excerpt of nuclear chart showing the nuclei that were proposed to exhibit seniority as a good quantum number (black dots for known data); gray dots regions where this behaviour is also expected. Experimental data of B(E2; 2J-1→ 2J-3) systematics for the magic nuclei are indicated in order to show seniority like behaviour. The figure is taken from [99].*

In collective nuclei, the B(E2; J→ J-2; J>2) values are increasing with angular momentum since the higher spins are built as the superposition of collective motions of the lower states. In order to check the evolution of the collectivity with J, the experimental values of B(E2; $6^+ \rightarrow 4^+$), B(E2; $4^+ \rightarrow 2^+$) and B(E2; $2^+ \rightarrow 0^+$) transitions in ^{72}Zn are compared with calculations in the pure seniority scheme with 2 particles in the $g_{9/2}$ orbital, and with ^{70}Ni and ^{92}Mo nuclei having two neutrons or two protons in the $g_{9/2}$ orbital as schematically shown in Fig. 6.9.

The B(E2) values in ^{72}Zn for $2^+ \rightarrow 0^+$ and $6^+ \rightarrow 4^+$ transitions follow the systematics of ^{70}Ni and ^{92}Mo in which seniority is a good quantum numbers. To compare the experimental B(E2) values as a function of J, between ^{72}Zn, ^{70}Ni and ^{92}Mo it is necessary to measure the missing B(E2; $4^+ \rightarrow 2^+$) in ^{70}Ni and ^{92}Mo. The same reduction of collectivity as a function of J (for J > 2) is observed in a system of 2 particles confined in the $g_{9/2}$ orbital in a pure seniority scheme. A discrepancy in the B(E2) values for $4^+ \rightarrow 2^+$ transition between pure seniority scheme and ^{72}Zn has

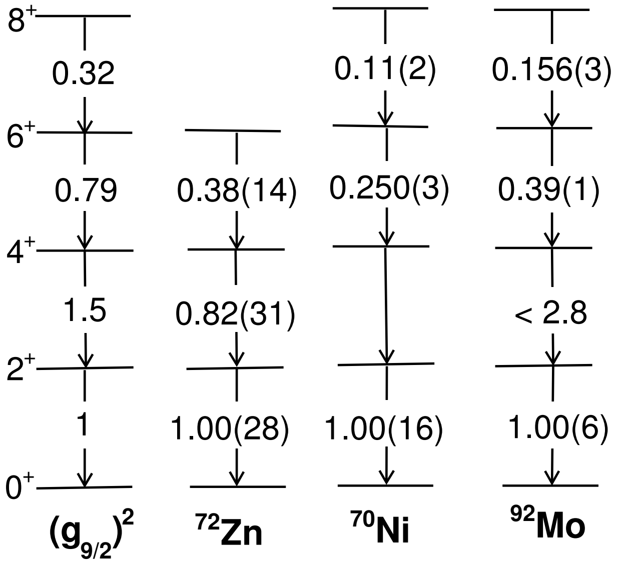
8+
6+
4+
2+
0+
0.32
0.79
1.5
1
0.38(14)
0.82(31)
1.00(28)
0.11(2)
0.250(3)
1.00(16)
0.156(3)
0.39(1)
< 2.8
1.00(6)
(g9/2)2
72Zn
70Ni
92Mo

Figure 6.9: *From left to right B(E2; J→ J-2) systematics for system with 2 particles in* $g_{9/2}$ *orbital are presented in a pure seniority scheme; for* ^{72}*Zn (2 neutrons in* $g_{9/2}$ *orbital with 2 additional protons outside the close shell) ; for* ^{70}*Ni(2 neutrons in* $g_{9/2}$ *orbital) and* ^{92}*Mo (two protons in the* $g_{9/2}$ *orbital). When known, the B(E2) values are normalised to B(E2;* $2^+ \rightarrow 0^+$*) transition for each isotope. The experimental energy levels for different nuclei are not equal, but they are arbitrarily set to the same value for all nuclei.*

been observed. In the pure seniority scheme with 2 particles in $g_{9/2}$ orbital, B_{42} was calculated to be 1.5, giving the upper value for B(E2) ratio, while the experimentally measured B_{42} ratio is 0.82 ± 0.39.

The constant energy levels of the 2^+ states along $^{72-76}$Zn isotopes, the evolution of the B(E2; $4^+ \rightarrow 2^+$)/B(E2; $2^+ \rightarrow 0^+$) ratio along the Zn isotopic chain as well as from the B(E2) values in ^{72}Zn as a function of J, indicate that the Zn isotopes exhibit behavours which are compatible to systems that have seniority as a good quantum number.

6.2 Systematics of the odd Zn isotopes

From the spectroscopy of the nuclei with one particle/hole outside the N = 40 it is possible to probe: single particle excitations, core polarisation, core coupled states, robustness of the shell-closure... The systematics of low-lying states in odd Zn isotopes around N=40 is compared with the evolution of the first 2^+ state in even Zn isotopes in Fig. 6.10. As it can be noticed, some of these states are close in energy to the 2^+ level in the neighbouring even Zn isotope. Since ^{69}Zn and ^{71}Zn have one neutron hole or particle away from N = 40, it is reasonable to study the nature of the populated low-lying states by applying the particle core coupling approach. The approach is performed in the same way as it was done in the thesis of A. Dijon [78].

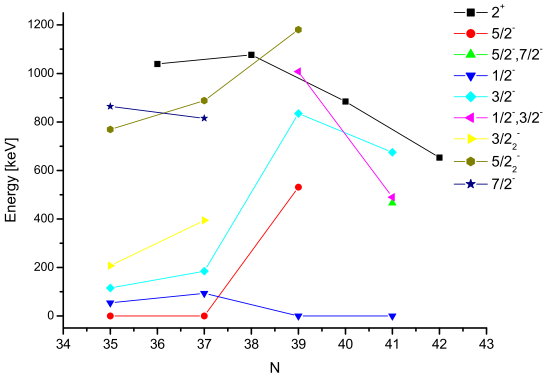

Figure 6.10: *Systematics of negative-parity low-lying states in odd-Zn compared with the energy of the first 2^+ state in neighbouring energy level of the neighbouring even-Zn isotopes.*

In the particle-core coupling approach, a state in an odd-mass nucleus $|J_i\rangle$ can be expressed as:

$$|J_i\rangle = \sum_{jL_k} c^{J_i}_{jL_k} |j \times L_k; J\rangle \tag{6.1}$$

with

$$(c^{J_i}_{jL_k})^2 = \frac{1}{\langle n_j\rangle}\frac{\langle J_i\|a^+_j\|L_k\rangle^2}{2J+1}$$

where $|L_k\rangle$ is an even-even nucleus coupled with a particle in orbital j to state J; $\langle J_i\|a^+_j\|L_k\rangle$ is the reduced matrix element of creation of particle in j orbital; $\langle n_j\rangle$ is the occupation of particles in orbital j for a given $|J_i\rangle$ state. The reduced matrix element of particle creation and occupation are calculated with a shell model code [100] using the JUN45 interaction.

A similar expression goes for states obtained from a hole coupled to an even-even core:

$$|J_i\rangle = \sum_{j^{-1}L_k} c^{J_i}_{j^{-1}L_k}|j^{-1}\times L_k; J\rangle \tag{6.2}$$

with

$$(c^{J_i}_{j^{-1}L_k})^2 = \frac{1}{\langle\widetilde{n_j}\rangle}\frac{\langle J_i\|a^+_j\|L_k\rangle^2}{2J+1}$$

where $\widetilde{n_j}$ is the occupancy of holes in the j orbital for the J_i state and can be extracted from particle occupational number as

$$\widetilde{n_j} = 2j+1-\langle n_j\rangle$$

From the γ spectrum of ^{71}Zn, the lifetime of the state tentatively assigned to $1/2^-$ or $3/2^-$ [85] decaying to the $1/2^-$ g.s. with a 490 keV γ-ray was found to be $\tau = 7.3 \pm 2.0$ ps. According to the Weisskopf estimates (details are given in Annex B):

$$\tau_{1/2w}(E2) = 1.37\,10^7 E_\gamma^{-5}A^{-4/3} = 1.6710^{-9}\,s \tag{6.3}$$

and

$$\tau_{1/2w}(M1) = 3.17\,10^{-5}E_\gamma^{-3} = 2.7310^{-13}s \tag{6.4}$$

one can reasonably assume that the transition is mainly M1 with a corresponding B(M1)=0.066 ± 0.018 μ_N^2.

From the particle-core coupling approach it was found that the ground state is dominantly (61 %) a hole in $(\nu p_{1/2})^{-1}$ coupled to 0^+ of ^{72}Zn:

$$\begin{aligned}|1/2^-_{g.s.}(^{71}Zn)\rangle = &\pm0.78|(\nu p_{1/2})^{-1}\times 0^+_1(^{72}Zn);1/2^-\rangle\\ &\pm0.36|(\nu p_{1/2})^{-1}\times 0^+_2(^{72}Zn);1/2^-\rangle\\ &\pm0.34|(\nu p_{1/2})^{+1}\times 0^+_1(^{70}Zn);1/2^-\rangle\end{aligned} \tag{6.5}$$

The $|3/2^-(^{71}Zn)\rangle$ in the same approach was found to be:

$$\begin{aligned}|3/2^-(^{71}Zn)\rangle = &\pm 0.7|(\nu p_{3/2})^{-1}\times 0_1^+(^{72}Zn);3/2^-\rangle\\ &\pm 0.32|(\nu p_{1/2})^{-1}\times 2_2^+(^{72}Zn);3/2^-\rangle\\ &\pm 0.29|(\nu p_{1/2})^{+1}\times 2_1^+(^{70}Zn);3/2^-\rangle\end{aligned} \tag{6.6}$$

The $|(1/2)_2^-(^{71}Zn)\rangle$ state can be expressed as:

$$\begin{aligned}|(1/2)_2^-(^{71}Zn)\rangle = &\pm 0.56|(\nu p_{1/2})^{-1}\times 0_2^+(^{72}Zn);1/2^-\rangle\\ &\pm 0.23|(\nu p_{1/2})^{-1}\times 0_1^+(^{72}Zn);1/2^-\rangle\end{aligned} \tag{6.7}$$

Assuming the state at E*=490 keV to be the first calculated $3/2^-$ state, we obtained a wave function where the major component (around 50%) comes from a neutron hole in $\nu p_{3/2}$ coupled to the 0^+ ground state of ^{72}Zn while $1/2^-_{g.s.}$ is dominantly a neutron hole in $\nu p_{1/2}$ coupled to the ground state of ^{72}Zn, which supports the assumption of an M1 transition and indicates the single particle nature of the $3/2^-$ state. If we now assume that this state is the excited $1/2^-$ calculated by the SM, its major component (just 30%) is a neutron hole in $\nu p_{1/2}$ coupled to the 0_2^+ state of ^{72}Zn, indicating a more collective nature of the $1/2_2^-$ state.

The transitions rates were estimated by using the shell model with the JUN45 interaction in a full space. For the M1 transition, the standard orbital and spin nucleon g-factors were used (g_l(p)=1, g_l(n)=0, g_s(p)=5.586, g_s(n)=-3.826). Again if we assume that the state at E*=490 keV is the first calculated $3/2^-$ state decaying with E_γ = 0.894 MeV we obtain B(M1; $3/2^- \rightarrow 1/2^-$) = 0.562 μ_N^2. On the other hand, if it corresponds to the $1/2^-$ state, the M1 transition associated to the E_γ = 1.062 MeV is calculated to be: B(M1; $1/2_2^- \rightarrow 1/2^-$) = 0.0003 μ_N^2. A much better agreement with experimental B(M1) data was obtained if the state is assumed to be a $3/2^-$ rather than $1/2_2^-$. The comparison is just qualitative and cannot be used to assign the state.

From the γ spectrum of ^{71}Zn, the upper limit for the lifetime of the $(3/2)_2^-$ state decaying to the $1/2^-$ g.s. with a 674 keV γ-ray was found to be $\tau \leq 0.6$ ps. The limits of lifetimes for different EM transitions was estimated with the Weisskopf single particle estimate which gives: τ_w(M1) = 1.03 10^{-13} s and τ_w(E2) = 3.34 10^{-10} s. Since the obtained upper limit of lifetime is comparable to the Weisskopf estimate obtained for an M1 transition, one can assume that the $(3/2)_2^- \rightarrow 1/2^-_{g.s.}$ transition is mainly M1.

In the particle-core coupling approach, the $3/2_2^-$ state can be expressed as:

$$\begin{aligned}|3/2_2^-(^{71}Zn)\rangle = &\pm 0.41|(\nu p_{3/2})^{-1}\times 0_1^+(^{72}Zn);3/2_2^-\rangle\\ &\pm 0.38|(\nu p_{1/2})^{-1}\times 2_2^+(^{72}Zn);3/2_2^-\rangle\end{aligned} \tag{6.8}$$

The wave function of $3/2_2^-$ state is very fragmented suggesting its more collective nature.

The upper limit for the lifetime associated to the unassigned transition in ^{71}Zn at 991(3) keV energy, was found to be 0.6 ps. Due to the discrepancy between the experimental and calculated level schemes, it was not possible to even tentatively assign spin and parity to this transition.

From the γ-ray spectrum of ^{69}Zn we were able to identify the shifted component of the $3/2^-$ state which allowed us to extract an upper limit for its lifetime found to be smaller than 0.44 ps. The Weisskopf estimate gives: $\tau_w(\mathrm{M1}) = 5.52\ 10^{-14}$ s, $\tau_w(\mathrm{E2}) = 1.21\ 10^{-10}$ s. Therefore we assume a dominant M1 character for this transition.

In the framework of the particle-core coupling approach the $3/2^-$ state can be expressed as:

$$\begin{aligned}|3/2^-(^{69}Zn)\rangle = &\pm 0.69|(\nu p_{3/2})^{-1} \times 0^+_1(^{70}Zn); 3/2^-\rangle \\ &\pm 0.25|(\nu p_{1/2})^{-1} \times 2^+_2(^{70}Zn); 3/2^-\rangle \\ &\pm 0.25|(\nu p_{1/2})^{+1} \times 2^+_1(^{68}Zn); 3/2^-\rangle\end{aligned} \tag{6.9}$$

which is mainly a neutron hole in $\nu \mathrm{p}_{3/2}$ coupled to the ground state of ^{70}Zn (48%). The $1/2^-_{g.s.}$ is composed of:

$$\begin{aligned}|1/2^-_{g.s.}(^{69}Zn)\rangle = &\pm 0.69|(\nu p_{1/2})^{-1} \times 0^+_1(^{70}Zn); 1/2^-\rangle \\ &\pm 0.43|(\nu p_{1/2})^{-1} \times 0^+_2(^{70}Zn); 1/2^-\rangle \\ &\pm 0.44|(\nu p_{1/2})^{+1} \times 0^+_1(^{68}Zn); 1/2^-\rangle\end{aligned} \tag{6.10}$$

making a $1/2^-_{g.s.}$ state mainly a neutron hole in $\nu \mathrm{p}_{1/2}$ coupled to the ground state of ^{70}Zn (48%). Therefore the major transition goes from $|(\nu p_{3/2})^{-1} \times 0^+_1(^{70}Zn); 3/2^-\rangle$ to $|(\nu p_{1/2})^{-1} \times 0^+_1(^{70}Zn); 1/2^-\rangle$ indicating a single-particle nature of $3/2^-$ state.

From the spectrum of ^{69}Zn the upper limit of lifetime for $5/2^-_2 \rightarrow 5/2^-_1$ transition was found to be 0.6 ps. Since $5/2^-_2$ state deexcites also to $1/2^-_{g.s.}$ and $(3/2)^-$ states the measured lifetime is just a partial lifetime.

6.3 Systematics of the Cu isotopes

The systematics of Cu isotopes has already been discussed in the introductory chapter. In Fig. 2.9 the systematics of $1/2^-$, $5/2^-$ and $7/2^-_2$ states have been shown [55]. It was summarised that low-lying states in odd-mass Cu isotopes around N=40 and beyond are triple in their nature: the $5/2^-$ levels has a single-particle nature, the $1/2^-$ state shows a surprising collective nature at low energies, while the $7/2^-_2$ state can be associated to a particle coupled to the neighbouring even-even core.

From our experiment, we could extract only an upper limit for the lifetime of the $7/2^-_2$ state in ^{69}Cu. The obtained upper limit $\tau \leq 0.7$ ps is in agreement with a previous measurement $\tau = 0.45 \pm 0.7$ ps obtained by Stefanescu et al. [55].

Part II

The partial conservation of seniority in the $g_{9/2}$ shell

7 The partial conservation of seniority in the $g_{9/2}$ shell

7.1 Pairing and seniority

For two identical nucleons in a single j-shell coupled with a short-range attractive interaction between them, the state with $J = 0^+$ is the lowest in energy. This follows from the fact that two particles have a large spatial overlap when their angular momenta are antiparallel. A pairing interaction is defined through its matrix elements by:

$$\nu_J \equiv \left\langle j^2; JM_J \left| \hat{V} \right| j^2; JM_J \right\rangle = -g(2j+1)\delta_{J0} \tag{7.1}$$

where j is the total angular momentum of a single nucleon, J comes from the coupling of nucleons and M_J is the projection of J on the z axis. The strength of the pairing force is denoted by g. The pairing force is stronger between nucleons in higher j orbitals.

The concept of seniority has been introduced by Racah [7] in order to describe electrons in an atomic l^n configuration. He assumed pairing interaction $\hat{V}$ between the electrons which vanishes unless the two electrons' orbital angular momenta are coupled to a total orbital angular momentum $L = 0$. He proved that any eigenstate of the pairing interaction is characterized by a "seniority number" υ which is defined as the number of electrons that are not in pairs coupled to $L = 0$.

The same concept of seniority can be applied in the nucleus. The seniority is then defined as the number of identical nucleons that are not in pairs coupled to total angular momentum $J = 0$. From the definition of seniority it follows that for a single nucleon, the seniority υ is equal to 1. For a system of two nucleons coupled to the $J = 0$, seniority is $\upsilon = 0$, while levels with a J = 2, 4, 6... have seniority $\upsilon =$ 2.

Some important properties of the seniority scheme (a few of them were already given in the first chapter) are:

- The energy difference between states with seniority $\upsilon = 0$ and $\upsilon = 2$ in an n-particle configuration are independent of n and identical to the difference in the two-particle system.

- The B(E2) values for seniority conserving transitions ($\Delta\upsilon = 0$) are zero at mid-shell.

- The number of seniority-violating interactions is $\lfloor(2j-3)/6\rfloor$ where $\lfloor x \rfloor$ denotes the largest integer smaller than $x$contained therein [101]. (This will be discussed more in the following section)

7.2 Total and partial conservation of seniority

Seniority is conserved if states have exact seniority and cannot be expressed as linear combination of states with different seniorities. From $\lfloor(2j-3)/6\rfloor$ it follows that for $j \leq 7/2$ any interaction conserves seniority while for $9/2 \leq j \leq 13/2$ there is a single necessary and sufficient condition for the interaction to conserve seniority.

It was shown by several authors [8, 102, 103] that the necessary and sufficient conditions for a general interaction to conserve seniority are:

$$\sum_{J=2}^{2j-1}(2J+1)\sqrt{2I+1}\left(\frac{\delta_{IJ}}{\sqrt{(2J+1)(2I+1)}}+2\left\{\begin{array}{ccc} j & j & J \\ j & j & I \end{array}\right\}-\frac{4}{(4j^2-1)}\right)\nu_J = 0 \tag{7.2}$$

with I = 2, 4,... $2j$ - 1. The symbol between curly brackets is a Racah coefficient and the matrix elements ν_J are defined in eq. (7.1).

This condition for $j = 9/2$ is [103]:

$$65\nu_2 - 315\nu_4 + 403\nu_6 - 153\nu_8 = 0 \tag{7.3}$$

Van Isacker and Heinze have shown that the seniority quantum number can be conserved for some but not all eigenstates [104] and introduced the notion of partial conservation of seniority. For example, a four-particle state having odd total angular momentum J cannot have $\upsilon = 0$ or $\upsilon = 2$, but must have seniority $\upsilon = 4$.

A non-trivial example of partial conservation of seniority was given by Escuderos and Zamick [101]. They have found that in a system of four particles confined to a $j = 9/2$ shell exists one $J = 4$ and one $J = 6$ state with exact seniority $\upsilon = 4$. It was shown that the property of partial conservation of seniority is crucial for the existence of seniority isomers in nuclei [105].

An illustrative example of seniority isomers is given for $N = 50$ isotones with protons confined to the $\pi g_{9/2}$ shell. In Fig. 7.1a observed in the low energy levels of $N = 50$ isotones ^{92}Mo, ^{94}Ru, ^{96}Pd, ^{98}Cd are compared with results obtained in a $(g_{9/2})^n$ shell model calculation (the figure is adapted from [105]).

Two 4^+ and 6^+ states in the four-particle ^{94}Ru and in the four-hole ^{96}Pd system with exact seniority ($\upsilon = 4$) are presented with thick lines. The 6^+ and 4^+ states with exact seniority in ^{94}Ru and ^{96}Pd are predicted to appear above the yrast 8^+ and 6^+ states, respectively (see Fig. 7.1a). Therefore, the $J^\pi = 8^+$ levels in ^{94}Ru and ^{96}Pd will decay to yrast states with seniority $\upsilon \approx 2$. Now one recalls that electric

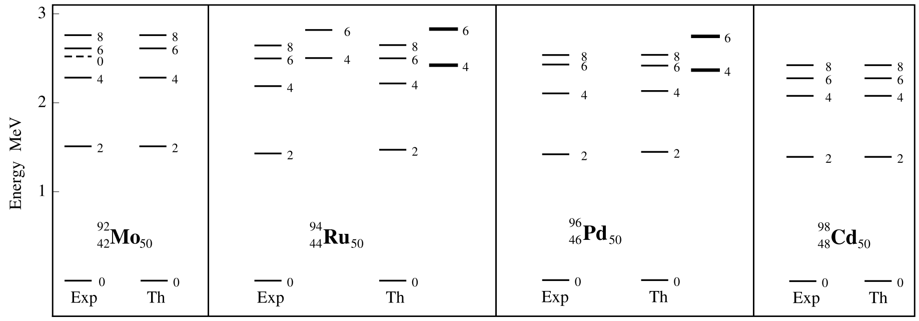

(a) *Systematics of low-lying states in N=50 isotones with protons filling the* $\pi g_{9/2}$ *shell*

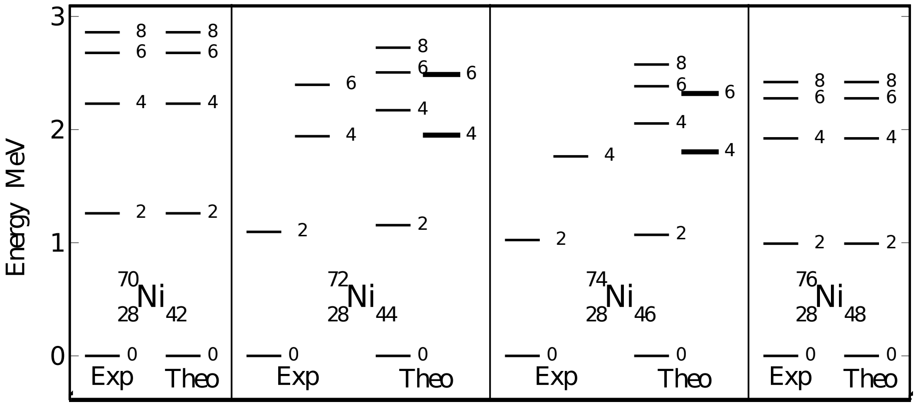

(b) *Systematics of low-lying states Ni isotopes with neutrons filling the* $\nu g_{9/2}$ *shell*

Figure 7.1: *The low energy spectra of the N=50 isotones* ^{92}*Mo,* ^{94}*Ru,* ^{96}*Pd,* ^{98}*Cd (upper figure) and Ni isotopes* $^{70-76}$*Ni (bottom figure). The observed states presented on left-hand side of each isotope are compared with results from the* $(g_{9/2})^n$ *shell model calculation. States* 4^+ *and* 6^+ *with exact seniority* $v = 4$ *are shown with thick lines.*

quadrupole transitions between states with the same seniority are small when the valence shell is close to half-filled. Hence, the 8^+ states in ^{94}Ru and ^{96}Pd appear to be isomeric due to the combined effects of slow quadrupole transition with a small energy difference between 8^+ and 6^+ state [105].

In analogy to the $N = 50$ isotones with protons confined to the $\pi g_{9/2}$ shell one would expect to observe 8^+ isomeric states in nickel isotopes with four-particles or four-holes confined to the $\nu g_{9/2}$ shell, but the situation is somewhat different. In Fig. 7.1b experimental data presented on the left-hand side of each panel are compared with a $(g_{9/2})^n$ shell model calculation (taken from [106]). The two-body matrix elements ν_J are taken from ^{70}Ni and ^{76}Ni, while for ^{72}Ni and ^{74}Ni are extracted from interpolation between ^{70}Ni and ^{76}Ni as described in [106]. From the theoretical predictions shown in Fig. 7.1 one notices that, contrary to the situation in ^{94}Ru and ^{96}Pd, the 6^+ and 4^+ states with exact seniority $\upsilon = 4$ in ^{72}Ni and ^{74}Ni lie below the yrast 8^+ and 6^+ states with $\upsilon \approx 2$. This opens an additional decay channel from 8^+ and 6^+ states with $\upsilon \approx 2$ to 6^+ and 4^+ states with exact seniority $\upsilon = 4$ leading to a fast E2 transition. Therefore, the 8^+ and 6^+ states in ^{72}Ni and ^{74}Ni are not expected to be isomeric. This was recently confirmed by Chiara et al. who established an upper lifetime limit of the 8^+ states in ^{72}Ni [107].

Another interesting property of partial conservation of seniority will be discussed in the following section.

7.3 Seniority and one-particle transfer

By definition of seniority comes out that a single nucleon carries seniority $\upsilon = 1$. Therefore one nucleon transfer reaction changes seniority by 1, i.e. $\Delta\upsilon = \pm 1$.

For the sake of convenience it is worth to underline again that, the shell model calculations confined in the $(g_{9/2})^n$ shell, predict two 4^+ and 6^+ states lying close in energy in (^{72}Ni) and (^{74}Ni), respectively four-particle and four-hole systems. One of each state has exact seniority $\upsilon = 4$, while the two other ones have $\upsilon \approx 2$. The state with exact seniority $\upsilon = 4$ does not mix with other states, while the state with $\upsilon \approx 2$ can mix with another state with seniority $\upsilon \approx 4$.

Knowing 1) the one nucleon transfer selection rules and 2) the fact that there are two 4^+ states and two 6^+ states that lie close in energy but with a different seniority it would be interesting to explore the effect of partial conservation of seniority using one-particle transfer as a probe. In order to do so, the spectroscopic factors for one-particle transfer reaction were calculated. These calculations were carried out in the Shell Model framework using first a confined $(g_{9/2})^n$ space and then a large scale realistic valence space. Results were compared with spectroscopic factors calculated assuming exact seniority scheme in the $g_{9/2}$ shell.

Spectroscopic factors are defined in terms of reduced matrix elements of the particle creation operator as:

$$S = \left| \left\langle j^n \alpha J \left\| a_j^+ \right\| j^{n-1} \alpha_1 J_1 \right\rangle \right|^2 \frac{1}{2J+1} \tag{7.4}$$

where a_j^+ denotes a creation operator for a particle in a j-shell. The J_1 and J are angular momenta of a system with $n-1$ and n particles in j-shell. The $(2J+1)$ factor is by convention associated with the larger n.

Shell model calculations were performed using the ANTOINE code [100] with single particle energies and two-body matrix elements taken from reference [15]. Due to a very large model space, some restrictions had to be imposed (see Fig. 7.2).

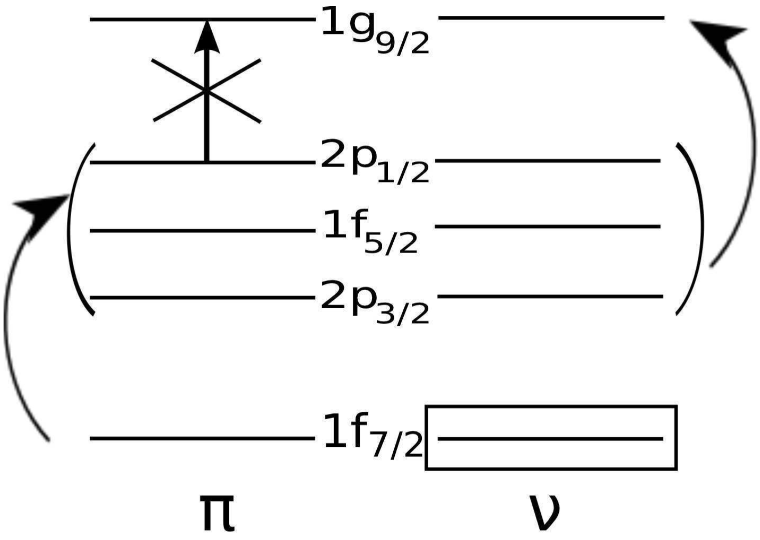

Figure 7.2: *Schematic representation of the valence space using $pfg_{9/2}$ interaction. Neutrons were blocked in the $f_{7/2}$ orbital while excitations from $pf_{5/2}$ to $g_{9/2}$ orbital. In the proton space, the $g_{9/2}$ shell was blocked and only excitations from $f_{7/2}$ to $pf_{5/2}$ were allowed.*

We blocked neutrons in the $f_{7/2}$ orbital and excitations were allowed from $pf_{5/2}$ to the $g_{9/2}$, while in the proton space, the $g_{9/2}$ shell was blocked and only excitations from $f_{7/2}$ to the $pf_{5/2}$ shell were allowed. Even in this model space we could not calculate energy levels of ^{70}Ni and ^{72}Ni without truncation. Therefore, by gradually increasing the truncation, starting from 1 p-h excitation, we have tried to see if convergence could be obtained and whether we could trust the results. Allowing in total 5 or 6 particle excitations, it looks like the convergence was almost achieved, but the calculations gave higher values for levels obtained with 7 particle excitations. Since the computational limit of the cluster was reached, it was not possible to include more particle excitations and it was not possible to know whether the calculations were reliable or not.

Since it was not possible to calculate one particle transfer between 2, 3 and 4 particles in $\nu g_{9/2}$ for ^{70,71,72}Ni, with ANTOINE in a defined space, we have calculated the spectroscopic factors between 2, 3 and 4 holes, i.e. for ^{76,75,74}Ni isotopes. In ANTOINE, the spectroscopic amplitudes are defined as the square root of the usual spectroscopic factors:

$$S_a = \left|\left\langle j^n \alpha J \left\| a_j^+ \right\| j^{n-1} \alpha_1 J_1 \right\rangle\right| \frac{1}{\sqrt{2J+1}} \tag{7.5}$$

For the analytical calculation in the exact seniority scheme for the $g_{9/2}$ shell we have the expressed spectroscopic factors in terms of overlap integral. If the final state with angular momentum J can be made by coupling the particle in j to the core with J_1 without fragmentation, then the overlap integral would be unity leading to a spectroscopic factor of 1. For one active shell, the spectroscopic factors can be expressed as:

$$S = n_1 \left[j^{n-1} \left(\alpha_1 J_1 \right) jJ \,|\}\, j^n \alpha J \right]^2 \tag{7.6}$$

where $[j^{n-1}(\alpha_1 J_1) jJ|\} j^n \alpha J]$ is a Coefficient of Fractional Parentage (CFP). CFPs can be understood as the probability that the wave function in (j^n) configuration can be written as (j^{n-1}) configuration coupled to a one-particle configuration.

The CFPs are given up to the first half-filled shell. Since in the shell model calculations, the spectroscopic factors were calculated between ^{76}Ni, ^{75}Ni and ^{74}Ni isotopes it is necessary to adjust the CFP for the hole representation. Therefore, going from particle to hole representation, one can obtain for the CFP [8]:

$$\left[j^{n-1} \left(\alpha_1 J_1 \right) jJ \,|\}\, j^n \alpha J \right] = \left[j^{n-1-(2j+1)} \left(\alpha_1 J_1 \right) jJ \,|\}\, j^{n-(2j+1)} \alpha J \right] \tag{7.7}$$

By substituting the number of particles n for the number of holes $n_1 = n - (2j+1)$, after a few transformations one can obtain [8]

$$\left[j^{-(n_1+1)} \left(\alpha_1 J_1 \right) jJ \,|\}\, j^{-n_1} \alpha J \right] = (-1)^{J-j-J_1+\Delta\nu+n_1} \sqrt{\frac{(n_1+1)(2J_1+1)}{(2j+1-n_1)(2J+1)}} \left[j^{n_1} (\alpha J) jJ_1 \,|\}\, j^{n_1+1} \alpha_1 J_1 \right] \tag{7.8}$$

The spectroscopic amplitudes calculated with the ANTOINE shell-model code can be compared with the following analytical expression for spectroscopic factors [8]:

$$S_A = \sqrt{n}(-1)^{J-j-J_1+\Delta\nu+n_1} \sqrt{\frac{(n_1+1)(2J_1+1)}{(2j+1-n_1)(2J+1)}} \left[j^{n_1} \left(\alpha J \right) jJ_1 \,|\}\, j^{n_1+1} \alpha_1 J_1 \right] \tag{7.9}$$

Before comparing the spectroscopic factors, let us consider the schematic representation of one-particle transfer reaction in the exact seniority scheme. If we assume that states have exact seniority and looking at the system with 2, 3 and 4

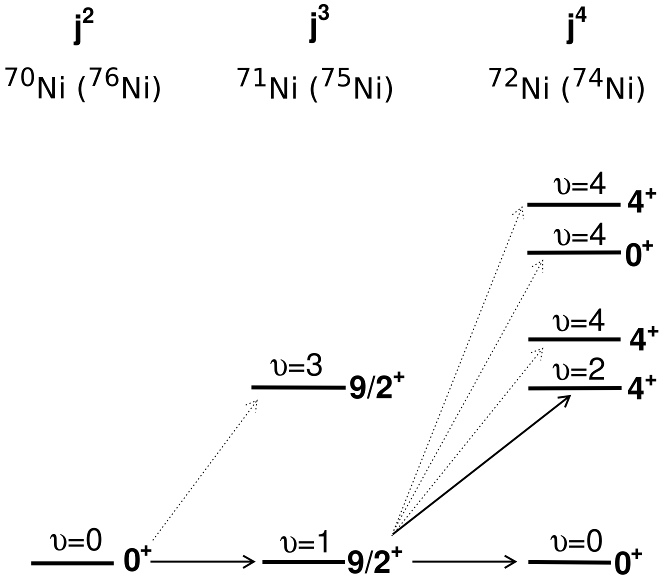
j2
70Ni (76Ni)
j3
71Ni (75Ni)
j4
72Ni (74Ni)
υ=4 4+
υ=4 0+
υ=4 4+
υ=2 4+
υ=3 9/2+
υ=0 0+
υ=1 9/2+
υ=0 0+

Figure 7.3: *Schematic representation of single nucleon transfer in the $j = 9/2$ shell for the 2, 3 and 4 particle or hole systems (^{70}Ni, ^{71}Ni and ^{72}Ni or ^{76}Ni, ^{75}Ni and ^{74}Ni) with the assumption that seniority is conserved. Allowed transitions are indicated with a full arrow, while forbidden transitions are indicated with a dotted arrow.*

Table 7.1: *Spectroscopic amplitudes (SA) for transfer from the* 0^+_1 *ground state of* ^{76}*Ni to the* $9/2^+_1$ *ground state and* $9/2^+_2$ *state of* ^{75}*Ni in a* $(1g_{9/2})^n$ *configuration with ANTOINE and with using eq. 7.9 expression.*

^{75}Ni / ^{76}Ni	J = $9/2^+_1$		J = $9/2^+_2$	
J	$(1g_{9/2})^n$	analytical SA	$(1g_{9/2})^n$	analytical SA
0^+	2.826	2.828	-0.013	0

nucleons in the $g_{9/2}$ shell, the following scheme of one nucleon transfer can be drawn (Fig. 7.3).

The first step is to compare spectroscopic amplitudes between two and three particle/hole systems. In Table 7.1 the spectroscopic amplitudes between two $9/2^+$ states of ^{75}Ni and 0^+, ground state of ^{76}Ni, SA($(g_{9/2})^3 9/2^+; (g_{9/2})^2 J = 0$), obtained with the shell model calculations in $(1g_{9/2})^n$ are compared with the spectroscopic amplitudes calculated using equation (7.9).

One can notice that in the case of exact seniority, there is no single-particle transfer between the $9/2^+_2$ state in the $(g_{9/2})^3$ system (having seniority $v = 3$) and 0^+_1 state in $(g_{9/2})^2$ (with seniority $v = 0$), i.e.

$$\left|\left\langle \left(g_{9/2}\right)^3 (v = 3, J_1 = 9/2^+) \left\| a^+_{9/2} \right\| \left(g_{9/2}\right)^2 \left(v = 0, J = 0^+\right)\right\rangle\right| = 0 \tag{7.10}$$

This comes from the selection rule since the particle creation operator $a^+_{9/2}$ changes seniority by one. Conversely, the shell model calculations gives a value different than zero, meaning that $9/2^+_2$ state does not have an exact seniority and can be expressed as a linear combination of $9/2^+$ states with exact seniority $v = 1$ and $v = 3$. The small value of spectroscopic amplitude indicates a small mixing between $9/2^+$ states with seniority $v = 1$ and $v = 3$ hence a slightly broken seniority.

What we considered to do next was to investigate single particle transfer between systems with 3 and 4 particles/holes. In the case of exact seniority we would expect only to have transfer from the $9/2^+_1$ state in the $(g_{9/2})^3$ system to the 0^+_1 state (with seniority $v = 0$) and the 4^+_1 state (with seniority $v = 2$) in $(g_{9/2})^4$ system 7.3. Knowing that we have slightly a broken seniority scheme, several other transfers from the $9/2^+_1$ state in the $(g_{9/2})^3$ system to the $(g_{9/2})^4$ system become possible such as: transfer to the 0^+_2 state (with seniority $v \approx 4$), 4^+_2 and 6^+_2states (with exact seniority $v = 4$).

In Table 7.2 the spectroscopic amplitudes for transfer from the first $9/2^+$ state of ^{75}Ni to J=0^+, 4^+ and 6^+, states in ^{74}Ni calculated with ANTOINE using the $pfg_{9/2}$ interaction in $(1g_{9/2})^n$ and full space are presented. The results are compared with the analytical calculations.

From the Tables 7.1 and 7.2. one can draw a schematic representation of single nucleon transfer reaction in the $g_{9/2}$ orbital obtained with a slightly broken seniority.

Table 7.2: *Spectroscopic amplitudes (SA) for transfer from the $9/2_1^+$ ground state of ^{75}Ni to several states in ^{74}Ni in the $(1g_{9/2})^n$ space and in the large space with $pfg_{9/2}$ interaction with neutrons blocked in $f_{7/2}$ and with blocking of proton $g_{9/2}$ orbital. Results are compared with analytical calculations using expression (7.9). Table cells marked with / correspond to cases in which analytical results were not calculated.*

SA		^{75}Ni, J = $9/2_1^+$, $\upsilon \approx 1$		
^{74}Ni	seniority	$(1g_{9/2})^n$	full space	analytical SA
J = 0_1^+	$\upsilon \approx 0$	0.632	0.559	0.632
J = 0_2^+	$\upsilon \approx 4$	0	0.146	0
J = 4_1^+	$\upsilon \approx 2$	1.165	0.843	1.162
J = 4_2^+	$\upsilon = 4$	0	0.632	0
J = 4_3^+	$\upsilon \approx 4$	0.005	0.050	/
J = 6_1^+	$\upsilon \approx 2$	1.393	1.327	1.396
J = 6_2^+	$\upsilon = 4$	0	0.039	0
J = 6_3^+	$\upsilon \approx 4$	0.0059	0.081	/

It is interesting to note, that although two 4^+ and two 6^+ states are calculated to lie close in energy they are predicted to be differently excited in particle transfer. For simplicity, particle transfers are drawn only for 4^+ states in Fig. 7.4, while the same representation for 6^+ states has been omitted.

From the analytical calculations given in Table 7.2 a few unexpected results of the single nucleon transfers can be observed:

$$\begin{aligned} \left|\left\langle (g_{9/2})^4 0_2^+ \left\| a_{9/2}^+ \right\| (g_{9/2})^3 9/2_1^+ \right\rangle\right| &= 0 \\ \left|\left\langle (g_{9/2})^4 4_2^+ \left\| a_{9/2}^+ \right\| (g_{9/2})^3 9/2_1^+ \right\rangle\right| &= 0 \\ \left|\left\langle (g_{9/2})^4 6_2^+ \left\| a_{9/2}^+ \right\| (g_{9/2})^3 9/2_1^+ \right\rangle\right| &= 0 \end{aligned} \tag{7.11}$$

Since $\left|(g_{9/2})^3 9/2_1^+\right\rangle$ and $\left|(g_{9/2})^3 9/2_2^+\right\rangle$ are not states with exact seniority (as shown is Table 7.1) one would expect that $\left|\left\langle (g_{9/2})^4 0_2^+ \left\| a_{9/2}^+ \right\| (g_{9/2})^3 9/2_1^+ \right\rangle\right|$ is different from 0. We have proved (see Annex B for details) that transfer from the $9/2_1^+$ state of three-particle/hole system to the second 0^+ four-particle state, remains exactly 0 due to identical seniority mixing in the $9/2_1^+$ and 0_2^+ states which cancel each other restoring the selection rules.

The two other results from expression (7.11) come from the fact that following CFPs vanish(proof given in Annex B):

$$\begin{aligned} \left[(g_{9/2})^3(\upsilon = 3, J_1 = 9/2) g_{9/2} J = 4 \,|\}\, (g_{9/2})^4 \upsilon = 4, J = 4\right] &= 0 \\ \left[(g_{9/2})^3(\upsilon = 3, J_1 = 9/2) g_{9/2} J = 6 \,|\}\, (g_{9/2})^4 \upsilon = 4, J = 6\right] &= 0 \end{aligned} \tag{7.12}$$

From Table 7.2 it is interesting to check spectroscopic amplitudes to the first and second 4^+ and 6^+ states since they have different seniority in the schematic

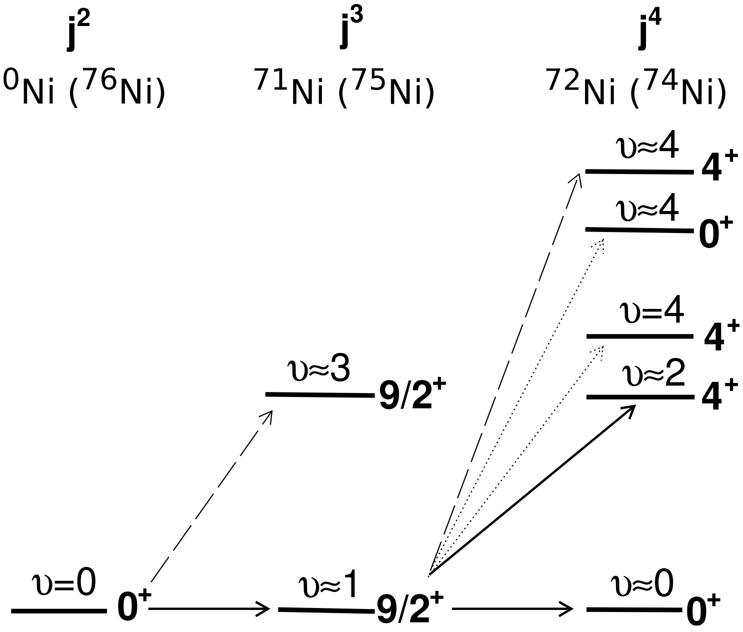
j2
70Ni (76Ni)
j3
71Ni (75Ni)
j4
72Ni (74Ni)
υ=0
0+
υ≈1
9/2+
υ≈0
0+
υ≈3
9/2+
υ≈4
4+
υ≈4
0+
υ=4
4+
υ≈2
4+

Figure 7.4: *Schematic representation of a single nucleon transfer in the $j = 9/2$ shell for the 2, 3 and 4 particles or holes system (^{70}Ni, ^{71}Ni and ^{72}Ni or ^{76}Ni, ^{75}Ni and ^{74}Ni) with slightly broken symmetry. Transfer reactions are drawn for 4^+ states (the same results are obtained with 6^+ states. Allowed transitions are indicated with a full arrow, weak transitions are indicated with dashed lines, while forbidden transitions are indicated with a dotted arrow.*

calculations. In the case of 4_1^+ and 4_2^+ states, large shell model calculations gave the same order of spectroscopic amplitudes indicating that their seniorities are mixed. On the other hand spectroscopic amplitudes to the 6_1^+ and 6_2^+ states obtained by LSSM calculations are in agreement with spectroscopic amplitudes calculated in seniority scheme (although with the reversed order) indicating that seniority character of these states is well preserved.

7.4 Conclusion

In this chapter, the partial conservation of seniority in the $g_{9/2}$ shell and its influence on one-particle transfer have been investigated. It was shown both analytically and using large scale shell model calculations, that two 4^+ states and two 6^+ states predicted to be close in energy, should be differently excited in one-particle transfer. Namely, spectroscopic amplitudes calculated in the seniority scheme, obtained for 3, 4 particle/hole systems in the $\mathrm{g}_{9/2}$ shell, indicate that it is not possible to populate 4^+ and 6^+ states (with exact seniority) in the $(g_{9/2})^4$ system by one particle transfer reaction from the $9/2_1^+$ state in the $(g_{9/2})^3$ system. In the case of large shell-model calculations, spectroscopic amplitudes between the $9/2_1^+$ state in the $(g_{9/2})^3$ system to the 4_1^+ and 4_2^+ states in the $(g_{9/2})^4$ system are of the same order of magnitude, indicating that their seniorities are mixed, while the spectroscopic amplitudes to the 6_1^+ and 6_2^+ states are in agreement with the spectroscopic amplitudes calculated in the seniority scheme, indicating that the seniority character of these states is well preserved.

It would be interesting to perform a one-particle transfer experiment in neutron rich Ni isotopes above N=40 or in the N=50 isotones from molybdenium to cadmium. From the relative population of the 6^+ states close in energy in $(g_{9/2})^4$ particle system from the $9/2_1^+$ ground state in the $(g_{9/2})^3$ system we would be able to conclude about seniority conservation.

Part III

Search for new isotopes and isomers in the vicinity of ^{100}Sn

8 Motivation

Nuclei with identical numbers of protons and neutrons (N = Z nuclei), especially in the region of double shell closures, are unique test-ground for evaluating and further developing nuclear models. These studies in particular, provide information on the interactions between protons and neutrons occupying identical orbitals. Nuclei with N = Z at low masses lie near the line of beta stability, while heavier ones lie further away from this line. It is expected [108] that ^{100}Sn is the heaviest N = Z nucleus stable against ground-state proton decay. This stability is due to its magic character. For heavier N = Z nuclei the condition of double shell closure is not sufficient to ensure stability against the emission of protons and alpha particles and ^{164}Pb (the next doubly magic nucleus with N=Z=82) most probably lies far beyond the proton drip line. The main objectives of studies in the N=Z ^{100}Sn region near the proton drip-line could be summarised as follows [109]:

1. Shell structure and single particle energies
2. Proton – neutron interaction in isospin symmetric matter
3. Particle – hole excitation of the ^{100}Sn core and E2 polarisation
4. GT β^+/EC decay; experimental and structural sources of the observed quenching
5. Isospin mixing
6. Proton decay from ground and excited states
7. Super- and hyper- deformation in N$\sim$Z nuclei

Single particle energies of ^{100}Sn and neighbouring nuclei are shown in Fig. 8.1. The energy gap between the fully occupied orbitals (both proton and neutron orbitals: $f_{7/2}, f_{5/2}, p_{3/2}, p_{1/2}$ and $g_{9/2}$) and the first valence orbits $d_{5/2}$ and $g_{7/2}$ is around 6 MeV, giving ^{100}Sn its magic character [110, 111]. Due to the Coulomb interaction, the proton single particle energies lie higher than the corresponding neutron single particle states.

Going away from the valley of β stability the Q - values for β - decay increase and the nuclei become less and less stable. Those nuclei situated on the neutron deficient

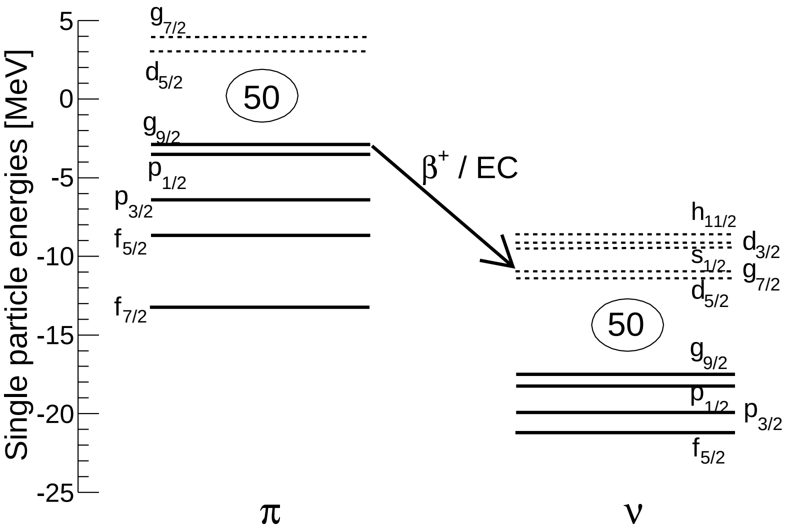

Figure 8.1: *The proton and neutron single particle energies of the orbitals in the* ^{100}*Sn nucleus predicted by Grawe et al. [110]. Fully occupied orbitals are indicated with solid line, while dashed lines indicate empty orbitals. Decay governed by only possible Gamow - Teller spin-flip transition from proton in* $g_{9/2}$ *to neutron in* $g_{7/2}$ *is illustrated.*

side undergo β^+ and electron capture (EC) decay, while those nuclei situated on the neutron rich side decay by β^-.

The β-decay of nuclei located far from the valley of stability, can populate states at high excitation energy, even above the particle separation energy in the daughter nuclei. This can occur when particle separation energy is small compared to the Q – value. Therefore, in the ^{100}Sn region, close to the proton drip-line, we also expect β–delayed proton radioactivity.

Depending on the spin orientation of the fermions involved in the β – decay process, two types of decay can be distinguished:

- Fermi decay in which the neutrino and the electron are emitted with antiparallel spins resulting in a total spin $\mathbf{S} = \mathbf{0}$. Due to the conservation of angular momentum, it is required that the spin of the parent and daughter nuclei have the same direction. The selection rules in Fermi β – decay impose that there is no change of the isospin (ΔT = 0), no change of the parity ($\Delta\pi = 0$) and no change of nuclear spin (ΔI = 0).

- Gamow – Teller (GT) decay in which neutrino and electron are emitted with parallel spins leading $\mathbf{S} = \mathbf{1}$ and therefore, it is required that the spins of the parent and daughter nuclei have opposite directions. The selection rules for allowed GT transition say that there can be change of the isospin (ΔT = 0,

±1); no change of the parity ($\Delta\pi = 0$) and change of the nuclear spin by 0 or 1 (ΔI = 0, 1). Transition from $0^+ \rightarrow 0^+$ is forbidden.

In the Gamow – Teller decay, the transition matrix element M_{AV} can be written as:

$$|M_{AV}^2| = B_{GT} = \langle\psi_f|\vec{\sigma}\tau_\pm|\psi_i\rangle \tag{8.1}$$

where ψ_i and ψ_f denote the wave function of the initial and final states, σ represents the operator that changes the spin of the converted nucleon and $\tau_\pm$ is the isospin operator that changes the z – component of the isospin, keeping its absolute value unchanged.

^{100}Sn is predicted to have the purest GT decay since its decay should be governed only by the spin flip transition from a proton in $g_{9/2}$ to a neutron in $g_{7/2}$ as indicated in Fig. 8.1. Other transitions like $\pi f_{7/2} \rightarrow \nu f_{5/2}$ and $\pi p_{5/2} \rightarrow \nu p_{3/2}$ are forbidden due to the Pauli principle, since the final states are fully occupied. The SM calculations of Grawe et al. [111] predict that the GT transition populates mainly the 1^+ state in ^{100}In (Fig. 8.2).

For the pure GT decay, the strength can be expressed in terms of several measured quantities as:

$$B_{GT}^{exp} = \frac{6147[s]}{(g_A/g_V)^2}\frac{I_\beta}{f(E_0)T_{1/2}} \tag{8.2}$$

where g_A and g_V are axial vector and vector coupling constant, I_β is the β – decay intensity to the final level, $f(E_0)$ is Fermi integral and $T_{1/2}$ is the half-life of the decaying nucleus.

In the shell model, the GT strength can be calculated as [112]:

$$B_{GT}^{ESPM} = \frac{4l}{2l+1}\left(1 - \frac{N_{\nu g_{7/2}}}{8}\right)N_{\pi g_{9/2}} \tag{8.3}$$

where $l = 4$ is the orbital angular momentum, $N_{\pi g_{9/2}}$ and $N_{\nu g_{7/2}}$ are occupational numbers for proton and neutron orbitals, respectively. In Fig. 8.3 are presented several theoretical values of the GT strength calculated in various frameworks: Extreme single particle shell model – B_{GT}^{ref} [112], Finite Fermi System – B_{GT}^{FFS} [113], Quasiparticle Random Phase Approximation – B_{GT}^{QRPA} [113] are compared with the existing experimental values [114, 115, 116].

Large discrepancies are found between the experimental and theoretical values. Those discrepancies, called GT quenching, can originate from both the theoretical and the experimental sides. For the theoretical part, the quenching could originate from core polarization effects (i.e. due to considering the core as inert one, which would decrease the theoretical value of the GT strength), Δ resonances...

Experimentally, the quenching is due to missing strength arising from the small Q_{EC} window. Going away from the valley of beta – stability, Q_{EC} becomes larger,

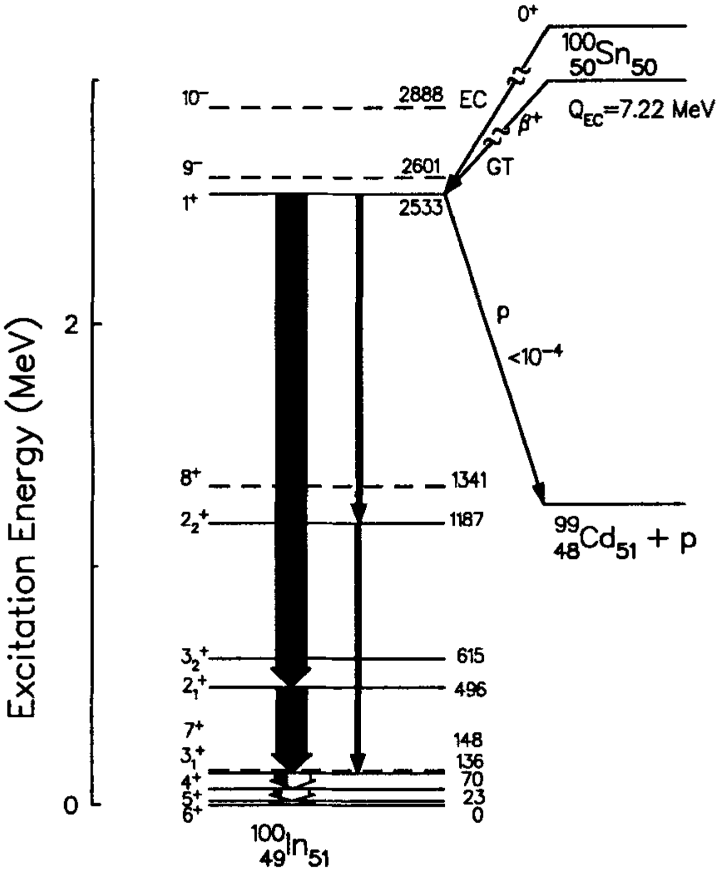
Excitation Energy (MeV)
0
2
0⁺
$^{100}_{50}Sn_{50}$
Q_{EC}=7.22 MeV
EC
β⁺
GT
10⁻
2888
9⁻
2601
1⁺
2533
p
<10⁻⁴
8⁺
1341
2_2^+
1187
$^{99}_{48}Cd_{51}$ + p
3_2^+
615
2_1^+
496
7⁺
148
3_1^+
136
4⁺
70
5⁺
23
6⁺
0
$^{100}_{49}In_{51}$

Figure 8.2: *Shell model prediction for the* ^{100}Sn β^+/EC *decay. The level scheme is taken from [111]*

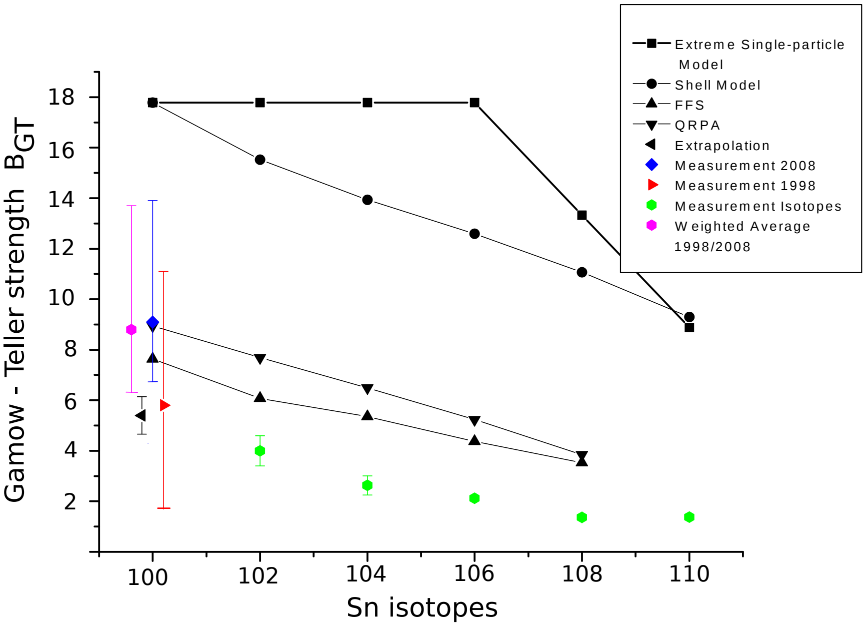

Figure 8.3: *Gamow – Teller strength in the decay of various Sn isotopes. Comparison of results from different theoretical models (B_{GT}^{ref} [112], B_{GT}^{FFS} [113], Quasiparticle Random Phase Approximation – B_{GT}^{QRPA} [113] with available experimental results [114, 115, 116]. The extrapolated value for ^{100}Sn was estimated by Batist et al. [117]. The figure is taken from [118].*

making it possible to measure a larger fraction of the GT strength. Finally, ^{100}Sn, with $Q_{EC} \approx 7$ MeV is a unique case to study this effect since it is calculated that 97 % of the full Gamow – Teller strength can be reached by β – decay as shown in Fig. 8.4.

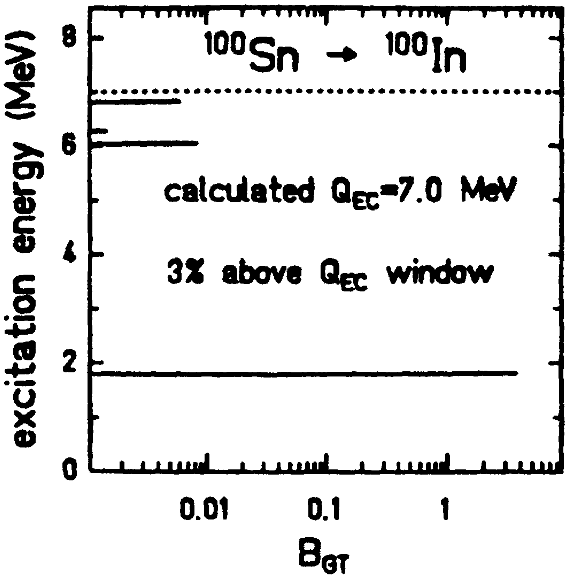

Figure 8.4: *Theoretical calculations of the GT strength distribution in ^{100}Sn nucleus [119].*

8.1 Search for new isotopes

With the development of new accelerators and techniques, it becomes possible to produce and identify new isotopes far from the line of stability. The discovery of new isotopes in the vicinity of drip lines gives an important input for testing nuclear mass models and therefore for understanding the nuclear forces.

In addition, measuring the production cross section and optimising experimental setup can serve as a basis for planning future experiments, such as decay spectroscopy of these nuclei.

The drip line is defined as line connecting nuclei in which nucleon separation energy goes to zero [120]. The nucleon separation energy near the valley of stability is of the order of 8 MeV and is decreasing toward the proton/neutron drip line. The uncertainties in the determination of the binding energy are not important for the valley of stability, while close to the drip line it is comparable to the proton(neuron) separation energy. Different mass formulas such as: empirical mass formula [121], Finite-range droplet model [122], Hartree-Fock-Bogolyubov model [123] predict different positions of the the proton drip line. Therefore, the detection of new nuclei along the drip line could serve as an input to check different mass models.

Mapping the proton drip line in this region and adjusting the mass formulas is important for the description of the astrophysical rapid proton capture process (rp-process). The rp-process takes place in hot, explosive proton rich environment, such as X-ray bursts, in which nucleus captures high energy protons. This process has to compete with its inverse process: (γ, p) reaction. If the proton separation energy has a negative or small positive value, then the inverse process will dominate and the rp-process will stall at that point (called waiting point) and "wait" for the two proton capture which will allow the rp-process to proceed beyond the waiting point or will undergo β-decay [124].

8.2 Experimental overview

For many reasons ^{100}Sn has attracted the interest of a large number of physicists:

- it is the heaviest self conjugate doubly magic nucleus,
- it is the heaviest N=Z isotope stable against ground – state proton decay,
- it decays by pure GT – decay in one single-decay branch,
- its high Q_{EC} allows to determine GT – decay strength over a large energy range

The first successful identification of ^{100}Sn was obtained at GSI by fragmentation of 1.1 GeV/nucleon ^{124}Xe beam [115]. At the same time, at GANIL, ^{100}Sn was identified by medium energy fragmentation (63 MeV/nucleon) of ^{112}Sn on a natural Ni target. With a primary beam intensity of 2.4 pnA over 44 hours, eleven ^{100}Sn nuclei were identified [125]. In another experiment, also performed at GANIL, ^{100}Sn nuclei were produced via the fusion – evaporation reaction ^{50}Cr + ^{58}Ni at energy of 5.1 MeV/nucleon aiming at measuring the mass of ^{100}Sn and ^{100}In [126]. The nuclei produced by fusion – evaporation reaction were accelerated by the second cyclotron of GANIL that was used as a high precision spectrometer. The obtained mass excesses were:

$$\begin{aligned} M.E.(^{100}Sn) &= -57.770 \pm 0.300(syst) \pm 0.900(stat)MeV \\ M.E.(^{100}In) &= -64.650 \pm 0.300(syst) \pm 0.100(stat)MeV \end{aligned} \tag{8.4}$$

In another experiment performed at GSI, ^{100}Sn and neighbouring nuclei were produced by the fragmentation of 1 A GeV ^{112}Sn beam on a Be target, only one ^{100}Sn nucleus was identified [114], which combined with the previous GSI experiment [115], gives information on the half- life, beta – endpoint energy, Q_{EC} and finally the GT – strength. The combined results of GT - strength from both experiments are still given with a large uncertainty as shown in Fig. 8.3.

Attempt to use heavy – ion induced fusion – evaporation reactions between ^{58}Ni beam and ^{50}Cr target with energies set to 4.6 MeV/nucleon and 5.8 MeV/nucleon to maximise the cross – section for ^{102}Sn and ^{100}Sn (according to HIVAP calculations) ended with no positive identification of ^{100}Sn. Based on the cross – sections for nuclei ^{101}Sn to ^{105}Sn obtained in this experiment, the extrapolated cross – section for ^{100}Sn was about 3 nb [127].

Another experiment aiming at producing ^{100}Sn by fragmentation of ^{112}Sn at an energy of 120 MeV/nucleon was performed at the A1900 fragment separator at MSU [128]. ^{9}Be and ^{58}Ni targets were used to study the effect of the reaction mechanism on the production of neutron deficient Sn isotopes and it was found that the ^{9}Be target has a higher yield by a factor of 5. During the 11.5 days of irradiation with an average intensity of 10.7 particle nA, fourteen ^{100}Sn nuclei were identified and its lifetime was measured.

In the most recent experiment in which I was involved, exotic nuclei around ^{100}Sn were produced by the fragmentation of 1GeV/nucleon ^{124}Xe beam with an intensity of 10^9 ions/s, on 4008 mg/cm2 beryllium target [116]. The ^{100}Sn production cross – section was determined to be 5.8(21) pb, lower than the 11(4) pb obtained previously [129]. Out of the 259 identified ^{100}Sn, it was possible to assign 126 decay chains of ^{100}Sn. The half – life of ^{100}Sn was deduced to be 1.16(20) s, much more precise than in the previous experiments. However the extracted GT – strength of the ^{100}Sn ground state was $B_{GT} = 9.1^{+4.8}_{-2.3}$ with still a large relative error of 50 %. The log(ft) $= 2.62^{+0.13}_{-0.19}$ value for GT decay of ^{100}Sn decay was found to be the smallest ever measured in any nucleus (Fig. 8.5 [116]). Since the strength of the GT decay of ^{100}Sn is much larger than for the superallowed $0^+ \rightarrow 0^+$ Fermi decay, GT decay is also called as a “superallowed” Gamow – Teller decay.

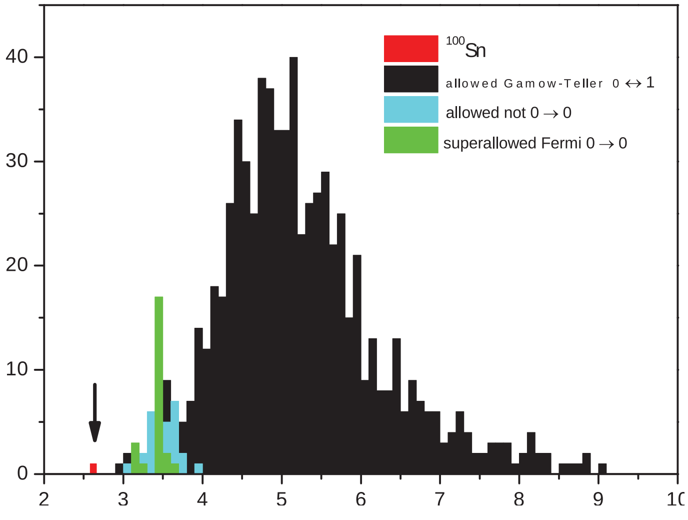

Figure 8.5: *Log(ft) values for the allowed nuclear β – decays. The decay is the fastest β – decay in the nuclear chart.[116].*

A ^{100}Sn experiment was proposed in 2006 and scheduled in 2011 (test) and 2013 at RIBF, RIKEN Institute with a beam of ^{124}Xe, with an expected intensity of 10 particle nA. Due to the lower energy (350 MeV/nucleon) compared to GSI, a stack of silicon detectors, for detecting β particles and measuring β endpoint energy, could be placed only after the implantation detectors, while at GSI, those detectors were placed also before the implantation detectors [116]. Hence efficiency of measuring β endpoint energy will be reduced by factor 2 compared to experiment at GSI. Also, at lower energies, only a fraction of the ^{100}Sn are fully stripped. Therefore some ^{100}Sn are lost in the separator due to the charge state distribution. Taking all this into account the production rate of ^{100}Sn at RIBF was expected to be about one order of magnitude higher than that in previous GSI experiment.

In order to optimise the settings of the BigRIPS separator for the production and separation of ^{100}Sn an one-day test experiment has been performed and its results are discussed in the following chapter. Based on those results, the optimal configuration setting was chosen for the main ^{100}Sn experiment aiming at measuring the Gamow-Teller strength in the decay of ^{100}Sn to ^{100}In. In chapter 10, the results from the main ^{100}Sn experiment, for the search of new isotopes along the proton drip-line in the region of Te-Ru is presented.

9 The ^{100}Sn test experiment

In this chapter, the experimental setup and results of the ^{100}Sn test experiment are discussed. The aim of the test experiment was to investigate the optimal settings of the BigRIPS separator for the ^{100}Sn production and selection. Two different configurations with a thick and thin Be target are discussed. Finally, production cross section of N=50 isotones is calculated and the results are compared with the previous ones.

9.1 Choosing optimal settings

An efficient way to produce proton rich nuclei is using projectile fragmentation preferably with neutron deficient beam. Among the available beams at RIKEN, the best one with respect to the production of proton rich nuclei around ^{100}Sn is ^{124}Xe. The ^{124}Xe beam, delivered from a ion source (SC-ECRIS) was accelerated using the linear accelerator (RILAC2) and a cascade of four ring cyclotrons: RRC (Riken Ring Cyclotron), fRC (fixed frequency Ring Cyclotron), IRC (intermediate-stage ring cyclotron) and SRC (separate-sector superconducting ring cyclotron). The ^{124}Xe^{52+} beam accelerated to 345 MeV/u after the SRC is transported to the BigRIPS separator for the production and separation of radioactive beams. [130].

The BigRIPS separator has been designed as a two-stage separator where first stage is used for production and separation of radioactive isotope beams and the second stage for particle identification. The target is placed at the focus F0 for particle production, while an achromatic wedge degrader is placed at the focus F1 for isotope separation (indicated in Fig. 9.1). The Beryllium was chosen for the target as a good compromise between high production cross section and small energy loss and small straggling as well. The Be target can be produced very homogeneously and has the highest melting points of all light metals and the best heat dissipation characteristics. In order to maximise the production rate of the fragments of interest, the optimal target thickness was simulated using the LISE++ [81]. By increasing the target thickness, the production rate of fragment increases, but also its momentum distribution becomes wider decreasing therefore the transmission through the separator. Secondary reactions in the target also increase with the thickness and therefore their contribution to the production rate was also included.

The ions produced in fragmentation using 345 MeV/u beam are not always fully

Table 9.1: *Experimental charge state distributions of ^{124}Xe for both target thicknesses, compared with calculated charge state distributions using GLOBAL code [131].*

Target		CS 54^{+} [%]	CS 53^{+} [%]
4 mm Be	GLOBAL	86.7	13.0
	experiment	83.9	11.0
8 mm Be +	GLOBAL	81.9	17.3
0.2 mm W	GLOBAL	64.1	31.6
0.2 mm W	experiment	63.0	24.5

stripped. For the estimation of the charge state distribution the program GLOBAL [131] based on the parametrisation of charge-changing cross-section was used. For the optimal transmission of ^{100}Sn through the spectrometer, the magnetic rigidity (Bρ) of the dipoles should be set on one charge state of ^{100}Sn, and therefore those ^{100}Sn nuclei produced with other charge states are lost. The number of contaminants (detected reaction products that are not of interest) also increases with a target thickness. The total counting rate of nuclei detected at the final focal plane should be kept as low as possible (not to "blind" the detector at the final focal plane) but ensuring at the same time the highest counting rate of ^{100}Sn.

Based on the above-mentioned criteria and mechanisms, two different thicknesses of Be were chosen for the test experiment. One is a 4 mm Be target, while the other is 8 mm thick with a 0.2 mm W foil.

In the setting with 8 mm thick Be target, a W foil is used to increase the number of ^{100}Sn^{49+} ions produced by transfer of one electron to fully stripped ^{100}Sn ions produced after the Be target. By setting the $B\rho$ of the first dipole for ^{100}Sn^{49+} (other dipoles to ^{100}Sn^{50+}) the first main selection of contaminants produced at target is obtained. In this way, most of the $A/q = 2$ contaminants are rejected. Using the code GLOBAL [131] it was estimated that in the 8 mm Be target among the produced ^{100}Sn: 88.2% of them are fully stripped ^{100}Sn^{50+} ions, while 11.4% of ^{100}Sn are with charge state 49+. If the stripper foil is introduced after the target 72.2% of ^{100}Sn are calculated to be fully stripped, while 25.2% of ^{100}Sn have a charge state of 49+. Although, the fully stripped ions ^{100}Sn^{50+} are produced 8 times more than ^{100}Sn^{49+} ions, due to the strong selection of contaminants in the first dipole, configuration with the thick target and W foil should be investigated. The measured charge state distributions of ^{124}Xe, for both target thicknesses are compared with the calculated ones using the code GLOBAL. A good agreement is obtained, as shown in Table 9.1.

Magnetic dipoles cannot separate different isotopes with the same A/Z ratio according to the formula:

$$B\rho = \frac{A/Q\beta\gamma}{c} a.m.u. \tag{9.1}$$

where a.m.u. is the atomic mass unit, β is the ratio between velocity of fragment and the speed of light, while γ is the Lorentz factor defined as $\gamma = 1/\sqrt{1-\beta^2}$.

Therefore, besides $B\rho$ selection, for the further purification of the beam, a wedge should be used which exploits energy loss characteristics of the selected isotopes. The location of the wedge is at a dispersive plane of the separator, where the isotopes are dispersed in X according to their magnetic rigidity. Since the slowing down of the ions is roughly proportional to Z^2/v^2, different isotopes with different Z will have different velocities after passing through the degrader, which as the result will allow for a separation of nuclei with the same A/Z. The wedge is designed in a way that the position of a selected isotope in the focal plane is not changed after introducing the wedge (called achromatic wedge). The energy loss depends on the particle velocity and therefore for a higher velocity the wedge should be thicker. In the LISE++ program, the optimal wedge angle corresponds to the one that gives the narrowest spatial distribution of the selected nuclei. For the experiments with rare isotopes, the wedges are usually constructed from low Z materials in order to minimize the straggling. For this experiment we have used Al wedges that are common in BigRIPS experiments.

Achromatic wedges were placed in both the dispersive planes F1 and F5. During the optimization process, the choice of the optimal target and wedge thicknesses is done taking into account the range of the selected fragments, since they should stop in the middle of the implantation detector placed at the final focal plane F12 (for the test experiment, or F11 for the main experiment). For the energy loss the code ATIMA 1.2 [132] incorporated in LISE++ was used.

A one-day test was performed in order to optimize the settings of the in-flight separator BigRIPS [130] for the production and selection of ^{100}Sn. The following two different configurations were used:

- **configuration A:**
  Target: 4 mm Be at the F0 focal plane;
  Wedges: 3 mm Al located at F1 focal plane
  3 mm Al located at F5 focal plane

- **configuration B:**
  Target: 8.14 mm Be with 0.22 mm W foil at the F0 focal plane;
  Wedges: 1.4 mm Al located at F1 focal plane
  0.7 mm Al located at F5 focal plane

In Table 9.2 summary of the beam current intensities, the total measurement time and the live-time for three different settings are presented. The configuration with the 4 mm target was used with two different settings: more open slits and more closed slits in order to adjust the counting rate at the final focal plane. The beam intensity was calculated from the intensity monitor consisting of the three plastic scintillators placed at the F0 focal plane.

Table 9.2: *Summary of the beam intensities for each configuration*

Configuration description	Run numbers	Beam intensity [pnA]	Live - time	Total measurement time [h]
4 mm target (open slits)	150-151	9.9	0.80	3.59
4 mm target (closed slits)	152-157	9.0	0.97	4.94
8 mm target (closed slits)	166-174	9.0	0.95	6.49

9.2 Particle identification

Nuclei around ^{100}Sn were produced in the fragmentation of a 343.96 MeV/nucleon ^{124}Xe^{52+} beam with an intensity of $\sim$ 9 pnA impinging on a Be target.

The particle identification (PID) is performed in the second stage of BigRIPS separator. It is made on an event-by-event basis using the focal plane detectors of the BigRIPS with the standard $TOF - \Delta E - B\rho$ method.

Standard beam line detectors were used such as follows:

at F3 focal plane: two PPACs, plastic scintillator;

at F5 focal plane: two PPACs;

at F7 focal plane: two PPACs, plastic scintillator, ionisation chamber;

at F12 focal plane: two PPACs, plastic scintillator;

At the final focal plane F12, the particles were implanted and energy measured by silicon strip detectors surrounded by a Ge array used for γ-ray detection. In Fig. 9.1 the BigRIPS separator with indicated positions of target, wedges and beam line detectors is schematically presented.

The time of flight (TOF) is measured between two plastic scintillators placed at the F3 and F7 focal planes. The energy loss (ΔE) is measured with multi-sampling ionisation chamber (MUSIC) [133] placed at the F7 focal plane. From the two parallel plate avalanche counters (PPACs)[134] installed at F3, F5 and F7 the position and angle of the fragments are measured which, combined with ion-optics transfer matrices, give the $B\rho$ values.

Finally, from ΔE and TOF the atomic number Z is extracted, while from TOF and $B\rho$ the mass to charge ratio (A/Q) is determined. The particle identification matrix in the Z vs A/Q for the setting with a thick target, is shown on the upper part of Fig. 9.2.

In the setup with the thick target, around 70 % of all events originating from nuclei close to projectile, with ^{116}Xe and ^{117}Xe as the major contaminants. By checking the horizontal X space distribution of the ^{116}Xe and ^{117}Xe in each focal

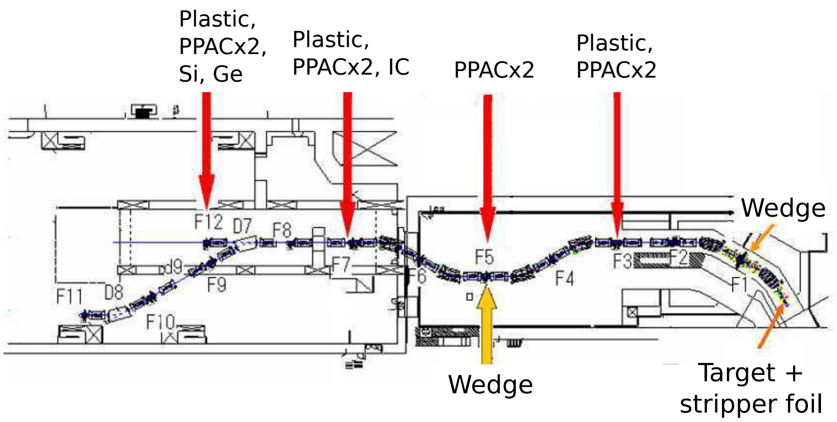

Figure 9.1: *Scheme of BigRIPS separator with indicated positions of target, wedges and beam-line detectors at each focal plane.*

plane, one can conclude that it will be difficult to exclude those contaminants without severely closing the slits.

In order to clean the particle identification plot and to reduce the background of miss identified nuclei, several different conditions were applied. First step was to gate on energy loss to select region of interest and to exclude nuclei close to projectile. Next step was to apply different cleaning conditions. The timing signal for each plastic scintillator is used to measure the horizontal and vertical positions for the same detector: those signals should be correlated. All events coming from the uncorrelated timing were excluded. The TOF between scintillators at F3 and F7 focal plane and TOF between scintillators at F7 and F12 were also compared. From the MUSIC ionisation chamber, 6 energy-loss signals were obtained. Each of those signals should be correlated with the other one. Another criterion for cleaning the particle identification spectra was the rejection of uncorrelated energy losses between MUSIC and the scintillators. The energy losses were checked for all scintillators installed at different focal planes. The correlations between magnetic rigidities measured between the F3 and F5 focal planes and the F5 and F7 were also checked. By applying gate around region of interest and all above-mentioned corrections, improved particle identification has been obtained (see the lower part of Fig. 9.2).

A confirmation of the identification in Z and A/Q was obtained by the observation of characteristic γ-lines of known isomers in ^{98}Cd and ^{96}Pd (Fig. 9.3). We were searching for delayed γ-lines in all identified nuclei. Time window was set between $0.2\mu s < t < 3\mu s$ after implantation of the nuclei. Besides known isomers in ^{98}Cd and ^{96}Pd, we did not find any indication for other isomers.

The particle identification plots around the ^{100}Sn region, for the 8 mm and 4 mm configurations with closed slits, after applying cleaning procedures are shown in Fig. 9.4. In the case of the 8 mm configuration, a much better separation of nuclei

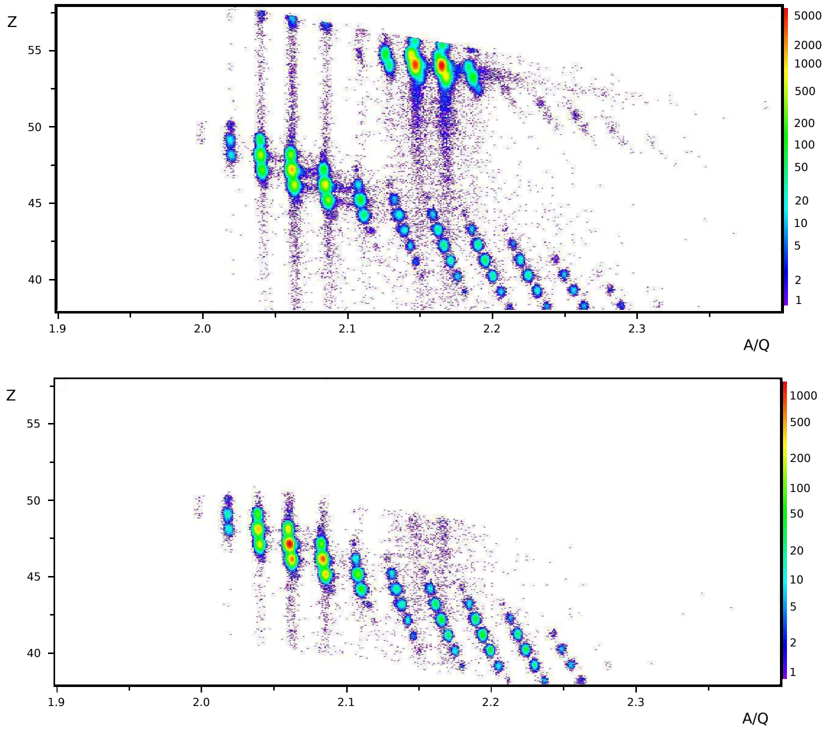

Figure 9.2: *Particle identification matrix in Z vs A/Q for configuration A: (top figure) without applied cleaning conditions (major contaminants consisting of nuclei close to the projectile are also shown) and (bottom figure) gated around isotopes of interest and applied cleaning conditions.*

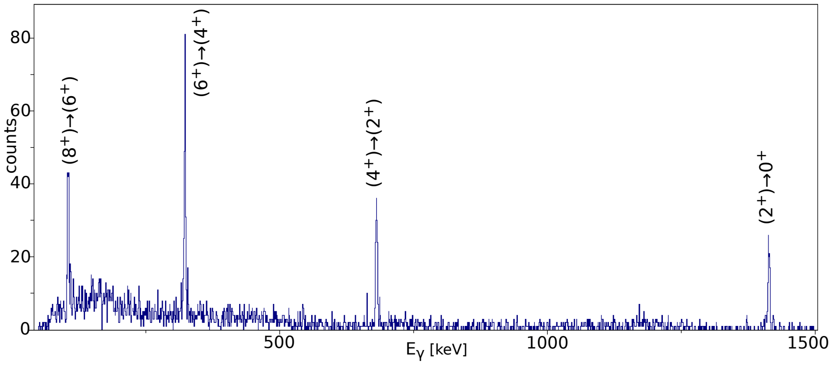

(a) *Delayed spectrum of* ^{96}Pd

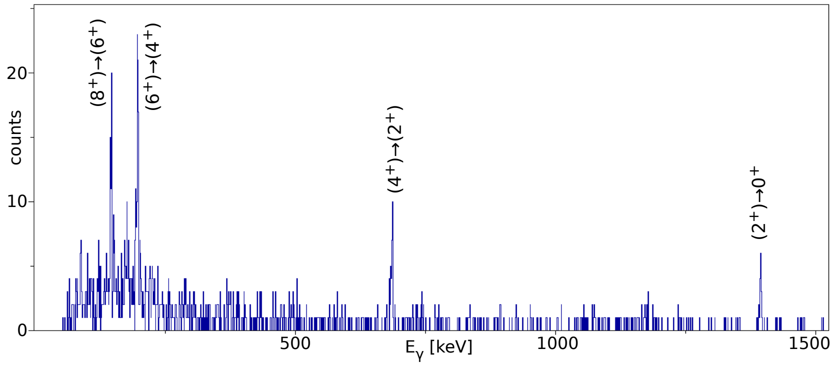

(b) *Delayed spectrum of* ^{98}Cd

Figure 9.3: *Delayed* γ *spectra of* ^{96}Pd *and* ^{98}Cd *from the 4 mm configuration, used for identification in Z and A/Q..*

was obtained than in the case of the 4 mm configuration.

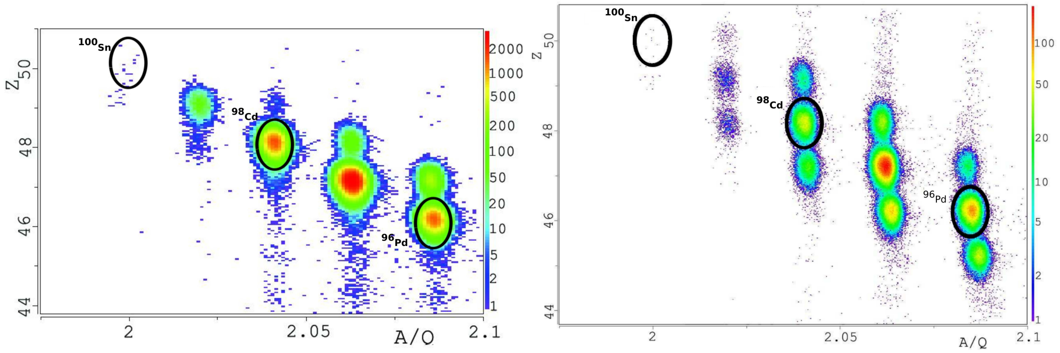

Figure 9.4: *Particle identification plot around the ^{100}Sn region, for configurations A (left hand side) and B (right hand side) after applying cleaning procedures. The ^{98}Cd and ^{96}Pd used for particle identification are indicated.*

The efficiency of all detectors was checked separately. The efficiency of the whole BigRIPS was calculated as a ratio between the raw 2D signals originating from the ionization chamber and time of flight, and the corresponding calibrated 2D spectra in Z and A/Q. Estimated efficiency was found to be 81% for 8 mm configuration and 92% for 4 mm configuration.

A good resolution in Z and A/Q was obtained for all nuclei. The resolutions in Z and A/Q for ^{98}Cd for configuration with 8 mm and 4 mm target respectively, were found to be:

$$\begin{aligned} \frac{\Delta Z}{Z} &= 4.4 \cdot 10^{-3} \qquad & \frac{\Delta(A/Q)}{A/Q} &= 7.5 \cdot 10^{-4} \\ \frac{\Delta Z}{Z} &= 4.4 \cdot 10^{-3} \qquad & \frac{\Delta(A/Q)}{A/Q} &= 9.4 \cdot 10^{-4} \end{aligned} \tag{9.2}$$

The obtained counting rate for all configurations are summarised in Table 9.3.

9.3 Production cross section

The production cross section of nuclei σ was estimated by the following formula:

$$\sigma = \frac{N_0}{\varepsilon_{lt}\varepsilon_d N_{atoms}\,[1/cm^2]\, I_0\,[pps]\, t\,[s]\, T} \tag{9.3}$$

where N_0 is the total number of selected nuclei, ε_{lt} is the lifetime for current setting, ε_d is the detection efficiency, N_{atoms} corresponds to the number of atoms per cm^2 for selected target, I$_0$ is the beam intensity, t is the total measurement time, and T is the transmission of the nuclei through the BigRIPS.

Table 9.3: *Counting rate based on the PID plot after applied cleaning conditions. All counting rates are normalised on the beam intensity of 10 pnA.*

Nuclide	8 mm target		4 mm open slits		4 mm closed slits	
	No. of counts from cleaned spectra	Counting rate [pps] scaled on 10 pnA	No. of counts from cleaned spectra	Counting rate [pps] scaled on 10 pnA	No. of counts from cleaned spectra	Counting rate [pps] scaled on 10 pnA
^{100}Sn	9	$4.3 \cdot 10^{-4}$	6	$4.3 \cdot 10^{-4}$	11	$6.9 \cdot 10^{-4}$
^{99}In	1267	0.060	3419	0.27	3972	0.25
^{98}Cd	30235	1.43	212908	16.6	108887	6.81
^{97}Ag	94451	4.47	1300894	101	259626	16.2
^{96}Pd	52523	2.48	1044604	81.4	102107	6.38
^{95}Rh	6998	0.33	152697	11.9	9950	36.6
total yield	1466279	69.4	3541047	276	585308	33.6
beam [pnA]	9.0		9.9		9.0	
time [h]	~ 6.5		~ 3.6		~ 3.6	

The uncertainty of the production cross section was estimated as a combined error originating from the statistical uncertainty (coming from the number of detected nuclei) and the uncertainty coming from the estimation of the transmission. The transmission is the only unmeasured parameter which we have to estimate in order to calculate the production cross section. The transmission was estimated as the mean value of the one calculated by Monte Carlo and Distribution Methods available in LISE++, while the error was estimated as a standard deviation between two transmissions.

In order to better estimate cross-section, the momentum distribution of the produced nuclei was measured and compared with a LISE++ simulation. In Fig. 9.5. the momentum distribution of the strongest contaminant ^{97}Ag measured in the 8 mm configuration setup is shown.

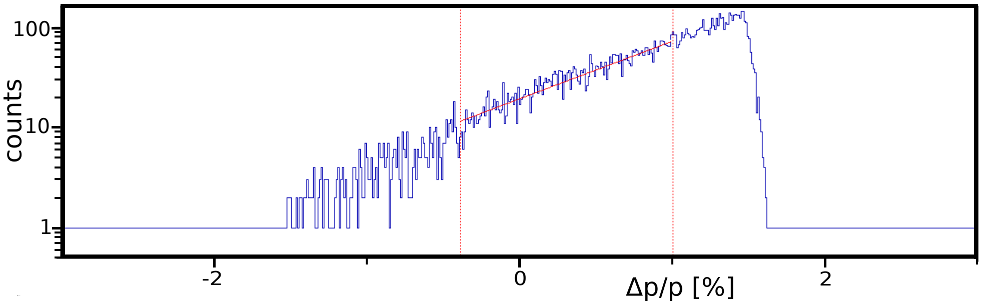

Figure 9.5: *Momentum distribution for ^{97}Ag measured in the setup with 8 mm target*

The momentum distribution was calculated with LISE++ using the Universal parametrisation [135] in which the final momentum distribution is obtained by the convolution of Gaussian distribution describing the shape of the prefragment momentum distribution and an exponential attenuation using the following formulas[135]:

$$\begin{aligned} f(p) \cong & exp\left(\frac{p}{\tau}\right)\left[1 - erf\left(\frac{p - p_0 + \sigma_{pf}^2/\tau - s\tau}{\sqrt{2}\sigma_{pf}}\right)\right] \\ \text{with} \quad & \tau = coef \cdot A_{PF} \cdot E_S/\beta \\ \text{and} \quad & \sigma_{pf}^2 = \beta\sigma_{conv}^2 A_{PF}(A - A_{PF})/(A_P - 1) \end{aligned} \tag{9.4}$$

where E_S is the surface energy of contact, A_{PF} is the mass number of the prefragment, β is the projectile velocity, $p0$ is the momentum of a final fragment while s, $coef$ and σ_{conv} are parameters fitted to the data [135].

In the 8 mm thick target configuration, a change of momentum $\Delta p/p = 1.5$ % corresponds to a change in yield of ^{97}Ag by 7.5 times. With the default parameter ($coef = 3$), momentum distribution is less steep compared to the experimental result and in order to adjust the slope, $coef$ should be set to 2.11. A similar procedure is applied for the 4 mm target configuration and coef factors should be changed to coef=1.48 in order to adjust the slope of the momentum distribution.

A simulation of the production rate in LISE++, was performed in order to estimate the charge state distribution for each nucleus at the final focal plane and therefore to estimate the amount of contaminants having the same A/Q as the nuclei of interest. The strongest channel was a fully stripped one, while charge state with Q = Z -1 can be neglected.

In the configuration with 8 mm Be target a W foil was included and therefore we have estimated a number of the nuclei of interest produced on the W foil. The estimate was performed with LISE++ assuming that only W foil exists as a target. The energy loss of the primary beam through the Be target was taken into account. The production rate of ^{100}Sn in the W foil was less than 3 % of the production rate obtained in the 8 mm Be target and thus its contribution was not taken into account.

After applying the above mentioned corrections to LISE++ configuration files, the transmission for all nuclei were calculated by the Monte Carlo and Distribution Methods. The transmission was estimated as the mean value of the one calculated by Monte Carlo and Distribution Method. Transmission was considered reliable if it was larger than 1 percent, but for the estimation of the production cross-section nuclei whose transmission was up to 0.01 percent were taken into account. For small transmissions, discrepancies between the Monte Carlo and Distribution methods are reaching few orders of magnitude. A summary of the production cross sections for nuclei whose separation was well established is presented in Table 9.4. The results are compared with the results from the GSI experiment [116] and with EPAX estimates (versions 2.15 [136] and 3.01 [137]) as well.

The production cross section for N=50 isotones are presented in Fig. 9.6 and compared with previous results and theoretical calculations.

A reasonable overall agreement between the measured cross-sections and the ones calculated using EPAX 2.15 and 3.01 was obtained although large discrepancies were found for some nuclei. For the ^{100}Sn, the measured production cross section on the 4 mm target was $(7.3 \pm 2.4) \cdot 10^{-10}$ mb using the Monte Carlo simulation and $(5.0 \pm 1.7) \cdot 10^{-10}$ mb using the Distribution Method. The obtained result is one order of magnitude smaller than the cross section estimated using EPAX 2.15 and 3.01 with $7.4 \cdot 10^{-9}$ and $5.8 \cdot 10^{-9}$ mb, respectively. In the fragmentation of a 1GeV/nucleon ^{124}Xe beam on 4008 mg/cm^2 Be target, the production cross-cross section was determined to be $(5.8 \pm 2.1) \cdot 10^{-9}$ mb [116]. The confirmation of our result is obtained by the excellent agreement with the experiment performed in RIKEN with the same configuration A analysed by H.Suzuki. In that experiment we have obtained $(7.4 \pm 1.7) \cdot 10^{-10}$ mb which nicely fits our data [138]. For the ^{100}Sn, the production cross-section for configuration with the 8 mm target was found to be $(1.5 \pm 0.6) \cdot 10^{-9}$ mb. Although the measured and estimated charge state of ^{124}Xe is in a good agreement for the fully stripped ion, for the charge state 53^+ estimated value differs around 30% from the measured charge state as shown in Table 9.1.

Table 9.4: *Transmission calculated by LISE++ and production cross-section obtained for configurations with 4 and 8 mm target thickness are presented. Results are compared with experimental results from experiment at GSI and with EPAX parametrisation ver. 2.15 and 3.01.*

Nuclide	8 mm target		4 mm target				
	mean transmission [%]	cross section [mb]	mean trasmission [%]	cross section [mb]	GSI experiment [mb]	EPAX 2.15 [mb]	EPAX 3.01 [mb]
^{100}Sn	5.7 ± 1.2	$(1.5 \pm 0.6) \cdot 10^{-9}$	42 ± 11	$(5.9 \pm 2.3) \cdot 10^{-10}$	$(5.8 \pm 2.1) \cdot 10^{-9}$	$7.4 \cdot 10^{-9}$	$5.8 \cdot 10^{-9}$
^{101}Sn	0.39 ± 0.30	$(3.9 \pm 3.0) \cdot 10^{-7}$			$(3.5 \pm 1.3) \cdot 10^{-7}$	$3.1 \cdot 10^{-7}$	$1.7 \cdot 10^{-7}$
^{98}In	4.3 ± 1.6	$(3.4 \pm 1.5) \cdot 10^{-9}$				$1.8 \cdot 10^{-8}$	$1.2 \cdot 10^{-8}$
^{99}In	3.3 ± 0.4	$(3.8 \pm 0.4) \cdot 10^{-7}$	16.4 ± 1.1	$(5.5 \pm 0.4) \cdot 10^{-7}$		$7.9 \cdot 10^{-7}$	$3.6 \cdot 10^{-8}$
^{100}In	$(2.42 \pm 0.03) \cdot 10^{-2}$	$(2.23 \pm 0.04) \cdot 10^{-4}$				$3.5 \cdot 10^{-5}$	$1.5 \cdot 10^{-5}$
^{97}Cd	(1.4 ± 0.9)	$(7.3 \pm 4.6) \cdot 10^{-7}$				$1.8 \cdot 10^{-6}$	$7.3 \cdot 10^{-7}$
^{98}Cd	0.3 ± 0.2	$(8.8 \pm 6.0) \cdot 10^{-5}$	0.60 ± 0.47	$(4.2 \pm 3.3) \cdot 10^{-4}$		$7.3 \cdot 10^{-5}$	$3.0 \cdot 10^{-5}$
^{96}Ag	(0.19 ± 0.16)	$(7.3 \pm 6.3) \cdot 10^{-5}$				$1.5 \cdot 10^{-4}$	$6.1 \cdot 10^{-5}$
^{97}Ag	0.034 ± 0.028	$(2.7 \pm 2.3) \cdot 10^{-3}$	0.011 ± 0.011	0.054 ± 0.055		$3.1 \cdot 10^{-3}$	$1.8 \cdot 10^{-3}$

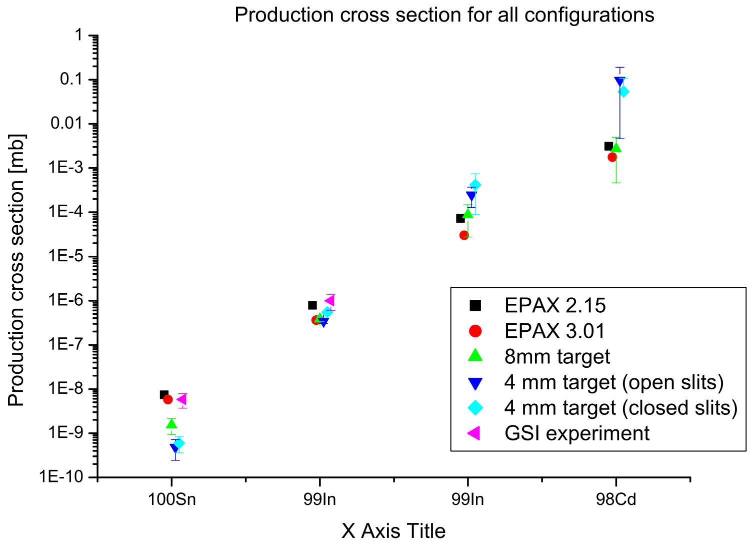

Figure 9.6: *Production cross-section compared with previous results and theoretical calculations*

Therefore, the estimated charge state distribution of ^{100}Sn (particularly for charge state 49^{+}) might be wrong, which could lead to wrong estimation of production rate (due to loss of events with different A/Q ratio) and therefore production cross section. Additional small effect can be due to the increased target thickness since it lead to increased secondary reactions produced in the thicker target.

9.4 Conclusion

A one-day test experiment was performed in order to optimize the settings of the BigRIPS separator for the ^{100}Sn production and selection. Two configurations with 4 mm thin Be target (configuration A) and 8 mm thick Be target with 0.2 mm W foil (configuration B) were used for careful evaluation. The counting rate of ^{100}Sn detected in the final focal plane, normalised to 10 pnA, was found to be 2.5 particles per hour for configuration A and 1.5 particles per hour for configuration B. In the case of 8 mm configuration, a much better separation of nuclei was obtained than in the case of 4 mm configuration. The major contaminants in the configuration A (around 70%) come from the nuclei close to projectile, which would be difficult to exclude without severely closing slits. From the above-mentioned results configuration A, with a thinner target is preferable to be used in the main ^{100}Sn experiment.

The cross-sections of nuclei around ^{100}Sn were measured. In order to estimate transmission through the BigRIPS separator, the slope of the momentum distribution was measured. It was found that measured tail of momentum distribution decreases faster than the one coming from the Universal parametrisation [135] used in LISE++ and the parameter $coef$ was set to adjust the slope with the experimental one. The transmission was estimated as an average of transmissions obtained using the Monte-Carlo and Distribution methods.

We have measured the cross-section of several nuclei produced around ^{100}Sn. Data are in fair agreement with the cross-sections estimated using EPAX 2.15 and 3.01. The ^{100}Sn production cross-section obtained with a 4 mm Be target is around one order of magnitude smaller than those estimated using EPAX 2.15 and 3.01 or measured using fragmentation of 1GeV/nucleon ^{124}Xe beam on 4008 mg/cm^2 thick Be target [116]. Our results are confirmed by the results of analysis of the independent measurement with the same setup [138]. The large discrepancy between measured ^{100}Sn production cross-section is not understood. One of the explanation might be that in the GSI experiment, with a much thicker target and higher beam energy [116], the production rate coming from the secondary reactions produced in the target is larger. This effect was checked using LISE++ code and calculations did not give any increase of production cross-section when production of secondary reactions in target was included. The increased cross-section that we obtain with 8 mm target compared to 4 mm target supporting assumption of influence of secondary reactions in target on total production rate, although existence of W foil in configuration B, makes the conclusion less straightforward. Therefore, in order to understand this discrepancy and the possible target thickness dependence, it would be interesting to perform a dedicated experiment to measure ^{100}Sn cross-section at various energies and using different target thicknesses.

In addition, we were searching for new μs isomers in all identified nuclei, but besides characteristic γ-lines of known isomers in ^{98}Cd and ^{96}Pd other isomeric states have not been observed.

10 The main ^{100}Sn experiment

The ^{100}Sn test experiment was performed in order to optimise the configuration settings of the BigRIPS separator for the production and selection of ^{100}Sn. This study has been used subsequently to set up our main ^{100}Sn experiment, which was dedicated to the measurement of the Gamow-Teller strength in the decay of ^{100}Sn to ^{100}In, to the mapping of the proton drip-line in the region of Te-Ru and to the study of short-lived isomeric states in this region of the nuclear chart. Nuclei around ^{100}Sn were produced by the fragmentation of a 345 MeV/nucleon ^{124}Xe^{52+} beam impinging a Be target. In the scope of this thesis, we search for new isotopes along the proton drip-line in the region of Te-Ru. In the first section of this chapter, the experimental setup will be described. In the second one, the particle identification will be presented with an emphasis on the identification of new isotopes.

10.1 Experimental setup

Based on the conclusions of the test experiment and the experience gained from recent experiments performed in RIKEN in the same region of nuclides, we decided to use the thin Be target for the main ^{100}Sn experiment with the following target-wedges configuration:

Target:	4 mm Be at the F0 focal plane;
Wedges:	3 mm Al located at F1 focal plane 2.2 mm Al located at F5 focal plane

A variable Al degrader which was not present during the test experiment, was placed at the final focal plane in order to adjust the range of produced nuclei of interest in the Si implantation detectors. The additional degrader thickness, compared to the test experiment, was compensated by a thinner wedge at F5.

The first stage of the BigRIPS separator was used for the production and separation of the fragments while the second stage was used for particle identification. The identification is performed on an event-by-event basis using the standard BigRIPS focal plane detectors with the $TOF - \Delta E - B\rho$ method. Similar detectors, as well as procedures for particle production, separation and identification were applied as for the ^{100}Sn test-experiment. From the two parallel plate avalanche counters

(PPACs)[134] installed at F3, F5 and F7, the positions and angle of fragments were measured which, together with ion-optics matrix elements gave trajectory reconstruction and Bρ values. Using the plastic scintillators placed at the F3 and F7 focal planes, the time of flight *TOF* was measured. At the final focal plane F11, corresponding to the end of the Zero-degree spectrometer, a multi-sampling ionisation chamber (MUSIC) [133] was used to measure the energy loss. Fig. 10.1 shows a schematic representation of the BigRIPS separator and Zero-degree spectrometer including the positions of target, wedges and detectors at each focal plane.

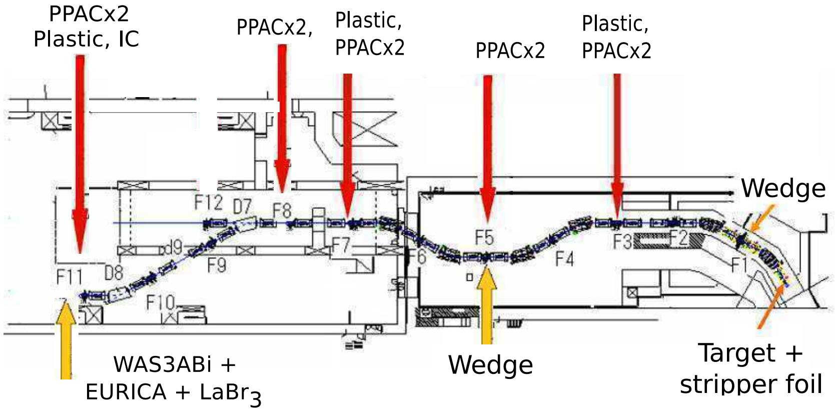

Figure 10.1: *Scheme of BigRIPS separator and Zero-degree spectrometer with all detectors indicated at different focal planes. The positions of target and wedges are also indicated.*

Due to the different goals of the test and the main ^{100}Sn experiments, different detector systems were needed. The requirements for the detection system at the final focal plane are discussed based on the physics goals that we intend to achieve.

For the main goal of the experiment which is the measurement of the Gamow-Teller strength in the decay of ^{100}Sn to ^{100}In, it was necessary to measure the lifetime of ^{100}Sn and the energy of the emitted positrons in the β^+ decay. In order to precisely measure the lifetime of ^{100}Sn and the neighbouring nuclei, we need to determine the position of the implanted ions with the high precision. This can be achieved with highly segmented detectors, providing good spatial resolution, correlated to the detectors measuring the decay. This technique also allows us to reduce random coincidences. For the measurement of the emitted positrons it is desired to have detectors that cover the solid angle as much as possible. In addition, detectors should be thick enough to measure the total energy of the positrons. Since their energy is expected to be up to 4-5 MeV, the Si detectors should be 8-10 mm thick. Following the β-decay, the excited daughter nuclei deexcite by γ emission. Providing enough statistics is acquired (hence large detection efficiency), γ-γ coincidences can be used to build the level scheme of the daughter nucleus.

In order to meet the above-mentioned requirements, the following detector setup at F11 was used: after a variable Al degrader used to adjust the implantation depth of the produced fragments, a 0.3 mm thick double sided silicon strip detector (DSSD) with 60 x 40 strips in X and Y directions respectively was used as an XY detector to provide the 2D position of the implanted nuclei. The XY detector was followed by 3 double-sided silicon strip detectors DSSSD called Wide-range Active Silicon-Strip Stopper Array for Beta and ion detection (WAS3ABi). Each DSSD is 1 mm thick and with the use of 3 WAS3ABi detectors, ^{100}Sn and neighbouring nuclei are stopped in the middle detector. Good spatial resolution is provided since each detector is highly segmented with 60 x 40 strips in X and Y direction, respectively. The implantation detectors were followed by a beta-calorimeter which consists of a stack of 10 single-sided silicon strip detectors (SSSSD) used to stop β-particles with 4-5 MeV energies, emitted from nuclei stopped in the implantation detector. Each SSSD detector is vertically segmented into 7 strips allowing therefore "β-tracking" and a reconstruction of total energy deposited in beta-absorbers. A schematic representation of the Si stack detectors placed at the final focal plane (F11) is shown in Fig. 10.2.

The γ-rays emitted after the decay of isomeric states in β-delayed γ emission in the excited daughter nucleus are detected using EURICA (EUroball RIken Cluster Array). The EURICA cluster detector, previously used as RISING at GSI, consists of 12 seven-element germanium cluster detectors. Compared to the previous spectroscopy experiments performed at RIKEN, EURICA provides a one order of magnitude higher detection efficiency for single γ-ray and two orders of magnitude for $\gamma - \gamma$ coincidences. In addition, 18 LaBr$_3$ detectors were installed in the space of missing cluster detectors.

10.2 Particle identification and identification of new isotopes

During the experiment, the BigRIPS separator was set to a few different configurations in order to achieve different goals. In one configuration BigRIPS was optimised for high purity of ^{100}Sn and the low counting rate at the final focal plane in order to reduce false correlations between the implantation of fragments and the decay of nuclei implanted in adjacent pixels. In another configuration, the slits of the BigRIPS were opened in such a way to optimise the transmission of more exotic nuclei, in order to search for the isotopes along the proton drip line in region from Te-Ru.

As it was already mentioned, the PID is performed on an event-by-event basis applying $TOF - \Delta E - B\rho$ method. From the ΔE and TOF atomic number Z is extracted, while from the TOF and $B\rho$, the mass to charge ratio (A/Q) is extracted. A confirmation of Z and A/Q identification was obtained by the observation of characteristic γ-lines of known isomers in ^{98}Cd and ^{96}Pd.

On the left-hand side of Fig. 10.3 the particle identification around ^{100}Sn, ob-

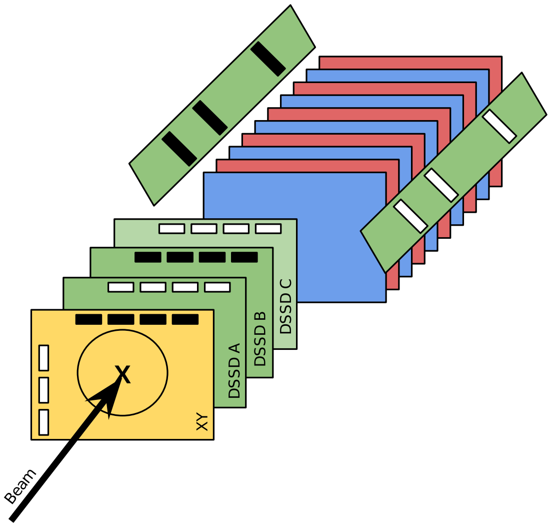

Figure 10.2: *Schematic representation of the WAS3ABi detector placed at the F11 focal plane showing the XY detector, followed by 3 DSSD WAS3ABi detectors for heavy ion implantation and a stack of 10 SSSSD used as beta-absorbers.*

tained for the full statistics is presented. The full statistics corresponds to the irradiation of the Be target with an average beam intensity of 1540 enA (29.6 pnA) during 203.2 hours. The lifetime of the BigRIPS data acquisition system was 98.2%. The solid line separates known isotopes located on the right side from "possibly" new ones located on the left side.

On the left-hand side of Fig. 10.4, we show the Z distribution obtained for N=Z nuclei, while on the right-hand side, the A/Q projection for Sn isotopes is presented. The Z and A/Q resolutions estimated for Sn isotopes were 0.41% and 0.09%, respectively. The separation of two neighbouring Z values was found to be 5σ, while the separation between adjacent A/Q peaks is 11σ. Therefore, a clear separation in A/Q has been achieved, while around 1.2 % of the events could be assigned the wrong Z value.

A possible contamination of the fully stripped nuclei identified at PID plot can come from the identification of lighter isotopes that are not fully stripped but have a similar A/Q value (i.e. fully stripped ^{100}Sn^{+50} and ^{98}Sn^{49+}). However, such kind of contamination for the most neutron deficient isotopes is not expected. Since the "new isotopes" (indicated in Fig. 10.3), are produced with a few counts, the detection of non-fully stripped nuclei having the same A/Q value (as the new isotopes) would mean production of even more neutron deficient nuclei, which is highly unlikely due to the much smaller production cross-section.

In order to check the consistency of the particle identification, various signals were checked. Several redundant signals from the PPACs, the plastic scintillators and the ionisation chambers allow us to apply different gates to clean the particle

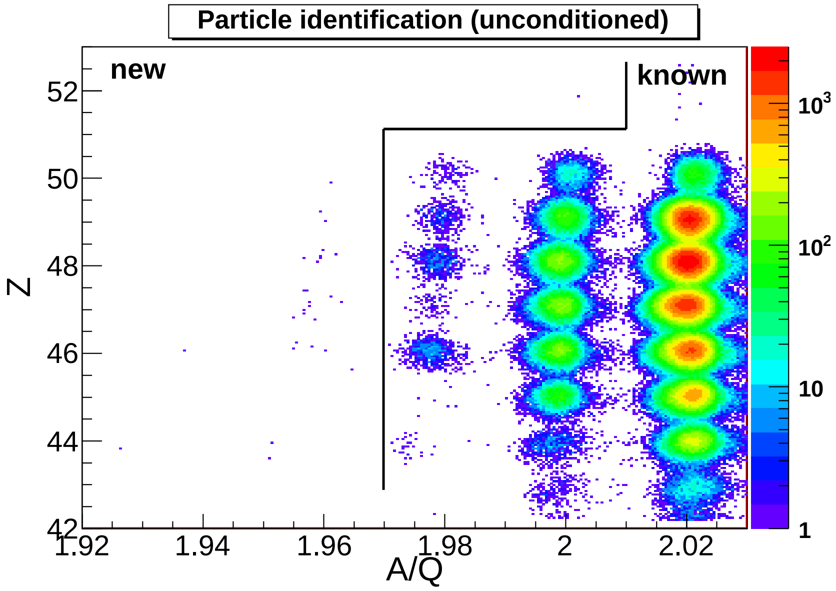

(a) *Unconditioned PID matrix*

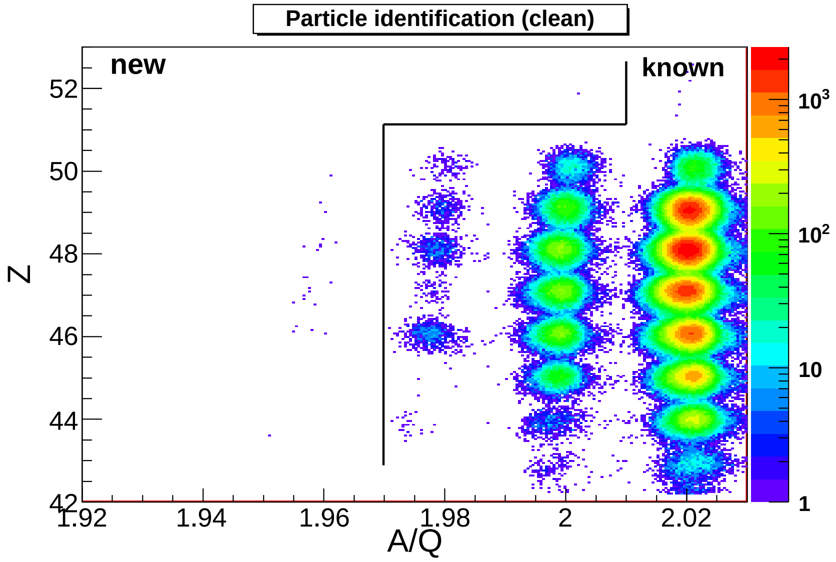

(b) *PID matrix with applied cleaning procedure*

Figure 10.3: *Particle identification matrices in Z vs A/Q plot around the* ^{100}Sn *without any cleaning conditions applied (Fig. a) and with applied cleaning procedures described in the text (Fig. b).*

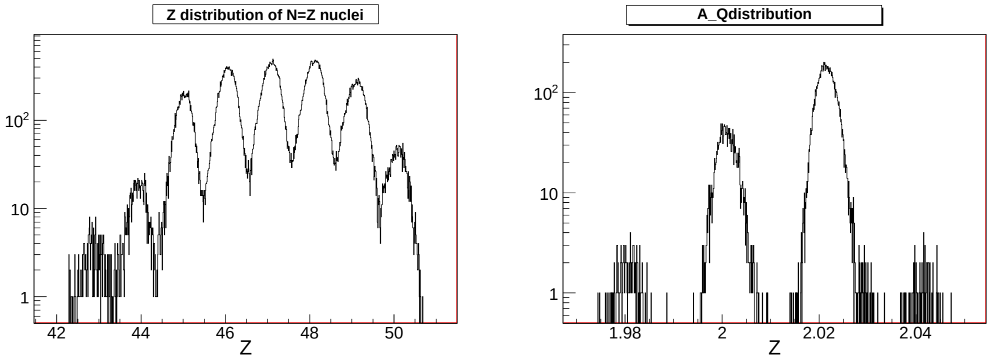

(a) *Z resolution of the N=Z nuclei*

(b) *A/Q resolution of the Sn isotopes*

Figure 10.4: *a) Z distribution obtained for N=Z nuclei and b) A/Q distribution measured for Sn isotopes*

identification plot, i.e. to reduce the background and possible miss-identification.

For the position measurements and trajectory reconstruction, the two double layer PPACs at F3, F5, F7 and F11 focal planes were used. Since each PPAC consists of 2 layers, it is possible to get two independent measurements of X and Y positions. The ADC signals coming from both layers should correlate since they measure the same position. This correlation was checked at each PPAC and uncorrelated events were rejected. Since the set-up did not have any dispersive elements in Y direction,we did not apply any "cleaning" conditions in Y position and angle in yz-plane. Although it is possible to estimate X position at each focal plane from only one layer out of 4 (2 PPACS at each focal plane), events in which position was measured from only one layer out of 4 were also rejected. Namely, in order to measure the angle in the xz-plane, it is necessary to have at least one signal coming from each PPAC. From the ADC values from each PPAC, it is possible to extract the position of the interaction at each focal plane. Another criterion to check consistency of the data was to compare whether the measured X position for each nucleus falls inside the slits of each focal plane or not.

A time was measured with plastic scintillators placed at F3, F5 and F7. Similarly to the PPACs, the correlation between the two signals coming from the same plastic was compared. The trigger of the BigRIPS data acquisition was the plastic scintillator at F7. Therefore, only signals from F3 and F11 were compared. An additional criteria condition applied to clean the PID matrix was the correlation between the TOFs measured between F3 - F7 and F7-F11 focal planes.

The ionisation chamber located at F11 consists of 6 segments. The energy loss is calculated from the averaged ADC signal coming from all 6 segments. The signals coming from each segment of the IC should be correlated and uncorrelated events were excluded.

If any of the above-mentioned criteria did not meet, the event was rejected. The cleaning procedures were applied for nuclei in the region of interest, located around ^{100}Sn.

Comparing the conditioned and unconditioned PID matrix presented in Fig. 10.3 one can noticed that some of the possible candidates for new isotopes have vanished after applying the cleaning procedure: the event potentially corresponding to ^{85}Ru has been rejected since the timing at F3 was not measured and therefore it was not possible to extract its TOF. The events assigned to ^{86}Ru and ^{89}Pd before cleaning conditions, have also been rejected since they do not have a reconstructed value of X position in one PPAC placed at F3, making it therefore impossible to reconstruct the trajectory of those nuclei. One ^{92}Ag nucleus has been rejected since its X position at different pairs of PPACs did not correlate.

In Table 10.1 are presented the remaining possible candidates for new isotopes, the number of detected nuclei and their average Z and A/Q value. For the sake of comparison, true values of A/Q are also indicated. The Z and A/Q values of all nuclei of interest are in good agreement with their expected value. The only discrepancy comes from Z value of ^{86}Ru whose point is around 2σ away from its expected value.

Table 10.1: *New isotopes identified. The number of nuclei in each isotope is indicated with their average Z and A/Q values.*

New Isotopes	No. of nuclei	A/Q	A/Q averaged	Z averaged
^{104}Te	1	2	2.002	51.86
^{98}Sn	1	2	2.001	50.06
^{96}In	2	1.959	1.960	49.13
^{94}Cd	6	1.958	1.959	48.2
^{92}Ag	9	1.957	1.957	47.1
^{90}Pd	4	1.957	1.958	46.15
^{86}Ru	1	1.955	1.951	43.6

Finally, we have discovered 3 new isotopes with more than 3 counts: ^{94}Cd, ^{92}Ag, ^{90}Pd. All measured signals of interest for each nucleus have a reasonable value and the assignment of these new isotopes is unambiguous. The rest of the nuclei are identified just with one count: ^{104}Te, ^{98}Sn or two counts: ^{96}In and therefore their assignment is tentative. One event, tentatively assigned to ^{86}Ru has been recently reported, although the results are still not published [138].

10.3 Conclusion

Based on the experience from the ^{100}Sn one-day test experiment and recent experiments performed in RIKEN, we have decided to use configuration with thin

Be target. In average, the ^{124}Xe beam intensity was 29.6 pnA over the 203.2 hours. Within this thesis, we searched for new isotopes along the proton drip-line in the region of Te-Ru. Possible candidates for new isotopes were carefully investigated by each relevant signal coming from different detectors: PPACs, plastics and ionisation chamber. We have succeeded to separate and identify 3 new isotopes with more than 3 counts for each. Those nuclei are ^{94}Cd, ^{92}Ag, ^{90}Pd. Moreover, we have tentatively assign a few other isotopes with just one or two counts: ^{104}Te, ^{98}Sn, ^{96}In and ^{86}Ru. A good resolution in Z and A/Q and clean PID matrix for nuclei with $N \leq Z$ makes these results reliable. In the same experiment, 2283 events of the ^{100}Sn were observed. This number is about 10 times higher than the number of ^{100}Sn nuclei produced in all previous experiments together. Full analysis of the decay data for ^{100}Sn and other neighbouring nuclei is going on in several laboratories participating in the ^{100}Sn experiment at RIBF.

11 Conclusion

In this document we have described the work we have performed in nuclear structure around magic/doubly-magic nuclei with three different topics: evolution of the collectivity in nuclei around ^{68}Ni; production and separation of proton-rich nuclei in the vicinity of the doubly-magic ^{100}Sn to search for new isotopes/isomers; and theoretical considerations of partial conservation of seniority in the $g_{9/2}$ orbital and its implications on single nucleon transfer reactions. In the following, we will summarize the main outcomes of each part.

In the first part, the structure of nuclei around ^{68}Ni has been investigated, as part of a series of experiments performed at GANIL in order to investigate the rapid change of collectivity in this mass region and the interplay between collective and single-particle degrees of freedom. For this study we focused first on the even neutron-rich Zn isotopes beyond N = 40. This has been done by measuring the lifetimes of the low-lying states above the 2^+ state using the plunger device and the recoil-distance Doppler-shift method. We then performed the spectroscopy of nuclei with one particle/hole outside N = 40 in order to probe properties like single-particle excitations, core polarisation and core coupled states in ^{69,71}Zn. The B(E2) values of low lying states measured in ^{68,70,72}Zn were compared with other experimental results and with theoretical models using beyond-mean-field [94, 95, 54] as well as shell model calculations with the JUN45 [53] and LNPS [39] interactions. The measured B(E2; $2^+ \rightarrow 0^+$) values for Zn isotopes are in agreement with the previous experiments performed using different techniques and types of reactions, as well as with shell model calculations. Conversely, the existing experimental data for B(E2; $4^+ \rightarrow 2^+$) are sparse and not always in agreement. In the case of ^{70}Zn, our value is much lower than a previous DSAM measurement and indicates a slight increase of collectivity giving a smooth evolution of B(E2; $4^+ \rightarrow 2^+$) values with N. The B(E2) value calculated with a JUN45 interaction is in agreement with our experimental data. For ^{72}Zn, our experimental B(E2) values for the $4^+ \rightarrow 2^+$ and $6^+ \rightarrow 4^+$ transitions are all consistent with the previous ones and nicely follows B(E2) trend obtained for lighter isotopes for the $4^+ \rightarrow 2^+$ transition.

The LNPS interaction nicely reproduces the energies of the first 2^+ and 4^+ states in Zn isotopes, while JUN45 systematically overestimates energies of those states for all N $\geq$ 40 isotopes. The measured B(E2; $2^+ \rightarrow 0^+$) and B(E2; $4^+ \rightarrow 2^+$) values increase starting from ^{68}Zn which is consistent with the shell model picture. On the one side, the proton occupancy of $f_{5/2}$ orbital increases from ^{68}Zn to ^{70}Zn and beyond. On the other side, by going from ^{68}Zn to ^{70}Zn, the neutron occupancy of $g_{9/2}$ orbital increases faster with the LNPS interaction as compared to JUN45, allowing the development of collectivity which nicely reproduces the observed decrease in energy of the 2^+ and 4^+ states and the increase of their B(E2) values. In addition, a larger valence space including the $d_{5/2}$ orbital (for LNPS interaction) additionally influence development of collectivity, and led to a nice agreement between the experimental data and the values calculated using the LNPS interaction.

The B(E2) ratios, $B_{42} = B(E2; 4^+ \rightarrow 2^+)/B(E2; 2^+ \rightarrow 0^+)$ obtained for ^{70}Zn and ^{72}Zn are close to 1 and below the value expected for the pure rotational object. Together with the nearly energy of the 2^+ state along the Zn isotopic chain and the evolution of B(E2) values as a function of angular momentum in ^{72}Zn, the measured B_{42} values seem to indicate that in Zn isotopes exhibit behavours which are compatible to systems that have seniority as a good quantum number. More detailed microscopic assessment is necessary to further shed a light on the nature of Zn isotopes.

With respect to odd nuclei, several new γ-rays for ^{69,71,73}Zn and ^{69}Cu were identified, but some unknown transitions could not be placed in the level schemes. Lifetimes or only upper limits have been measured for the first time in ^{69,71}Zn isotopes. The analysis of their nature indicates consistently an M1 dominant character and as a general statement, we conclude that the low-lying states in Zn isotopes with one particle/hole outside the N=40 shell exhibit both single-particle and collective nature.

In the second part of the thesis, partial conservation of seniority in the $g_{9/2}$ shell and its influence on one-particle transfer has been discussed. It was shown analytically that two 4^+ states and two 6^+ states predicted to be close in energy, should be differently excited in one- particle transfer. The spectroscopic amplitudes calculated using large scale shell model calculations indicate that it is not possible to populate 6^+ state with exact seniority in the $(g_{9/2})^4$ system by one particle transfer reaction from $9/2^+$ state in the $(g_{9/2})^3$ system. This work has been published [139].

With these predictions, we propose to perform one-particle transfer experiments in neutron rich nickel isotopes above N=40 and in the N=50 isotones from molybdenum to cadmium.

The third part of the thesis is dedicated to an experiment aiming at studying nuclei around the heaviest doubly-magic N=Z nucleus, ^{100}Sn. The full setting of the BigRIPS separator has been optimized during an test experiment. Results indicate the discrepancy between the cross section we deduced and the one obtained at higher energy at GSI and using EPAX calculations, an effect which might be attributed to the contribution of secondary reactions in the thicker target and higher beam energy at GSI. In order to understand this discrepancy, it would be interesting to perform a dedicated experiment to measure the ^{100}Sn production cross-section at various energies and using different target thicknesses. In the scope of this thesis, search for the new isotopes along the proton drip line have been investigated. From the main ^{100}Sn experiment, 3 new isotopes with more than 3 counts for each isotope has been identified. Those nuclei are ^{94}Cd, ^{92}Ag, ^{90}Pd. In addition 4 nuclei:^{104}Te, ^{98}Sn, ^{96}In and ^{86}Ru were tentatively assigned as new, since they were detected by only one or two counts. The discovery of those new isotopes, located along the drip lines gives an important input for testing nuclear mass models and consequently for better understanding of the astrophysical rp-process that goes close to the proton drip line.

In the same experiment 2283 events of ^{100}Sn were observed which is ten times larger than the number of ^{100}Sn nuclei detected in all previous experiments together. Full analysis of the decay data for ^{100}Sn and neighbouring nuclei is ongoing in several laboratories that participated in the ^{100}Sn experiment and will led to much improved spectroscopic data for the decay of ^{100}Sn and neighbouring nuclei.

12 Annex A: Electromagnetic transitions

Most of α, β decays and nuclear reactions leave the final nucleus in excited state. These states decay rapidly (unless the final state is isomeric) to the ground state by emission of one or more γ-rays. The interaction between a nucleus and an electromagnetic field is well known and therefore represents a direct way to obtain information about this nucleus. The electromagnetic transition between an initial state with angular momentum $J_i^{\pi_i}$ and a final state with angular momentum $J_f^{\pi_f}$ can take place if the emitted γ-ray carries angular momentum $\overrightarrow{L}$ with the condition: $\overrightarrow{J_f} = \overrightarrow{J_i} + \overrightarrow{L}$. This means that angular momentum of the emitted γ-ray is constrained by:

$$|J_i - J_f| \leq L \leq J_i + J_f \tag{12.1}$$

The L value determines the multipolarity of the transition. L=1 corresponds to dipole, L=2 to quadrupole, L=3 to octupole, etc. A L=0 transition is not the photon, which as a boson, has an intrinsic spin equal to one. Therefore γ-ray transition $0 \rightarrow 0$ is forbidden and this decay corresponds to the electron conversion or pair formation.

Transition has an electric character if $\pi_i \pi_f = (-1)^L$ or magnetic if $\pi_i \pi_f = (-1)^{L+1}$.

The probability that an excited state J_i de-excites to a lower lying state J_f by γ-ray with the multipolarity L is given by:

$$P(L; J_i \rightarrow J_f) = 8\pi \frac{L+1}{L\left[(2L+1)!!\right]^2} \frac{1}{\hbar} \left(\frac{E_\gamma}{\hbar c}\right)^{2L+1} B({}^E_M L; J_i \rightarrow J_f) \tag{12.2}$$

where EL and ML stands for electric and magnetic multipole and $B({}^E_M L; J_i \rightarrow J_f)$ is the reduced transition probability.

The reduced transition probability $B({}^E_M L; J_i \rightarrow J_f)$ is related to the nuclear matrix element of the corresponding multipole operator as:

$$B({}^E_M L; J_i \rightarrow J_f) = \sum_{M, M_f} |\langle J_f M_f | O({}^E_M L, M) | J_i M_i \rangle|^2 \tag{12.3}$$

representing a sum of the values of the transition operator $O(^E_M L, M)$ for a given initial state (J_i, M_i) over all final states (J_f, M_f).

By applying Wigner-Eckart theorem expression 12.3 reduces to:

$$B(^E_M L; J_i \rightarrow J_f) = \frac{1}{2J_i + 1} |\langle J_f | O(^E_M L) | J_i \rangle|^2 \tag{12.4}$$

assuming that initial states M_i are equally populated.

The reduced transition probabilities of the most important multipoles L calculated from the 12.2 formula are given below:

$$B(E1) = 6.3012 \cdot 10^{-16} E_\gamma^{-3} P(E1) \tag{12.5}$$

$$B(E2) = 8.1766 \cdot 10^{-10} E_\gamma^{-5} P(E2) \tag{12.6}$$

$$B(E3) = 1.755 \cdot 10^{-3} E_\gamma^{-7} P(E3) \tag{12.7}$$

$$B(M1) = 5.6211 \cdot 10^{-14} E_\gamma^{-3} P(M1) \tag{12.8}$$

$$B(M2) = 7.2939 \cdot 10^{-8} E_\gamma^{-5} P(M2) \tag{12.9}$$

$$B(M3) = 1.5657 \cdot 10^{-1} E_\gamma^{-7} P(M3) \tag{12.10}$$

where E_γ is expressed in MeV, the transition probability P is expressed in s^{-1}, the reduced transition probability B(EL) is in fm^{2L} while B(EL) in $\mu_N^2 fm^{2L-2}$ where $\mu_N^2 = \frac{e\hbar}{2Mc}$.

For the transitions that have the lowest multipolarity of electric type, the higher multipole is strongly suppressed, while for magnetic type $M(L)$ the next higher electric multipole $E(L+1)$ could be important. The most important case is the so-called $E2/M1$ mixing ratio.

Usually, the experimental reduced transition probabilities can be expressed in terms of matrix elements calculated for only one particle (Weisskopf units - W.u.)

$$B(^E_M L)[W.u.] = \frac{B(^E_M L)_{exp.}}{B_w(^E_M L)} \tag{12.11}$$

where single particle estimates are given with:

$$B_w(EL) = \frac{1}{4\pi} \left(\frac{3}{3+L} \right)^2 \left(1 - 2A^{1/3} \right)^{2L} \tag{12.12}$$

$$B_w(ML) = \frac{10}{\pi} \left(\frac{3}{3+L} \right)^2 \left(1 + 2A^{1/3} \right)^{2L+2} \tag{12.13}$$

This gives an indication on the transition strength and its collective or single-particle nature.

A Weisskopf single particle estimate for the lifetime as a function of mass number A and γ-ray energy E_γ for different transition multipolarities are given in following formulas:

$$\begin{aligned}
\tau(E1) &= (1.02 \cdot 10^{14} A^{2/3} E_\gamma^3)^{-1} \\
\tau(E2) &= (7.23 \cdot 10^{7} A^{4/3} E_\gamma^5)^{-1} \\
\tau(E3) &= (3.37 \cdot 10^{1} A^{2} E_\gamma^7)^{-1} \\
\tau(E4) &= (1.06 \cdot 10^{-5} A^{8/3} E_\gamma^9)^{-1} \\
\tau(M1) &= (3.12 \cdot 10^{13} E_\gamma^3)^{-1} \\
\tau(M2) &= (2.21 \cdot 10^{7} A^{2/3} E_\gamma^5)^{-1} \\
\tau(M3) &= (1.03 \cdot 10^{1} A^{4/3} E_\gamma^7)^{-1} \\
\tau(M4) &= (3.25 \cdot 10^{-6} A^{2} E_\gamma^9)^{-1}
\end{aligned} \tag{12.14}$$

13 Annex B: Seniority and particle transfer: detailes and proofs

In the second part of the thesis, in tables of spectroscopic factors, only the most important results were presented. In this annex, complete tables of spectroscopic amplitudes between 2 and 3 as well as 3 and 4 particle/hole system are given. Also, some of the important results that come from the shell model calculations are here given with a proof.

In Table 13 the spectroscopic amplitudes between two $9/2^+$ states of ^{75}Ni and 0^+, 2^+, 4^+, 6^+, 8^+ of ^{76}Ni, $\mathrm{S}((g_{9/2})^3 9/2^+; (g_{9/2})^2 J)$, obtained with the shell model calculations in $(1g_{9/2})^n$ are compared with the spectroscopic amplitudes calculated using equation (7.9).

From Table 13 one can noticed a few unexpected results of the single nucleon transfers:

$$\begin{aligned}
\left|\left\langle (g_{9/2})^4 0_2^+ \left\| a^+_{9/2} \right\| (g_{9/2})^3 9/2_1^+ \right\rangle\right| &= 0\\
\left|\left\langle (g_{9/2})^4 4_2^+ \left\| a^+_{9/2} \right\| (g_{9/2})^3 9/2_1^+ \right\rangle\right| &= 0\\
\left|\left\langle (g_{9/2})^4 6_2^+ \left\| a^+_{9/2} \right\| (g_{9/2})^3 9/2_1^+ \right\rangle\right| &= 0
\end{aligned} \tag{13.1}$$

and similarly

Table 13.1: *Spectroscopic amplitudes (SA) for transfer from the $9/2_1^+$ ground state and $9/2_2^+$ state of ^{75}Ni to several states in ^{76}Ni in a $(1g_{9/2})^n$ configuration and analytical calculations using 7.9 expression.*

^{75}Ni / ^{76}Ni	J = $9/2_1^+$		J = $9/2_2^+$	
J	$(1g_{9/2})^n$	analytical SA	$(1g_{9/2})^n$	analytical SA
0^+	2.826	2.828	-0.013	0
2^+	-0.709	-0.707	-0.441	-0.444
4^+	-0.702	-0.707	1.198	1.195
6^+	0.712	0.707	1.055	1.058
8^+	-0.706	-0.707	0.311	0.307

Table 13.2: *Spectroscopic amplitudes (SA) for transfer from the* $9/2_1^+$ *ground state and* $9/2_2^+$ *state of* ^{75}*Ni to several states in* ^{74}*Ni in the full space with regular* $pfg_{9/2}$ *interaction with neutrons blocked in* $f_{7/2}$ *and with blocking of proton* $g_{9/2}$ *orbital. Results are compared with analytical calculations using expression 7.9. Table cells marked with / correspond to cases in which analytical results were not calculated.*

SA		^{75}Ni, J = $9/2_1^+$, $\upsilon \approx 1$			^{75}Ni, J = $9/2_2^+$, $\upsilon \approx 3$		
^{74}Ni	seniority	$(1g_{9/2})^n$	full space	analytical SA	$(1g_{9/2})^n$	full space	analytical SA
J = 0_1^+	$\upsilon \approx 0$	0.632	0.559	0.632	0	0.031	0
J = 0_2^+	$\upsilon \approx 4$	0	0.146	0	0.632	0.462	0.632
J = 2_1^+	$\upsilon \approx 2$	0.865	0.671	0.866	0.183	0.356	0.181
J = 2_2^+	$\upsilon \approx 4$	0.003	0.374	0	0.377	0.596	0.376
J = 4_1^+	$\upsilon \approx 2$	1.165	0.843	1.162	0.6537	0.037	0.6545
J = 4_2^+	$\upsilon = 4$	0	0.632	0	0	0.411	/
J = 4_3^+	$\upsilon \approx 4$	0.005	0.050	/	0.658	0.424	/
J = 6_1^+	$\upsilon \approx 2$	1.393	1.327	1.396	0.698	0.225	0.697
J = 6_2^+	$\upsilon = 4$	0	0.039	0	0	0.010	/
J = 6_3^+	$\upsilon \approx 4$	0.0059	0.081	/	0.758	0.371	/
J = 8_1^+	$\upsilon \approx 2$	1.568	1.492	1.597	0.227	0.399	0.231
J = 8_2^+	$\upsilon \approx 4$	0.0052	0.0255	/	0.671	0.253	0.672

$$\begin{aligned}
&\left|\left\langle (g_{9/2})^4 0_1^+ \left\| a_{9/2}^+ \right\| (g_{9/2})^3 9/2_2^+ \right\rangle\right| = 0 \\
&\left|\left\langle (g_{9/2})^4 4_2^+ \left\| a_{9/2}^+ \right\| (g_{9/2})^3 9/2_2^+ \right\rangle\right| = 0 \\
&\left|\left\langle (g_{9/2})^4 6_2^+ \left\| a_{9/2}^+ \right\| (g_{9/2})^3 9/2_2^+ \right\rangle\right| = 0
\end{aligned} \tag{13.2}$$

13.1 Proof that $\left|\left\langle (g_{9/2})^4 0_2^+ \left\| a_{9/2}^+ \right\| (g_{9/2})^3 9/2_1^+ \right\rangle\right| = 0$

The $\left|(g_{9/2})^3 9/2_1^+\right\rangle$ and $\left|(g_{9/2})^3 9/2_2^+\right\rangle$ states can be expressed as a linear combination of states $9/2^+$ with exact seniority $\upsilon = 1$ and $\upsilon = 3$, i.e.

$$\begin{aligned}
\left|(g_{9/2})^3 9/2_1^+\right\rangle &= \alpha_3 \left|(g_{9/2})^3 \upsilon = 1, 9/2^+\right\rangle + \beta_3 \left|(g_{9/2})^3 \upsilon = 3, 9/2^+\right\rangle \\
\left|(g_{9/2})^3 9/2_2^+\right\rangle &= \beta_3 \left|(g_{9/2})^3 \upsilon = 1, 9/2^+\right\rangle - \alpha_3 \left|(g_{9/2})^3 \upsilon = 3, 9/2^+\right\rangle
\end{aligned} \tag{13.3}$$

In the same manner, 0^+ states can be described as:

$$\begin{aligned}
\left|(g_{9/2})^4 0_1^+\right\rangle &= \alpha_4 \left|(g_{9/2})^4 \upsilon = 0, 0^+\right\rangle + \beta_4 \left|(g_{9/2})^4 \upsilon = 4, 0^+\right\rangle \\
\left|(g_{9/2})^4 0_2^+\right\rangle &= \beta_4 \left|(g_{9/2})^4 \upsilon = 0, 0^+\right\rangle - \alpha_4 \left|(g_{9/2})^4 \upsilon = 4, 0^+\right\rangle
\end{aligned} \tag{13.4}$$

A single nucleon transfer $\left|\left\langle (g_{9/2})^4 0_2^+ \left\| a_{9/2}^+ \right\| (g_{9/2})^3 9/2_1^+ \right\rangle\right|$ expressed in the basis of states with exact seniority can be written as:

$$\begin{aligned} &\left|\left\langle \left(g_{9/2}\right)^4 0_2^+ \left\| a_{9/2}^+ \right\| \left(g_{9/2}\right)^3 9/2_1^+ \right\rangle\right| = \\ \alpha_3\beta_4 &\left[\left(g_{9/2}\right)^3 (\upsilon = 1, J_1 = 9/2) g_{9/2} J = 0 \,|\}\, \left(g_{9/2}\right)^4 \upsilon = 0, J = 0\right] - \\ \alpha_4\beta_3 &\left[\left(g_{9/2}\right)^3 (\upsilon = 3, J_1 = 9/2) g_{9/2} J = 0 \,|\}\, \left(g_{9/2}\right)^4 \upsilon = 4, J = 0\right] \end{aligned} \tag{13.5}$$

using the condition that particle creation operator $a_{9/2}^+$ changes seniority only by ± 1.

In order to estimate the mixing of seniorities (i.e. to obtain the $\alpha_3, \beta_3, \alpha_4, \beta_4$ coefficients) it is necessary to calculate the energy of the states and the off-diagonal matrix elements.

For the evaluation of energy of the n-particle system $\langle j^n\alpha; JM|V|j^n\alpha; JM\rangle$ we need to transform the n-particle matrix elements in a linear combination of two-body matrix elements $\langle j^2\alpha; J'M'|V|j^n\alpha; J'M'\rangle$ [8].

$$\langle j^n\alpha; JM \,|V|\, j^n\alpha; JM\rangle = \frac{n(n-1)}{2} \sum_{\alpha_2, J_2, J'} \left[j^{n-2}(\alpha_2 J_2) j^2(J') J \,|\}\, j^n \alpha J\right]^2 \left\langle j^2; J'M' \,|V|\, j^2; J'M'\right\rangle \tag{13.6}$$

where factor $\frac{n(n-1)}{2}$ originates from a two-body matrix operator $V = \sum_{i<k}^n V(i,k)$, since it can be expressed as an interaction by any of the two particles, i.e. V(n-1, n).

In the literature, the tables of CFPs are given for one particle. To calculate two-particle CFPs we express them in terms of one particle CFP's [8]:

$$\begin{aligned} \left[j^{n-2}(\alpha_1 J_1) j^2 (J_2) J \,\|\}\, j^n \alpha J\right] = \sum_{\alpha_1', J_1'} &\left[j^{n-2}(\alpha_1 J_1) j J_1' \,\|\}\, j^{n-1} \alpha_1' J_1'\right] \left[j^{n-1}(\alpha_1' J_1') j J \,\|\}\, j^n \alpha J\right] \\ &\sqrt{J_2+1}\sqrt{J_1'+1}(-1)^{2j+J+J_1} \left\{ \begin{array}{ccc} J_1 & j & J_1' \\ j & J & J_2 \end{array} \right\} \end{aligned} \tag{13.7}$$

where $\left\{ \begin{array}{ccc} J_1 & j & J_1' \\ j & J & J_2 \end{array} \right\}$ is Wigner 6j-symbol.

Using equations 13.6 and 13.7 to calculate the energy of the n-particle system, one obtains the following energies:

- Energies of 0^+ states and off-diagonal matrix elements in $(g_{9/2})^4$ system:

$$\begin{aligned} E\left(\left(g_{9/2}\right)^4 \upsilon=0, J=0\right) &= \frac{8}{5}\nu_0+\frac{1}{2}\nu_2+\frac{9}{10}\nu_4+\frac{13}{10}\nu_6+\frac{17}{10}\nu_8 \\ E\left(\left(g_{9/2}\right)^4 \upsilon=4, J=0\right) &= \frac{13}{66}\nu_2+\frac{735}{286}\nu_4+\frac{961}{330}\nu_6+\frac{459}{1430}\nu_8 \\ \varDelta V\left(\left(g_{9/2}\right)^4 \upsilon=0, \upsilon=4\right) &= \frac{-65\nu_2+315\nu_4-403\nu_6+153\nu_8}{10\sqrt{429}} \end{aligned} \tag{13.8}$$

- Energies of $9/2^+$ states and off-diagonal matrix elements in $(g_{9/2})^3$ system:

$$\begin{aligned} E_1\left(\left(g_{9/2}\right)^3 \upsilon=1, J=9/2\right) &= \frac{4}{5}\nu_0+\frac{1}{4}\nu_2+\frac{9}{20}\nu_4+\frac{13}{20}\nu_6+\frac{17}{20}\nu_8 \\ E_2\left(\left(g_{9/2}\right)^3 \upsilon=3, J=9/2\right) &= \frac{13}{132}\nu_2+\frac{735}{572}\nu_4+\frac{961}{660}\nu_6+\frac{459}{2860}\nu_8 \\ \varDelta V\left(\left(g_{9/2}\right)^3 \upsilon=1, \upsilon=3\right) &= \frac{-65\nu_2+315\nu_4-403\nu_6+153\nu_8}{20\sqrt{429}} \end{aligned} \tag{13.9}$$

Since the diagonal and off-diagonal matrix elements between 0^+ states in $(g_{9/2})^4$ system and $9/2^+$ states in $(g_{9/2})^3$ system differ exactly by two, by diagonalizing matrix elements:

$$\begin{bmatrix} E_1(\upsilon=1) & \varDelta V(\upsilon=1,\upsilon=3) \\ \varDelta V(\upsilon=1,\upsilon=3) & E_2(\upsilon=3) \end{bmatrix} \tag{13.10}$$

and

$$\begin{bmatrix} E_1(\upsilon=0) & \varDelta V(\upsilon=0,\upsilon=4) \\ \varDelta V(\upsilon=0,\upsilon=4) & E_2(\upsilon=4) \end{bmatrix} \tag{13.11}$$

one can calculate that $\alpha_3=\alpha_4$ and $\beta_3=\beta_4$. By substituting the obtained results to equation 13.5, both contributions cancel each other and finally

$$\left|\left\langle (g_{9/2})^4 0_2^+ \left\| a^+_{9/2} \right\| (g_{9/2})^3 9/2_1^+ \right\rangle\right| = 0 \tag{13.12}$$

confirming the results obtained by the shell model calculations.

13.2 Proof that $\left|\left\langle (g_{9/2})^4 4_2^+ \left\| a^+_{9/2} \right\| (g_{9/2})^3 9/2_1^+ \right\rangle\right| = 0$

In order to understand why is the transition between $9/2^+$ state in $(g_{9/2})^3$ system and 4^+ and 6^+ states with exact seniority in $(g_{9/2})^4$ system equal to 0, i.e. $\left|\left\langle (g_{9/2})^4 4_2^+ \left\| a^+_{9/2} \right\| (g_{9/2})^3 9/2_1^+ \right\rangle\right| = 0$ one can start by expressing $9/2^+$ and 4^+ (the same goes for 6^+) states in the basis of exact seniority:

$$\begin{aligned} \left|(g_{9/2})^3 9/2_1^+\right\rangle &= \alpha_3 \left|(g_{9/2})^3 \upsilon = 1, 9/2^+\right\rangle + \beta_3 \left|(g_{9/2})^3 \upsilon = 1, 9/2^+\right\rangle \\ \left|(g_{9/2})^4 4_2^+\right\rangle &= \left|(g_{9/2})^4 \upsilon = 4, 4^+\right\rangle \end{aligned} \tag{13.13}$$

and having in mind that $a^+_{9/2}$ changes seniority only by one, for one nucleon transfer reactions between the first of second $9/2^+$ state and 4^+ (or 6^+) state with exact seniority it can be obtained:

$$\left|\left\langle (g_{9/2})^4 4_2^+ \left\| a^+_{9/2} \right\| (g_{9/2})^3 9/2^+_1 \right\rangle\right| = \beta_3 \left[(g_{9/2})^3 (\upsilon = 3, J_1 = 9/2) g_{9/2} J = 4 \,|\}\, (g_{9/2})^4 \upsilon = 4, J = 4\right] \tag{13.14}$$

There are two 4^+ and 6^+ states with seniority $\upsilon \approx 4$ in the $(g_{9/2})^4$ system. In the tables of CFPs between systems of 3 and 4 particles in the $(g_{9/2})$ orbital [8], the values are given as a linear combination of CFPs for two 4^+ states. It is therefore not possible to take directly the CFP value between ($\upsilon = 3, J = 9/2^+$) state in $(g_{9/2})^3$ system and ($\upsilon = 4, J = 4^+$ or 6^+) in $(g_{9/2})^4$ system. One should instead write CFP involving the state with exact seniority as a linear combination of CFPs given in the table [8]. i.e.

$$\begin{aligned} &\left[(g_{9/2})^3 (\upsilon = 3, J_1 = 9/2) g_{9/2} J = 4 \,|\}\, (g_{9/2})^4 \upsilon = 4, J = 4\right] = \\ &= \mu_4 \left[(g_{9/2})^3 (\upsilon = 3, J_1 = 9/2) g_{9/2} J = 4 \,|\}\, (g_{9/2})^4 \upsilon = 4a, J = 4\right] + \\ &\nu_4 \left[(g_{9/2})^3 (\upsilon = 3, J_1 = 9/2) g_{9/2} J = 4 \,|\}\, (g_{9/2})^4 \upsilon = 4b, J = 4\right] \end{aligned} \tag{13.15}$$

By substituting values of CFPs from [8] into 13.15 one gets:

$$\left[(g_{9/2})^3 (\upsilon = 3, J_1 = 9/2) g_{9/2} J = 4 \,|\}\, (g_{9/2})^4 \upsilon = 4, J = 4\right] = \mu_4 \frac{8\sqrt{3 \cdot 7}}{11\sqrt{13 \cdot 23}} + \nu_4 \frac{-5\sqrt{5 \cdot 15}}{3 \cdot 11\sqrt{23}} \tag{13.16}$$

By diagonalizing matrix elements:

$$\begin{bmatrix} E_1(\upsilon = 4a) & \mathit{\Delta} V(\upsilon = 4a, \upsilon = 4b) \\ \mathit{\Delta} V(\upsilon = 4a, \upsilon = 4b) & E_2(\upsilon = 4b) \end{bmatrix} \tag{13.17}$$

where E_1, E_2 and $\mathit{\Delta} V$ are obtained by applying the 13.6 and 13.7 formulas:

$$\begin{aligned} E\left((g_{9/2})^4 \upsilon = 4a, J = 0\right) &= \frac{13172}{8349}\nu_2 + \frac{48275}{36179}\nu_4 + \frac{56339}{41745}\nu_6 + \frac{314466}{180895}\nu_8 \\ E\left((g_{9/2})^4 \upsilon = 4b, J = 0\right) &= \frac{23987}{25047}\nu_2 + \frac{4908}{2783}\nu_4 + \frac{246662}{125235}\nu_6 + \frac{18217}{13915}\nu_8 \\ \mathit{\Delta} V\left((g_{9/2})^4 \upsilon = 4a, \upsilon = 4b\right) &= \frac{8\sqrt{595}}{2783\sqrt{39}}(65\nu_2 - 45\nu_4 - 65\nu_6 + 45\nu_8) \end{aligned} \tag{13.18}$$

one will obtain μ_4 and ν_4 coefficients:

$$\mu_4 = \tfrac{5\sqrt{1105}}{24\sqrt{21}} \quad \nu_4 = 1 \tag{13.19}$$

And finally, by substituting μ_4 and ν_4 from 13.19 into 13.16 one gets:

$$\Big[(g_{9/2})^3(v = 3, J_1 = 9/2)g_{9/2}J = 4\,|\}\,(g_{9/2})^4 v = 4, J = 4\Big] = 0 \tag{13.20}$$

confirming that it is not possible to populate the 4^+ state with an exact seniority in the $(g_{9/2})^4$ system by transfer reaction from the $9/2^+$ state in the $(g_{9/2})^3$ system. The same result is obtained for the 6^+ state with exact seniority.

Bibliography

[1] N. Bohr. On the constitution of atoms and molecules. *Philosophical Magazine*, 26, 1913.

[2] Maria Goeppert Mayer. On closed shells in nuclei. ii. *Phys. Rev.*, 75:1969–1970, 1949.

[3] Otto Haxel, J. Hans D. Jensen, and Hans E. Suess. On the magic numbers in nuclear structure. *Phys. Rev.*, 75:1766–1766, 1949.

[4] Roger D. Woods and David S. Saxon. Diffuse surface optical model for nucleon-nuclei scattering. *Phys. Rev.*, 95:577–578, 1954.

[5] R. F. Casten. *Nuclear Structure from a Simple Perspective.* Oxford University Press, 1990.

[6] Marianne Dufour and Andrés P. Zuker. Realistic collective nuclear hamiltonian. *Phys. Rev. C*, 54:1641–1660, 1996.

[7] Giulio Racah. Theory of complex spectra. iii. *Phys. Rev.*, 63:367–382, 1943.

[8] Igal Talmi. *Simple Models of Complex Nuclei: The Shell Model and Interacting Boson Model.* Harwood Academic Publishers, 1993.

[9] S.G. Nilsson. Binding states of individual nucleons in strongly deformed nuclei. *Dan. Mat. Fys. Medd.*, 29(16):1, 1955.

[10] Aage Bohr and Ben R. Mottelson. *Nuclear structure: Nuclear deformations.* W.A. Benjamin, INC, 1975.

[11] B. Blank, M. Chartier, S. Czajkowski, J. Giovinazzo, M. S. Pravikoff, J.-C. Thomas, G. de France, F. de Oliveira Santos, M. Lewitowicz, C. Borcea, R. Grzywacz, Z. Janas, and M. Pfützner. Discovery of Doubly Magic ^{48}Ni. *Phys. Rev. Lett.*, 84:1116–1119, 2000.

[12] Ch. Engelmann, F. Ameil, P. Armbruster, M. Bernas, S. Czajkowski, Ph. Dessagne, C. Donzaud, H. Geissel, A. Heinz, Z. Janas, C. Kozhuharov, Ch. Miehé, G. Münzenberg, M. Pfützner, C. Röhl, W. Schwab, C. Stéphan, K. Sümmerer, L. Tassan-Got, and B. Voss. Production and identification

of heavy Ni isotopes: evidence for the doubly magic nucleus $^{78}_{28}$Ni. *Zeitschrift für Physik A Hadrons and Nuclei*, 352:351–352, 1995.

[13] M. Bernas, Ph. Dessagne, M. Langevin, J. Payet, F. Pougheon, and P. Roussel. Magic features of ^{68}Ni. *Physics Letters B*, 113(4):279 – 282, 1982.

[14] R. Broda, B. Fornal, W. Królas, T. Pawłat, D. Bazzacco, S. Lunardi, C. Rossi-Alvarez, R. Menegazzo, G. de Angelis, P. Bednarczyk, J. Rico, D. De Acuña, P. J. Daly, R. H. Mayer, M. Sferrazza, H. Grawe, K. H. Maier, and R. Schubart. N = 40 Neutron Subshell Closure in the ^{68}Ni Nucleus. *Phys. Rev. Lett.*, 74:868–871, 1995.

[15] O. Sorlin, S. Leenhardt, C. Donzaud, J. Duprat, F. Azaiez, F. Nowacki, H. Grawe, Zs. Dombrádi, F. Amorini, A. Astier, D. Baiborodin, M. Belleguic, C. Borcea, C. Bourgeois, D. M. Cullen, Z. Dlouhy, E. Dragulescu, M. Górska, S. Grévy, D. Guillemaud-Mueller, G. Hagemann, B. Herskind, J. Kiener, R. Lemmon, M. Lewitowicz, S. M. Lukyanov, P. Mayet, F. de Oliveira Santos, D. Pantalica, Yu.-E. Penionzhkevich, F. Pougheon, A. Poves, N. Redon, M. G. Saint-Laurent, J. A. Scarpaci, G. Sletten, M. Stanoiu, O. Tarasov, and Ch. Theisen. $^{68}_{28}$Ni$_{40}$: Magicity versus superfluidity. *Phys. Rev. Lett.*, 88:092501, 2002.

[16] C. Guénaut, G. Audi, D. Beck, K. Blaum, G. Bollen, P. Delahaye, F. Herfurth, A. Kellerbauer, H.-J. Kluge, J. Libert, D. Lunney, S. Schwarz, L. Schweikhard, and C. Yazidjian. High-precision mass measurements of nickel, copper, and gallium isotopes and the purported shell closure at N = 40. *Phys. Rev. C*, 75:044303, 2007.

[17] H. Grawe and M. Lewitowicz. Shell structure of nuclei far from stability. *Nuclear Physics A*, 693(1–2):116 – 132, 2001.

[18] K. L. Yurkewicz, D. Bazin, B. A. Brown, C. M. Campbell, J. A. Church, D. C. Dinca, A. Gade, T. Glasmacher, M. Honma, T. Mizusaki, W. F. Mueller, H. Olliver, T. Otsuka, L. A. Riley, and J. R. Terry. Nuclear structure in the vicinity of N=Z=28 ^{56}Ni. *Phys. Rev. C*, 70:054319, 2004.

[19] O. Perru, O. Sorlin, S. Franchoo, F. Azaiez, E. Bouchez, C. Bourgeois, A. Chatillon, J. M. Daugas, Z. Dlouhy, Zs. Dombrádi, C. Donzaud, L. Gaudefroy, H. Grawe, S. Grévy, D. Guillemaud-Mueller, F. Hammache, F. Ibrahim, Y. Le Coz, S. M. Lukyanov, I. Matea, J. Mrazek, F. Nowacki, Yu.-E. Penionzhkevich, F. de Oliveira Santos, F. Pougheon, M. G. Saint-Laurent, G. Sletten, M. Stanoiu, C. Stodel, Ch. Theisen, and D. Verney. Enhanced core polarization in ^{70}Ni and ^{74}Zn. *Phys. Rev. Lett.*, 96:232501, 2006.

[20] URL. http://www.nndc.bnl.gov/ensdf/.

[21] G. Audi, A.H. Wapstra, and C. Thibault. The Ame2003 atomic mass evaluation: (ii). tables, graphs and references. *Nuclear Physics A*, 729(1):337 – 676, 2003.

[22] H. Grawe, M. Górska, C. Fahlander, M. Palacz, F. Nowacki, E. Caurier, J.M. Daugas, M. Lewitowicz, M. Sawicka, R. Grzywacz, K. Rykaczewski, O. Sorlin, S. Leenhardt, and F. Azaiez. Experimental approach towards shell structure at ^{100}Sn and ^{78}Ni. *Nuclear Physics A*, 704(1–4):211 – 222, 2002.

[23] K. Langanke, J. Terasaki, F. Nowacki, D. J. Dean, and W. Nazarewicz. How magic is the magic ^{68}Ni nucleus? *Phys. Rev. C*, 67:044314, 2003.

[24] O. Kenn, K.-H. Speidel, R. Ernst, J. Gerber, P. Maier-Komor, and F. Nowacki. Measurements of g factors and lifetimes of low lying states in $^{58-64}$Ni and their shell model implications. *Phys. Rev. C*, 63:064306, 2001.

[25] O. Sorlin and M.-G. Porquet. Nuclear magic numbers: New features far from stability. *Progress in Particle and Nuclear Physics*, 61(2):602 – 673, 2008.

[26] M. Lewitowicz, J.M. Daugas, R. Grzywacz, L. Achouri, J.C. Angélique, D. Baiborodin, R. Bentida, R. Béraud, C. Bingham, C. Borcea, W. Catford, A. Emsallem, G. de France, M. Glogowski, H. Grawe, D. Guillemaud-Mueller, M. Houry, S. Hurskanen, K.L. Jones, R.C. Lemmon, A.C. Mueller, A. Nowak, F. de Oliveira-Santos, A. Płochocki, M. Pfützner, P.H. Regan, K. Rykaczewski, M.G. Saint-Laurent, J.E. Sauvestre, M. Sawicka, M. Schaefer, G. Sletten, O. Sorlin, M. Stanoiu, J. Szerypo, W. Trinder, S. Viteritti, and J. Winfield. Study of μs-isomers in neutron-rich nuclei around Z=28 and N=40 shell closures. *Nuclear Physics A*, 654(1, Supplement 1):687c – 690c, 1999.

[27] H. Mach, M. Lewitowicz, M. Stanoiu, F. Becker, J. Blomqvist, M.J.G. Berge, R. Boutami, B. Cederwall, Z. Dlouhy, B. Fogelberg, L.M. Fraile, G. Georgiev, H. Grawe, R. Grzywacz, P.I. Johansson, W. Klamra, S. Lukyanov, M. Mineva, J. Mrazek, G. Neyens, F. de Oliveira Santos, M. Pfützner, Yu.E. Penionzhkevich, E. Ramström, and M. Sawicka. Coupling of valence particles/holes to ^{68,70}Ni studied via measurements of the B(E2) strength in ^{67,69,70}Ni and ^{71}Cu. *Nuclear Physics A*, 719(0):C213 – C216, 2003.

[28] A. F. Lisetskiy, B. A. Brown, M. Horoi, and H. Grawe. New T = 1 effective interactions for the $f_{5/2}$ $p_{3/2}$ $p_{1/2}$ $g_{9/2}$ model space: Implications for valence-mirror symmetry and seniority isomers. *Phys. Rev. C*, 70:044314, 2004.

[29] S. Franchoo, M. Huyse, K. Kruglov, Y. Kudryavtsev, W. F. Mueller, R. Raabe, I. Reusen, P. Van Duppen, J. Van Roosbroeck, L. Vermeeren, A. Wöhr, K.-L. Kratz, B. Pfeiffer, and W. B. Walters. Beta decay of $^{68-74}$Ni and level structure of neutron-rich Cu isotopes. *Phys. Rev. Lett.*, 81:3100–3103, 1998.

[30] H. Grawe. *The Euroschool Lectures on Physics with Exotic Beams Vol. I*, chapter Shell Model from Partitioner's Point of View, page 33. Springer, Berlin-Heidelberg, 2004.

[31] N. A. Smirnova, A. De Maesschalck, A. Van Dyck, and K. Heyde. Shell-model description of monopole shift in neutron-rich Cu. *Phys. Rev. C*, 69:044306, 2004.

[32] Takaharu Otsuka, Toshio Suzuki, Rintaro Fujimoto, Hubert Grawe, and Yoshinori Akaishi. Evolution of nuclear shells due to the tensor force. *Phys. Rev. Lett.*, 95:232502, 2005.

[33] C. Mazzocchi, R. Grzywacz, J.C. Batchelder, C.R. Bingham, D. Fong, J.H. Hamilton, J.K. Hwang, M. Karny, W. Krolas, S.N. Liddick, A.F. Lisetskiy, A.C. Morton, P.F. Mantica, W.F. Mueller, K.P. Rykaczewski, M. Steiner, A. Stolz, and J.A. Winger. Low energy structure of even–even Ni isotopes close to ^{78}Ni. *Physics Letters B*, 622(1–2):45 – 54, 2005.

[34] M. Hannawald, T. Kautzsch, A. Wöhr, W. B. Walters, K.-L. Kratz, V. N. Fedoseyev, V. I. Mishin, W. Böhmer, B. Pfeiffer, V. Sebastian, Y. Jading, U. Köster, J. Lettry, H. L. Ravn, and the ISOLDE Collaboration. Decay of Neutron-Rich Mn Nuclides and Deformation of Heavy Fe Isotopes. *Phys. Rev. Lett.*, 82:1391–1394, 1999.

[35] P. Adrich, A. M. Amthor, D. Bazin, M. D. Bowen, B. A. Brown, C. M. Campbell, J. M. Cook, A. Gade, D. Galaviz, T. Glasmacher, S. McDaniel, D. Miller, A. Obertelli, Y. Shimbara, K. P. Siwek, J. A. Tostevin, and D. Weisshaar. In-beam γ-ray spectroscopy and inclusive two-proton knockout cross section measurements at N $\approx$ 40. *Phys. Rev. C*, 77:054306, 2008.

[36] J. Ljungvall, A. Görgen, A. Obertelli, W. Korten, E. Clément, G. de France, A. Bürger, J.-P. Delaroche, A. Dewald, A. Gadea, L. Gaudefroy, M. Girod, M. Hackstein, J. Libert, D. Mengoni, F. Nowacki, T. Pissulla, A. Poves, F. Recchia, M. Rejmund, W. Rother, E. Sahin, C. Schmitt, A. Shrivastava, K. Sieja, J. J. Valiente-Dobón, K. O. Zell, and M. Zielińska. Onset of collectivity in neutron-rich Fe isotopes: Toward a new island of inversion? *Phys. Rev. C*, 81:061301, 2010.

[37] W. Rother, A. Dewald, H. Iwasaki, S. M. Lenzi, K. Starosta, D. Bazin, T. Baugher, B. A. Brown, H. L. Crawford, C. Fransen, A. Gade, T. N. Ginter, T. Glasmacher, G. F. Grinyer, M. Hackstein, G. Ilie, J. Jolie, S. McDaniel, D. Miller, P. Petkov, Th. Pissulla, A. Ratkiewicz, C. A. Ur, P. Voss, K. A. Walsh, D. Weisshaar, and K.-O. Zell. Enhanced Quadrupole Collectivity at $N = 40$: The Case of Neutron-Rich Fe Isotopes. *Phys. Rev. Lett.*, 106:022502, 2011.

[38] S. Lunardi, S. M. Lenzi, F. Della Vedova, E. Farnea, A. Gadea, N. Mărginean, D. Bazzacco, S. Beghini, P. G. Bizzeti, A. M. Bizzeti-Sona, D. Bucurescu, L. Corradi, A. N. Deacon, G. de Angelis, E. Fioretto, S. J. Freeman, M. Ionescu-Bujor, A. Iordachescu, P. Mason, D. Mengoni, G. Montagnoli, D. R. Napoli, F. Nowacki, R. Orlandi, G. Pollarolo, F. Recchia, F. Scarlassara, J. F. Smith, A. M. Stefanini, S. Szilner, C. A. Ur, J. J. Valiente-Dobón, and B. J. Varley. Spectroscopy of neutron-rich Fe isotopes populated in the ^{64}Ni+^{238}U reaction. *Phys. Rev. C*, 76:034303, 2007.

[39] S. M. Lenzi, F. Nowacki, A. Poves, and K. Sieja. Island of inversion around ^{64}Cr. *Phys. Rev. C*, 82:054301, 2010.

[40] Yutaka Utsuno, Takaharu Otsuka, Takahiro Mizusaki, and Michio Honma. Varying shell gap and deformation in N$\sim$20 unstable nuclei studied by the Monte Carlo shell model. *Phys. Rev. C*, 60:054315, 1999.

[41] N. Hoteling, W. B. Walters, R. V. F. Janssens, R. Broda, M. P. Carpenter, B. Fornal, A. A. Hecht, M. Hjorth-Jensen, W. Królas, T. Lauritsen, T. Pawłat, D. Seweryniak, X. Wang, A. Wöhr, J. Wrzesiński, and S. Zhu. Yrast structure of ^{64}Fe. *Phys. Rev. C*, 74:064313, 2006.

[42] R. F. Casten and N. V. Zamfir. Valence correlation schemes and signatures of nuclear structure: A simple global phenomenology for $B(E2{:}2_1^+\rightarrow 0_1^+)$ values. *Phys. Rev. Lett.*, 70:402–405, 1993.

[43] O. Kenn, K.-H. Speidel, R. Ernst, S. Schielke, S. Wagner, J. Gerber, P. Maier-Komor, and F. Nowacki. Measurements of g factors and lifetimes of low-lying states in $^{62-70}$Zn and their shell model implication. *Phys. Rev. C*, 65:034308, 2002.

[44] J. Leske, K.-H. Speidel, S. Schielke, O. Kenn, D. Hohn, J. Gerber, and P. Maier-Komor. Experimental g factors and B(E2) values of $2_1^+, 4_1^+, 2_2^+$, and 3_1^- states in ^{64}Zn and ^{68}Zn compared to shell model predictions. *Phys. Rev. C*, 71:034303, 2005.

[45] J. Leske, K.-H. Speidel, S. Schielke, J. Gerber, P. Maier-Komor, T. Engeland, and M. Hjorth-Jensen. Dominant $(g_{9/2})^2$ neutron configuration in the 4_1^+ state of ^{68}Zn based on new g factor measurements. *Phys. Rev. C*, 72:044301, 2005.

[46] J. Leske, K.-H. Speidel, S. Schielke, J. Gerber, P. Maier-Komor, T. Engeland, and M. Hjorth-Jensen. Experimental g factor and B(E2) value of the 4_1^+ state in Coulomb-excited ^{66}Zn compared to shell-model predictions. *Phys. Rev. C*, 73:064305, 2006.

[47] D. Mücher, G. Gürdal, K.-H. Speidel, G. J. Kumbartzki, N. Benczer-Koller, S. J. Q. Robinson, Y. Y. Sharon, L. Zamick, A. F. Lisetskiy, R. J. Casperson, A. Heinz, B. Krieger, J. Leske, P. Maier-Komor, V. Werner, E. Williams,

and R. Winkler. Nuclear structure studies of ^{70}Zn from g-factor and lifetime measurements. *Phys. Rev. C*, 79:054310, 2009.

[48] E. Fiori, G. Georgiev, A. E. Stuchbery, A. Jungclaus, D. L. Balabanski, A. Blazhev, S. Cabaret, E. Clément, M. Danchev, J. M. Daugas, S. Grevy, M. Hass, V. Kumar, J. Leske, R. Lozeva, S. Lukyanov, T. J. Mertzimekis, V. Modamio, B. Mouginot, F. Nowacki, Yu. E. Penionzhkevich, L. Perrot, N. Pietralla, K. Sieja, K.-H. Speidel, I. Stefan, C. Stodel, J. C. Thomas, J. Walker, and K. O. Zell. First $g(2^+)$ measurement on neutron-rich ^{72}Zn, and the high-velocity transient field technique for radioactive heavy-ion beams. *Phys. Rev. C*, 85:034334, 2012.

[49] S. Leenhardt, O. Sorlin, M.G. Porquet, F. Azaiez, J.C. Angélique, M. Belleguic, C. Borcea, C. Bourgeois, J.M. Daugas, C. Donzaud, I. Deloncle, J. Duprat, A. Gillibert, S. Grévy, D. Guillemaud-Mueller, J. Kiener, M. Lewitowicz, S.M. Lukyanov, F. Marie, N.A. Orr, Yu.-E. Penionzhkevich, F. de Oliveira Santos, F. Pougheon, M.G. Saint-Laurent, W. Shuying, Yu. Sobolev, and J.S. Winfield. Coulomb excitation of $^{72}_{30}$Zn$_{42}$. *The European Physical Journal A - Hadrons and Nuclei*, 14:1–5, 2002.

[50] J. Van de Walle, F. Aksouh, T. Behrens, V. Bildstein, A. Blazhev, J. Cederkäll, E. Clément, T. E. Cocolios, T. Davinson, P. Delahaye, J. Eberth, A. Ekström, D. V. Fedorov, V. N. Fedosseev, L. M. Fraile, S. Franchoo, R. Gernhauser, G. Georgiev, D. Habs, K. Heyde, G. Huber, M. Huyse, F. Ibrahim, O. Ivanov, J. Iwanicki, J. Jolie, O. Kester, U. Köster, T. Kröll, R. Krücken, M. Lauer, A. F. Lisetskiy, R. Lutter, B. A. Marsh, P. Mayet, O. Niedermaier, M. Pantea, R. Raabe, P. Reiter, M. Sawicka, H. Scheit, G. Schrieder, D. Schwalm, M. D. Seliverstov, T. Sieber, G. Sletten, N. Smirnova, M. Stanoiu, I. Stefanescu, J.-C. Thomas, J. J. Valiente-Dobón, P. Van Duppen, D. Verney, D. Voulot, N. Warr, D. Weisshaar, F. Wenander, B. H. Wolf, and M. Zielińska. Low-energy Coulomb excitation of neutron-rich zinc isotopes. *Phys. Rev. C*, 79:014309, 2009.

[51] M. Niikura, B. Mouginot, S. Franchoo, I. Matea, I. Stefan, D. Verney, F. Azaiez, M. Assie, P. Bednarczyk, C. Borcea, A. Burger, G. Burgunder, A. Buta, L. Cáceres, E. Clément, L. Coquard, G. de Angelis, G. de France, F. de Oliveira Santos, A. Dewald, A. Dijon, Z. Dombradi, E. Fiori, C. Fransen, G. Friessner, L. Gaudefroy, G. Georgiev, S. Grévy, M. Hackstein, M. N. Harakeh, F. Ibrahim, O. Kamalou, M. Kmiecik, R. Lozeva, A. Maj, C. Mihai, O. Möller, S. Myalski, F. Negoita, D. Pantelica, L. Perrot, Th. Pissulla, F. Rotaru, W. Rother, J. A. Scarpaci, C. Stodel, J. C. Thomas, and P. Ujic. First direct lifetime measurement of the 2_1^+ state in ^{72,74}Zn: New evidence for a shape transition between $N = 40$ and $N = 42$ close to $Z = 28$. *Phys. Rev. C*, 85:054321, 2012.

[52] C. Louchart, A. Obertelli, A. Görgen, W. Korten, D. Bazzacco, B. Birkenbach, B. Bruyneel, E. Clément, P. J. Coleman-Smith, L. Corradi, D. Curien, G. de Angelis, G. de France, J.-P. Delaroche, A. Dewald, F. Didierjean, M. Doncel, G. Duchêne, J. Eberth, M. N. Erduran, E. Farnea, C. Finck, E. Fioretto, C. Fransen, A. Gadea, M. Girod, A. Gottardo, J. Grebosz, T. Habermann, M. Hackstein, T. Huyuk, J. Jolie, D. Judson, A. Jungclaus, N. Karkour, S. Klupp, R. Krücken, A. Kusoglu, S. M. Lenzi, J. Libert, J. Ljungvall, S. Lunardi, G. Maron, R. Menegazzo, D. Mengoni, C. Michelagnoli, B. Million, P. Molini, O. Möller, G. Montagnoli, D. Montanari, D. R. Napoli, R. Orlandi, G. Pollarolo, A. Prieto, A. Pullia, B. Quintana, F. Recchia, P. Reiter, D. Rosso, W. Rother, E. Sahin, M.-D. Salsac, F. Scarlassara, M. Schlarb, S. Siem, P. P. Singh, P.-A. Söderström, A. M. Stefanini, O. Stézowski, B. Sulignano, S. Szilner, Ch. Theisen, C. A. Ur, J. J. Valiente-Dobón, and M. Zielinska. Collective nature of low-lying excitations in ^{70,72,74}Zn from lifetime measurements using the AGATA spectrometer demonstrator. *Phys. Rev. C*, 87:054302, 2013.

[53] M. Honma, T. Otsuka, T. Mizusaki, and M. Hjorth-Jensen. New effective interaction for f_5pg_9-shell nuclei. *Phys. Rev. C*, 80:064323, 2009.

[54] J. P. Delaroche, M. Girod, J. Libert, H. Goutte, S. Hilaire, S. Péru, N. Pillet, and G. F. Bertsch. Structure of even-even nuclei using a mapped collective Hamiltonian and the D1S Gogny interaction. *Phys. Rev. C*, 81:014303, 2010.

[55] I. Stefanescu, G. Georgiev, D. L. Balabanski, N. Blasi, A. Blazhev, N. Bree, J. Cederkäll, T. E. Cocolios, T. Davinson, J. Diriken, J. Eberth, A. Ekström, D. Fedorov, V. N. Fedosseev, L. M. Fraile, S. Franchoo, K. Gladnishki, M. Huyse, O. Ivanov, V. Ivanov, J. Iwanicki, J. Jolie, T. Konstantinopoulos, Th. Kröll, R. Krücken, U. Köster, A. Lagoyannis, G. Lo Bianco, P. Maierbeck, B. A. Marsh, P. Napiorkowski, N. Patronis, D. Pauwels, G. Rainovski, P. Reiter, K. Riisager, M. Seliverstov, G. Sletten, J. Van de Walle, P. Van Duppen, D. Voulot, N. Warr, F. Wenander, and K. Wrzosek. Interplay between Single-Particle and Collective Effects in the Odd-A Cu Isotopes beyond $N = 40$. *Phys. Rev. Lett.*, 100:112502, 2008.

[56] K. T. Flanagan, P. Vingerhoets, M. Avgoulea, J. Billowes, M. L. Bissell, K. Blaum, B. Cheal, M. De Rydt, V. N. Fedosseev, D. H. Forest, Ch. Geppert, U. Köster, M. Kowalska, J. Krämer, K. L. Kratz, A. Krieger, E. Mané, B. A. Marsh, T. Materna, L. Mathieu, P. L. Molkanov, R. Neugart, G. Neyens, W. Nörtershäuser, M. D. Seliverstov, O. Serot, M. Schug, M. A. Sjoedin, J. R. Stone, N. J. Stone, H. H. Stroke, G. Tungate, D. T. Yordanov, and Yu. M. Volkov. Nuclear spins and magnetic moments of ^{71,73,75}Cu: Inversion of $\pi 2p_{3/2}$ and $\pi 1f_{5/2}$ levels in ^{75}Cu. *Phys. Rev. Lett.*, 103:142501, 2009.

[57] A.M Oros-Peusquens and P.F Mantica. Particle-core coupling around ^{68}Ni: a study of the subshell closure at N=40. *Nuclear Physics A*, 669(1–2):81 – 100, 2000.

[58] P. H. Regan, J. W. Arrison, U. J. Hüttmeier, and D. P. Balamuth. Yrast γ-ray spectroscopy of the neutron rich isotopes ^{61,63}Co. *Phys. Rev. C*, 54:1084–1097, 1996.

[59] D. Pauwels, O. Ivanov, N. Bree, J. Büscher, T. E. Cocolios, M. Huyse, Yu. Kudryavtsev, R. Raabe, M. Sawicka, J. Van de Walle, P. Van Duppen, A. Korgul, I. Stefanescu, A. A. Hecht, N. Hoteling, A. Wöhr, W. B. Walters, R. Broda, B. Fornal, W. Krolas, T. Pawlat, J. Wrzesinski, M. P. Carpenter, R. V. F. Janssens, T. Lauritsen, D. Seweryniak, S. Zhu, J. R. Stone, and X. Wang. Structure of ^{65,67}Co studied through the β decay of ^{65,67}Fe and a deep-inelastic reaction. *Phys. Rev. C*, 79:044309, 2009.

[60] A. Dijon, E. Clément, G. de France, P. Van Isacker, J. Ljungvall, A. Görgen, A. Obertelli, W. Korten, A. Dewald, A. Gadea, L. Gaudefroy, M. Hackstein, D. Mengoni, Th. Pissulla, F. Recchia, M. Rejmund, W. Rother, E. Sahin, C. Schmitt, A. Shrivastava, J. J. Valiente-Dobón, K. O. Zell, and M. Zielińska. Lifetime measurements in ^{63}Co and ^{65}Co. *Phys. Rev. C*, 83:064321, 2011.

[61] K. Alder, A. Bohr, T. Huus, B. Mottelson, and A. Winther. Study of nuclear structure by electromagnetic excitation with accelerated ions. *Rev. Mod. Phys.*, 28:432–542, 1956.

[62] H. Mach, R.L. Gill, and M. Moszyński. A method for picosecond lifetime measurements for neutron-rich nuclei: (1) outline of the method. *Nuclear Instruments and Methods in Physics Research Section A: Accelerators, Spectrometers, Detectors and Associated Equipment*, 280(1):49 – 72, 1989.

[63] A. Dewald, S. Harissopulos, and P. Brentano. The differential plunger and the differential decay curve method for the analysis of recoil distance Doppler-shift data. *Zeitschrift für Physik A Atomic Nuclei*, 334:163–175, 1989.

[64] J. Lindhard, M. Scharff, and H.E. Schiott. Range concepts and heavy ion ranges. *Matematisk-fysiske Meddelelser Det Kongelige Danske Videnskabernes Selskab*, 33(14):1–42, 1963.

[65] D. Mengoni, J.J. Valiente-Dobón, E. Farnea, A. Gadea, A. Dewald, and A. Latina. Lifetime measurements of neutron-rich nuclei around ^{48}Ca with the CLARA-PRISMA setup. *The European Physical Journal A*, 42(3):387–391, 2009.

[66] L.G. Moretto and R.P. Schmitt. Deep inelastic reactions: a probe of the collective properties of nuclear matter. *Rep. Prog. Phys.*, 44(5):533, 1981.

[67] R.Kaufmann and R. Wolfgang. Complex nucleon transfer reactions of heavy ions. *Phys. Rev. Lett.*, 3(5):232–234, 1959.

[68] J. Galin, D. Guerreau, M. Lefort, J. Peter, X. Tarrago, and R. Basile. Mechanism of single-nucleon and multi-nucleon transfer reactions in grazing collisions of heavy ions on silver. *Nuclear Physics A*, 159(2):461 – 480, 1970.

[69] H. Freiesleben and J.V. Kratz. NZ-equilibration and nucleon exchange in dissipative heavy-ion collisions. *Physics Reports*, 106(1-2):1–120, 1984.

[70] K.S. Krane. *Introductory Nuclear Physics*. John Wiley and Sons, New York, 1988.

[71] Patrick Regan. *Post Graduate Nuclear Experimental Techniques (4NET) Course Notes*. 2003.

[72] R. Broda, R. H. Mayer, I. G. Bearden, Ph. Benet, P. J. Daly, Z. W. Grabowski, M. P. Carpenter, R. V. F. Janssens, T. L. Khoo, T. Lauritsen, E. F. Moore, S. Lunardi, and J. Blomqvist. Yrast isomers in tin nuclei from heavy ion collisions and the $\nu h_{11/2}$ subshell filling. *Phys. Rev. Lett.*, 68:1671–1674, 1992.

[73] R. Broda. High-spin states in neutron-rich nuclei explored with deep-inelastic HI reactions. *Eur. Phys. J. A*, 1:1–4, 2002.

[74] S. Pullanhiotan, M. Rejmund, A. Navin, W. Mittig, and S. Bhattacharyya. Performance of VAMOS for reactions near the Coulomb barrier. *Nuclear Instruments and Methods in Physics Research Section A: Accelerators, Spectrometers, Detectors and Associated Equipment*, 593:343, 2008.

[75] Hervé Savajols. VAMOS: A variable mode high acceptance spectrometer for identifying reaction products induced by SPIRAL beams. *Nuclear Instruments and Methods in Physics Research Section B: Beam Interactions with Materials and Atoms*, 204(0):146 – 153, 2003.

[76] J. Simpson, F. Azaiez, G. de France, J. Fouan, J. Gerl, R. Julin, W. Korten, P.J. Nolan, B.M. Nyako, G. Sletten, P.M. Walker, and the EXOGAM Collaboration. The EXOGAM Array: A radioactive Beam Gamma-Ray Spectrometer. *Acta Physica Hungarica, New Series, Heavy Ion Physics*, 11:159–188, 2000.

[77] M. Rejmund, B. Lecornu, A. Navin, C. Schmitt, S. Damoy, O. Delaune, J.M. Enguerrand, G. Fremont, P. Gangnant, L. Gaudefroy, B. Jacquot, J. Pancin, S. Pullanhiotan, and C. Spitaels. Performance of the improved larger acceptance spectrometer: VAMOS++. *Nuclear Instruments and Methods in Physics Research Section A: Accelerators, Spectrometers, Detectors and Associated Equipment*, 646(1):184 – 191, 2011.

[78] Aurore Dijon. *Evolution de la collectivitè auotur du* ^{68}*Ni: rôle des états intrus*. PhD thesis, Université de Caen Basse Normandie, 2012.

[79] C. Schmitt, M. Rejmund, A. Navin, B. Lecornu, B. Jacquot, G. de France, A. Lemasson, A. Shrivastava, P. Greenlees, J. Uusitalo, K. Subotic, L. Gaudefroy, Ch. Theisen, B. Sulignano, O. Dorvaux, and L. Stuttgé. New gas-filled mode of the large-acceptance spectrometer VAMOS. *Nuclear Instruments and Methods in Physics Research Section A: Accelerators, Spectrometers, Detectors and Associated Equipment*, 621(1–3):558 – 565, 2010.

[80] A. Drouart, C. Mazur, Ph. Bourgeois, E. Bougamont, A. Gillibert, V. Lapoux, L. Nalpas, E.C. Pollacco, and M. Riallot. Very large emissive foil detectors for the tracking of low-energy heavy ions. *Nuclear Instruments and Methods in Physics Research Section A: Accelerators, Spectrometers, Detectors and Associated Equipment*, 579(3):1090 – 1095, 2007.

[81] O.B. Tarasov and D. Bazin. Lise++: Radioactive beam production with in-flight separators. *Nuclear Instruments and Methods in Physics Research Section B: Beam Interactions with Materials and Atoms*, 266(19–20):4657 – 4664, 2008.

[82] RADWARE. Software package for interactive graphical analysis of gamma-ray coincidence data. http://radware.phy.ornl.gov/download.html.

[83] J.K. Tuli. Nuclear Data Sheets for A = 70. *Nuclear Data Sheets*, 103(3):389 – 514, 2004.

[84] M. Rejmund, S. Bhattacharyya, A. Navin, W. Mittig, L. Gaudefroy, M. Gelin, G. Mukherjee, F. Rejmund, P. Roussel-Chomaz, and Ch. Theisen. Shell evolution and the N=34 “magic number”. *Phys. Rev. C*, 76:021304, 2007.

[85] D. von Ehrenstein and J. P. Schiffer. Study of the (d,p) Reactions on ^{64,66,68,70}Zn. *Phys. Rev.*, 164:1374–1385, 1967.

[86] M. Huhta, P. F. Mantica, D. W. Anthony, P. A. Lofy, J. I. Prisciandaro, R. M. Ronningen, M. Steiner, and W. B. Walters. New evidence for deformation in ^{73}Zn. *Phys. Rev. C*, 58:3187–3194, 1998.

[87] K. Takada and S. Tazaki. E0 transition and coupling between quadrupole and pairing-vibrational modes. *Nuclear Physics A*, 395(1):165 – 181, 1983.

[88] K. Sieja and F. Nowacki. Shell quenching in ^{78}Ni: A hint from the structure of neutron-rich copper isotopes. *Phys. Rev. C*, 81:061303, 2010.

[89] R.B. Firestone, V.S. Shirley, C.M. Baglin, S.Y.F. Chu, and Zipkin J. *Table of Isotopes, 8th Edition.* John Wiley & Sons, Inc., New York, 1999.

[90] E.A. McCutchan. Nuclear Data Sheets for A = 68. *Nuclear Data Sheets*, 113(6–7):1735 – 1870, 2012.

[91] B. Pritychenko, J. Choquette, M. Horoi, B. Karamy, and B. Singh. An update of the B(E2) evaluation for $0_1^+ \rightarrow 2_1^+$ transitions in even–even nuclei near N∼Z∼28. *Atomic Data and Nuclear Data Tables*, 98(4):798 – 811, 2012.

[92] K. P. Singh, D. C. Tayal, and H. S. Hans. Low-lying levels in Cu and Zn isotopes. *Phys. Rev. C*, 58:1980–1985, 1998.

[93] P.H. Stelson and F.K. McGowan. Coulomb excitation of the first 2^+ state of even nuclei with $58 \leq \mathrm{A} \leq 82$. *Nuclear Physics*, 32(0):652 – 668, 1962.

[94] J.F. Berger, M. Girod, and D. Gogny. Time-dependent quantum collective dynamics applied to nuclear fission. *Computer Physics Communications*, 63(1–3):365 – 374, 1991.

[95] J. Dechargé and D. Gogny. Hartree-Fock-Bogolyubov calculations with the D1S effective interaction on spherical nuclei. *Phys. Rev. C*, 21:1568–1593, 1980.

[96] T. Baugher, A. Gade, R. V. F. Janssens, S. M. Lenzi, D. Bazin, B. A. Brown, M. P. Carpenter, A. N. Deacon, S. J. Freeman, T. Glasmacher, G. F. Grinyer, F. G. Kondev, S. McDaniel, A. Poves, A. Ratkiewicz, E. A. McCutchan, D. K. Sharp, I. Stefanescu, K. A. Walsh, D. Weisshaar, and S. Zhu. Intermediate-energy Coulomb excitation of $^{58,60,62}\mathrm{C}r$: The onset of collectivity toward N = 40. *Phys. Rev. C*, 86:011305, 2012.

[97] R. B. Cakirli, R. F. Casten, J. Jolie, and N. Warr. Highly anomalous yrast B(E2) values and vibrational collectivity. *Phys. Rev. C*, 70:047302, 2004.

[98] M. Koizumi, A. Seki, Y. Toh, A. Osa, Y. Utsuno, A. Kimura, M. Oshima, T. Hayakawa, Y. Hatsukawa, J. Katakura, M. Matsuda, T. Shizuma, T. Czosnyka, M. Sugawara, T. Morikawa, and H. Kusakari. Multiple Coulomb excitation experiment of ^{68}Zn . *Nuclear Physics A*, 730(1–2):46 – 58, 2004.

[99] J. J. Ressler, R. F. Casten, N. V. Zamfir, C. W. Beausang, R B. Cakirli, H. Ai, H. Amro, M. A. Caprio, A. A. Hecht, A. Heinz, S. D. Langdown, E. A. McCutchan, D. A. Meyer, C. Plettner, P. H. Regan, M. J. S. Sciacchitano, and A. D. Yamamoto. Transition from the seniority regime to collective motion. *Phys. Rev. C*, 69:034317, 2004.

[100] E. Caurier and F. Nowacki. Present status of shell model techniques. *Acta Physica Polonica B*, 30:705–714, 1999.

[101] A. Escuderos and L. Zamick. Seniority conservation and seniority violation in the $g_{9/2}$ shell. *Phys. Rev. C*, 73:044302, 2006.

[102] D. J. Rowe and G. Rosensteel. Partially solvable pair-coupling models with seniority-conserving interactions. *Phys. Rev. Lett.*, 87:172501, 2001.

[103] G. Rosensteel and D. J. Rowe. Seniority-conserving forces and USp($2j + 1$) partial dynamical symmetry. *Phys. Rev. C*, 67:014303, 2003.

[104] P. Van Isacker and S. Heinze. Partial conservation of seniority and nuclear isomerism. *Phys. Rev. Lett.*, 100:052501, 2008.

[105] P. Van Isacker. Seniority isomers in nuclei. *Journal of Physics: Conference Series*, 322(1):012003, 2011.

[106] P. Van Isacker. Partial conservation of seniority in nuclei. *International Journal of Modern Physics E*, 20(02):191–198, 2011.

[107] C. J. Chiara, W. B. Walters, I. Stefanescu, M. Alcorta, M. P. Carpenter, B. Fornal, G. Gürdal, C. R. Hoffman, R. V. F. Janssens, B. P. Kay, F. G. Kondev, W. Królas, T. Lauritsen, C. J. Lister, E. A. McCutchan, T. Pawłat, A. M. Rogers, D. Seweryniak, N. Sharp, J. Wrzesiński, and S. Zhu. Seniority, collectivity, and B(E2) enhancement in ^{72}Ni. *Phys. Rev. C*, 84:037304, 2011.

[108] Peter E. Haustein. An overview of the 1986–1987 atomic mass predictions. *Atomic Data and Nuclear Data Tables*, 39(2):185 – 200, 1988.

[109] H. Grawe, M. Górska, M. Lipoglavšek, J. Nyberg, R. Grzywacz, M. Lewitowicz, K. Rykaczewski, K.H. Maier, and R. Schubart. High spin spectroscopy of exotic nuclei. *Progress in Particle and Nuclear Physics*, 38(0):15 – 27, 1997.

[110] H Grawe, R. Schubart, K. H. Maier, and D. Seweriniak. The shell model at ^{100}Sn-an experimental status report. *Physica Scripta*, T56:71–78, 1995.

[111] H. Grawe, M. Górska, M Lipoglavšek, C. Fahlander, J. Nyberg, A. Gadea, G. de Angelis, Z. Hu, and E. Roeckl. Nuclear structure near the doubly-magic ^{100}Sn. *AIP Conference Proceedings*, 481(1):177–186, 1999.

[112] A. de Shalit and I. Talmi. *Nuclear Shell Theory.* Academic Press, New York and London, 1963.

[113] A. Bobyk, W. Kamińsi, and I.N. Borzov. Gamow-Teller beta-decay strengths of neutron-deficient tin isotopes: Comparison of FFST and pnBCS + QRPA results. *Acta Physica Polonica B*, 31(953), 2000.

[114] T. Faestermann, R. Schneider, A. Stolz, K. Sümmerer, E. Wefers, J. Friese, H. Geissel, M. Hellström, P. Kienle, H.-J. Körner, M. Mineva, M. Münch, G. Münzenberg, C. Schlegel, K. Schmidt, P. Thirolf, H. Weick, and K. Zeitelhack. Decay studies of N $\approx$ Z nuclei from ^{72}Sr to ^{100}Sn. *The European Physical Journal A - Hadrons and Nuclei*, 15(1-2):185–188, 2002.

[115] R. Schneider, J. Friese, J. Reinhold, K. Zeitelhack, T. Faestermann, R. Gernhäuser, H. Gilg, F. Heine, J. Homolka, P. Kienle, H.J. Körner, H. Geissel, G. Münzenberg, and K. Sümmerer. Production and identification of ^{100}Sn. *Zeitschrift für Physik A Hadrons and Nuclei*, 348(4):241–242, 1994.

[116] C.B. Hinke, M. Böhmer, P. Boutachkov, T. Faestermann, H. Geissel, J. Gerl, R. Gernhauser, M. Gorska, A. Gottardo, H. Grawe, J. L. Grebosz, R. Krûcken, N. Kurz, Z. Liu, L. Maier, F. Nowacki, S. Piétri, Zs. Podolyak, K. Sieja, K. Steiger, K. Straub, H. Weick, P. J.Woods, N. Al-Dahan, N. Alkhomashi, A. Ataç, A. Blazhev, N. F. Braun, I. T.Cˇelikovic, T. Davinson, I. Dillmann, C. Domingo-Pardo, P. C. Doornenbal, G. De France, G. F. Farrelly, F. Farinon, N. Goel, T.C. Habermann, R. Hoischen, R. Janik, M. Karny, A. Kaskas, I.M. Kojouharov, Th. Kroll, Y. Litvinov, S. Myalski, F. Nebel, S. Nishimura, C. Nociforo, J. Nyberg, A. R. Parikh, A. Prochazka, P. H. Regan, C. Rigollet, H. Schaffner, C. Scheidenberger, S. Schwertel, P.-A. Soderstrom, S.J. Steer, A. Stolz, and P. Strmen. Superallowed Gamow-Teller decay of the doubly magic nucleus ^{100}Sn. *Nature*, 486:341–345, 2012.

[117] L. Batist, M. Górska, H. Grawe, Z. Janas, M. Kavatsyuk, M. Karny, R. Kirchner, M. La Commara, I. Mukha, A. Plochocki, and E. Roeckl. Systematics of Gamow-Teller beta decay "Southeast" of ^{100}Sn. *The European Physical Journal A*, 46(1):45–53, 2010.

[118] C.B. Hinke. *Spectroscopy of the doubly magic nucleus* ^{100}Sn *and its decay.* PhD thesis, Technische Universität München, 2012.

[119] A. Brown and K. Rykaczewski. Gamow-Teller strength in the region of ^{100}Sn. *Phys. Rev. C*, 50:R2270–R2273, 1994.

[120] P.G. Hansen and J.A. Tostevin. Direct reactions with exotic nuclei. *Annual Review of Nuclear and Particle Science*, 53:219–261, December 2003.

[121] T. Tachibana, M. Uno, M. Yamada, and S. Yamada. Empirical mass formula with proton-neutron interaction. *Atomic Data and Nuclear Data Tables*, 39(2):251 – 258.

[122] P. Moller, J.R. Nix, W.D. Myers, and W.J. Swiatecki. Nuclear ground-state masses and deformations. *Atomic Data and Nuclear Data Tables*, 59(2):185 – 381, 1995.

[123] S. Goriely, M. Samyn, P.-H. Heenen, J. M. Pearson, and F. Tondeur. Hartree-Fock mass formulas and extrapolation to new mass data. *Phys. Rev. C*, 66:024326, Aug 2002.

[124] M. Thoennessen. Reaching the limits of nuclear stability. *Rep. Prog. Phys.*, 67:1187–1232, 2004.

[125] M. Lewitowicz, R. Anne, G. Auger, D. Bazin, C. Borcea, V. Borrel, J.M. Corre, T. Dörfler, A. Fomichov, R. Grzywacz, D. Guillemaud-Mueller, R. Hue, M. Huyse, Z. Janas, H. Keller, S. Lukyanov, A.C. Mueller, Yu. Penionzhkevich, M. Pfützner, F. Pougheon, K. Rykaczewski, M.G. Saint-Laurent, K. Schmidt, W.D. Schmidt-Ott, O. Sorlin, J. Szerypo, O. Tarasov, J. Wauters, and

J. Żylicz. Identification of the doubly-magic nucleus ^{100}Sn in the reaction ^{112}Sn+^{nat}Ni at 63 MeV/nucleon. *Physics Letters B*, 332(1–2):20 – 24, 1994.

[126] M. Chartier, G. Auger, W. Mittig, A. Lépine-Szily, L. K. Fifield, J. M. Casandjian, M. Chabert, J. Fermé, A. Gillibert, M. Lewitowicz, M. Mac Cormick, M. H. Moscatello, O. H. Odland, N. A. Orr, G. Politi, C. Spitaels, and A. C. C. Villari. Mass Measurement of ^{100}Sn. *Phys. Rev. Lett.*, 77:2400–2403, 1996.

[127] M. Karny, L. Batist, A. Banu, F. Becker, A. Blazhev, K. Burkard, W. Brüchle, J. Döring, T. Faestermann, M. Górska, H. Grawe, Z. Janas, A. Jungclaus, M. Kavatsyuk, O. Kavatsyuk, R. Kirchner, M. La Commara, S. Mandal, C. Mazzocchi, K. Miernik, I. Mukha, S. Muralithar, C. Plettner, A. Płochocki, E. Roeckl, M. Romoli, K. Rykaczewski, M. Schädel, K. Schmidt, R. Schwengner, and J. Żylicz. Beta-decay studies near ^{100}Sn. *The European Physical Journal A - Hadrons and Nuclei*, 25(1):135–138, 2005.

[128] D. Bazin, F. Montes, A. Becerril, G. Lorusso, A. Amthor, T. Baumann, H. Crawford, A. Estrade, A. Gade, T. Ginter, C. J. Guess, M. Hausmann, G. W. Hitt, P. Mantica, M. Matos, R. Meharchand, K. Minamisono, G. Perdikakis, J. Pereira, J. Pinter, M. Portillo, H. Schatz, K. Smith, J. Stoker, A. Stolz, and R. G. T. Zegers. Production and β Decay of *rp*-Process Nuclei ^{96}Cd, ^{98}In, and ^{100}Sn. *Phys. Rev. Lett.*, 101:252501, 2008.

[129] K. Sümmerer, R. Schneider, T. Faestermann, J. Friese, H. Geissel, R. Gernhäuser, H. Gilg, F. Heine, J. Homolka, P. Kienle, H.J. Körner, G. Münzenberg, J. Reinhold, and K. Zeitelhack. Identification and decay spectroscopy of ^{100}Sn at the GSI projectile fragment separator FRS. *Nuclear Physics A*, 616(1–2):341 – 345, 1997.

[130] Toshiyuki Kubo. In-flight RI beam separator BigRIPS at RIKEN and elsewhere in Japan. *Nuclear Instruments and Methods in Physics Research Section B: Beam Interactions with Materials and Atoms*, 204(0):97 – 113, 2003.

[131] C Scheidenberger, Th Stöhlker, W.E Meyerhof, H Geissel, P.H Mokler, and B Blank. Charge states of relativistic heavy ions in matter. *Nuclear Instruments and Methods in Physics Research Section B: Beam Interactions with Materials and Atoms*, 142(4):441 – 462, 1998.

[132] H. Geissel, C. Scheidenberger, J. Kunzendorf P. Malzacher, and H. Weick. ATIMA code. http://web-docs.gsi.de/ weick/atima/. (unpublished).

[133] K. Kimura, T. Izumikawa, R. Koyama, T. Ohnishi, T. Ohtsubo, A. Ozawa, W. Shinozaki, T. Suzuki, M. Takahashi, I. Tanihata, T. Yamaguchi, and Y. Yamaguchi. High-rate particle identification of high-energy heavy ions using a tilted electrode gas ionization chamber. *Nuclear Instruments and Methods in Physics Research Section A: Accelerators, Spectrometers, Detectors and Associated Equipment*, 538(1–3):608 – 614, 2005.

[134] H. Kumagai, A. Ozawa, N. Fukuda, K. Sümmerer, and I. Tanihata. Delay-line PPAC for high-energy light ions. *Nuclear Instruments and Methods in Physics Research Section A: Accelerators, Spectrometers, Detectors and Associated Equipment*, 470(3):562 – 570, 2001.

[135] O. Tarasov. Analysis of momentum distributions of projectile fragmentation products. *Nuclear Physics A*, 734(0):536 – 540, 2004.

[136] K. Sümmerer and B. Blank. Modified empirical parametrization of fragmentation cross sections. *Phys. Rev. C*, 61:034607, 2000.

[137] K. Sümmerer. Improved empirical parametrization of fragmentation cross sections. *Phys. Rev. C*, 86:014601, 2012.

[138] H. Suzuki et al. Production cross section measurements of radioactive isotopes by BigRIPS separator at RIKEN RI Beam Factory (to be published).

[139] P. Van Isacker and I. Čeliković. The seniority quantum number in nuclei. In *Proc. XIV Int. Symp. on Capture Gamma-ray Spectroscopy and Related Topics*, pages 44–51, 2013.

List of Figures

2.1 The structure of the spherical mean field (Modified from Casten [5]). Starting from the left-hand side single particle energies (SPE) are presented for a simple harmonic oscillator, followed by the modification of SPE due to a surface-correction $\vec{l}^2$ term and a spin-orbit $\vec{l}\cdot\vec{s}$ term. 7

2.2 Systematics of B(E2) values as a function of fractional filling f=$\frac{n}{2j+1}$ of j orbital for seniority conserving transition (lower part) and in case when seniority is changed (upper part). n is the number of identical nucleons in the j orbital. 10

2.3 Nilsson diagram for Z $\leq$ 50. The abscissa is deformation parameter ε close to β. 13

2.4 The occupation of proton and neutron orbitals for ^{68}Ni 14

2.5 Systematics of the first 2^+ energies (upper figure), B(E2;$2^+ \rightarrow 0^+$) values (middle figure) and δ_{2n} in Ni isotopes. Data are taken from [18, 19, 20, 21] 15

2.6 Systematics of a) E(2^+_1) energies, b) B(E2; $2^+ \rightarrow 0^+$) values for even-even nuclei along several isotopic chain. In c) are presented scaled B(E2) values for Se and Kr isotopes and results of SM calculations with LNPS interaction. The figure is taken from [37]). 17

2.7 Systematics of the low-lying states in Zn isotopes. 18

2.8 Systematics of the experimental B(E2; $2^+ \rightarrow 0^+$) and B(E2; $4^+ \rightarrow 2^+$) values compared with several theoretical calculations. The figure is taken from [52]). 20

2.9 Systematics of: the energies of the $5/2^-$ and $1/2^-$ in $^{63-73}$Cu isotopes (top left figure), the energies of the $7/2^-$ in Cu isotopes and 2^+ state in Ni isotopes (top right figure). Systematics of the experimental B(E2) values for transitions from $5/2^-$ and $1/2^-$ to the $3/2^-$ ground state (bottom left figure) in $^{63-73}$Cu isotopes and the experimental B(E2) value for transition from $7/2^-$ to ground state in Cu isotopes with B(E2; $2^+ \rightarrow 0^+$) values in corresponding Ni isotopes. Figure is taken from [55]. 22

3.1 Schematic illustration of lifetime measurements using the RDDS method. v_1 and v_2 correspond to recoils velocities before and after the degrader placed at a distance d after the target. The corresponding peaks intensities are denoted I^s and I^u. The evolution of the peak intensity of the shifted (I^s) and unshifted (I^u) components as a function of the target-degrader distance is given in the case of ^{50}Ca [65]. 27
3.2 Photography of the Köln plunger device placed in the target chamber 29
3.3 Schematic representation of the experimental setup used. VAMOS spectrometer was set-up in dispersive mode and its focal plane detectors were used to identify recoiling nuclei. The segmented Ge clover detectors of the EXOGAM array were placed around the reaction chamber to detect prompt γ-rays. 31
3.4 Complete configuration of VAMOS spectrometer. 32
3.5 Mapping of silicon detectors. 35
3.6 Flow chart for particle identification. 37
3.7 Photo of a few clower detectors also showing the segmentation of the 4 crystals. 37
3.8 A scheme of the escape suppression shield. 38

4.1 Response of SED detector in X position to different pulse intensities before and after calibration. 40
4.2 Determination of X$_{ref}$ with 3 runs with U beam set on different charge states. The position where the distributions overlap corresponds to the reference position. 40
4.3 Linearity of response of a) IC pads and b) central Si detectors tested with pulse generator. 41
4.4 Calibration of TSED1_HF time of flight with a time calibrator: a) calibration of the TAC with a time interval of 10 ns b) check of the linearity of the TAC module. 42
4.5 The M/Q spectra of Zn isotopes, detected on the central Si detector, obtained with 2 different timings: a) TSED1_HF and b) TSi_HF. A clear separation of M/Q values was obtained with TSED1_HF signal contrary to TSi_HF signal. (The M/Q values were not aligned.) . . 44
4.6 M/Q distribution of Zn isotopes obtained for the central group of Si detectors. The M/Q distribution of Zn isotopes coming from the central Si detector is in a dark blue. The charge states that correspond to the M/Q peaks of ^{70}Zn are indicated. The peaks positioned on the right-hand side of those coming from ^{70}Zn correspond to ^{71}Zn nuclei with the same charge as for ^{70}Zn , while those peaks positioned on the left-hand side of ^{70}Zn correspond to M/Q value of ^{69}Zn. 46
4.7 M vs M/Q spectra 47
4.8 Z identification 48

4.9 Z vs A identification matrix obtained from all charge states and all Si detectors for one target-degrader distance. 49
4.10 a) Z and b) A distribution obtained from the Z vs A matrix. 49
4.11 Summary of events in which are detected all 4 coordinates in SED1 and SED2, events in which one of coordinates was not measured and events where 2 or more coordinates were missing. 50
4.12 Different γ spectra obtained from a ^{60}Co source for different corrections applied. 52
4.13 Relative efficiency of EXOGAM array obtained with a ^{152}Eu source. 53
4.14 A recoil nuclei vector and vector of emitted γ-ray are shown in spherical coordinate system. The origin is the target position and Oz is the beam axis at that origin. The indicated ψ angle is determined from the scalar products of those vectors. 54
4.15 The matrix of the Doppler uncorrected γ-ray energies that coincide with the ^{72}Zn nuclei as a function of the angle of emitted γ-ray are shown. The red dotted line shows the calculated γ-ray energy of the $2^+ \rightarrow 0^+$ transition of ^{72}Zn as a function of the angle between trajectory of the recoil nuclei and the emitted γ-ray. Good agreement between measured and calculated Doppler uncorrected γ-ray energies confirm a proper reconstruction of the angle between a recoil nuclei vector and a vector of emitted γ-ray with respect to the beam axis. . 55
4.16 A schematic decay scheme of the L_i - level of interest, populated by levels L_h and dexciting to L_j levels 56

5.1 γ-ray spectrum of ^{70}Zn obtained for two target-degrader distances. With a ♦ symbol are indicated the unshifted components while with a ♠ are indicated the shifted components of the transitions. 60
5.2 Level scheme of ^{70}Zn obtained from the measured γ-ray spectrum . . 61
5.3 Decay curve and lifetime of 2^+ and 4^+ states of ^{70}Zn. The red-dotted lines represent an error bar of the mean lifetime calculated for both distances. 62
5.4 γ-ray spectrum of ^{72}Zn for the 99 μm target-degrader distance (left-hand side) and corresponding level scheme (right side). With a ♦ symbol are indicated the unshifted components while with a ♠ are indicated the shifted components of transitions. 63
5.5 Evolution of γ-ray spectrum of $2^+ \rightarrow 0^+$ (upper figure), $4^+ \rightarrow 2^+$ (middle figure) and $6^+ \rightarrow 4^+$ (lower figure) transitions in ^{72}Zn obtained for two target-degrader distances. With a ♦ symbol are indicated the unshifted components while with a ♠ are indicated the shifted components. 65
5.6 γ-ray spectrum of ^{68}Zn for 33 μm target-degrader distance (left side) and corresponding level scheme (right side) 66

5.7 The total energy of ^{68}Zn as a function of the angle of the emitting recoil nucleus. Different selection of excitation energies is indicated: a red long-dashed line encompasses nuclei with a low excitation energy, with black line nuclei with medium excitations are selected, while the region selected by short-dashed line corresponds to a low excitation energy. The corresponding evolution for the $2^+ \rightarrow 0^+$ transition as a function of the selected excitation region is shown on the right-hand side of the figure. Spectra from the top till the bottom of the figure corresponds to the ^{68}Zn spectrum obtained for a low (a), medium (b) and high (c) excitation energy selection. 66

5.8 γ-ray spectrum of ^{69}Zn for 33 μm target-degrader distance (left-hand side) and the corresponding level scheme (right-hand side) 68

5.9 Partial γ-ray spectrum of ^{69}Zn showing the unassigned transitions at E_γ=1109(3) keV measured at 33.6 μm (left-hand side of figure) and 99 μm (right-hand side) target-degrader distances. 69

5.10 γ-ray spectrum of ^{71}Zn for 99 μm target-degrader distance (left-hand side) and corresponding level scheme (right-hand side). The shifted components are indicated with a ♠ symbol, the unshifted ones with a ⧫, while unknown transitions are indicated with a * symbol. 70

5.11 γ-ray spectra of ^{71}Zn zooming around several transitions for two target-degrader distances. Shifted components are indicated with a ♠ symbol and unshifted with a ⧫ symbol. Each peak was fitted from the spectrum where it is better pronounced and its energy was then fixed for fitting in the other spectrum. 71

5.12 γ-ray spectrum of ^{73}Zn (left-hand side). Unknown transitions were indicated with a * symbol. The corresponding level scheme is presented on the right-hand side. 73

5.13 γ-ray spectrum of ^{69}Cu (left-hand side). The shifted components are indicated with a ♠ symbol, the unshifted ones with a ⧫, while unknown transitions are shown with a * symbol. The corresponding level scheme is presented on the right-hand side. 73

5.14 Fit of the $(7/2^-) \rightarrow 3/2^-_{g.s.}$, $(7/2^-_2) \rightarrow 3/2^-_{g.s.}$ transitions from the spectrum obtained for the 33.6 μm target-degrader distance (upper spectrum) and 99.0 μm (lower spectrum). 74

6.1 Systematics of low-lying states in Zn and Ni isotopes with neutrons filling the $\nu g_{9/2}$ orbital and N=50 isotones with protons confined in $\pi g_{9/2}$ orbital. 78

6.2 The Nilsson orbitals around N=40 (modified from [89]) 79

6.3 The proton occupancy of the 0^+ (left-hand side) and 2^+_1 state (right-hand side) of Zn isotopes obtained with a JUN45 interaction [53] . . 79

6.4 Schematic representation of ^{70}Zn and valence space used for JUN45 interaction [53] (left hand side) and LNPS interaction [39] (right hand side) 80

6.5 Results of B(E2; $2^+ \rightarrow 0^+$) (top figure) and B(E2; $4^+ \rightarrow 2^+$) (bottom figure) values for Zn isotopes obtained in this experiment, compared with a recent deep-inelastic experiment and other experimental results. The results are compared with a beyond mean-field calculations with Gogny D1S interaction and shell model calculations using JUN45 [53] and LNPS [39] interactions. 81

6.6 Experimental energy for the 2^+ and 4^+ states as a function of the neutron number N for Zn isotopes compared with theoretical calculations: shell model with the JUN45 and LNPS interactions and with a beyond mean-field calculations using the Gogny D1S interaction . 84

6.7 Systematics of the B(E2; $4^+ \rightarrow 2^+$)/B(E2; $2^+ \rightarrow 0^+$) ratio for the Zn isotopes 85

6.8 An excerpt of nuclear chart showing the nuclei that were proposed to exhibit seniority as a good quantum number (black dots for known data); gray dots regions where this behaviour is also expected. Experimental data of B(E2; 2J-1→ 2J-3) systematics for the magic nuclei are indicated in order to show seniority like behaviour. The figure is taken from [99]. 86

6.9 From left to right B(E2; J→ J-2) systematics for system with 2 particles in $g_{9/2}$ orbital are presented in a pure seniority scheme; for ^{72}Zn (2 neutrons in $g_{9/2}$ orbital with 2 additional protons outside the close shell) ; for ^{70}Ni(2 neutrons in $g_{9/2}$ orbital) and ^{92}Mo (two protons in the $g_{9/2}$ orbital). When known, the B(E2) values are normalised to B(E2; $2^+ \rightarrow 0^+$) transition for each isotope. The experimental energy levels for different nuclei are not equal, but they are arbitrarily set to the same value for all nuclei. 87

6.10 Systematics of negative-parity low-lying states in odd-Zn compared with the energy of the first 2^+ state in neighbouring energy level of the neighbouring even-Zn isotopes. 88

7.1 The low energy spectra of the N=50 isotones ^{92}Mo, ^{94}Ru, ^{96}Pd, ^{98}Cd (upper figure) and Ni isotopes $^{70-76}$Ni (bottom figure). The observed states presented on left-hand side of each isotope are compared with results from the $(g_{9/2})^n$ shell model calculation. States 4^+ and 6^+ with exact seniority $v = 4$ are shown with thick lines. 97

7.2 Schematic representation of the valence space using $pfg_{9/2}$ interaction. Neutrons were blocked in the $f_{7/2}$ orbital while excitations from $pf_{5/2}$ to $g_{9/2}$ orbital. In the proton space, the $g_{9/2}$ shell was blocked and only excitations from $f_{7/2}$ to $pf_{5/2}$ were allowed. 99

7.3 Schematic representation of single nucleon transfer in the j = 9/2 shell for the 2, 3 and 4 particle or hole systems (^{70}Ni, ^{71}Ni and ^{72}Ni or ^{76}Ni, ^{75}Ni and ^{74}Ni) with the assumption that seniority is conserved. Allowed transitions are indicated with a full arrow, while forbidden transitions are indicated with a dotted arrow. 101

7.4 Schematic representation of a single nucleon transfer in the j = 9/2 shell for the 2, 3 and 4 particles or holes system (^{70}Ni, ^{71}Ni and ^{72}Ni or ^{76}Ni, ^{75}Ni and ^{74}Ni) with slightly broken symmetry. Transfer reactions are drawn for 4^+ states (the same results are obtained with 6^+ states. Allowed transitions are indicated with a full arrow, weak transitions are indicated with dashed lines, while forbidden transitions are indicated with a dotted arrow. 104

8.1 The proton and neutron single particle energies of the orbitals in the ^{100}Sn nucleus predicted by Grawe et al. [110]. Fully occupied orbitals are indicated with solid line, while dashed lines indicate empty orbitals. Decay governed by only possible Gamow - Teller spin-flip transition from proton in $g_{9/2}$ to neutron in $g_{7/2}$ is illustrated. . . . 110

8.2 Shell model prediction for the ^{100}Sn β^+/EC decay. The level scheme is taken from [111] 112

8.3 Gamow – Teller strength in the decay of various Sn isotopes. Comparison of results from different theoretical models (B_{GT}^{ref} [112], B_{GT}^{FFS} [113], Quasiparticle Random Phase Approximation – B_{GT}^{QRPA} [113] with available experimental results [114, 115, 116]. The extrapolated value for ^{100}Sn was estimated by Batist et al. [117]. The figure is taken from [118]. 113

8.4 Theoretical calculations of the GT strength distribution in ^{100}Sn nucleus [119]. 114

8.5 Log(ft) values for the allowed nuclear β – decays. The decay is the fastest β – decay in the nuclear chart.[116]. 116

9.1 Scheme of BigRIPS separator with indicated positions of target, wedges and beam-line detectors at each focal plane. 123

9.2 Particle identification matrix in Z vs A/Q for configuration A: (top figure) without applied cleaning conditions (major contaminants consisting of nuclei close to the projectile are also shown) and (bottom figure) gated around isotopes of interest and applied cleaning conditions. 124

9.3 Delayed γ spectra of ^{96}Pd and ^{98}Cd from the 4 mm configuration, used for identification in Z and A/Q.. 125

9.4 Particle identification plot around the ^{100}Sn region, for configurations A (left hand side) and B (right hand side) after applying cleaning procedures. The ^{98}Cd and ^{96}Pd used for particle identification are indicated. 126

9.5 Momentum distribution for ^{97}Ag measured in the setup with 8 mm target . . . 128

9.6 Production cross-section compared with previous results and theoretical calculations . . . 131

10.1 Scheme of BigRIPS separator and Zero-degree spectrometer with all detectors indicated at different focal planes. The positions of target and wedges are also indicated. . . . 134

10.2 Schematic representation of the WAS3ABi detector placed at the F11 focal plane showing the XY detector, followed by 3 DSSD WAS3ABi detectors for heavy ion implantation and a stack of 10 SSSSD used as beta-absorbers. . . . 136

10.3 Particle identification matrices in Z vs A/Q plot around the ^{100}Sn without any cleaning conditions applied (Fig. a) and with applied cleaning procedures described in the text (Fig. b). . . . 137

10.4 a) Z distribution obtained for N=Z nuclei and b) A/Q distribution measured for Sn isotopes . . . 138

List of Tables

4.1 Time resolution of different TOFs 43
4.2 Charge state distributions obtained after fine tuning of T_{offset} (see text) for ^{70}Zn detected in Si8 and Si12. 45

5.1 The measured lifetimes in ^{70}Zn 63
5.2 Results of measured lifetimes in ^{72}Zn 64
5.3 Evolution of $2^+ \rightarrow 0^+$ and $4^+ \rightarrow 2^+$ transition intensities in ^{68}Zn as a function of selection of excitation energy E*. 67
5.4 Measured lifetime in ^{68}Zn 67
5.5 The results of measured lifetimes in ^{69}Zn 68
5.6 Measured lifetimes in ^{71}Zn 72
5.7 Summary of measured lifetimes in this experiment. The lifetimes reported for the first time are in bold characters. 75
5.8 Summary of new γ-rays identified in this experiment. 76

6.1 Measured lifetimes and B(E2; J→ J-2) values for low-lying states in ^{68}Zn, ^{70}Zn and ^{72}Zn, compared with previous experiments and shell-model calculations. 80

7.1 Spectroscopic amplitudes (SA) for transfer from the 0_1^+ ground state of ^{76}Ni to the $9/2_1^+$ ground state and $9/2_2^+$ state of ^{75}Ni in a $(1g_{9/2})^n$ configuration with ANTOINE and with using eq. 7.9 expression. . . 102
7.2 Spectroscopic amplitudes (SA) for transfer from the $9/2_1^+$ ground state of ^{75}Ni to several states in ^{74}Ni in the $(1g_{9/2})^n$ space and in the large space with $pfg_{9/2}$ interaction with neutrons blocked in $f_{7/2}$ and with blocking of proton $g_{9/2}$ orbital. Results are compared with analytical calculations using expression (7.9). Table cells marked with / correspond to cases in which analytical results were not calculated. 103

9.1 Experimental charge state distributions of ^{124}Xe for both target thicknesses, compared with calculated charge state distributions using GLOBAL code [131]. 120
9.2 Summary of the beam intensities for each configuration 122

9.3 Counting rate based on the PID plot after applied cleaning conditions. All counting rates are normalised on the beam intensity of 10 pnA. . 127
9.4 Transmission calculated by LISE++ and production cross-section obtained for configurations with 4 and 8 mm target thickness are presented. Results are compared with experimental results from experiment at GSI and with EPAX parametrisation ver. 2.15 and 3.01. . . 130

10.1 New isotopes identified. The number of nuclei in each isotope is indicated with their average Z and A/Q values. 139

13.1 Spectroscopic amplitudes (SA) for transfer from the $9/2_1^+$ ground state and $9/2_2^+$ state of ^{75}Ni to several states in ^{76}Ni in a $(1g_{9/2})^n$ configuration and analytical calculations using 7.9 expression. 149
13.2 Spectroscopic amplitudes (SA) for transfer from the $9/2_1^+$ ground state and $9/2_2^+$ state of ^{75}Ni to several states in ^{74}Ni in the full space with regular $pfg_{9/2}$ interaction with neutrons blocked in $f_{7/2}$ and with blocking of proton $g_{9/2}$ orbital. Results are compared with analytical calculations using expression 7.9. Table cells marked with / correspond to cases in which analytical results were not calculated. . 150

Résumé:

Nous avons étudié la structure des noyaux autour de ^{68}Ni, ainsi que la production, séparation et identification des isotopes se trouvant dans le voisinage du noyau doublement magique 100Sn. Dans la première partie, est discutée l'évolution de la collectivité et l'interaction entre degrés de liberté particule indépendante et collectifs autour de ^{68}Ni. Nous avons mesuré des temps de vie dans les noyaux de Zn autour de N=40, produits par réactions profondément inélastiques ^{238}U+^{70}Zn à GANIL, à l'aide d'un "plunger". Les noyaux d'intéérêt, étaient identifiés par le spectromètre VAMOS, les gamma par le détecteur EXOGAM. Des durées de vie, nous avons extrait les probabilités de transition réduites. De nouvelles transitions ainsi que des durées de vie sont mesurées pour la première fois. Les résultats sont discutés dans le cadre de calculs modèle en couches. Dans la deuxième partie, la conservation partielle de séniorité dans la couche $g_{9/2}$ et son influence sur le transfert d'une particule est discuté. La troisième partie présente un test réalisé à RIKEN (Japon), visant à évaluer deux configurations du séparateur BigRIPS, afin d'optimiser la production et la sélection des noyaux de ^{100}Sn. Cette étude a été utilisée par la suite pour notre expérience, consacrée à la mesure de la force Gamow-Teller dans la désintégration de ^{100}Sn. Les noyaux autour de ^{100}Sn ont été produits par fragmentation d'un faisceau de ^{124}Xe à 345 MeV/u. La section efficace de production des noyaux autour de ^{100}Sn a été mesurée. La recherche de nouveaux isotopes et de nouveaux isomères est présentée.

Abstract:

In this thesis we investigated the structure of nuclei around ^{68}Ni as well as the production, separation and identification of proton-rich isotopes lying in the vicinity of the doubly-magic ^{100}Sn nucleus. In the first part, we discuss the evolution of collectivity and the interplay between collective and single-particle degrees of freedom in nuclei around ^{68}Ni. We measured lifetimes in Zn isotopes around N = 40 produced in ^{238}U + ^{70}Zn deep-inelastic collisions at GANIL. We used a plunger device and the recoil-distance Doppler-shift method. The nuclei of interest were identified by the VAMOS spectrometer and the γ-rays with the EXOGAM array. The reduced electromagnetic transitions probabilities were extracted from the lifetimes. Several transitions and lifetimes are reported for the first time. The experimental results are discussed in the framework of shell model calculations. In the second part, the partial conservation of seniority in the $g_{9/2}$ shell and its influence on one-particle transfer is discussed. The third part presents the analysis of a test performed at RIKEN (Japan) to evaluate two settings of the BigRIPS separator for optimizing the production and selection of ^{100}Sn. This study has been used to setup our subsequent experiment, dedicated to the measurement of the Gamow-Teller strength in the decay of ^{100}Sn. Nuclei around ^{100}Sn were produced by fragmentation of a 345 MeV/u ^{124}Xe beam on a Be target. The production cross-sections of nuclei around ^{100}Sn were measured. The search for new isotopes and new isomers in all identified nuclei is presented.

Mots clés: Struture Nucléaire; Isotopes; Modèles en couches (physique nucléaire); Durée de vie (ingénierie)
Discipline: Constituants élémentaires et physique théorique

Grand Accélérateur National d'Ions Lourds
Bd Henri Becquerel- BP 55027 - 14076 CAEN Cedex 05